

HZDR-100

MEASURING SUB-FEMTOSECOND TEMPORAL STRUCTURES IN MULTI-TEN KILOAMPERE ELECTRON BEAMS

Omid Zarini

Wissenschaftlich-Technische Berichte
HZDR-100 · ISSN 2191-8708

**WISSENSCHAFTLICH-
TECHNISCHE BERICHTE**

hZDR



**HELMHOLTZ
ZENTRUM DRESDEN
ROSSENDORF**

Wissenschaftlich-Technische Berichte
HZDR-100

Omid Zarini

**MEASURING SUB-FEMTOSECOND TEMPORAL
STRUCTURES IN MULTI-TEN KILOAMPERE
ELECTRON BEAMS**

HZDR

 **HELMHOLTZ**
| ZENTRUM DRESDEN
| ROSSENDORF

Druckausgabe: ISSN 2191-8708

Elektronische Ausgabe: ISSN 2191-8716

Die elektronische Ausgabe erscheint unter Creative Commons License (CC BY 4.0):

<https://www.hzdr.de/publications/Publ-29222>

<urn:nbn:de:bsz:d120-qucosa2-339775>

Die vorliegende Arbeit wurde sowohl als Dissertation an der Fakultät Mathematik und Naturwissenschaften der Technischen Universität Dresden sowie als Wissenschaftlich-Technischer Bericht des Helmholtz-Zentrum Dresden – Rossendorf mit der Berichtsnummer **HZDR-100** veröffentlicht.

2019

Herausgegeben vom

Helmholtz-Zentrum Dresden - Rossendorf

Bautzner Landstraße 400

01328 Dresden

Germany

MEASURING SUB-FEMTOSECOND TEMPORAL STRUCTURES IN MULTI-TEN KILOAMPERE ELECTRON BEAMS

Omid Zarini, Diplom

Born on: 1st May 1984 in Mashhad

DISSERTATION

to achieve the academic degree

DOCTOR RERUM NATURALIUM (DR. RER. NAT.)

First referee

Prof. Dr. Ulrich Schramm

Second referee

Prof. Dr. Thomas Cowan

Prof. Dr. Michael Downer

Supervisors

Dr. Arie Irman

Dr. Alexander Debus

Submitted on: 18th December 2018

Defended on: 15th April 2019

*I dedicate this to my mom.
Her selflessness will always be remembered.*

ABSTRACT

In laser wakefield acceleration, an ultra-short high-intensity laser pulse excites a plasma wave, which can sustain accelerating electric fields of several hundred GV/m. This scheme advances a novel concept for compact and less expensive electron accelerators, which can be hosted in a typical university size laboratory. Furthermore, laser wakefield accelerators (LWFA) feature unique electron bunch characteristics, namely micrometer size with duration ranging from several fs to tens of fs. Precise knowledge of the longitudinal profile of such ultra-short electron bunches is essential for the design of future table-top X-ray light-sources and remains a big challenge due to the resolution limit of existing diagnostic techniques.

Spectral measurement of broadband coherent and incoherent transition radiation (TR) produced when electron bunches passing through a metal foil is a promising way to analyze longitudinal characteristics of these bunches. Due to the limited reproducibility of the electron source this measurement highly requires single-shot capability. An ultra-broadband spectrometer combines the TR spectrum in UV/NIR (200-1000 nm), NIR (0.9-1.7 μm) and mid-IR (1.6-12 μm). A high spectral sensitivity, dynamic bandwidth and spectral resolution are realized by three optimized dispersion and detection systems integrated into a single-shot spectrometer. A complete characterization and calibration of the spectrometer have been done concerning wavelengths, relative spectral sensitivities, and absolute photometric sensitivities, also taking into account for the light polarization. The TR spectrometer is able to characterize electron bunches with charges as low as 1 pC and can resolve time-scales of 0.4 fs. Electron bunches up to 16 fs (rms width) can be reconstructed from their TR spectrum.

In the presented work, the self-truncated ionization induced injection (STII) scheme has been explored to study the relevant beam parameters especially its longitudinal bunch profile and the resulting peak current. Proper focusing of a high power laser pulse into a supersonic gas-jet target and tailoring the conditional laser and plasma density and taking advantage of the relativistic self-focusing effects are investigated in this PhD thesis in order to study the final beam parameters as well as the consequent beam loading effects by producing nC-class mono-energetic electron beams.

In the experiment at HZDR, the DRACO 100TW Ti:Sa based laser system is used in conjunction with a He-N₂ mixed, supersonic gas-jet target. Under optimized conditions, mono-energetic electron bunches are accelerated, which are massively loaded up to several 100 pC at 300 MeV peak energy with a narrow energy spread of a few 10 MeV. Reconstruction results of TR spectra, measured by TR spectrometer, show that the shortest electron bunch duration is at about 13 fs FWHM corresponding to a peak current as high as 20 kA. Such peak current is about one order of magnitude higher than those generated by conventional RF linear accelerator. This landmarks a significant finding of this thesis.

PUBLICATIONS BY THE AUTHOR

- O. Zarini
"Entwicklung eines breitbandigen optischen Spektrometers zur Pulsdauermessung ultrakurzer Elektronenpulse" (Technische Universität Dresden, 2013)^[1].
- O. Zarini, A. Köhler, J. Couperus, R. Pausch, T. Kurz, S. Schöbel, H. Meißner, M. Bussmann, U. Schramm, A. Irman & A. Debus
"Advanced Methods For Temporal Reconstruction Of Modulated Electron Bunches"
In: IEEE conf. proc. of 18th AAC, 1-5 (2018)^[2].
- O. Zarini, J. Couperus Cabadağ, A. Köhler, T. Kurz, S. Schöbel, W. Seidel, M Bussmann, U. Schramm, A. Irman & A. Debus
"A Single-shot, ultra-broadband and highly sensitive spectrometer for short pulse, high resolution and low light diagnostic applications"
In: Physical Review Accelerators and Beams, (2018, in preparation)^[3].
- J.P. Couperus, R. Pausch, A. Köhler, O. Zarini, J.M. Krämer, M. Garten, A. Huebl, R. Gebhardt, U. Helbig, S. Bock, K. Zeil, A. Debus, M. Bussmann, U. Schramm & A. Irman.
"Demonstration of a beam loaded nanocoulomb-class laser wakefield accelerator"
In: Nature Communications, 8, 487 (2017)^[4].
- A. Irman, J.P. Couperus, A. Debus, A. Köhler, J.M. Krämer, R. Pausch, O. Zarini & U. Schramm.
"Improved performance of laser wakefield acceleration by tailored self-truncated ionization injection"
In: Plasma Physics and Controlled Fusion, 60, 044015 (2018)^[5].
- U. Schramm, M. Bussmann, A. Irman, M. Siebold, K. Zeil, D. Albach, C. Bernert, S. Bock, F. Brack, J. Branco, J.P. Couperus, T.E. Cowan, A. Debus, C. Eisenmann, M. Garten, R. Gebhardt, S. Grams, U. Helbig, A. Huebl, T. Kluge, A. Köhler, J.M. Krämer, S. Kraft, F. Kroll, M. Kuntzsch, U. Lehnert, M. Loeser, J. Metzkes, P. Michel, L. Obst, R. Pausch, M. Rehwald, R. Sauerbrey, H.P. Schlenvoigt, K. Steiniger & O. Zarini.
"First results with the novel petawatt laser acceleration facility in Dresden."
In: Journal of Physics: Conference Series, 874, 12028 (2017)^[6].
- J.M. Krämer, A. Jochmann, M. Budde, M. Bussmann, J.P. Couperus, T.E. Cowan, A. Debus, A. Köhler, M. Kuntzsch, A. Laso Garcia, U. Lehnert, P. Michel, R. Pausch, O. Zarini, U. Schramm & A. Irman.
"Making spectral shape measurements in inverse Compton scattering a tool for advanced diagnostic applications"
In: Scientific Reports, 8, 1 (2018)^[7].
- J.P. Couperus, A. Köhler, T.A.W. Wolterink, A. Jochmann, O. Zarini, H.M.J. Bastiaens, K.J. Boller, A. Irman & U. Schramm.
"Tomographic characterisation of gas-jet targets for laser wakefield acceleration."
In: Nuclear Instruments and Methods in Physics Research Section A: Accelerators, Spectrometers, Detectors and Associated Equipment, 830, 504-509 (2016)^[8].

- A. Köhler, J.P. Couperus, O. Zarini, A. Jochmann, A. Irman, & U. Schramm.
“Single-shot betatron source size measurement from a laser-wakefield accelerator.”
In: Nuclear Instruments and Methods in Physics Research Section A: Accelerators, Spectrometers, Detectors and Associated Equipment, 829, 265-269 (2016)^[9].
- J.M. Krämer, J.P. Couperus, A. Irman, A. Köhler, M. Kuntzsch, U. Lehnert, P. Michel, U. Schramm & O. Zarini.
“Bunch Arrival-Time Monitoring for Laser Particle Accelerators and Thomson Scattering X-Ray Sources.”
In: Proceedings of the 5th International Beam Instrumentation Conference (IBIC2016), TUPG53, 468-470 (2016)^[10].
- T. Kurz, J.P. Couperus, J.M. Krämer, H. Ding, S. Kuschel, A. Köhler, O. Zarini, D. Hollatz, D. Schinkel, R. D’Arcy, J.P. Schwinkendorf, A. Irman, U. Schramm & S. Karsch.
“Calibration and cross-laboratory implementation of scintillating screens for electron bunch charge determination.”
In: Review of Scientific Instruments, 89, 0933039 (2018)^[11].
- T. Heinemann, B. Hidding, R.W. Assmann, A. Martinez de la Ossa, A. Knetsch, O. Kononenko, J.P. Couperus, A. Irman, A. Köhler, T. Kurz, U. Schramm & O. Zarini.
“Investigating the Key Parameters of a Staged Laser- and Particle Driven Plasma Wakefield Accelerator Experiment.”
In: Proceedings of International Particle Accelerator Conference (IPAC17), TUPIK010, 1703-1706 (2017)^[12].

NOTE

Some of the work presented in this thesis has been previously published in above-mentioned publications.

Explicitly: A large part of the phase retrieval procedure presented in sections 6.1 and 6.2 has been published in ref.^[2]. Some specifics on the electron spectrometer design and accuracy discussed in section 5.1.3 have been published in ref.^[11] and ref.^[6]. The presented work on transition radiation spectrometer in chapter 4 will be published in ref.^[3].

CONTENTS

Abstract	v
1. Introduction	1
1.1. Laser wakefield acceleration	1
1.2. Non-destructive bunch duration measurement methods	3
1.3. Thesis outline	3
2. Basics of laser plasma acceleration	4
2.1. Ionisation	4
2.2. Ponderomotive force	5
2.3. Relativistic self-guiding of high-intensity ultra-short laser pulses	6
2.4. Plasma based acceleration	8
2.4.1. Bubble regime	9
2.5. Injection schemes	11
2.6. Beam loading	13
3. Theory of Transition radiation	16
3.1. Transition radiation from single electron	16
3.1.1. Calculation of spectral and angular TR	17
3.1.2. Radiation energy spectrum	18
3.2. Transition radiation from electron bunch	19
3.2.1. Electron bunch distribution	22
3.2.2. Effect of diffraction	24
3.3. Summary	24
4. Transition Radiation Spectrometer	25
4.1. Design and setup	26
4.1.1. Basics of prism spectrometers	27
4.1.2. Choice of beam splitters	30
4.1.3. Prisms design	30
4.1.4. Echelle spectrometer	32
4.1.5. Detectors	34
4.2. Calibration	36
4.2.1. Wavelength calibration	37
4.2.2. Achieved resolution and resolving power	38

4.2.3.	Relative response calibration	40
4.2.4.	Absolute calibration	41
4.2.5.	Detection threshold	44
4.3.	Conclusion	45
5.	Experimental setup	47
5.1.	LWFA experiment at HZDR	47
5.1.1.	DRACO laser system	49
5.1.2.	LWFA target	51
5.1.3.	Electron spectrometer	52
5.2.	Transition radiation beam-line & screen	52
5.3.	Transverse profile of TR	56
6.	Electron bunch profile reconstruction	58
6.1.	Introduction to Foldwrap reconstruction procedure	58
6.1.1.	Gerchberg-Saxton algorithm	59
6.1.2.	Hybrid Input Output algorithm	61
6.1.3.	Parameter optimization of Foldwrap procedure	61
6.1.4.	Odd-phase constraint	62
6.1.5.	Zero-frequency constraint	62
6.1.6.	Kramers-Kronig analysis	63
6.2.	Tests with synthetic data	64
6.2.1.	Modeling structured bunches	64
6.2.2.	Reconstructing single and triple Gaussians	65
6.2.3.	Post-selection algorithm for highly modulated distributions	67
6.3.	Bunch profile reconstruction from experimental CTR spectra	71
6.3.1.	Preparation of CTR data	71
6.3.2.	Results of reconstruction	75
7.	High peak current from a nanocoulomb-class laser wakefield acceleration	83
7.1.	Experimental parameters	83
7.2.	Variation of bunch duration with beam charge	86
7.2.1.	Influence of zero-frequency constraint on present reconstructions	86
7.2.2.	Variation of bunch Charge with nitrogen doping	87
7.2.3.	Analysis of peak current	88
7.3.	Particle-in-cell simulations	91
7.4.	Discussions & outlook	95
7.4.1.	Influence of metallic foils on electron bunch quality	96
7.4.2.	Quasi-monoenergetic and high energy electron beam	97
7.4.3.	Analysis of absolute and relative energy spread	97
7.4.4.	Analysis of geometrical and normalized divergence	97
8.	Summary & outlook	103
A.	Supplementary figures	107
A.1.	Transition radiation spectra	107
A.2.	Examples for bunch reconstruction	108
	Bibliography	108

1. INTRODUCTION

Particle accelerators are playing an important role in many fields, not only in science but also in medicine, industry, and security. Since the first demonstration of particle accelerator in the early 1930s by Cockcroft and Walton^[13], they have been rapidly developed and continuously improved to attain higher charge and higher energies. Although the accelerator technology is still an ongoing development, conventional radio-frequency (RF) accelerators are limited by electrical breakdown at the metal walls to accelerating fields of around 100 MV/m^[14]. Therefore one requires large-scale accelerators and expensive infrastructures in order to achieve GeV-class high-quality electrons such as the kilometer long Stanford Linear Accelerator Center (SLAC).

The enormous complexity and cost of these machines, as well as their kilometer long dimension, complicate to realize such machines at industry or university scale. With the limited number of advanced light sources such as synchrotrons and X-ray free-electron lasers (FELs) and the high demand on their application, a new generation of electron accelerators which is not a subject of physical limitations is highly desired.

1.1. LASER WAKEFIELD ACCELERATION

Laser plasma accelerators (LPA) allow us to overcome the upper limit on the accelerating field and to reach markedly high accelerating gradients. As the plasma is a pre-ionized gas, the generated accelerating field is not limited by the vacuum electrical breakdown^[15]. On the other hand, the high peak power of available lasers is incomparable and is capable of sustaining orders of magnitude increases in accelerating gradients to as high as several 100 GV/m. This technology offers the potential to shrink the size and cost of this new generation of particle accelerators to the university research level while the attained energies are comparative to the large-scale conventional accelerators. The concept was first proposed by Tajima and Dawson in 1979^[16]: The ponderomotive force of a high-intensity laser pulse expels electrons from its path and thereby creates unshielded ions directly behind the driver. The Coulomb force induced by the charge separation pulls electrons back to the path of the laser and overshoots the equilibrium position. This plasma oscillation creates a plasma wave behind the driver laser. Electrons can be trapped into this plasma wake and accelerated to high energies. In this manner, the plasma mediates the transfer of energy from the laser to the electron bunch.

To illustrate the concept of the LPA, the wake is analogous to the set up behind a motorboat in water, and the electrons have been said to “surf” down the crests^[15] (see figure 1.1). This concept was extended by Chen et al.^[17] to include wakefields driven by particle beams instead

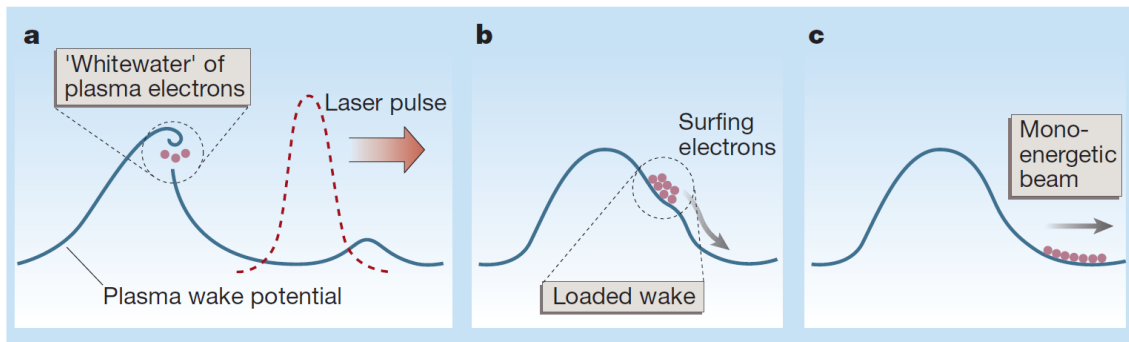


Figure 1.1.: **Self-injection and subsequent acceleration (until dephasing).** **a**, a laser pulse excites a plasma and gains the wake potential until it breaks, leading to some electrons becoming injected into the wake, i.e., *whitewater* and *surf* the wave. **b**, The load of the electrons deforms the wake, stopping further trapping of electrons from the plasma. **c**, the bunch of electrons surf to the bottom of the wake potential and gain energy. Figure is taken from ref.^[15]

of lasers^[18–20]. The results presented by Geddes et al.^[21], Mangles et al.^[22] and Faure et al.^[23] are a milestone in the LPA. They provide the first demonstration that a beam of electrons can be accelerated in a wakefield to quasi-monoenergetic energy. In 2002, Malka et al.^[19] showed that well-collimated beams of 10^8 electrons could be produced in the wave-breaking regime of the LPA. However, the energy spread of the beams was 100 %. This wide range of energies occurred because the particles were trapped from the background plasma rather than injected into a single location near the peak of the plasma density modulation.

Despite the high accelerating gradients in laser plasma accelerators, the accelerated electron bunches inherently have a duration of a few fs up to 10s of fs^[24–26]. The ultra-short bunch duration is due to the fact that the electrons can be accelerated if they only become injected into the accelerating region of the plasma cavity which is at about half of the corresponding plasma wavelength. Furthermore, due to the bubble shape of cavities, a large amount of charge can be injected into the cavity^[27,28]. As a consequence, the attained peak current in LPAs can be impressively high^[4,25,29]. The achievable high peak current has strong impact on emerging applications and makes laser plasma accelerators, in particular, laser wakefield acceleration (LWFA) a promising driver for the next-generation of compact light sources, such as high field THz^[30,31], high-brightness X-ray^[32,33] and γ -ray sources^[34], compact FELs^[35,36] and laboratory-size beam driven plasma accelerators (PWFA)^[37,38].

For typical LWFA electron bunches, the bunch envelope could reach several tens of fs (plasma wavelength) while its potential sub-structures could extend into the sub-fs range (driver laser wavelength). A detailed understanding of the longitudinal current profile of these electron bunches is essential for the achievement and control of FEL generated ultrashort photon pulses based on the self-amplified spontaneous emission (SASE) process^[35,39,40]. The resulting X-ray pulse duration could differ as much as a factor of two from that of the electron bunch, as reported by some early experiments^[41,42]. This deviation could be due to a non-uniform lasing inside the electron bunch since the time-dependent electron beam properties strongly determine the intensity of the FEL power profile^[43]. To control such complex light sources and to accurately interpret the experimental photon data, temporal characterization of the electron bunches on a shot-by-shot basis is critical and highly desired.

1.2. NON-DESTRUCTIVE BUNCH DURATION MEASUREMENT METHODS

Traditional techniques to measure the electron bunch duration, such as streak cameras and transverse deflecting structures (TDS)^[44–46], firstly destroy the beam since they are direct measurements methods, secondly, do not have the temporal resolution required for fs bunch duration.

Electro-optical (EO) methods are often used to determine the temporal profile of electron bunches^[26,47–49]. These methods are based on cross-correlation of two laser pulses: While one laser pulse provides the reference, the other laser pulse incorporates an EO-crystal (for example ZnTe) which modulates the laser polarization according to the temporal characteristic of the electric field from the transition radiation or the self-field of the electron bunch. This modulation can then be separated from the non-modulated portion of the laser pulse using a crossed polarizer and then cross-correlated with the reference pulse. However optical crystals are limited in temporal resolution. Due to the transversal-optical resonances in EO-materials, it will become more and more challenging to realize temporally resolved measurements below 100 fs^[50].

The previously used methods for determining the duration of the bunch either do not work with ultra-short electron pulses or require several reproducible shots to scan the longitudinal profile of an electron bunch. However, electron pulses from LWFAs vary from shot to shot due to the variations in the laser pulse characteristic or due to the irregularities in the gas nozzle providing the plasma medium.

In this work, measuring the transition radiation (TR) emitted by an electron bunch traversing a metallic-vacuum interface^[51,52] is investigated. It is a promising method to non-destructively analyze the longitudinal bunch characteristics ranging from tens of fs down to sub-fs with single-shot capability. In this method, the TR spectrum provides a frequency dependent coherent radiation signature of the electron bunch from which its form factor can be obtained. The longitudinal distribution of the corresponding electron bunch can be reconstructed by using an appropriate phase retrieval algorithm^[2,53]. Synchronous measurement of the absolute electron energy spectrum, on the other hand, enables to measure its corresponding peak current.

1.3. THESIS OUTLINE

The thesis at hand is structured as follows: The basic concept of laser-wakefield accelerators is introduced in chapter 2. Chapter 3 gives a detailed description of the theory of transition radiation, in which relevant formulas and expressions will be derived in order to calculate the emitted TR by an electron bunch. Furthermore, the design and calibration of the ultra-broad-band TR spectrometer are described in chapter 4. Following this, the LWFA setup, as well as commissioning of the TR spectrometer is presented in chapter 5. The Foldwrap phase retrieval algorithm is presented in chapter 6. Here we demonstrate the capabilities of this algorithm first on synthetic data and then on single-shot measured TR spectra. Chapter 7 demonstrates a thorough analysis of electron bunch parameters and discusses the variation of the beam parameters such as the bunch duration and the peak current in dependence of injected charge. A summary and outlook of this work are presented in chapter 8.

2. BASICS OF LASER PLASMA ACCELERATION

In this chapter, we review some basic theory in laser wakefield acceleration (LWFA). Experiment, presented in this work, is based on LWFA in bubble-regime which will be thus the focus of the theoretical descriptions presented here.

An ultra-short high power laser pulse is applied to ionize a gas medium and subsequently to form a plasma wave behind the driving laser. Electrons can thereby get trapped in this so-called *plasma density wake* and accelerated to high energies.

The ultra-short (tens of fs) pulse length of the driver laser is the key parameter in LWFAs. In contrast, in self-modulated laser-wakefield accelerators^[54,55] or the plasma beat-wave accelerators (PBWA)^[56,57] the plasma wake can be driven by longer pulses (\sim ps), each relies on its associated advantages and drawbacks.

In LWFA an ultra-short laser pulse with sufficiently high power is required to reach, firstly, high laser intensity to fulfill the acceleration criteria as will be discussed in section 2.1 and secondly to generate an effective wake in the background plasma, which is initiated by ponderomotive forces. The latter is discussed in section 2.2. Relativistic laser pulse guiding in a plasma is discussed in section 2.3. Basic concepts in formation of plasma wakefield are presented in section 2.4. A brief overview of different injection schemes is given in section 2.5. Finally, in section 2.6 beam loading and its consequence on the wakefield structure is discussed.

2.1. IONISATION

The fundamental component for realizing LWFA is the plasma medium in which a high-intensity laser pulse drives the plasma wakefield and, by trapping the electron into this wakefield, the electrons can be accelerated to higher energies. Here we describe plasma generation induced by laser via Tunneling ionization (TI) and Barrier suppression ionization (BSI). Both processes depend on the strength of an external electric field, e.g., the laser electric field, being strong enough to distort the atomic Coulomb potential according to^[58]

$$V_{\text{eff}}(x) = -\frac{Ze^2}{x} - eEx, \quad (2.1)$$

where Z is the charge state of the atom or ion. As can be seen from eq. 2.1, the Coulomb potential is suppressed by the laser electric field E . Depending on the strength of the laser electric field, this suppression can perturb the Coulomb potential to initiate a TI. In the case of BSI, the distortion is large enough to suppress the Coulomb potential below the electron binding potential completely. As a result, the bound electrons can escape from the atom potential. The required laser intensity to reach the BSI threshold is given by^[58]

$$I_{\text{BSI}} [\text{W/cm}^2] = 4 \times 10^9 \frac{E_{\text{ion}}^4 [\text{eV}]}{Z^2}, \quad (2.2)$$

where E_{ion} denotes the ionization energy for a bound electron. Since the ionization threshold for inner shell electrons is highest, the atom will be completely ionized once this threshold is reached. In the LWFA experiment described in this thesis, a mixture of He atoms and N_2 molecules is used as a plasma source. While the majority of plasma background electron are originating from He atoms ($\sim 99\%$) the K-shell N_2 electrons are served to be subsequently trapped and accelerated in the wakefield as will be later discussed in more detail.

Using high power lasers, e.g., $I_{\text{peak}} \sim 10^{19} \text{ W/cm}^2$ in combination with low- Z atoms like He has the advantage that the ionization probability is one even prior the main laser pulse arrives at the target. As a result, the pure laser-plasma interaction and its consequent relativistic self-focusing of the laser pulse in the created plasma channel are expected, as will be described in more detail in section 2.3. Due to the discrete ionization thresholds, the associated electrons can only become ionized if the laser field approaches their threshold. This fact is a key property of the BSI scheme that the inner shell electrons of N_2 atoms become ionized later in the wakefield and therefore can be injected into the plasma cavity. As mentioned above, a mixture of helium and nitrogen gas is used in the presented work. According to the eq. 2.2 the helium and nitrogen L-shell ($\text{N}^{1+} - \text{N}^{5+}$) electrons are ionized by the laser pedestal at laser intensities between 1.4×10^{14} and $1.5 \times 10^{15} \text{ W/cm}^2$, whereas nitrogen K-shell (N^{6+} and N^{7+}) electrons are only ionized close to the laser peak intensity at 1.0×10^{19} and $1.6 \times 10^{19} \text{ W/cm}^2$ respectively.

2.2. PONDEROMOTIVE FORCE

For the description of the plasma wakefield generation excited by the ponderomotive force of a high-intensity laser pulse, we take some assumptions according to the experimental conditions, presented in this work. A fully ionized plasma is assumed, which is created by an ultra-short high intense laser pulse according to the I_{BSI} ionization process. Furthermore, the plasma is assumed to be cold and unmagnetized, i.e., the thermal motion of electrons is negligible compared to the quiver motion. A collision-less plasma is assumed since we utilized a low-density gas jet target (see also section 5.1.2). The ions are assumed to remain stationary during the acceleration process due to their high mass compared to electron mass. Following these assumptions, the motion of the free electrons in an electromagnetic field is given by the Lorentz equation:

$$\frac{d\vec{p}}{dt} = -e \left(\vec{E} + \vec{v} \times \vec{B} \right), \quad (2.3)$$

where \vec{E} and \vec{B} are the electric and the magnetic field respectively and $\vec{p} = \gamma m_e \vec{v}$ the momentum of an electron. Furthermore, e , m_e , c denote the elementary unit of charge, the electron rest mass, the speed of light in vacuum respectively and $\gamma = 1/\sqrt{1 - v^2/c^2}$ denotes the relativistic Lorentz factor. Here and throughout this thesis, SI units are used.

For the non-relativistic case of electron motion ($v \ll c$) the contribution of the laser magnetic field, the second term on the right hand side of the eq. 2.3 can be neglected.

The ponderomotive force as perceived by an electron in the laser field E with frequency ω_0 can be derived as^[58]

$$\vec{F}_p \equiv m_e \overline{\frac{d\vec{v}}{dt}} = -\frac{e^2}{4m_e\omega_0} \nabla \vec{E}^2. \quad (2.4)$$

The ponderomotive force, also known as the radiation pressure, pushes electrons away from the region of the high-intensity. This process arising from the interaction between laser field and electrons and can be represented in terms of the normalized electrostatic potential, $\phi = e\Phi/m_e c^2$, and the normalized electromagnetic vector potential, $\mathbf{a} = e\mathbf{A}/m_e c$, where Φ and \mathbf{A} indicate the non-normalized potentials respectively.

On the short time scale, plasma electrons will oscillate in the laser field. This motion following the laser frequency ω_0 is called the quiver motion and the associated quiver momentum is given by:

$$\vec{p} \approx \frac{e\vec{A}}{c}. \quad (2.5)$$

In the case of relativistic motions, i.e., $v \rightarrow c$ the contribution of the magnetic field of the laser on the electron motion, i.e., $\vec{v} \times \vec{B}$ in eq. (2.3), has to be included. The latter will induce a force on the electron along the z-propagation axis. To determine the intensity threshold for which the relativistic effects have to be taken into account, the normalized vector potential is normally used. For a linear polarized laser pulse with peak intensity I_0 and peak power P_0 and for a Gaussian transverse profile, the normalized vector potential is given in practical units as^[59]

$$a_0 = \sqrt{\frac{e^2 \lambda_0^2 I}{2\pi^2 \epsilon_0 m_e^2 c^5}} \approx 8.6 \times 10^{-10} \lambda [\mu\text{m}] \sqrt{I [\text{W}/\text{cm}^2]}, \quad (2.6)$$

where λ_0 indicates the laser wavelength and ϵ_0 the vacuum permittivity. Once a_0 exceeds unity ($a_0 \geq 1$) the relativistic effects become relevant and the expression for the ponderomotive force given in eq. 2.4 has to be modified by including the magnetic field contribution of the laser field. This more complex treatment can be found in refs.^[60,61].

2.3. RELATIVISTIC SELF-GUIDING OF HIGH-INTENSITY ULTRA-SHORT LASER PULSES

In LWFA the properties of the wakefield are strongly determined by the laser parameters, i.e., laser energy, focus dimension, and pulse duration. The laser intensity has to overcome the ionization threshold of the atoms, as discussed in the previous section 2.1, which for available laser systems (~ 100 TW) means that the laser beam has to be focused down to a few tens of micrometers. On the other hand, the beam must be kept in focus for several millimeters in order to achieve a longer interaction length such that the electrons can gain significant energies. According to the expression for the Rayleigh length,

$$z_R = \frac{\pi w_0^2}{\lambda_0}, \quad (2.7)$$

with w_0 and λ_0 denoting the beam waist and the laser central wavelength respectively. For a laser pulse with 800 nm central wavelength and 17 μm beam waist the Rayleigh length is only 0.8 mm. However, due to the self-guiding of the laser pulse in the plasma medium, the laser focus still can extend over several millimeters. We briefly outline this effect in the following. Note that the LWFA experiment presented in this work is performed in a highly relativistic regime with $a_0 > 2$.

In the weakly relativistic regime, the first order expansion of the refractive index of the plasma can be expressed by^[62,63]

$$\eta = 1 - \frac{1}{2} \frac{\omega_p^2}{\omega_0^2} \left(1 + \frac{\delta n}{n_0} - \frac{\langle a \rangle^2}{2} + \frac{\Delta n_c}{n_0} \frac{r^2}{w_0^2} \right), \quad (2.8)$$

where n is the plasma density, $\delta n/n$, is the normalized density perturbation, $\omega_p = (e^2 n / \epsilon_0 m_e)^{1/2}$ is the plasma frequency and the angled brackets $\langle \rangle$ indicate averaging over the fast laser oscillations. Note that for a linear polarized Gaussian pulse envelope $\langle a \rangle^2$ can be expressed in terms of the normalized laser potential as $\langle a \rangle^2 = a_0^2/2$. From eq. (2.8) it is obvious that the index of refraction, η , can be altered by either modulating the plasma density or the laser intensity. The term $\frac{\Delta n_c}{n_0} \frac{r^2}{w_0^2}$ represents an external density channel. It becomes relevant if a pre-formed density channel, e.g., a plasma capillary, is present. A Gaussian laser pulse with a spot size w_0 can thus be guided in a channel depth given by $\delta n_c = 1/(\pi r_e w_0^2)$ ^[63], where $r_e = e^2/(4\pi\epsilon_0 m c^2)$ represents the classical electron radius. Since the expressions for phase velocity and group velocity are given as $v_\phi = c\eta^{-1}$ and $v_g = c\eta$ respectively¹, it is clear that a change in η leads to changes in both the phase and group velocity of the propagating laser pulse. In the following we shortly discuss the related effects on the laser pulse arising from the laser-plasma interaction:

DEFOCUSING EFFECTS

In the eq. (2.8), the $\delta n/n_0$ term indicates the local variation in the plasma density in the vicinity of the laser pulse. At the front of the laser pulse focused into a neutral gas, first on-axis atoms become ionized. Off-axis atoms subsequently become ionized. This forms a transverse gradient in the refractive index of the plasma and leads to the so-called *ionization defocusing* effect due to the variation in plasma electron density. However in the context of the high power laser this effect is of minor importance since the ionization of the gas occurs in the pedestal of the laser pulse before the main peak arrives.

Another defocusing effect arises during the wake excitation. The ponderomotive forces expel the plasma electrons in the forward direction and so locally change the plasma density in front of the main pulse leading to a defocusing of the laser pulse. This effect is known as *Laser pulse etching*. If $a_0^2 \gg 1$ the electrons in front of the laser pulse continually take energy from the laser pulse while the ion space charge pulls the electrons back and forms a plasma wake behind the laser pulse. However, the energy transfer to the plasma and hence the etching of the pulse front is fast enough to counteract the diffraction of the laser pulse front.^[64]

RELATIVISTIC SELF-FOCUSING

The second term in the eq. (2.8), i.e., $\langle a \rangle^2/2$ is responsible for relativistic mass correction. In general a change in the spot size, w happens because of transverse variation in v_ϕ . First, the wavefronts curve, since energy flows normal to the phase front, the outer part must curve forward in order for focusing to occur, in other words, the transverse gradient of the index of refraction must be negative, i.e., $\partial\eta/\partial x_\perp < 0$. Second, the energy must focus inwards, which requires the condition, $v_{\phi 1} > v_{\phi 2}$, where position 2 is located on axis and position 1 is located at the edge of the beam.

¹Note that $v_g \neq c\eta$ when the relativistic term is included.

In order for relativistic self-focusing (RSF) to occur, one needs to take into account the variation of v_ϕ according to the relativistic term in eq. (2.8) as well as the effect of diffraction. The threshold condition for RSF is given as^[62]

$$\frac{a_0^2}{32} w_0^2 \frac{\omega_p^2}{c^2} > 1 \quad (2.9)$$

Since the eq. (2.9) is proportional to the laser power, the latter can be expressed as a critical power as

$$P_c = 17 \frac{\omega_0^2}{\omega_p^2} [\text{GW}]. \quad (2.10)$$

According to the eq. (2.10), if $P > P_c$, it is possible to guide the laser pulse over several Rayleigh length inside an ion channel, even if the pulse length is shorter than the plasma wavelength λ_p . For comparison, the response of the plasma to the laser pulse is on the order of $\tau = \omega_p^{-1}$.

In the context of blow-out regime (see subsection 2.4.1), a high enough laser power initiates the RSF resulting in a reduction of the beam diameter and therefore increase of the a_0 . The self-focused pulse expels the electrons from the axis and leaves a positively charged ion channel. In this case, self-focusing stops to occur due to the lack of plasma electrons. Notably, the higher order relativistic effects can alter the final self-focusing, which is not included in the expression for the index of refraction (2.8)^[65].

From this point, the total evacuation of the electrons under the effect of the ponderomotive forces enables the guiding of the backside of the laser pulse inside the ion channel, even for short pulses, i.e., $t < \lambda_p/c$. It also results in suppression of the filamentation and the possibility to channel power well above the nominal critical power of self-focusing for a distance of many Rayleigh lengths^[66,67].

2.4. PLASMA BASED ACCELERATION

Propagation of a high-intensity laser pulse or a dense bunch of charged particles through a plasma leads to a displacement of the electrons out of their original position by the ponderomotive force or by the Coulomb potential respectively. While the heavy ions are stationary in the time scale of the beam propagation, the electrons are attracted back by the Coulomb field of the ions and overshoot their original position and thus form a plasma wave behind the propagation axis of the driver pulse. In the case of the laser pulse, the plasma oscillation, i.e., the phase velocity of the plasma wave propagates with the laser group velocity v_g and with a plasma period of $\lambda_p = 2\pi c/\omega_p$.

In the non-relativistic regime ($a_0 \ll 1$) the induced wakefields can be solved analytically. If the plasma perturbation by the laser expressed by δn is small, the linear perturbation theory can be applied to the cold-fluid Maxwell-equations and thus the wave equation for the plasma density perturbation can be obtained. Here we outline relevant expressions for density perturbation and the parallel electric field generation. A comprehensive derivation of this can be found in ref.^[68].

According to the laser ponderomotive force, the potential within the plasma medium in normalized units reads as

$$\Psi(\xi) = \frac{e\phi(\xi)}{m_e c^2}. \quad (2.11)$$

Assuming the normalized phase velocity of the plasma wave is approximately equal to the group velocity of the laser, i.e., $\beta_p = v_\phi/c \approx v_g/c$ and its corresponding Lorentz factor is $\gamma_p = 1/\sqrt{1 - \beta_p^2}$. The plasma wakefield Ψ can be found by solving the second order differential equation:

$$\frac{\partial^2 \Psi}{\partial \xi^2} = k_p^2 \gamma_p^2 \left[\beta_p \left(1 - \frac{1 + a^2(\xi)}{\gamma_p^2 (1 + \Psi(\xi))^2} \right)^{-1/2} - 1 \right], \quad (2.12)$$

where $k_p = \omega_p/c$ is the plasma wave number and $\xi = z - c \cdot t$ denotes the longitudinal coordinate in the co-moving frame of the laser pulse. For a given laser pulse with a laser envelope $a(\xi)$ expressed in normalized field strength a_0 , the solutions for the potential as well as longitudinal electric field E_z can be found to be:

$$\frac{E_z}{E_0} = -\frac{c}{\omega_p} \frac{\partial \Psi}{\partial \xi} \quad (2.13)$$

$$\frac{n_e}{n_0} = \gamma_p^2 \beta_p \left[\left(1 - \frac{1 + a^2(\xi)}{\gamma_p^2 (1 + \Psi(\xi))^2} \right)^{-1/2} - \beta_p \right], \quad (2.14)$$

where n_0 denotes the unperturbed electron density of the plasma and $E_0 = m_e c \omega_p / e$ denotes the critical electric field of the plasma.

Figure 2.1 shows the solution to equations (2.12)-(2.14) for two exemplary laser wakefield scenarios with a peak laser field strength of $a_0 = 0.5$ and $a_0 = 1.5$ both at a plasma density of $3.4 \times 10^{18} \text{ cm}^{-3}$. The linear regime (see figure 2.1a) exhibits a sinusoidal modulation of the depicted quantities. In contrast, in the mildly relativistic regime (figure 2.1b) the periodic plasma density modulations are altered by the intense laser pulse, and the plasma response becomes non-linear which exhibits high-density electron densities at the end of each plasma period. This behavior will be enhanced by increasing the laser field strength. The longitudinal accelerating gradient E_z grows further in amplitude and becomes more linear.

2.4.1. BUBBLE REGIME

The nonlinear theory of the LWFA in one dimension was developed by Bulanov et al.^[69] and Sprangle et al.^[70,71]. The nonlinear theory of the LWFA in two dimensions, including the self-consistent evolution of the laser pulse, was analyzed by Sprangle et al.^[72] and Esarey et al.^[73]. However, for a radially bounded pulse in three dimensions in the high-intensity limit, i.e., $a_0^2 \geq 1$, the wakefield calculation must be modeled numerically as this will be the case for LWFA experiment presented in this thesis. For this purpose, we discuss relevant properties of the so-called blowout regime or bubble-regime in the following:

In the bubble-regime, the laser intensity is sufficiently high that it completely expels plasma electrons from the vicinity of the axis leading to total cavitation behind the laser pulse^[74–76]. Despite the electron cavitation, a fraction of the plasma electron can become trapped into the created cavity and be consequently accelerated to high energies^[21–23]. Different injection schemes are outlined in section 2.5.

An ultra-short laser pulse at high intensities alters the wakefield structure significantly from its sinusoidal form described by the linear theory. It causes a wave steepening and period lengthening, which is also visible at 1D theory, as can be seen in figure 2.1. In contrast, 2D and 3D wakefield simulations exhibit nonlinearities in the radial wakefield structure such that

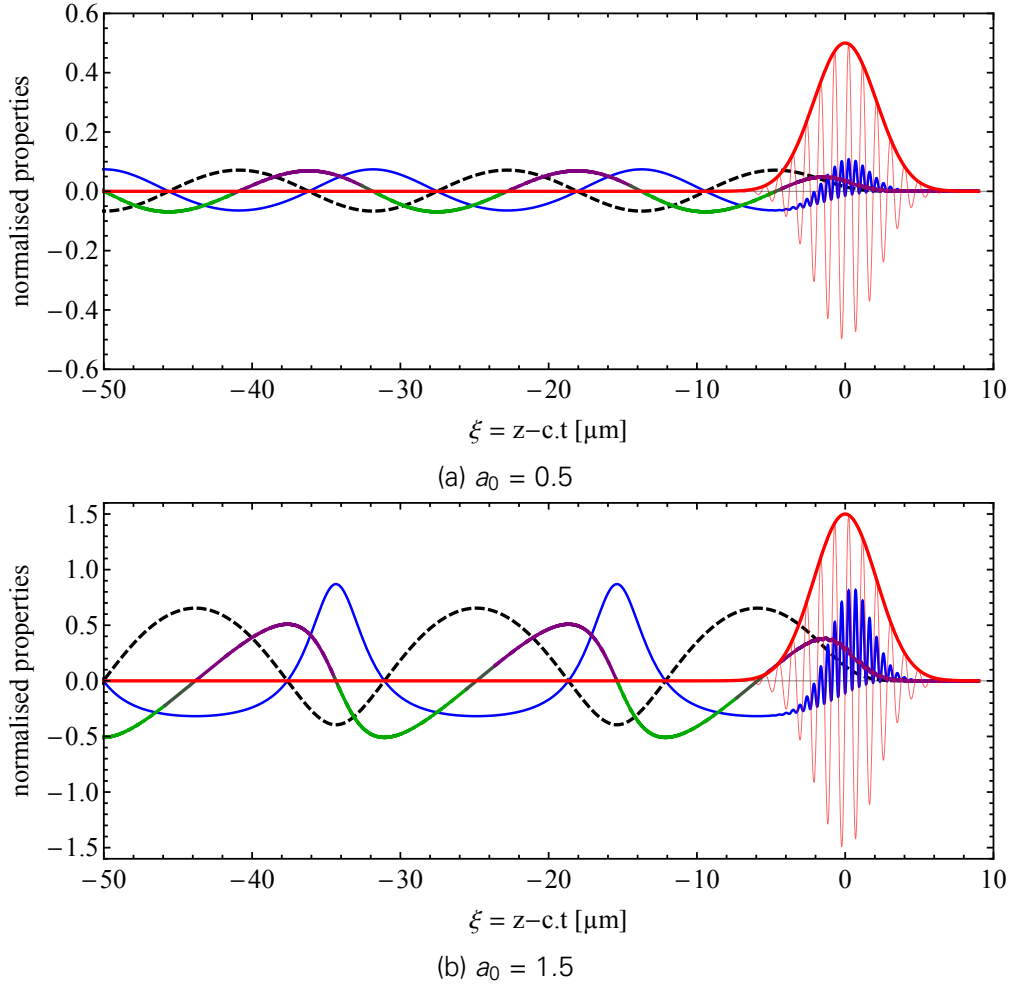


Figure 2.1.: **One-dimensional description of wakefield generation behind an ultra short laser pulse in the quasi-static approximation.** Shown are one-dimensional wakefields generated by a $\sigma = 10$ fs laser pulse at two different a_0 and with $\lambda_0 = 800$ nm central wavelength (*red line*) at a plasma density of $3.4 \times 10^{18} \text{ cm}^{-3}$ in both cases. The *dashed line* represents the wakefield normalized potential Ψ according to eq. (2.12), the *blue line* represents the plasma density according to eq. (2.14). The *green/purple line* represents the normalized electric field according to eq. (2.14), where *green* and *purple* indicate the accelerating and decelerating gradients respectively.

the wavefront of the plasma behind the driver laser pulse is curved. This curvature increased with greater distance behind the laser pulse. As a result, the nonlinear plasma wavelength is becoming greater on-axis than off-axis.

The accelerating field in the bubble region is constant as a function of the radius and varies linearly as a function of the distance behind the driver pulse. Furthermore, the focusing field is linear as a function of the radius, which leads to the preservation of the normalized emittance of an accelerated electron bunch. This focusing field can be huge.^[77]

Furthermore, since the laser pulse in the LWFA is of short duration, $L < \lambda_p$, various instabilities that can be detrimental to the propagation of long pulses can be reduced.

2.5. INJECTION SCHEMES

Following the generation of the wakefield, described in the previous section, injection of the electrons into this wakefield is the next step, which is the subject of several complications in order to achieve a high-quality electron beam. In conventional LINACs in which the RF cavities are of macroscopic dimension, i.e., tens of centimeters the timing of injection process is more relaxed. In contrast in LWFA accelerators, the dimension of the cavity is on the order of the associated plasma wavelength, i.e., several micrometers which makes the injection challenging especially for the case of external injection.

External injection External injection has been experimentally reported^[78–80], however, these experiments have failed so far to provide mono-energetic electron bunches and instead exhibit a broadband energy distribution. External injection of pre-accelerated electron beams from RF accelerators has also been proposed^[81–83]. Although this scheme predicts electron beams with a few pC of charge and an energy spread at the percent level, it has not been experimentally demonstrated yet, since the coupling of an RF-injector and an LPA is technically very challenging. Alternative injection schemes suggest the use of background plasma electrons as a potential source for injection. Although this concept is easier to realize, it reduces the tunability of the accelerator regarding the final beam parameters.

Wave-breaking injection The wave-breaking injection scheme^[84,85] was the first widely used scheme in the bubble-regime due to its simple technical implementation. In this mechanism, the wakefield is strongly driven, and the nonlinear plasma waves exceed the wave breaking threshold. At this point the electrons formed a density spike at the end of the plasma cavity would move faster than the phase velocity of the wake which leads to the so-called wave-breaking and consequently a portion of the background electrons can become injected into the wake structure.

Colliding pulse scheme In the colliding pulse injection (CPI) scheme^[63,86,87] the injection and the subsequent acceleration of electrons can be controlled by using a second laser pulse. The collision of the two laser pulses provides a pre-acceleration stage which provokes the injection of electrons into the wakefield. Colliding pulse scheme provides tunable and stable injection since the injection volume is localized by the overlap of the driver and injection laser. However, the amounts of injected charge are limited to tens of pico-Coulomb^[86].

Down-ramp & shockwave injection Down-ramp and shockwave injection schemes^[88–92] rely on suddenly varying plasma density. This mechanism requires a well-defined gas target,

which can provide a step-like density function. Due to the elongation of the bubble in this transition region, some background plasma electrons can be trapped at the end of the plasma wakefield.

Ionization injection The ionization injection (II) scheme^[93–96] is easy to implement and enables the injection of a large amount of charge. The acceleration medium, normally helium, is doped by a controlled amount of high-Z gas, e.g., nitrogen. Electrons from the nitrogen K-shell atoms are ionized near the peak of the laser pulse and are injected into the wake structure which is created by the helium and L-shell nitrogen atoms. This injection scheme is found to increase the beam charge by as much as an order of magnitude compared to pure helium at the same electron density^[94]. However, this method produces a large energy spread because the ionization-induced injection usually continues until the end of the gas mixture if no injection truncation mechanism is employed.

Self-truncated ionization injection A modified version of the II injection scheme is the so-called Self-truncated ionization injection (STII). It is theoretically introduced by Zeng et al.^[97] in 2004 and later experimentally demonstrated by Mirzaie et al.^[98] in 2015. In this method, the self-focusing process of an initially unmatched laser pulse is utilized which leads to strong wakefield evolution. This can subsequently truncate the injection process due to bubble deformation before the mixed gas ends. STII is supposed to provide a simple way for ionization-injection beam with high quality and low energy spread^[97].

In chapter 7, the STII process has been utilized to study the relevant beam parameters especially longitudinal bunch profile and the resulting peak current.

In order for an ionized electron to become trapped that is ionized close to the laser peak intensity, longitudinal and transversal trapping conditions have to be fulfilled. Considering the motion of the electrons in arbitrary wave potentials in the form, $A = A(x, y, z - v_\phi t)$ and $\Phi = \Phi(x, y, z - v_\phi t)$, the potential function $\Psi = \Phi - v_\phi A_z$ is related to the longitudinal wakefield by $E_z = -\partial_\xi \Psi$ where $\xi = z - v_\phi t$. Firstly, the longitudinal condition requires that an ionized electron gains enough momentum such that the longitudinal electron velocity $v_{z,e}$ reaches at least the wake phase velocity v_ϕ by the time the electron slips back to the peak of the potential at $\Psi = \Psi_{\max}$. Therefore, electrons born near the axis have a perpendicular velocity to the laser propagation direction which is much smaller than their parallel velocity. The trapping condition can be expressed as^[99]

$$m_e c^2 \left(1 - \frac{1}{\gamma_\phi} \right) \geq e(\Psi_{\max} - \Psi_i), \quad (2.15)$$

with $\gamma_\phi = \left(1 - \frac{v_\phi^2}{c^2} \right)^{1/2}$. Therefore the lowest threshold for trapping occurs for electrons born where $\Psi_i = \Psi_{\min}$.

The second trapping condition is related to the region in the wakefield where the focusing force exerted on electrons overlaps with the wakefields accelerating phase. An electron will be trapped if focusing fields are present at the point of injection, which prevents that the injected electrons leave the bubble due to the space charge effect. The latter is caused either by the defocusing transversal field or by the space charge effect from the injected bunch. The process of injection is conceptually depicted in figure 2.2.

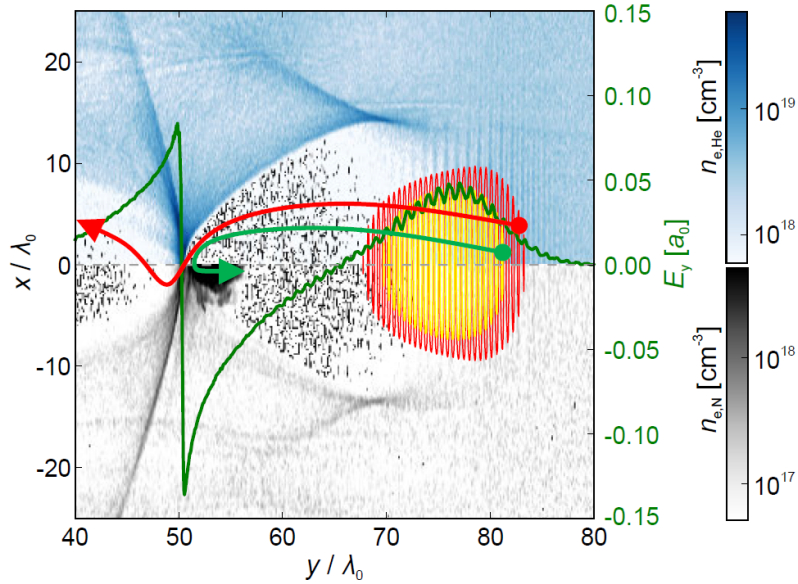


Figure 2.2.: Schematic representation of ionization injection in the bubble regime. The laser pulse is propagating to the right, forming a bubble-shaped wakefield. The top half of the figure shows the density distribution of helium electrons. The bottom half shows the density distribution of nitrogen K-shell electrons. In the *red* region of the laser pulse the N⁶⁺ electrons are ionized while the *yellow* region shows where the laser field is strong enough to ionize N⁷⁺. Two exemplary trajectories of ionized nitrogen K-shell electrons are shown. The *green* trajectory corresponds to an ionized electron which fulfills the trapping conditions and thus is trapped in the bubble. In contrast, the *red* trajectory indicates the situation where the ionized electron is ejected from the accelerating region. The longitudinal E-field is depicted by the *green line*.

2.6. BEAM LOADING

Comprehensive theoretical investigations on the beam loading phenomenon in LWFA can be found in refs.^[28,100,101] Acceleration of several hundred picocoulomb of charge has been demonstrated in LWFA^[4,5,102,103]. Such high loads of charge significantly alter the accelerating electric field and hence influence the final beam parameters.

Here, our focus will be on a phenomenological description of the beam loading via the 1D linear theory of the LPA outlined in section 2.4. Corresponding experimental results will be presented in chapter 7.

The first theory for beam loading in the LPA was developed by Katsouleas et al.^[100]. In this idealized one-dimensional model, it was found that there is an upper limit to the maximum amount of electrons which can be accelerated in a linear wake. As this number is reached, all the wakefield energy is absorbed by the bunch, giving a 100 % beam-loading efficiency.

LPAs generating such high currents contain enough charge such that the bunch self-field superimpose the wakefield. Consequently, the wakefield structure is reshaped and the effective accelerating field along the bunch is modified affecting the beam dynamics and final beam parameters, i.e., transverse dynamics, emittance, final energy, and energy spread. This phenomenon is generally known as beam loading.

This wakefield deformation is generally seen as an adverse effect since this potentially degrades the final beam quality. However, if properly controlled, beam loading can be employed to increase the accelerators performance and improve the electron properties such as relative energy spread and beam divergence as well as optimal laser/electron energy efficiency. In

chapter 7 we carry out a thorough analysis of experimental data for different beam parameters, specifically its longitudinal duration.

Figure 2.3 illustrates the beam loading effect on the longitudinal field in a one-dimensional wakefield. Figure 2.3a shows the first period of an unloaded non-linear wakefield where no charge is injected into the wakefield. Figure 2.3b-2.3d show the effect of increasingly high loads injected into the wakefield. Visible is that an injected charge deforms the wakefield and alters the accelerating field magnitude, while the wake period becomes elongated due to the presence of a load.

In the co-moving frame of the laser pulse, the bunch directly influences the accelerating field experienced by itself. On the one hand, it locally reduces the accelerating gradient, and this will consequently reduce the overall achievable electron energy for a certain acceleration length. On the other hand, a local flattening of the accelerating gradient distribution along the bunch can be employed to minimize the energy spread of an injected electron bunch, since the head and the tail of the bunch will thus experience the same accelerating field.

To illustrate this position-dependent accelerating field the weakly loaded case is illustrated in figure 2.3b, electrons at the front of the bunch experience a significant lower accelerating gradient compared to electrons at the back of the bunch. In this case, the energy spread within the bunch will grow during acceleration.

Figure 2.3c shows the so-called “optimum loading condition” at which the energy spread added during the acceleration process is minimized since the entire electron bunch experiences a constant accelerating field. However, this effect reduces the achievable maximum and average electron energy.

Figure 2.3d shows the overloaded case, where the heavy load overcompensates the wakefield gradient along the bunch. An even stronger reduction in accelerating field occurs, and the accelerating gradient again varies along the bunch. In contrast to the weakly loaded case, trailing electrons now experience a lower accelerating field compared to leading electrons. This situation is generally undesirable, except for the case where a previously chirped beam, e.g., by acceleration in the weakly loaded case, requires an energy de-chirping.

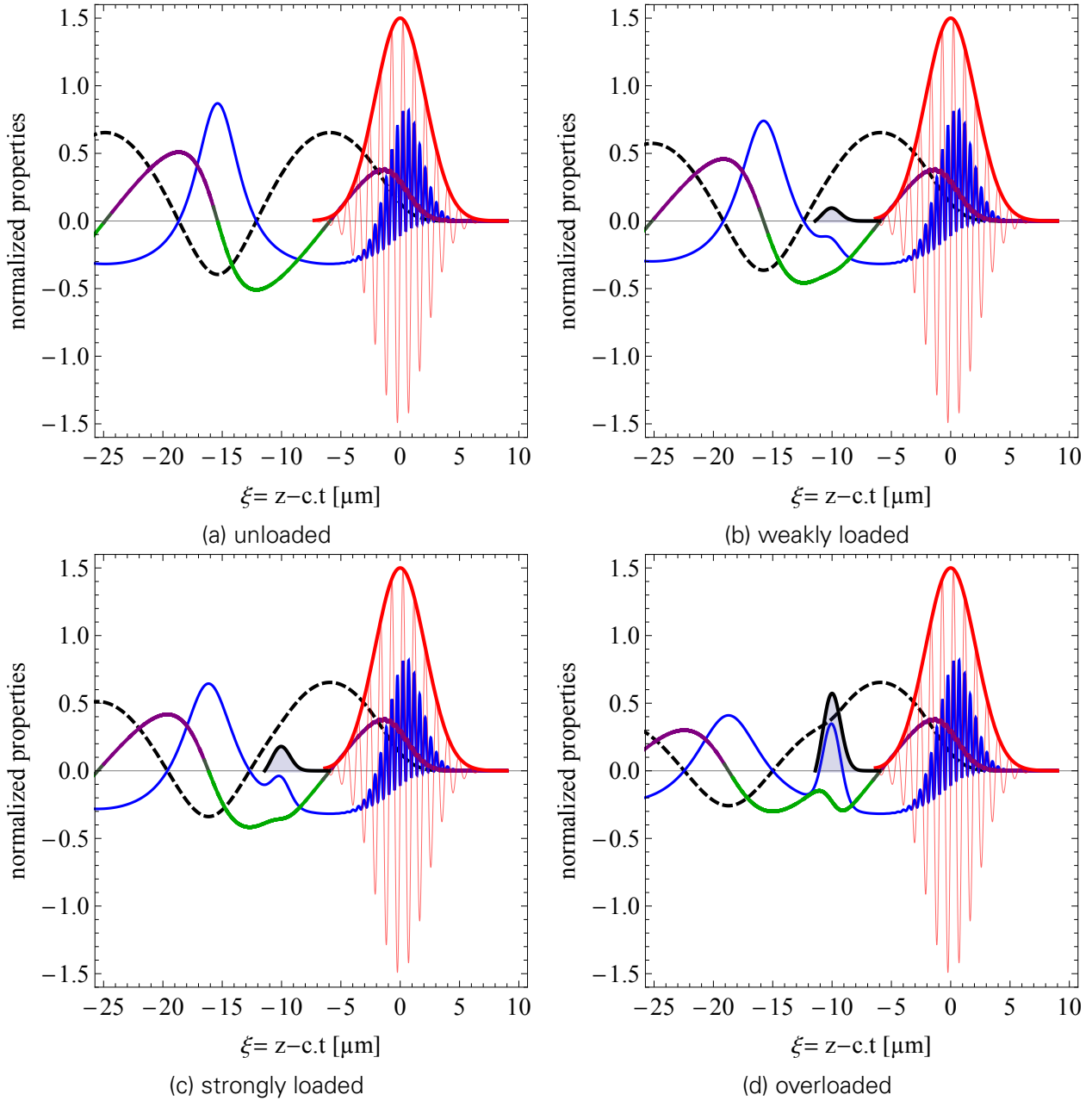


Figure 2.3.: **Effect of beam loading on wakefield.** Shown are one-dimensional wakefields in the quasi-static approximation, calculated similarly to figure 2.1. The wakefields are generated by a $\sigma = 10$ fs laser pulse with $\lambda_0 = 800$ nm central wavelength (red line) for a $a_0 = 1.5$ at a plasma density of $3.4 \times 10^{18} \text{ cm}^{-3}$. Within the laser-driven wakefield different electron bunch loads (*solid black line*) are placed to illustrate their effect on the wakefield. The *dashed line* represents the wakefield normalized potential. The *blue line* represents the plasma density. The accelerating electric field normalized to E_0 is represented by the purple/green line, with green the accelerating gradient and purple the decelerating gradient.

3. THEORY OF TRANSITION RADIATION

Transition radiation (TR) is emitted when a uniformly moving charged particle passes the boundary of a dielectric medium or metal. In general, the moving charge crossing a dielectric medium causes time-varying radial currents, so-called transient polarization current^[52] in the dielectric medium which makes the electrons in the medium swing and thus start to radiate along the material. In a homogeneous medium with $n > 1$ the phase velocity of the radiation does not reach the phase velocity of the moving charge, and all of the radiation contributions will cancel each other due to the destructive interference. However, when the charged particle passes mediums with a different index of refraction, like a metal-vacuum interface, the TR emitted at the boundary of two mediums will not interfere destructively due to the broken symmetry condition. In the case of the metal-vacuum interface, the radiation emitted from the surface of the metal foil when an electron passes by calls TR. Note that the TR is not to be mistaken with Cherenkov radiation, which is emitted when the velocity of the electron passing through a dielectric exceeds the phase velocity of light in that medium. The theory of transition radiation by a single electron is first studied by Ginzburg and Frank in 1946^[51,104] and later in a monograph by Ter-Mikaelian^[105]. In the past decades, several publications treated the derivation of TR with different formalisms for both a single electron and an electron bunch as we will describe some useful characteristics of TR radiation in the following.

3.1. TRANSITION RADIATION FROM SINGLE ELECTRON

There are several approaches to treat the derivation of TR, each starts with different assumptions.

The first approach to describe the generation of TR, which is originally employed by Ginzburg and Frank, relies on solving the Maxwell equations at a metal-vacuum boundary of infinite extent. This approach yields an expression for energy radiated per unit frequency and solid angle in the far field^[51]. A comprehensive derivation of this approach can be found in ref.^[52], which will be outlined in this section.

The second description is the model of virtual quanta^[50]. In this model, the Coulomb field of the electrons is described by virtual photons, which are converted into real photons by reflection at the finite metallic interface. This model requires a highly relativistic electron, where

the radially symmetric electromagnetic field of the electron is compressed in an almost flat disc perpendicular to the propagation direction of the electron. By entering the electron into the metallic foil at the boundary of the conductor, the tangential field of the electron to the surface of the foil must vanish. This leads to reflection of the incoming field from the surface of the foil and initiates the source of the backward TR. This method has the advantage that it is valid for both near and far field region.

Another formalism for modeling the generation of TR is the method of moving mirror charge^[106]. In this approach, the electron and its mirror charge moving from opposite directions into the screen surface and stopped abruptly at the screen boundary. For an observer, while the electron and its anti-particle are annihilating their electromagnetic fields are remaining which thus can be identified as TR emitted from the target.

3.1.1. CALCULATION OF SPECTRAL AND ANGULAR TR

In order to demonstrate the characteristics of TR emitted by a single electron passing a step-like dielectric boundary, we first use a simplified description of the transition radiation, which derived first by Ginzburg and Frank^[51,104]. For a single energetic electron transiting a metallic screen into vacuum, assuming the TR screen is an infinite ideal conductor and the electron passing normal to the screen surface, the angular energy distribution of transition radiation from a single electron per unit frequency $d\omega$ and per unit solid angle $d\Omega$ is given by

$$\frac{d^2 W_e}{d\omega d\Omega} = \frac{e^2}{4\pi^3 \epsilon_0 c} \frac{\beta^2 \sin^2 \theta}{(1 - \beta^2 \cos^2 \theta)^2}, \quad (3.1)$$

where θ is the observation angle with respect to the electron trajectory, β is the electron velocity normalizes to speed of light in vacuum c , e is charge of electron and ϵ_0 is the dielectric constant of vacuum. This formula is valid in the limit of an ideal conductor ($|\epsilon| \gg 1$) with infinite transverse size in the far-field regime, meaning for large distances from the source. The latter can be expressed by the so-called *radiation formation length*, $\gamma^2 \lambda$ ^[52]. For distances larger than the formation length the radiation can be assumed to be in the far-field regime. Figure 3.1 illustrates the properties of the TR angular distribution for a single electron by normal traversing a vacuum-metal interface. According to eq. (3.1) the radiation pattern of TR is frequency independent. In practice, the longest radiated wavelength is limited by the physical size of the radiator due to the diffraction limitation. The transverse expansion of the radiated wavelength for relativistic electrons scales with $\sim \gamma \lambda$ ^[52]. For long wavelengths and high electron energies, it could exceed the macroscopic dimension of the radiator whereas the emitted radiation will be reduced. On the contrary for short wavelengths or high frequencies that approach the plasma frequency of the TR-screen, the radiator becomes transparent and stops to radiate.

Beforehand, for the case of Coherent transition radiation (CTR) the short wavelength limit of CTR is the longitudinal dimension of the electron bunch as will be described in more detail in section 3.2.

Notably, the total radiated energy can approach the kinetic energy of the electron bunch, i.e., $W_b = Nm_e c^2 (\gamma - 1)$. Therefore energy loss of the electron bunch during the radiation process could be significant for high charge electron bunches with sufficiently low energy. For the description of TR radiation in the following, sufficiently high electron energies, i.e., $\gamma \gg 1$ are assumed as will be the case for LWFA experiment presented in this thesis. Thus the energy loss in the high energy electron bunches can be neglected.

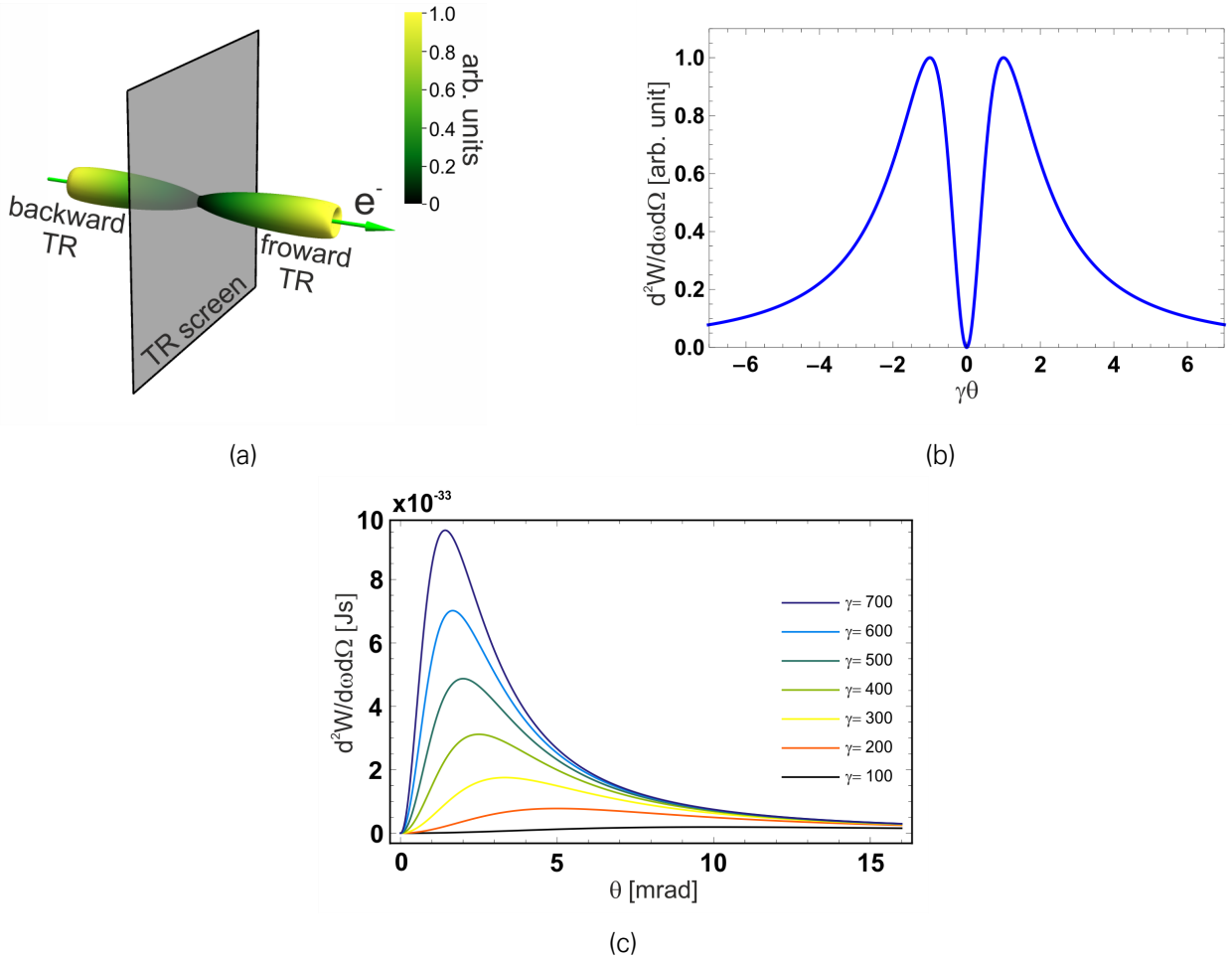


Figure 3.1.: **Illustration of TR angular distribution.** Plots are calculated according to the eq.(3.1). (a) shows a three-dimensional angular radiation emission normalized to one from a single electron in the far-field regime. Normal incidence of charge onto the TR-Screen results in a radially symmetric radiation cone. A line-out through its center plotted in (b), which shows that the radiation vanishes on-axis and reaches its maximum at $\theta = 1/\gamma$. For comparison in (c), the angular distribution of TR for various electron energies at one azimuthal angle.

3.1.2. RADIATION ENERGY SPECTRUM

The TR emitted by relativistic electrons is strongly concentrated into a small radiation cone around the propagation axis of the electrons with a cone half angle of $1/\gamma$. One can simplify the equation (3.1) according to experimental conditions such as small collection angles and relativistic electrons to find an expression for the radiated TR spectrum. Integrating equation (3.1) over all angles and considering the limit of the highly relativistic electrons $\gamma \gg 1$, it yields to^[52]

$$dW_e/d\omega \simeq \frac{e^2}{2\pi^2\epsilon_0 c} \ln(\gamma). \quad (3.2)$$

This shows that the total emission for the forward TR scales logarithmic with γ .

A more useful expression to experiments is the radiation energy spectrum into a small cone $0 \leq \theta \leq \theta_0 \ll 1$ about the propagation axis as^[52]

$$\frac{d^2W_e}{d\omega} \simeq \frac{e^2}{4\pi^2\epsilon_0 c\beta^2} \left[\ln(1 + \beta^2\gamma^2\theta_0^2) - \frac{\beta^2\gamma^2\theta_0^2}{1 + \beta^2\gamma^2\theta_0^2} \right]. \quad (3.3)$$

The above expressions are also valid for an idealized case of a short monoenergetic electron bunch in the limit of zero emittance and zero radius interacting with a semi-infinite ideal conductor by taking into account the number of electrons. For fully coherent TR emission (CTR) the above expression thus scales with $\sim N^2$, where N indicates the number of electrons. However for a non-ideal case of the electron bunch and of TR-screen, the coherence effect has to be taken into account, which can significantly alter the final TR emission. In the following section we derive a generalized model for calculating TR from an arbitrary electron bunch.

3.2. TRANSITION RADIATION FROM ELECTRON BUNCH

In this section we consider an electron bunch with arbitrary spatial and momentum distribution moving from a metallic foil ($\epsilon = \epsilon_1$ for $z < 0$) into vacuum ($\epsilon = 1$ for $z > 0$). The Coulomb field of the moving electron bunch induces a transient polarization at the boundary and radiation is emitted by the transient polarization current. Figure 3.2 shows the geometry of the calculation presented in the following. The Maxwell equations for linear dielectric media can be combined

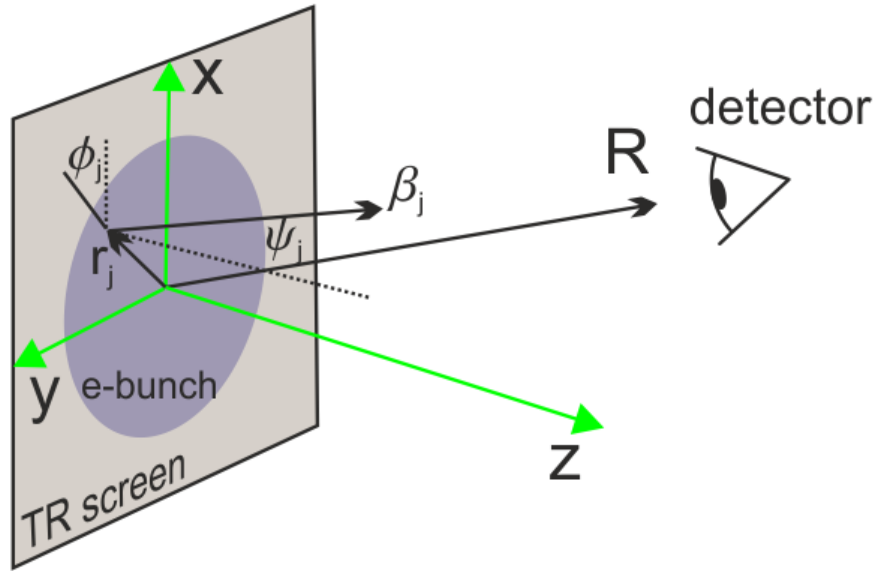


Figure 3.2.: Geometric arrangement of variables occurring in the calculation of transition radiation. (x, y) plane denotes the surface of radiator, the position of j th electron on the radiator indicated as r_j , traversing the conductor into vacuum at $z = 0$ with velocity β_j , which makes an angle of ψ_j with respect to z axis and ϕ_j is the angle formed by transverse projection of β_j and x axis, in figure the observation vector R makes an observation angle of θ with z axis.

and written in the following wave equation^[52]:

$$(c^2 \nabla^2 + \epsilon \omega^2) \mathbf{E} = \frac{4\pi}{i\omega \epsilon} [c^2 \nabla(\nabla \cdot \mathbf{J}_b) + \omega^2 \epsilon \mathbf{J}_b], \quad (3.4)$$

with \mathbf{E} the electric field and \mathbf{J}_b the current of the electron beam. The wave equation (3.4) can be solved in both metal and vacuum. Applying the continuity of the normal electric displacement field $\epsilon(\omega) \mathbf{E}(\omega)$ and tangential electric field across the boundary^[105] led to particular (particle field \mathbf{E}_p) and homogeneous electric fields (radiation field \mathbf{E}_h) as $\mathbf{E} = \mathbf{E}_p + \mathbf{E}_h$. The

radiation field generated by N electrons in the vacuum ($z > 0$) and in the far-field for an ideal conductor ($|\epsilon| \gg 1$) is found to be^[52]

$$\mathbf{E}_h(\omega, \mathbf{k}_\perp, z) = -i \frac{4\pi e}{\omega} \sum_{j=1}^N \frac{\mathcal{E}_j(\theta, u_j, \psi_j, \phi_j)}{\cos \theta} e^{-i\Psi_j} e^{iz\sqrt{\omega^2/c^2 - k_\perp^2}}, \quad (3.5)$$

where $\Psi_j = \mathbf{k}_\perp \cdot \mathbf{r}_{\perp j} + (\omega - \mathbf{k}_\perp \cdot \mathbf{v}_{\perp j}) z_j / v_{zj}$, \mathbf{k}_\perp denotes the wave vector perpendicular to the observation (\mathbf{k}) in the $\mathbf{k} - \hat{z}$ plane and $\mathcal{E}_j(\theta, u_j, \psi_j, \phi_j) = \mathcal{E}_{\parallel j} \hat{e}_\parallel + \mathcal{E}_{\perp j} \hat{e}_\perp$ is the normalized amplitude of the electric field. The latter is expressed in its components in the radiation plane expanded by \hat{z} and \hat{k} and perpendicular to the radiation plane (\hat{y}), as indicated in figure 3.2 respectively.

$$\mathcal{E}_{\parallel j}(\theta, u_j, \psi_j, \phi_j) = \frac{u_j \cos \psi_j \left[u_j \sin \psi_j \cos \phi_j - (1 + u_j^2)^{1/2} \sin \theta \right]}{\left[(1 + u_j^2)^{1/2} - u_j \sin \psi_j \cos \phi_j \sin \theta \right]^2 - u_j^2 \cos^2 \psi_j \cos^2 \theta}, \quad (3.6)$$

$$\mathcal{E}_{\perp j}(\theta, u_j, \psi_j, \phi_j) = \frac{u_j^2 \cos \psi_j \sin \psi_j \sin \phi_j \cos \theta}{\left[(1 + u_j^2)^{1/2} - u_j \sin \psi_j \cos \phi_j \sin \theta \right]^2 - u_j^2 \cos^2 \psi_j \cos^2 \theta}, \quad (3.7)$$

where $u = p/m_e c = \gamma\beta$ is the normalized momentum of the electrons. In the limit of no divergence and for a collimated radially symmetric beam with normal incidence onto the interface the transverse component of the electric field vanishes $\mathcal{E}_{\perp j} = 0$ and equation (3.6) results in the classical Ginzburg-Frank formula (3.1). Note that, only under these circumstances the TR from an electron bunch will be radially polarized. In general, oblique traversing the electrons onto the TR-screen or the beam divergence leads to an asymmetric TR cone and thus an asymmetrically distributed polarization pattern as illustrated in figure 3.3. However, in the TR setup presented in chapter 5 the TR screen is placed perpendicular to the electron beam axis, and hence the assumption for the aforementioned normal incidence holds.

A general expression for spectral and angular distribution of TR in the far-field can be found by substituting the equation (3.5) for the electric field into the integral for Poynting vector

$$dW = \frac{c}{4\pi} \int_{-\infty}^{\infty} dt \int d^2 \mathbf{x}_\perp (\mathbf{E} \times \mathbf{B}) \cdot \hat{z}. \quad (3.8)$$

Thus the angular energy distribution of TR can be found by an ensemble average over six-dimensional beam distribution $h(\mathbf{r}, \mathbf{p})$, with the normalization $\int d^3 \mathbf{r} \int d^3 \mathbf{p} h = 1$ and momentum distribution given by $g(\mathbf{p}) = \int d^3 \mathbf{r} h$. The result is given as,

$$\frac{d^2 W}{d\omega d\Omega} = \frac{e^2 N}{4\pi^3 \epsilon_0 c} \left\{ \underbrace{\int d^3 \mathbf{p} (\mathcal{E}_{\parallel}^2 + \mathcal{E}_{\perp}^2) g(\mathbf{p})}_{\text{Incoherent TR}} + (N-1) \underbrace{\left[\left| \int d^3 \mathbf{p} g(\mathbf{p}) \mathcal{E}_{\parallel} F \right|^2 + \left| \int d^3 \mathbf{p} g(\mathbf{p}) \mathcal{E}_{\perp} F \right|^2 \right]}_{\text{Coherent TR}} \right\}, \quad (3.9)$$

where F is the spatial form factor defined by^[52]

$$F = \frac{1}{g(\mathbf{p})} \int d^2 \mathbf{r}_\perp e^{-i\mathbf{k}_\perp \cdot \mathbf{r}_\perp} \int dz e^{-iz(\omega - \mathbf{k}_\perp \cdot \mathbf{v}_\perp)/v_z} h(\mathbf{r}, \mathbf{p}). \quad (3.10)$$

The energy spectrum of TR from the electron bunch (3.9) is given by the total emitted electric field during the TR radiation generation. The total field summing up coherently in case of

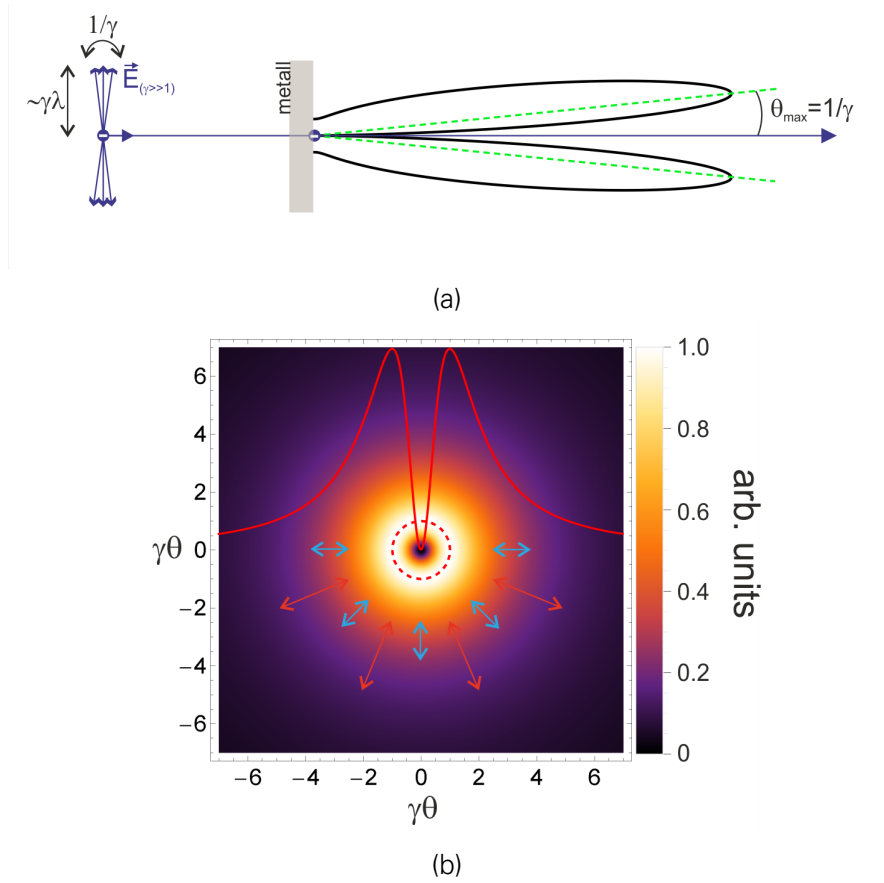


Figure 3.3.: **Angular radiation patter of transition radiation.** (a) The coulomb field of a relativistic electron is compressed to a nearly disc perpendicular to the propagation axis of the electron, which induces a radial surface current into the conductor, leading to radial polarization of TR with its maximum radiation intensity at $1/\gamma$ and no emission on-axis. (b) shows the TR radiation pattern in far-field, the shorter wavelength will be emitted from the inner part of the cone while the longer wavelength emitted from the outer ring and could reach the macroscopic dimensions in the order of $\sim \gamma\lambda$

no phase difference, applying for radiation wavelengths longer than the dimensions of the electron bunch. Therefore the total TR scales with $\propto N^2$. In contrast, for short wavelength compared to the bunch duration, the emitted TR scales linearly with the number of electrons $\propto N$

Equation (3.9) can be thus subdivided into the coherent and incoherent portions:

$$\frac{d^2 W_{\text{ITR}}}{d\omega d\Omega} = \frac{e^2}{4\pi^3 \epsilon_0 C} N \left[\langle \mathcal{E}_{\parallel}^2 \rangle + \langle \mathcal{E}_{\perp}^2 \rangle \right], \quad (3.11)$$

$$\frac{d^2 W_{\text{CTR}}}{d\omega d\Omega} = \frac{e^2}{4\pi^3 \epsilon_0 C} N(N-1) \left[|\langle \mathcal{E}_{\parallel} F \rangle|^2 + |\langle \mathcal{E}_{\perp} F \rangle|^2 \right], \quad (3.12)$$

where the $\langle \rangle$ stand for an average over the momentum distribution $g(\mathbf{p})$. Note, that for a collimated beam. i.e., $\langle \psi \rangle = 0$ the contribution of the perpendicular electric field vanishes. Also a cylindrical symmetric momentum distribution $g(u, \psi)$ with normal incidence onto the TR screen results in $\langle \mathcal{E}_{\perp} F \rangle = 0$. The resulting approach outlined here (3.9) can be used to model the TR from an arbitrary electron bunch in the far-field, while the form factor contains all information about the both spatial and momentum distribution of the electron bunch. However for more computational efficiency one can simplify the general expression (3.9) and (3.10) according to realistic experimental parameters.

3.2.1. ELECTRON BUNCH DISTRIBUTION

In this section the characteristics of electron beam distribution is investigated. The general expression for $h(\mathbf{r}, \mathbf{p})$ (3.10) is valid for correlated spatial and momentum distribution, however under certain conditions these correlations can be mitigated or completely omitted. Therefore, the phase space distribution can be given by $h(\mathbf{r}, \mathbf{p}) = g(\mathbf{p})f(\mathbf{r})$ and a fully uncorrelated beam distribution takes the form

$$h(\mathbf{r}, \mathbf{p}) = g(u, \psi, \phi) f(\mathbf{r}_\perp, z) \quad (3.13)$$

$$= g(u) g(\psi) g(\phi) \cdot f_\perp f_\parallel. \quad (3.14)$$

BEAM DISTRIBUTION SEPARABILITY

Considering LWFA experimental parameters presented in chapter 7, the assumption for an uncorrelated phase space bunch distribution is justified as will be discussed in the following. Note, that the correlation between X and Y is mathematically written as $0 < \text{corr}(X, Y) < 1$ with values between zero and 1 for uncorrelated and correlated terms respectively.

- Regarding to small transverse size of electron beam σ_\perp at the exit of the plasma wake-field (Nozzle), which is in the order of $(\sim 1 \mu\text{m})^{[107-110]}$, at the TR screen the transverse size of the beam is only determined by angular distribution of $g(\psi, \phi)$. In the experimental setup presented in chapter 5, the TR screen is located $d = 26 \text{ mm}$ behind the nozzle. Assuming a source of $\sim 1 \mu\text{m}$, the transverse projection of the electron bunch on the screen is obtained to be $\sim 130 \mu\text{m}$. Since σ_\perp for small divergence $\psi \ll 1$ scales linearly with divergence such $\psi_{\text{FWHM}} \cdot d \simeq \sigma_\perp$, consequently the transverse spatial distribution can be expressed by $f_\perp \simeq d \cdot g(\psi)$ and hence $\text{corr}(f_\perp, g(\psi)) = \text{corr}(g(\psi), g(\psi)) = 1$. However the transverse position-angle correlation has no significant effect on the resulting TR spectrum.
- Under the assumption, that the beam exhibits a cylindrical symmetric distribution $\text{corr}(g(\psi), g(\phi)) = 0$ is valid. This is experimentally confirmed for the global behavior of the transverse electron distribution by measuring the transverse dimension of the bunch at 40 cm downstream by using a LANEX screen beam profiler. However precise imaging the *point spread function* (PSF) of the electron bunch right after the nozzle exit has shown that the PSF exhibits a more complex pattern, which is related to multiple substructures inside the bunch. These structures are not visible in the beam profile measurement due to the lack of resolution in imaging of the utilized LANEX profiler. This point will be discussed in section 5.3.
- According to analyzed electron energy spectra that will be presented in section 6.3.2 it is found that the divergence of the electron beam in terms of $\sigma_\psi(\gamma)$ remains over a large part of the high energy range of the spectrum ($\gamma \gg 1$) about constant. Therefore $\text{corr}(g(u), g(\psi))$ is assumed to be negligible. Furthermore for a cylindrically symmetric beam $\text{corr}(g(u), g(\phi)) = 0$ is obtained.
- Possible correlations between the longitudinal charge distribution f_\parallel and momentum distribution $g(u)$ can arise providing that nonlinear energy chirp in the beam exists. A linear energy chirp (position-momentum correlation) leads to a bunch lengthening or a bunch shortening during the propagation of the beam from its source to the TR-screen for a positive or negative chirp respectively. This point will be discussed and considered in error analysis in section 6.3.2.

SPATIAL FORM FACTOR

The introduced expression (3.10) describes an arbitrary charge distribution in terms of its Fourier components. Since the electron beam distribution is separable in momentum and space as shown in the previous section, the spatial form factor is thus given by a Fourier transform as

$$F(\mathbf{k}) = \int d^2\mathbf{r}_\perp e^{-i\mathbf{k}_\perp \cdot \mathbf{r}_\perp} \int dz e^{-iz(\omega - k_\perp \cdot v_\perp)/v_z} f(\mathbf{r}), \quad (3.15)$$

where $f(\mathbf{r})$ is the beam spatial distribution. Consequently the spatial form factor can be expressed as $F = F_\perp F_\parallel$. A Gaussian spatial beam distribution for a cylindrical symmetric beam is defined as

$$f(r_\perp, z) = \frac{1}{(2\pi)^{3/2} \sigma_r^2 \sigma_z} e^{-\frac{r_\perp^2}{2\sigma_r^2}} e^{-\frac{z^2}{2\sigma_z^2}}, \quad (3.16)$$

where σ_\perp and σ_z indicate root-mean-square (rms) of transverse and longitudinal beam dimensions respectively. Note, that the transverse beam distribution for an elliptical beam can be defined by a bi-normal distribution. Substituting the beam distribution (3.16) into the expression for the form factor (3.15) and performing Fourier transformation leads to expressions for spatial form factor. Assuming the divergence of the beam is sufficiently small, i.e., $\psi \ll 1$ the spatial form factor in transverse and longitudinal terms read as

$$F_\perp(\omega, \theta) = e^{-\frac{1}{2} \left(\frac{\omega}{c} \sigma_r \sin \theta \right)^2}, \quad (3.17)$$

$$F_\parallel(\omega) = e^{-\frac{1}{2} \left(\frac{\omega \sigma_z}{v} \right)^2}, \quad (3.18)$$

where v is the velocity of electrons. From eq. (3.17), one can see that the transverse coherence is unity if the condition $2\pi/\lambda \gg \sigma_r \sin \theta$ is fulfilled. On the other hand, the longitudinal coherence (eq. (3.18)) is independent on collecting angle, i.e., $2\pi/\lambda \gg \sigma_z$ has to be fulfilled. Since the argument in the expression for transverse coherence additionally scales with $\sin \theta$, either by shrinking the transverse dimension of the electron bunch on the TR screen or by narrowing the collection angle of TR collimating optics, the degree of the transverse coherence can be significantly improved such that the transverse form factor can be assumed to be unity. As a consequence, the longitudinal form factor can be obtained from the spectral measurement of the broadband TR spectrum, which contains information about the longitudinal bunch profile.

The assumption for the transverse coherence will be experimentally discussed in section 5.3.

OTR POINT SPREAD FUNCTION

Adding to the widely used beam monitoring by utilizing a LANEX screen, analysis of transverse dimension of an electron bunch can be achieved by measuring the PSF of the emitted OTR radiation. Several authors described the assessment of OTR PSF as can be found in refs^[111-114]. The concept incorporates the single electron angular distribution CTR emission and the J_1 ordinary Bessel function to model the intensity pattern of the OTR radiation at a detector plane. It first considers the electric field distribution and then square it to calculate its intensity pattern $I(x, y)$. Considering a single ideal lens to image the OTR on the detector plane, the expression for PSF is read as

$$I(x, y) \propto \left[\int_0^{\theta_{\max}} \frac{\theta^2}{\theta^2 + 1/\gamma^2} J_1 \left(\frac{k\theta \sqrt{x^2 + y^2}}{M} \right) d\theta \right]^2, \quad (3.19)$$

where $k = 2\pi/\lambda$ with λ the wavelength of radiation under the emission angle of θ , x and y denote the spatial coordinates, M is the magnification of the lens. θ_{\max} denotes the maximum of collection angle.

The intensity pattern of the PSF is similar to the far-field angular distribution, as presented in figure 3.3b. However, the PSF represents this distribution in the image plane of the detector. Thus for normal incidence, radial polarization of the PSF is expected as well. By proper measuring the PSF of an electron bunch and applying the eq. (3.19) as a fit function, the corresponding transverse dimensions of the electron bunch can be extracted.

In the experimental setup presented in chapter 5 measuring the far- and near-field of the emitted OTR is realized. This approach will be discussed in section 5.3.

3.2.2. EFFECT OF DIFFRACTION

The Coulomb self-field of a relativistic electron bunch is compressed to a disc and extends a distance transversely on the order of $\sim \gamma\lambda$ as illustrated in figure 3.3a. Therefore diffraction radiation (DR) of the TR screen boundaries can be neglected if $\rho \gg \gamma\lambda$ is fulfilled, where ρ indicates the radius of the radiator. From this condition, it is obvious that DR for long wavelengths and/or small screen size leads to a reduction of the CTR emission.

According to the experiment presented in this work (see chapter 6), for a TR screen with a radius of 8 mm and longest measured wavelength of 12 μm , for electron energies up to $\gamma \sim 700$ the contribution of DR can be neglected.

3.3. SUMMARY

In this chapter, we outlined the basic properties of transition radiation and derived a number of important mathematical expressions in order to be able to calculate the emitted TR from an electron bunch under certain experimental conditions. In the expression for angular energy distribution 3.9 and the resulting equations for ITR and CTR, the effect of diffraction is neglected. For the case of relativistic electrons and very long radiation wavelengths, where the transverse extent of the bunch self-field exceeds the dimension of the radiator, i.e., $\rho \sim \gamma\lambda$ the diffraction term has to be taken into account. A comprehensive description of this issue can be found in refs.^[52,115]. In chapter 6 we will make use of the introduced theory here to calculate the TR emission from experimental data (see 6.3.1), and also we take advantage of this calculation in the bunch profile reconstruction.

We first introduce a single-shot, broadband spectrometer in the following chapter, which is designed for measuring the TR spectrum emitted from the LWFA electron bunches.

4. TRANSITION RADIATION SPECTROMETER

In this chapter, an ultra-broadband single shot spectrometer is presented, which is designed and set up by the author in his previous work^[1]. Following significant upgrades and improvements on the TR spectrometer, it is implemented in the LWFA experiment at HZDR in the framework of this thesis in order to determine electron bunch durations in the range from 0.7 fs to 40 fs^[3]. However, this high-tech spectrometer can be employed in any broadband spectral measurements that require both a high resolution and a single-shot acquisition.

In the case of LWFA accelerated electron bunches, the spectrum of the emitted TR could exploit a tremendous intensity bandwidth over the spectrum since the coherent fraction is typically several orders of magnitude stronger than the incoherent fraction. For instance, the coherent TR (CTR) intensity from a relativistic electron bunch ($v_e \approx c$) with a bunch duration of $\tau = 10$ fs at FWHM and with $N = 10^8$ electrons is upto 8 orders of magnitude higher than its incoherent TR (ITR) intensity for wavelength $\lambda < 3 \mu\text{m}$ ^[52]. The wavelength of this spectral cutoff is strongly correlated to the bunch duration τ , i.e. $\lambda_{\text{cutoff}} \sim c\tau$. Thus, a spectrometer with sensitive detection systems, with high dynamic bandwidth over several orders of magnitude and a broad spectral range is required. In order to resolve spectral modulations which would arise from bunch sub-structures at sub-fs timescales, a high spectral resolution is also required.

Commercial single-shot spectrometers are mostly designed for a specific application, and hence their capabilities are limited either in spectral bandwidth, sensitivity or resolution. Single-stage prism spectrometers are developed at LCLS at the SLAC^[116] and Deutsches Elektronen Synchrotron (Desy)^[117,118] to cover a broad range of mid-infrared of TR.

Due to the limited spectral bandwidth of the existing detection technologies and considering the limited dispersion and transmission properties of available spectroscopic materials, the use of a modular spectrometer is indispensable. The input spectrum is divided into middle-infrared (MIR), near-infrared (NIR), as well as visible (VIS) to ultraviolet (UV) fractions utilizing suitable beam splitters. Each fraction is thereafter spectrally decomposed using common dispersive elements such as prism or grating. The partial spectra are resolved employing three detectors and subsequently combined to the final extended spectrum. To sum up, three optimized dispersion and detection systems are combined to an ultra-broadband in the range from 250 nm to 11.35 μm (5.5 octaves), single-shot vacuum operated spectrometer in order to achieve the required bandwidth and resolution.

Due to the variation in the spectral response of the individual detectors (quantum efficiency

QE) as well as transmission and reflection properties of the optical elements in the spectrometer, in order to validate the extended spectrum a full characterization of the spectrometer has proceeded. This includes a wavelength calibration^[119–121], a relative spectral response calibration^[122,123] and finally an absolute photometric calibration of the mentioned partial spectra using appropriate calibration sources. The latter is an essential step toward calculating the electron bunch form factor in terms of absolute intensities of TR emission for electron bunch duration measurements experiments as will be discussed in detail in chapter 6.

Design and setup of TR spectrometer and its relevant properties as well are discussed in section 4.1. The calibration of the spectrometer is presented in section 4.2. It is done regarding wavelength calibration presented in section 4.2.1, relative response as well as absolute calibration presented in sections 4.2.3 and 4.2.4 respectively.

4.1. DESIGN AND SETUP

A spectrometer vacuum chamber is specifically designed and manufactured in order to firstly, house the NIR and MIR spectrometer arms, since many vibrational–rotational transitions of molecules such as H₂O or CO₂ fall within the range 3 – 10 μm, causing selective absorption of the transmitted radiation^[124]. Secondly, to enable a direct connection of the spectrometer to the LWFA vacuum chamber, avoiding the use of any vacuum window for TR beam transport. In order to ease the chamber construction, the spectrometer setup is directly mounted on the ground plate which is equipped by a mounting hole grid. Two detectors for NIR and MIR ranges (see Section 4.1.5) are attached to the chamber walls. The thickness of the chamber walls and ground plate are optimized using the simulation software ANSYS to minimize wall deformation and to preserve spectrometer alignment after pump-down, but also for its acceptable weight facilitating the mobility of the spectrometer. The maximum relative deformation of the chamber ground plate (10 cm aluminum) is estimated to be < 0.1 mm. The chamber walls are fabricated from 10 mm steel plates and strengthened by several ribs to improve the stability of the walls leading to a maximum relative deformation of < 0.3 mm.

A schematic overview of the main elements of the TR spectrometer and the construction of the spectrometer chamber is given in Fig. 4.1. Fig. 4.18 shows the top-view of the TR spectrometer setup.

The collimated TR enters from the LWFA chamber and first passes a Keplerian telescope arrangement consisting of two 90° off-axes-parabolas (OAPs) with equal effective focal lengths (EFL = 15 cm). A slit is placed in the focal plane of the first OAP to set the spectral resolution of the spectrometer^[125] (see Section 4.1.1). In fact, this OAP images the surface of the light source, i.e. the TR screen onto this slit. The recollimated beam is after that spectrally split by two beam splitters (see Section 4.1.2). A GaAs beam splitter reflects the UV to NIR region of the TR spectrum from 0.2 μm to 1.0 μm), which is later measured by a commercial echelle spectrometer (see Section 4.1.4). A ZnSe beam splitter in turn splits the transmitted portion of the TR through the GaAs into MIR and NIR arms. The NIR range from 0.9 μm to 1.7 μm of the TR passes through a second slit placed in the focal plane of a telescopic arrangement consisting of two OAPs. The recollimated beam is then spectrally decomposed by a glass prism (N-SF11, see also Section 4.1.3). The beam is subsequently focused by a spherical mirror (SM) and finally detected by an InGaAs array detector (see Section 4.1.5). The MIR arm covers the spectral range from 1.6 μm to 12 μm and is first spectrally decomposed by a ZnSe prism and then focused by an SM on a mercury cadmium telluride (MCT) array detector (see Section 4.1.5). The schematic design presented here shows the elemental components of the spectrometer. Additional optical elements such as polarizers, attenuators, and bandpass

filters as well as imaging optics for monitoring the beam pointing, which are used during the calibration and TR measurement are not shown here. Elements that have to be occasionally

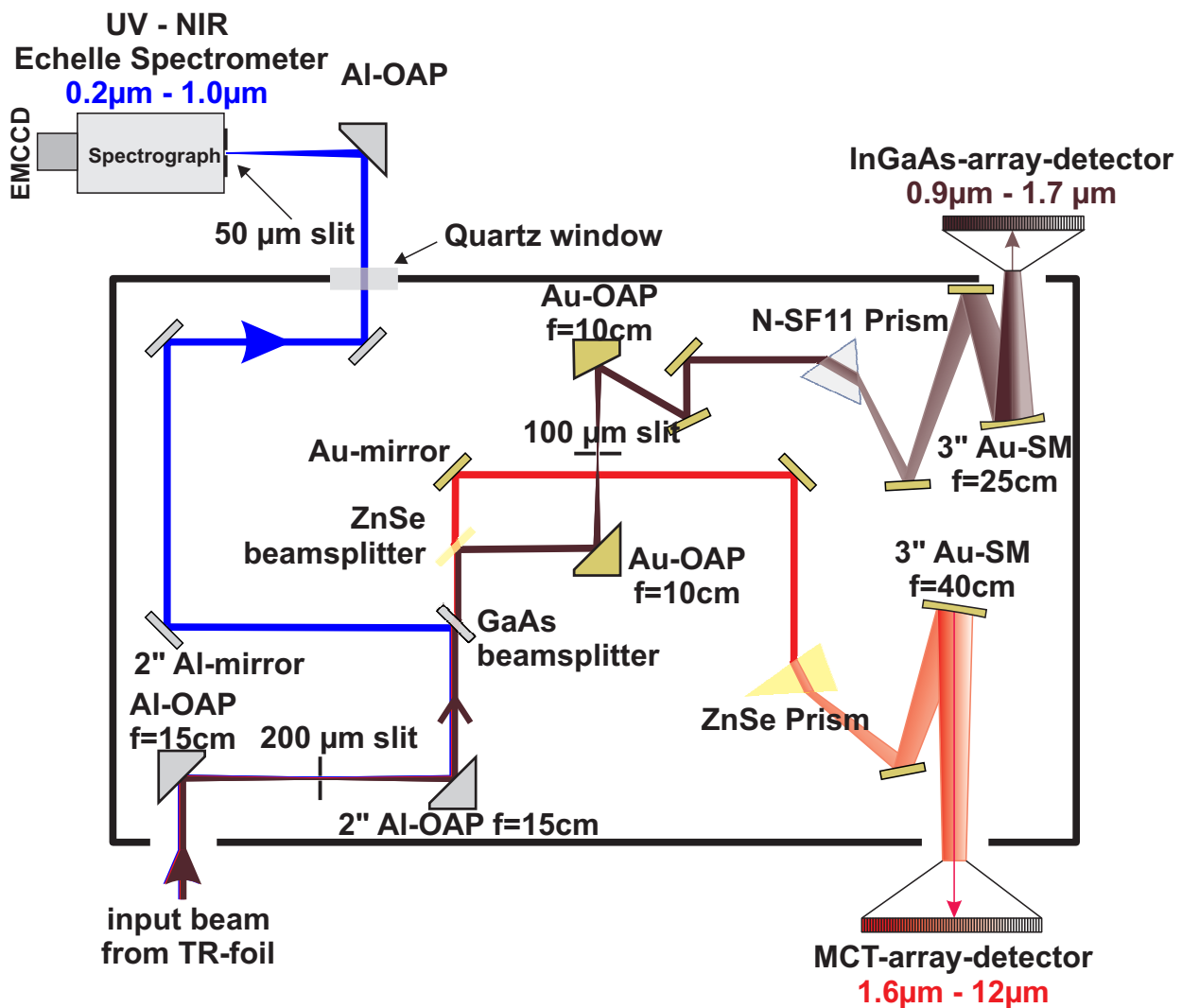


Figure 4.1.: Overview of the main components of the TR spectrometer.

translated or rotated during the calibration or experimental measurement are motorized. This enables precise alignment of relevant optics in the vacuum.

4.1.1. BASICS OF PRISM SPECTROMETERS

The concept of a prism spectrometer is depicted in figure 4.2. The collimated light source LS is focused by lens L_1 and illuminates the entrance slit S_1 , which is placed in the focal plane f_1 of the focusing lens L_1 . Behind L_1 the recollimated beam by L_2 passes through the prism P, where it is diffracted by an angle $\delta(\lambda)$ depending on the wavelength λ , incidence angle on the prism θ_1 and its apex angle α . The camera lens L_3 images the entrance slit S_1 onto the detector array S_2 . The position $x(\lambda)$ of this image in the focal plane of the camera lens, f_3 , is a function of the wavelength λ . The linear dispersion $dx/d\lambda$ of the spectrograph depends on the spectral dispersion $dn/d\lambda$ of the prism material and on the focal length of L_3 . Depending on the linear dispersion of the prism and lateral extension of the detector array $\Delta x = x_1 - x_2$, a certain spectral range $\Delta\lambda = \lambda_1(x_1) - \lambda_2(x_2)$ can be covered by the detector S_2 .

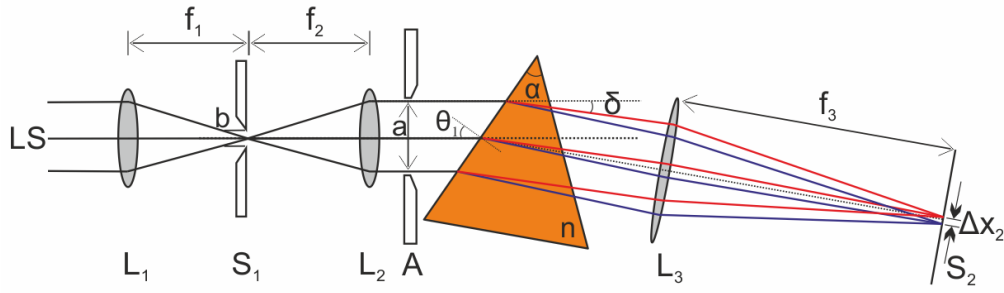


Figure 4.2.: **Concept of a prism spectrometer.** Angular dispersion of a prism depends on prism dispersion and the imaging optics.

BASIC PROPERTIES OF ANY SPECTROMETER

The selection of an optimum type of spectrometer is guided by some basic characteristics of spectrometers and their relevance to a particular application. For prism spectrometers, the spectral transmission depends on the material of the prism and lens systems. In the infrared region, several materials (for example, CaF₂, NaCl, and KBr crystals) are transparent up to 30 μm, while CsI and diamond are transparent up to as high as 80 μm. The basic properties that are important for all dispersive optical instruments are discussed as follows:

Angular dispersion Consider the spectral resolving power of a spectrometer when a beam passes a dispersive element (prism or grating), so that a collimated beam composed of two monochromatic waves with wavelengths λ and $\lambda + \Delta\lambda$ is split into two partial beams with the angular deviations δ and $\delta + \Delta\delta$ from their initial direction. The angular separation is defined as

$$\Delta\delta = \left(\frac{d\delta}{d\lambda} \right) \Delta\lambda, \quad (4.1)$$

where $d\delta/d\lambda$ denotes the **angular dispersion**, usually given in units [rad/nm].

Linear dispersion According to figure 4.2, the camera lens with focal length f_3 images the entrance slit S_1 into the plane S_2 , the distance Δx_2 between the two images $S_2(\lambda)$ and $S_2(\lambda + \Delta\lambda)$ is obtained by

$$\Delta x_2 = f_3 \Delta\delta = f_3 \frac{d\delta}{d\lambda} \Delta\lambda = \frac{dx}{d\lambda} \Delta\lambda. \quad (4.2)$$

The factor $dx/d\lambda$ denotes the **linear dispersion** of the instrument. It is generally measured in units mm/nm.

Spectral resolution The limit of the optical resolution of a spectrometer is set by the diffraction, which depends on the size of the aperture a and the focal length of the focusing optic f_3 as well as the wavelength λ (see fig. 4.3). According to the Rayleigh criterion, in order to clearly separate two intensity peaks the distance between two infinitesimally small slit images read as^[124]

$$\Delta x_2 = f_3 \left(\lambda/a \right). \quad (4.3)$$

Taking into account the finite size of the slit b and using the optical geometry, the width of the image of the slit is obtained by

$$\Delta x_2 = b \left(f_3/f_2 \right) \quad (4.4)$$

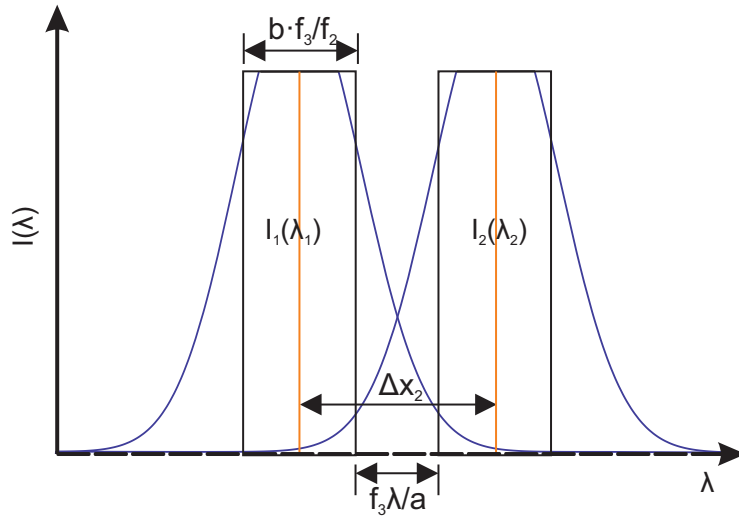


Figure 4.3.: spectral resolution of a prism.

For a finite entrance slit with width b the separation Δx_2 between the central peaks of the two images $I_1(\lambda_1)$ and $I_2(\lambda_2)$ according to Fig.4.3 must be larger than

$$\Delta x_2 \geq f_3 \frac{\lambda}{a} + b \frac{f_3}{f_2}. \quad (4.5)$$

The smallest resolvable wavelength interval $\Delta\lambda$, which is known as **spectral resolution** is obtained from (4.2) as

$$\Delta\lambda \geq \left(\frac{\lambda}{a} + \frac{b}{f_2} \right) \left(\frac{d\delta}{d\lambda} \right)^{-1}. \quad (4.6)$$

Note that for an infinite small entrance slit the spectral resolution is limited, not by the diffraction due to the entrance slit (eq. (4.4)), but by the diffraction caused by the much larger aperture a (eq. (4.3)), determined by the size of the optics. The diffraction due to the small size of the entrance slit reduces the transmitted intensity of the incident beam.

Spectral resolving power The spectral resolving power of any dispersing instrument is defined by the expression

$$R = \left| \frac{\lambda}{\Delta\lambda} \right| = \left| \frac{\omega}{\Delta\omega} \right|, \quad (4.7)$$

where $\Delta\lambda = \lambda_1 - \lambda_2$ stands for the minimum separation of the central wavelengths λ_1 and λ_2 of two closely spaced lines that are considered to be just resolved^[124].

In order to derive an expression for resolving power of a spectrometer with an entrance slit size b , substituting the equation (4.6) into the general expression for resolving power (4.7) results in

$$R = \left| \frac{\lambda}{\Delta\lambda} \right| = \lambda \left(\frac{\lambda}{a} + \frac{b}{f_2} \right)^{-1} \left(\frac{d\delta}{d\lambda} \right) \quad (4.8)$$

$$= \lambda \left(\frac{\lambda}{a} + \frac{b}{f_2} \right)^{-1} f_3^{-1} \left(\frac{dx}{d\lambda} \right), \quad (4.9)$$

which can be evaluated from the geometric sizes of the spectrometer optics and the angular (linear) dispersion of the prism.

4.1.2. CHOICE OF BEAM SPLITTERS

By using uncoated infrared bulk materials and taking advantage of its Fresnel reflection and transmission properties, two beam splitters are selected in order to spectrally separate the input beam into the three spectral ranges and to guide these into their associated spectrometer arms (see Fig. 4.1). A 6 mm thick Gallium-Arsenide-plate (GaAs) with 12 minutes wedge angle (manufacturer II-VI-INFRARED) is used to separate the UV-NIR range of the spectrum, 250 nm to 1000 nm, from the IR part of the TR-beam. Note that the Fresnel reflection from GaAs also contains longer wavelengths, however, the IR wavelength will be partially blocked by the utilized quartz vacuum window (Corning 7980) which only transmits from 200 nm up to $\approx 4 \mu\text{m}$ with an excellent transmission in UV-VIS range better than 99 %.

In the near and middle infrared Zinc-Selenide^[126] (ZnSe) is a preferred material for lenses and windows because of its low absorptivity at infrared wavelengths ($\leq 0.0005 \text{ cm}^{-1} @ 10.6 \mu\text{m}$) and its visible light transmission for alignment purposes. A 3 mm thick ZnSe plate with 6 minutes wedge angle (manufacturer KORTH KRISTALLE) is utilized to split the IR transmission through the GaAs beam splitter into two parts. Transmission and reflection curves of the mentioned beam splitters are calculated by means of Fresnel equations^[127] with respect to s- and p-polarization. Note that the p-polarization is defined to be in the optical plane of the spectrometer. The wavelength dependent refractive index of these materials are modeled by using Sellmeier-polynomials^[128]. The absorption, as well as losses because of second internal reflection in the GaAs material, is also taken into account, while the absorption in ZnSe bulk material for the infrared range of the spectrum is negligible. The results of this calculation are shown in Fig. 4.4.

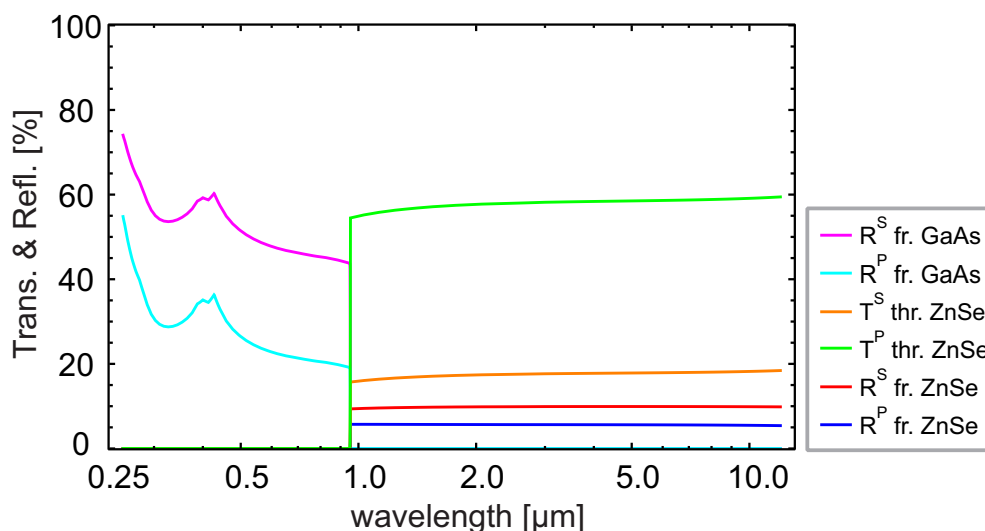


Figure 4.4.: Transmission of the input beam through the GaAs and ZnSe beam splitters. GaAs, with a sharp transmission edge at around 900 nm and low bulk absorption of $\leq 0.01 \text{ cm}^{-1}$, is suitable for spectral separation of the UV-NIR range from the near to the MIR range. ZnSe reflects on average 7 % of the beam and transmits 18 % and 60 % of the input beam for s- and p-polarization respectively

4.1.3. PRISMS DESIGN

The Free spectral range of a spectrometer is the wavelength interval, F_λ , for which there is a single relationship between λ and the position $x(\lambda)$ on the detector surface. Since the dispersion in prisms is related to its wavelength dependent index of refraction, a single prism

could cover a much broader spectral range, usually the whole region of its dispersion, than a grating. Prisms are therefore commonly used in spectrometers when the desired dispersion and therefore achievable resolution is weak compared to gratings. In contrast, F_λ for gratings is determined by the grating diffraction order m in which there is no interference or overlapping of light from adjacent orders. Therefore when using grating many diffraction orders may be formed and, if no order sorting filter is used, the higher orders could overlap and cause complications when measuring a broad spectrum of light.

On the other hand, prisms present better throughput and lower stray light characteristics than their gratings counterparts. By customizing the geometry of the prism as well as selecting a suitable prism material, one can design an optimum prism using a global optimization algorithm in order to accomplish the optimum performance in a specific spectrometer. When selecting the prism material and its geometry, the following criteria must be taken into account:

1. Free spectral range of a prism $F_\lambda = \lambda_{\text{high}} - \lambda_{\text{low}}$ is set with respect to the QE of available detectors, transmission and reflection properties of the involved optics. Due to the QE of the InGaAs detector (see Section 4.1.5), which is limited to 800 nm to 1.7 μm (limits @ 20 % level of QE) and the cutoff of the GaAs beam splitter at 900 nm (see Section 4.1.2) the spectral range for NIR is set from 900 nm to 1.7 μm .

According to the QE of the MCT detector (see Section 4.1.5) the spectral range of 1.6 μm to 12 μm is determined for the MIR range to allow an overlap of 100 nm between NIR and MIR ranges, which allows for a comparison of the detectors calibrations and to perform an absolute cross-calibration of the spectrometer arms. The latter will be discussed in detail in the calibration Section 4.2.

2. The induced linear dispersion in the beam $dx/d\lambda$ through the prism should cover the entire detector array concerning a focal length of a focusing optic, here a spherical mirror (SM), that can be realized in the setup (see Section 4.1.1). Using an SM to focus the beam under a small off-axis angle (here $\sim 10^\circ$) causes a slight astigmatism leading to elliptical foci on the detector array plane. This meets the squared shape of the InGaAs pixels (500x25 μm) thus no intensity losses are expected. On the other hand, the axial symmetry of an SM eases the alignment procedure compared to an OAP.

3. The prism should have the best possible linearity in the dispersion in order to achieve a uniform spectral resolution on the corresponding detector array. This is desirable in order to both realizing quasi-constant spectral resolution and for performing a precise wavelength calibration (see Section 4.2.1). The non-linearity (NL) of the dispersion is defined by the so-called *spectral sampling ratio* (SSR)

$$\text{SSR} = \max \left[\left| \frac{d\delta}{d\lambda} \right| \right] / \min \left[\left| \frac{d\delta}{d\lambda} \right| \right], \quad (4.10)$$

where $d\delta/d\lambda$ denotes the angular dispersion of the prism. The SSR gives the ratio of the maximum to the minimum dispersion in a given spectral range and, in the case of uniform dispersion, converges to 1. In practice, this value is a useful figure of merit in formulating target functions which has to be minimized for optimization calculations of the prism geometry.

4. Furthermore, large incidence and deflection angles (θ_1 and θ_2' in Fig. 4.5) on the prism cause significant losses due to reflection on the prism refractive surfaces and therefore the conditions $\theta_1 < 60^\circ$ and $\theta_2' < 60^\circ$ are implemented in the algorithm for prism optimization.

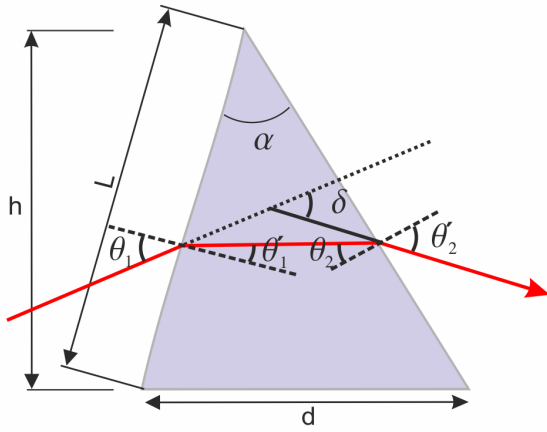


Figure 4.5.: Ray trace through a prism. $\theta_1, \theta_1', \theta_2, \theta_2'$ are the angles of incident and refraction on the first and second prism interface respectively, α the prism apex angle, d, L, h are the geometric dimensions of the prism and δ is the deflection angle to the incident beam. Note the sign convention of the angles θ and δ , in which clockwise angles with respect to the surface normal have negative sign and vice versa.

5. In addition, the prism geometry must be chosen such that its refractive surfaces are consistent with the beam diameter and the prism does not become too large to minimize manufacturing costs and adjustment difficulties.

The prism geometry is modeled in programming software MATHEMATICA^[129] according to geometrical optics (see Fig. 4.5) and ray paths are calculated with the help of Snell's law of refraction^[127] in the form of a system of equations. The deflecting angle of a beam by passing through the prism can be expressed as^[130]

$$\delta(\lambda, \theta_1, \alpha) = -\alpha + \theta_1 + \arcsin \left(n(\lambda) \sin \left(\alpha - \arcsin \left(\frac{\sin(\theta_1)}{n(\lambda)} \right) \right) \right), \quad (4.11)$$

assuming the refractive index of the environment medium being 1. The wavelength dependent refractive index of the prism $n(\lambda)$ can be modeled by the well-known Sellmeier equations^[128]. A comprehensive description of the above-outlined optimization criteria can be found in Refs.^[130–132]. A global optimization algorithm based on differential evolution method is thus employed in order to calculate the prism geometry for a series of known infrared materials. The selected prisms designs from N-SF11^[133] for the NIR range and ZnSe^[134] for the MIR range are documented in Fig. 4.6.

Notably, using the double prism design would lead to better spectral linearity compared to a single prism. For this reason, a double prism design consisting of a ZnSe prism and a NaCl prism was also investigated. However, the remaining gap between the prisms would lead to multiple reflections on the prisms deflecting surfaces and hence a reduction of the spectrometer throughput. Also, the hygroscopic property of NaCl is disadvantageous to its throughput in long terms. Therefore, in the present work, we used the single prism design of the MIR arm.

4.1.4. ECHELLE SPECTROMETER

An Echelle spectrometer consists of either a combination of two gratings or both a grating and a prism whose dispersion planes are perpendicular to each other. The echelle grating separates the spectrum into many spectral orders, each of which maps a portion of the high-resolution spectrum. The second grating or prism separates the orders from each other so that the spectrum can be imaged onto a 2D detector surface. In this way, overlaps of different grating orders are prevented and thus enables measurement of a spectral range over several optical octaves with high resolution in a single shot. A commercial Mechelle spectrometer

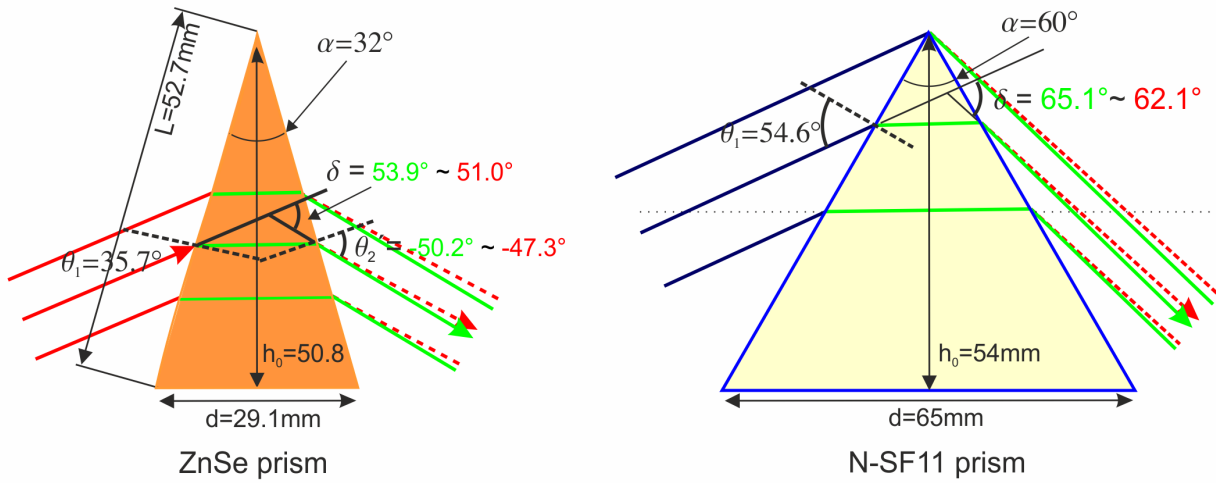


Figure 4.6.: **Prisms design.** Illustrated are the configurations of N-SF11 and ZnSe prisms, which are designed for NIR (0.9 μm to 1.7 μm) and MIR (1.6 μm to 12 μm) ranges of the spectrometer respectively

ME5000^[135] from the manufacturer ANDOR TECHNOLOGY is implemented in the TR spectrometer for the UV-NIR range, i.e. from 200 nm to 1030 nm. A scheme of the echelle spectrometer is presented in Fig. 4.7. The focusing beam enters the echelle spectrograph through a 50 μm wide entrance slit, is collimated by an F/7 SM and subsequently diffracted by a double prism. The dispersed beam, in turn, falls onto a grating and is thereby once again spectrally decomposed perpendicular to the deflection direction of the prism. A focusing mirror images the entrance slit onto an EMCCD detector chip. As a result, the spectrally decomposed beam through the prism-grating combination takes the form of a 2D surface on the EMCCD detector (see Section 4.1.5). The grating used in this spectrometer has a smaller groove density than conventional gratings, i.e. 52.13 mm^{-1} . It is used under higher grating orders, i.e. 20 to 100 and blazed at 32.35°. The free spectral range for any single order, m , is given by

$$F_{\lambda}^m = \frac{\lambda_m^0}{m(1 - (2m)^{-2})}, \quad (4.12)$$

where λ_m^0 denotes the central wavelength of any order. The overall bandwidth thus depends on the number of orders that can be fit onto the detector chip and is calculated by summation of the bandwidth of individual orders as defined in Eq. (4.12). The efficiency of the echelle spectrometer depends mainly on the efficiency of its grating and the QE of the coupled detector. The angular dispersion of the echelle grating can be read as

$$\frac{d\phi}{d\lambda} = \frac{m \cdot g}{\cos \phi}, \quad (4.13)$$

where g is the groove density (in the case of Mechelle $g = 52.13 \text{ mm}^{-1}$) and ϕ is the deflection angle with respect to the surface normal ($\phi \approx 60^\circ$). Although its gratings deflection angle ϕ is not varying much over a defined spectral order ($\leq 2^\circ$)^[136,137], the reflection coefficient of the grating and therefore the grating efficiency considerably drops from its maximum in the middle of each order toward the borders of each spectral order to about half of its value (see Fig. 4.8 (c)). The extremely varying spectral efficiency of the echelle spectrometer over its entire spectral range is evident in Fig. 4.8, where a continuous Quartz-Tungsten-Halogen (QTH) lamp is used as the light source.

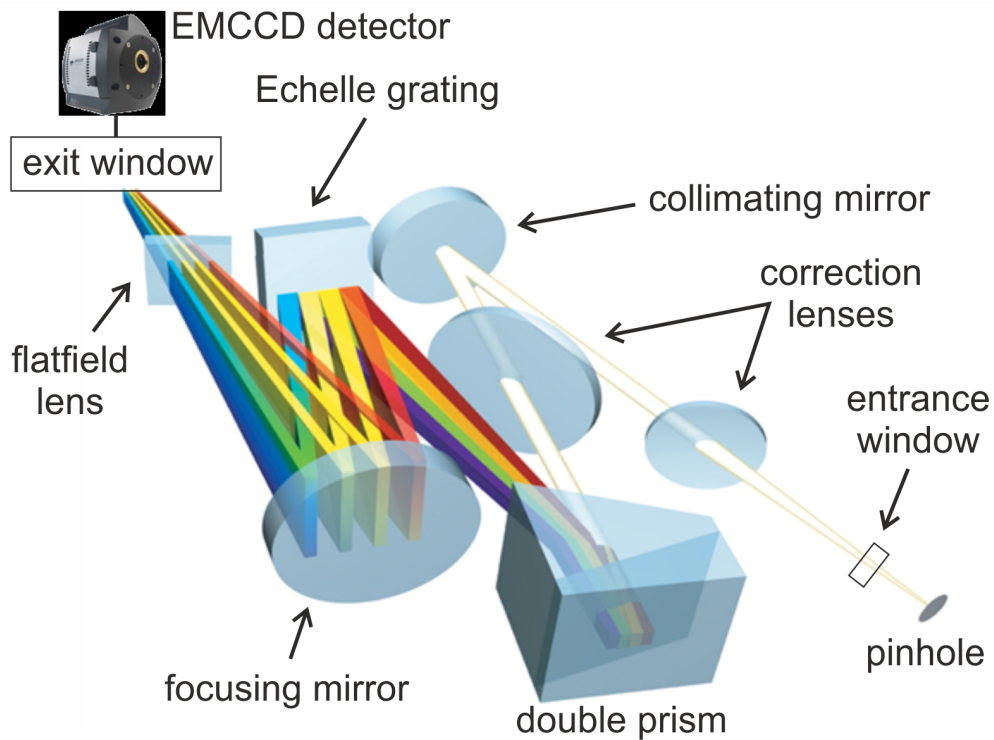


Figure 4.7.: Optical layout of the echelle design. (Figure taken from manual of Mechelle^[135], Courtesy of T. Pieper), the double prism acts as an order sorter, the latter works in combination with the correction lenses like an achromatic lens, providing a semi-equal order spacing on the focal plane of the focusing mirror, the position of the EMCCD detector.

4.1.5. DETECTORS

There are several detection technologies to measure an ultra-short light pulse in different spectral ranges. Each method has its advantages and drawbacks. Detection systems such as Pyro-electric detectors^[138,139] are widely used in the detection of infrared signals. They usually consist of a thin layer of single crystalline lithium tantalate (LiTaO_3) capacitor element. The pyroelectric crystal (normally from single crystalline LiTaO_3) generates a charge when heated, and this charge can be converted into an electric signal as the response of the detector. Its sensitivity to heat, hence to infrared wavelengths, makes these detectors widely applicable in measuring the far-infrared and THz radiation. However, compared to CCD detectors they exhibit lower resolution due to the relatively large size of individual detector elements. The pyroelectric detectors feature a specific detectivity in the order of $D^* < 10^8 \text{cmHz}^{1/2}/\text{W}$ which is orders of magnitude less than the specific detectivity of semiconductor based infrared detectors. The latter is typically in the order of $D^* > 10^{10} \text{cmHz}^{1/2}/\text{W}$. The applicability of pyroelectric detectors also suffers from their limited dynamic bandwidth which limits their use in broadband spectrometers for single-shot measurement of high intensity modulated signals.

In order to detect a broad range of TR spectrum at high resolution and high sensitivity, we utilized an MCT array detector, an InGaAs array detector, and an EMCCD detector.

In the following subsections, the main properties of the mentioned detectors are outlined. Beforehand, we shortly introduce the acquisition software of the TR spectrometer:

A dedicated LabVIEW^[140] Virtual Instrument (VI) is developed in order to handle the communication between the detectors and the control computer. The most useful functionalities of the mentioned detectors are implemented in this VI enabling the initialization and configuration of each detector individually. Data acquisition, online displaying of the spectra and

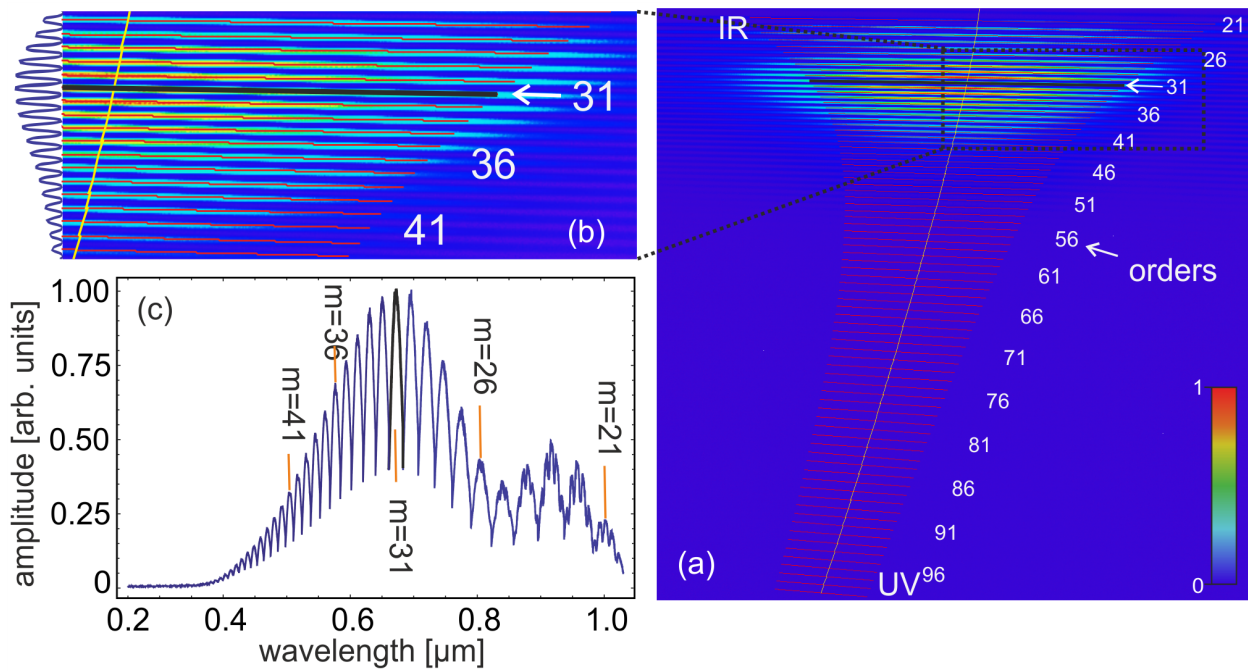


Figure 4.8.: **Sample measurement of the spectrum from a QTH lamp.** (a) illustrates the total image acquired with the echelle spectrometer. The horizontal red lines indicate the diffraction orders, numbered on the right side. The orange line connects the central wavelength, λ_m^0 , of each order. (b) shows a zoomed part of (a) including a vertical line out on the left side showing the separation of the diffraction orders. The vertical extension of any order covers around 10 pixels. (c) presents the constituted spectrum from all orders, starting from 200 nm located on the bottom right on (a) to 1030 nm on the top left accordingly.

saving are triggered by an external trigger signal and an electronic shot counter (NATIONAL INSTRUMENT, USB-6501) which is also implemented in this VI. The VI thus assigns the current counter number to the corresponding acquisition and creates a unique set of entries in a database (PostgreSQL^[141]). The database contains in particular information about the location of recorded data on the hard disc but also a set of metadata containing current detectors configurations that are of importance for data post-processing. The timing of the trigger signal with respect to the incoming light pulse can be precisely set by a delay generator and be monitored by an oscilloscope.

EMCCD detector The 2D spectrum of the echelle spectrograph (see Section 4.1.4) is recorded with a 14-bit, back illuminated Electron Multiplying Charged Coupled Devices (EMCCD detector, iXon3 888, model A-DU888-EC-BVF, ANDOR TECHNOLOGY). The detector active area consists of 1024 x 1024 pixels with a pixel size of 13x13 μm . The incident light on the active surface of the detector is after the end of the exposure time moved line by line in a similar, hidden by light, pixel area as a buffer (frame transfer). The EMCCD is a sensor technology that enables the measurement of feeble signals by suppressing the readout noise during the readout process. This feature is realized, in contrast to the conventional amplification techniques, by amplifying the signal in electron multiplier (EM) register, before it transferred into the output amplifier and A/D-converter. Note, that the cameras dynamic range decline with increasing EM gains as a result of the charge amplification in the register capacity.

The detector head is enclosed in a vacuum behind an AR coated quartz window. A built-in thermocouple and an external water cooling dissipate heat from the detector chip and cools the chip down to -95°C reducing the (thermal) dark current in the detector by more than

one order of magnitude. The electron-multiplying (EM) mode ensures that the photoelectron signal is amplified through the EM register before digitization to counteract the readout noise.

Indium-Gallium-Arsenide detector For the NIR measurement from 0.9 μm to 1.7 μm with simultaneously high QE, minimized noise and a high dynamic bandwidth, an InGaAs array-detector (ANDOR TECHNOLOGY, iDus 490) is used. The detector array consists of 512 pixels, each 25 μm wide and 500 μm high. The detector array is housed in a vacuum via an uncoated quartz window. Similar to the EMCCD detector (see Section 4.1.5), a thermocouple cools the detector head down to -90°C .

Mercury-Cadmium-Telluride detector To measure the spectrum in the MIR range from 1.6 μm to 12 μm , a photoconductive (PC) MCT array detector (INFRARED SYSTEMS, IR-6416) is used. The MCT detector is a semiconductor and is more sensitive and faster than thermal detectors and hence provides a spectrum with a higher signal-to-noise ratio (SNR). Disadvantages of these detectors are a narrow spectral bandwidth based on their composition and small dynamic bandwidth.

The wavelength of its peak response was customized by the manufacturer from $< 2 \mu\text{m}$ to $> 14 \mu\text{m}$ (@ 20 % QE) by adjusting the alloy composition of its ternary compound. The MCT detector array consists of 64 pixels. The actual active area of each pixel element is 300 μm wide and 600 μm high. An additional inactive space of 25 μm separates the pixels from each other. Since the detector head is susceptible to heat its chip is housed in a Dewar flask behind an AR-coated ZnSe window, which can be filled with liquid nitrogen LN_2 . As a result, the detector is cooled down to 74 K thus minimizing the thermal noise in the detector due to its thermal radiation. The integration time window for a recording can be set in 10 ns steps from 54 ns to 2614 ns. It should be noted that the MCT electronic measures changes in resistance. The readout amplifier thus uses as a reference the average bias current from the previous 30 μs for an acquisition. This measurement method is well suited for signals which occur within a ns- μs integration time. However, in order to perform a proper measurement regarding the absolute energy of a signal, the incidence pulse must be shorter than the time constant of the detector, i.e. $< 400 \text{ ns}$ in order to ensure the integration of the total amplified signal without increasing the integration time. This is due to the relatively long-term declination of the pre-amplifier output signal, which is at about 2.5 μs .

4.2. CALIBRATION

The calibration procedure is subdivided into three separate calibration tasks. Following the wavelength calibration, the relative calibration determines the sensitivity of the spectrometer at different wavelengths in relative proportions. The final absolute calibration is based on photometric, i.e. beam energy measurements, which returns the relative calibration curves to absolute photometric magnitudes such as radiant energy and number of photons, while at the same time accounting for s- and p-polarization. This calibration procedure is performed over all spectral ranges separately, i.e. 0.2 μm to 1.0 μm (echelle spectrometer), 0.9 μm to 1.7 μm (InGaAs) and 1.6 μm to 12 μm (MCT).

For this purpose, various calibration sources are used. An overview of utilized calibration sources is depicted in Fig. 4.9. These include laser sources, calibrated spectral emission lines sources, characterized absorption foils and band-pass filters (BPF) as well as calibrated continuous sources such as black body, Quartz-Tungsten-Halogen (QTH) and Deuterium lamps. The wavelength calibration in the MIR range is performed by means of absorption lines of plastic

films ($\approx 10 \mu\text{m}$ thick), the latter is back illuminated by a black body (BB) reference spectrum. Spectral emissions from an Argon source (Ar) and a Mercury-Argon source (HgAr) are used in the NIR and UV-VIS ranges respectively. In contrast, for relative response calibration photometrically calibrated broadband radiation sources are utilized. In order to reduce calibration errors, only the shape of the respective spectra is used and not the photometric calibration. The absolute calibration is instead performed via a number of different continuous-wave (CW) lasers at selected wavelengths.

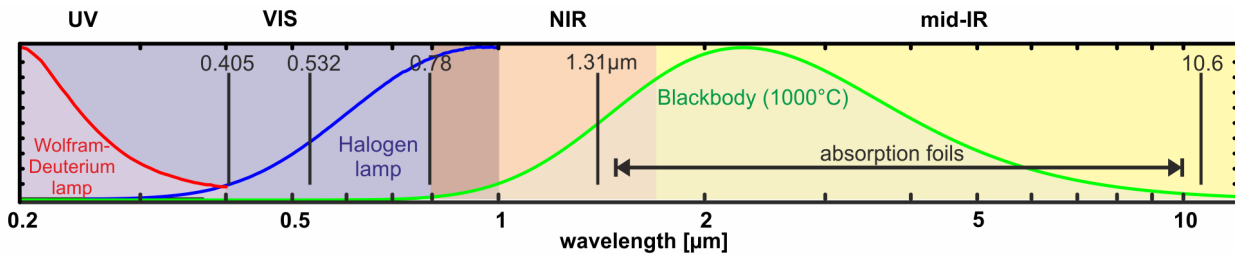


Figure 4.9.: Overview of the light sources used in the calibration procedures of the spectrometer

4.2.1. WAVELENGTH CALIBRATION

Wavelength calibration of a spectrometer typically involves measurements of lines at well-known wavelengths from the spectral emission of a calibration light source (LS)^[119] or absorption lines of a characterized absorber material. The relationship between the wavelength and the corresponding pixel positions on the detector is thus obtained by a polynomial fit^[121]. In the following, we discuss specifics for each of the spectrometer arms separately.

Echelle spectrometer A HgAr spectral LS produces first-order mercury and argon emission lines from 253 to 922 nm and second order argon emission lines up to 1700 nm for use in performing reliable spectrometer wavelength calibrations. A 50 μm diameter fiber optic (Andor, A-ME-OPT-8004) is used to couple the source emission into the echelle spectrometer. Identification of these spectral lines on EMCCD-detector is performed by using the implemented algorithm for wavelength calibration in its acquisition software ANDOR SOLIS. Following seeking of the relevant spectral lines, the boundaries of each diffraction orders with respect to their central wavelengths λ_m^0 are thereby determined. Since the spectral bandwidth of any order is small compared to its entire spectral range, linear interpolation on each order is performed to accomplish the wavelength calibration of individual diffraction orders. It is notable that the diffraction orders are arranged slightly oblique with respect to each pixel row. The global calibration curve is then carried out by attaching the mentioned diffraction orders and performing a 5th-order polynomial fit. In practice, the mentioned calibration curve addresses the central pixel of each wavelength, from which ± 5 pixels in the corresponding column, perpendicular to the orders, have to be summed up, in order to read out the total spectral intensities of a signal at a particular wavelength (see also Section 4.2.4).

Fig. 4.10 shows the result of the echelle wavelength calibration.

InGaAs detector Alignment of the NIR arm is performed by means of a single mode, polarization-maintaining, fiber optic coupled laser, $\lambda = 1.31 \mu\text{m}$ central wavelength and $\Delta\lambda = 10 \text{ nm}$ bandwidth (Thorlabs, S1FC1310PM). The central pixel hit by the mentioned laser is used as the first calibration point. It is also utilized for absolute calibration (see Section 4.2.4). The utilized Ar

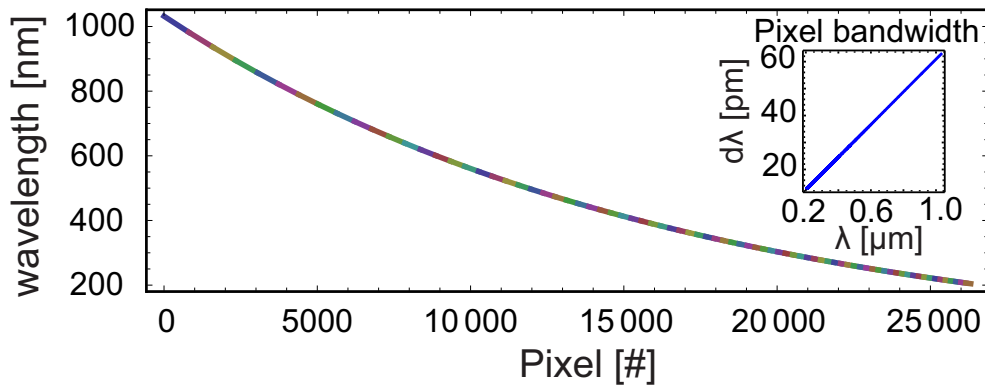


Figure 4.10.: **The wavelength calibration fit for the echelle spectrometer.** Each sequence of the curve (various colors) indicates a diffraction order, while the spectral bandwidth of each order is decreasing toward the shorter wavelength, the resolution is increasing with the number of orders. The inset shows the spectral bandwidth covered by individual pixels as a function of wavelength.

calibration source (OCEAN OPTICS) produces low-pressure argon emission lines from 700 nm to 1.7 μm . The Ar emission is guided from the LS by a fiber optic (Andor, A-ME-OPT-8004) and collimated by an OAP in order to transport it by further folding mirrors into the spectrometer chamber. The measured Ar-spectrum with InGaAs-detector is then compared to the known Ar spectral lines, provided by the manufacturer. Thus a wavelength calibration is performed. Additionally, transmission of two bandpass filters (BPF) at 950 nm and 1.65 μm are also included. Over all calibration points, a 3th-order polynomial fit is performed as shown in Fig. 4.11.

MCT detector The wavelength calibration of the MCT detector is performed using absorption lines of four different thin ($\approx 10 \mu\text{m}$) Teflon films (TPX, HDPE, PP, Mylar) whose transmission spectra are characterized over the spectral range of interest for the MCT detector by using a Fourier transform infrared (FTIR) spectrometer (Bruker, 4 cm^{-1} -resolution). The absorption spectra of the plastic foils as mentioned above are thus measured with the MCT detector using a BB spectrum as the reference LS. By comparing both absorption spectra, the central wavelengths of the absorption lines on the FTIR measured spectra are subsequently assigned to the corresponding central pixels on the MCT spectra. Over the calibration list, including, CO_2 laser line as well as two BPF at 1.65 μm and 2 μm , a 3th order polynomial is fitted.

Fig. 4.12 presents the results of this calibration procedure.

4.2.2. ACHIEVED RESOLUTION AND RESOLVING POWER

According to Eq. (4.9), the theoretical and experimental resolving power of each individual spectrometer arm are evaluated as a function of the wavelength, where the theoretical angular dispersion $d\delta/d\lambda$ is obtained from Eq. (4.11) and the experimental linear dispersion $dx/d\lambda$ follows from the wavelength fit. The latter is evaluated on a discrete grid regarding the dimension of the active area of the corresponding detector. A summary of this treatment is presented in Fig. 4.13.

Analogue to the resolving power, according to the Eq. (4.6) a summary of the spectral resolution of the spectrometer is shown in Fig. 4.14.

Although the smallest detectable wavelength by the echelle spectrometer is theoretically 200 nm, the low throughput of the spectrometer below 250 nm, prevents an accurate relative

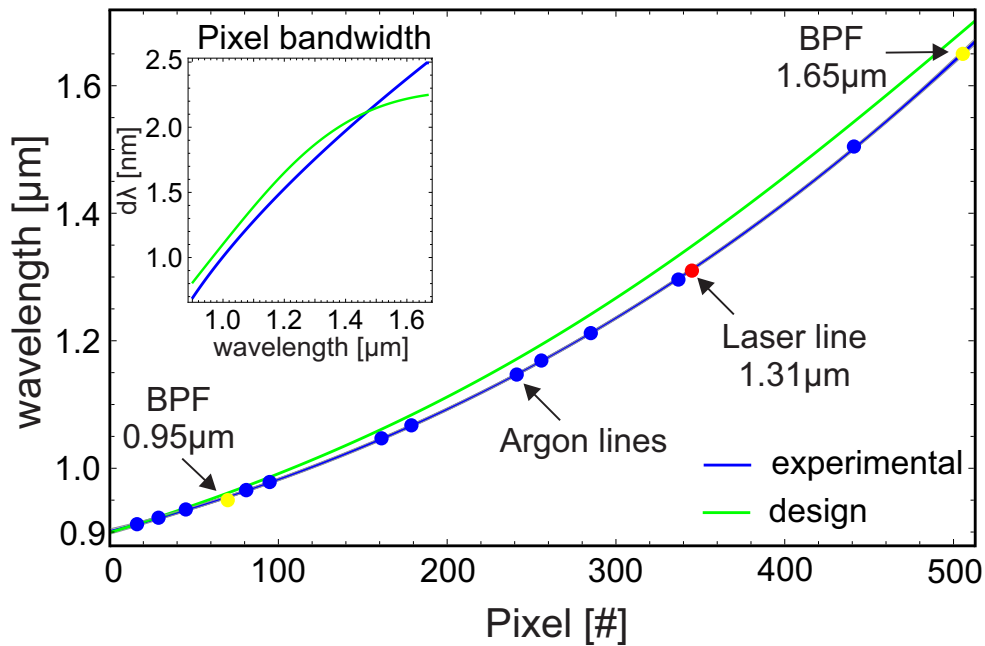


Figure 4.11.: The wavelength calibration of the InGaAs detector. Several Ar spectral lines are identified (marked in *blue*) according to their order of occurrence on the InGaAs array detector compared to the known spectral emission of the LS. The marks for the BPF's and the alignment laser are well in-line with the marks from Ar. The *blue solid line* indicates the 3rd order polynomial fit. Regarding the fit model 3σ standard deviation from the mean is obtained to be on average 0.34 %

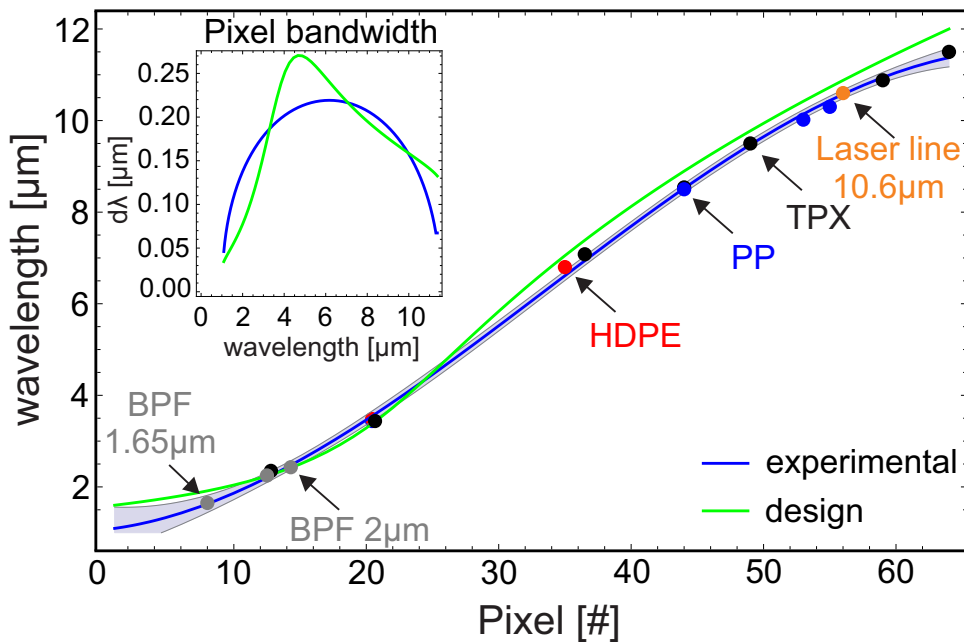


Figure 4.12.: The wavelength calibration of the MCT detector. The *blue solid line* indicates the 3rd order polynomial fit. In the spectral range from 1.6 μm to 11.3 μm corresponding to the pixel# 8 to 64 respectively, the average of the estimated relative error in term of 3σ standard deviation from the mean is obtained to be 4.0 %

response calibration in this range. Therefore, the lower limit of the echelle spectrometer is set to 250 nm. The upper spectral limit of the TR spectrometer is 11.35 μm given by the MCT calibration fit. For MCT detector the pixel values below a wavelength of 1.6 μm are not valid since the QE of the MCT is not sufficient to perform a valid calibration. For NIR spectrum, the wavelength above 1.6 μm as well as below 1.0 μm are not valid according to the low QE of the InGaAs detector and low transmission efficiency of GaAs beam splitter below 1 μm respectively.

In summary, the free spectral range of the TR spectrometer is 250 nm to 11.35 μm with about 100 nm spectral overlap between the different spectrometer detectors.

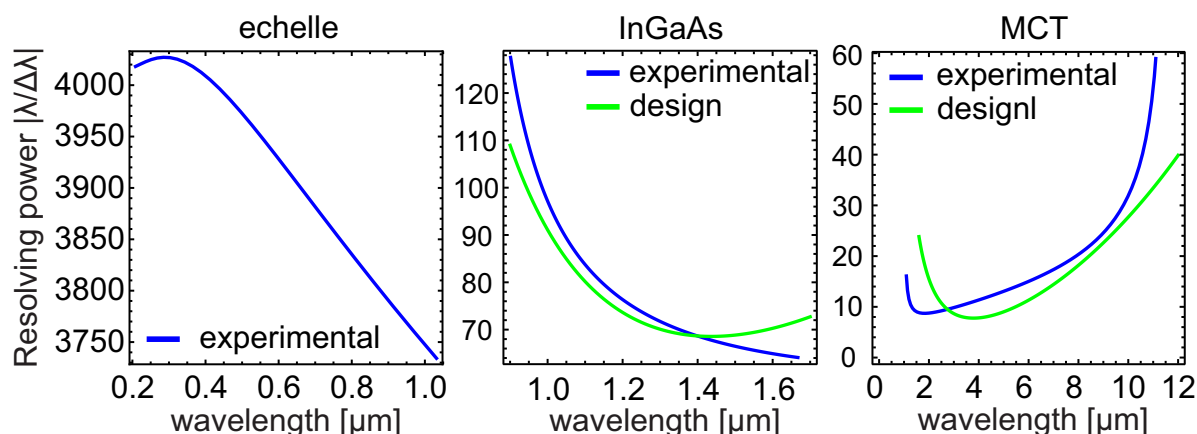


Figure 4.13.: The resolving power calculated for each spectrometer arm. Since the theoretical angular dispersion for the commercial echelle spectrometer was not available, only the experimental curve is presented here.

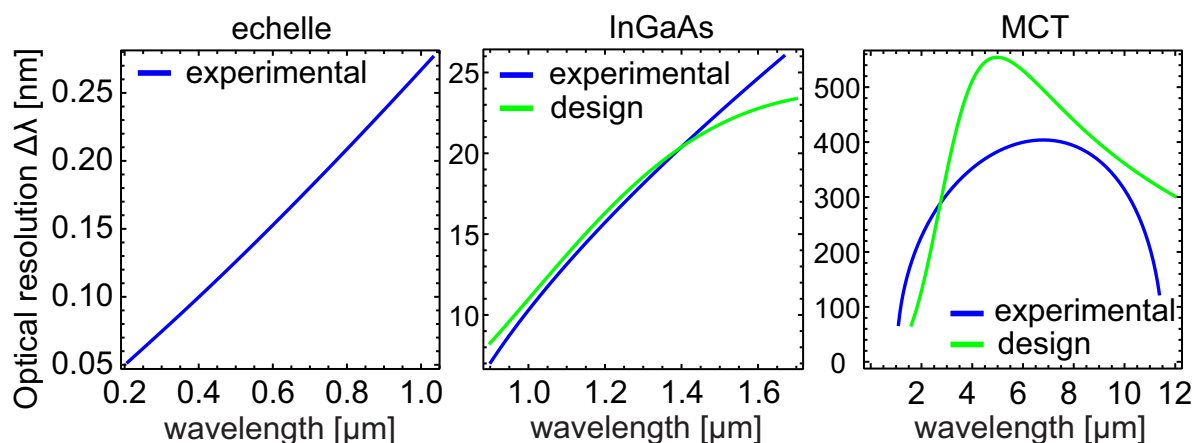


Figure 4.14.: The spectral resolution of the spectrometer, separately obtained for each spectrometer arm.

4.2.3. RELATIVE RESPONSE CALIBRATION

In general, relative calibration is performed by comparing a measured spectrum of a known continuous light source (LS), $T_{LS}(\lambda)$ to the theoretical or radiometric spectrum of the LS, $S_{LS}(\lambda)$. The ratio of these spectra contains information about the relative spectrometer response as a function of wavelength and reflects, in particular, the wavelength dependent QE of the detector which is convoluted by the transmission efficiency of the spectrometer itself. This method

enables precise measuring of the relative efficiency of the spectrometer for a broad range of the spectrum at once. However, it requires first a wavelength calibration and is not reliable for an absolute calibration. The incoherent emission of the available LSs cannot be precisely transported for long distances, which leads to a large uncertainty in the measured emission power of the LS.

Therefore, the calculated relative calibration is normalized to unity concerning the wavelength at which the absolute calibration has to be performed (see Section 4.2.4).

For the spectral ranges MIR and NIR, a calibrated BB source (IR-508/301, INFRARED SYSTEMS) is used as the calibration LS. Its emission spectrum in the range from 0.5 μm up to 99 μm is very close to an ideal BB spectrum (according to the manufacturer > 99 % emissivity) and is given by the general Planck formula. In UV and NIR, the QTH lamp is used as the primary calibration source and the BB and Deuterium lamp act as comparative sources to the QTH. Here, only the calibration result from QTH is presented.

The calculation of the relative calibration can thus be expressed by

$$T_{\text{Rel}}^{\text{s,p}}(\lambda) = \frac{T_{\text{LS}}^{\text{s,p}}(\lambda)}{S_{\text{LS}}(\lambda)} \cdot \frac{1}{R_{\text{mirrors}}^{\text{s,p}}(\lambda)} \cdot \frac{1}{T_{\text{polarizer}}(\lambda)} \quad (4.14)$$

$$T_{\text{Rel, N}}^{\text{s,p}}(\lambda) = T_{\text{Rel}}^{\text{s,p}}(\lambda) / T_{\text{Rel}}^{\text{s,p}}(\lambda_{\text{Cal}}), \quad (4.15)$$

where $T_{\text{Rel}}^{\text{s,p}}$ is the transmission of the LS through the spectrometer with respect to s- and p-polarization, S_{LS} denotes the emission spectrum of the LS, which has to be known either from an independent reliable spectral measurement (QTH and Deuterium sources) or from a theoretical curve (BB source). In order to compensate the distortions of the LS spectrum by the alignment optics before it enters the spectrometer, the contributions from the reflection of the alignment optics, $R_{\text{mirrors}}^{\text{s,p}}$ as well as transmission through the polarizer bulk material, $T_{\text{polarizer}}$ are also taken into account. For this purpose, $T_{\text{polarizer}}$ is experimentally measured by the FTIR spectrometer. The reflectivity of aluminum, gold and silver coated mirrors are provided by the manufacturer (Thorlabs).

Furthermore the derived relative calibration curves are normalized to unity with respect to the value of the central pixel $T_{\text{Rel}}^{\text{s,p}}(\lambda_{\text{Cal}})$, which will be hit by corresponding laser line with the central wavelength λ_{Cal} . The measurement of the spectra regarding s- and p-polarizations are performed at the same detector settings. As a result, we gain information about the relative intensity distribution of each polarization between the curves. Thus, both polarizations can be absolutely calibrated even with an energy measurement of one of the polarizations. The TR spectrometer chamber is purged by dried nitrogen over several hours before the calibration measurement started. This removes, in particular, moisture and creates a much drier calibration environment and minimizes IR absorption.

4.2.4. ABSOLUTE CALIBRATION

In order to return the normalized relative calibrations, $T_{\text{Rel, N}}^{\text{s,p}}$ (Eq. (4.15)) into the energy calibrated curves an energy measurement is required using an appropriate laser line for each individual detection system. Here, the calibration procedure for s- and p-polarization are separately performed.

In the case of absolute calibration of the EMCCD and InGaAs detectors, 532 nm and 1.31 μm CW laser sources are employed respectively. For signal acquisition the detector exposure time is internally set to $\tau_{\text{exp}} = 50$ ms in order to mitigate the error in the τ_{exp} originating from the intrinsic detector gating jitter and readout speed of the detector chip. Additionally, at the input of the echelle spectrometer, a programmable fast mechanical shutter is utilized. Its opening window is triggered by the EMCCD detector. Thus, the internal acquisition time can

be used for further calculation of the incoming laser pulse energy. Furthermore, the intensity of the laser beam is reduced by using specified neutral density (ND) filters such that the entire dynamic bandwidth of the detector is covered. The average power P_{avg} of the CW laser beam is measured by a calibrated thermal power detector (model XLP12 from gentec) while the ND attenuators are removed from the beam in order to increase the SNR of the measurement. The involved ND filters in this measurement are separately calibrated by the same laser beam, and in the final energy calculation included. For a CW laser, the energy contained within a specific acquisition time τ_{exp} is thus calculated by

$$E_{\text{laser}}[\text{J}] = P_{\text{avg}}[\text{W}] \cdot T_{\text{ND}} \cdot \tau_{\text{exp}}[\text{s}], \quad (4.16)$$

where P_{avg} and T_{ND} denote the laser average power and the attenuation factor respectively. Note that the detector linearity of the both InGaAs and EMCCD is better than 99 % according to the manufacturer.

The calibration of the MCT detector requires more effort since the detector time constant of 400 ns doesn't allow to perform valid measurements with pulses longer than this time constant. However, in the MIR range of the spectrum, the laser sources that can provide pulses below 400 ns are limited. One possibility is to use FEL light sources^[142], which are associated with much effort in the sense of availability of a FEL beam time but also the lack of repeatability of such complex calibration campaigns. Here, we use an alternative way to perform such calibration measurement by customizing a commercially available CO₂ laser beam in combination with an acousto-optical modulator (AOM) enabling the generation of short pulses down to 100 ns with kHz repetition rate.

The CO₂ calibration setup is depicted in Fig. 4.15. A quasi-CW CO₂ laser with 1 W output (model L4 from manufacturer SOLITON) is utilized. The body of the laser resonator is air cooled in a closed loop via a temperature controller, which brings stability in both laser power and wavelength. The utilized AOM system (model N37041-1 from ELS GmbH) uses a germanium (Ge) interaction material with a lithium niobate transducer. The focusing laser beam polarization axis is adjusted to the Bragg plane of the Ge-crystal (here p polarization) using a holographic wire-grid linear polarizer (WGP) (BaF₂ Thorlabs WP25H-B). By fine adjustment of the AOM assembly and its Bragg angle with respect to the incidence beam and supplying an operating radio-frequency (RF) at 40.68 MHz, the AOM can be externally triggered at $f = 1$ kHz with an output pulse width of 200 ns at FWHM.

The p-polarized output pulse train from the AOM setup is thereafter polarized to 45° by WGP2. In this manner, the WGP3 can determine the final output polarization of the AOM setup providing selective s- or p-polarized beam for the MCT detector calibration. The average power P_{avg} of each polarization is measured using a calibrated thermal power detector (model XLP12 from gentec). The MCT readout electronic is synchronized to this laser pulse train using a Stanford delay box and monitored by an oscilloscope (Rode & Schwarz).

In order to improve the SNR during the power measurement, the laser pulse width is increased by a factor of 1000 to $\tau_{\text{Laser}} = 200 \mu\text{s}$. The pulse energy of laser pulse is calculated by $E[\text{J}] = P_{\text{avg}}[\text{W}] \cdot f^{-1}[\text{s}]$ and hence the pulse energy during the MCT calibration measurement is obtained to be

$$E_{\text{laser}}[\text{J}] = \frac{\tau_{\text{exp}}}{\tau_{\text{Laser}}} \cdot P_{\text{avg}}[\text{W}] \cdot f^{-1}[\text{s}]. \quad (4.17)$$

The absolute calibration factor is therefore given by

$$F_{\text{Abs}}^{s,p} = \frac{S_{\text{laser}}}{E_{\text{laser}}}. \quad (4.18)$$

$S_{\text{laser}} = \sum_{\# = i}^j S_{\text{laser}}(\#)$ denotes the integrated signal from the calibration laser over the entire concerned pixels on the detector regarding the polarizations s and p, and E_{laser} is given from

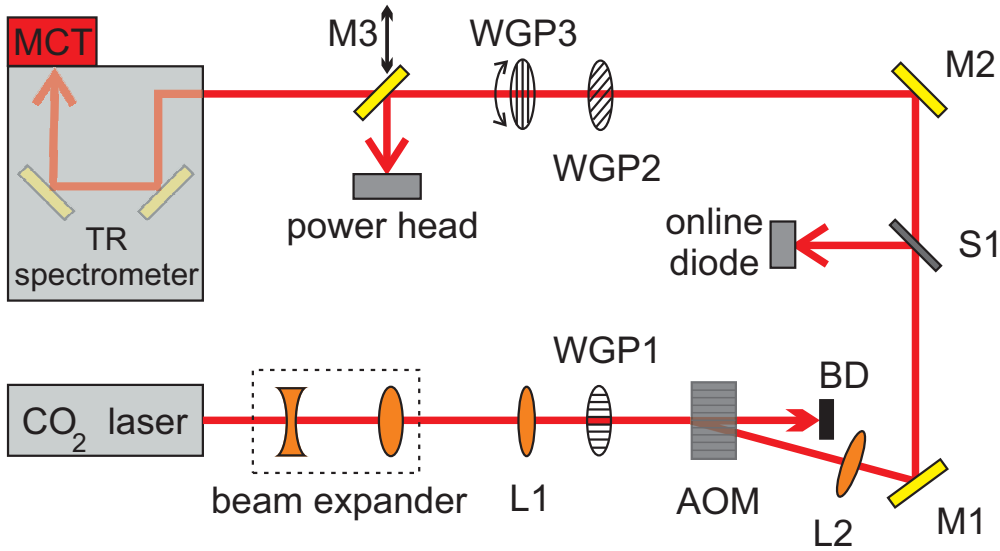


Figure 4.15.: Schematic of the CO₂ calibration setup. The beam expander, consists of a defocusing and a focusing ZnSe lens, enlarges the beam diameter from ~ 1 mm to about ~ 10 mm. The beam is focused on the AOM crystal by L1 and is polarized by WGP1. The zero-order transmission through AOM is blocked by BD. The deflected pulsed beam under 161 mrad deflection angle is recollimated by L2. Following the mirror M1, a fraction of the beam is reflected by the 1 mm thick silicon wafer S1 into a fast photo-diode to monitor the laser pulse length. Transmission through the S1 passes WGP2 set at 45° angle and further passes the adjustable WGP3 which is utilized to determine the output polarization of the setup. The mirror M3 can be either inserted into the beam for power measurement or removed from the beam for spectrometer calibration.

the Eq. (4.16) or (4.17). The bandwidth normalized, absolute calibration is therefore given by

$$T_{Abs}^{s,p}(\lambda) = T_{Rel, N}^{s,p}(\lambda) \cdot F_{Abs}^{s,p} \quad (4.19)$$

$$T_{Abs, BW}^{s,p}(\lambda) = T_{Re., N}^{s,p}(\lambda) \cdot F_{Abs}^{s,p} \cdot BW(\lambda), \quad (4.20)$$

where the quantity $BW(\lambda)$ indicates the discrete spectral bandwidth of the detector array per pixel and is calculated by utilizing the wavelength calibration curve of the corresponding detector (see inset on Fig. 4.11). The calculated absolute calibration curve from Eq. (4.19) is given in units [counts or voltage per unit J]. The BW normalized calibration curves are summarized in Fig. 4.16

The error band (depicted in gray) indicates one standard deviation and constituted from all error sources as follows:

1. The relative error from readout noise of each detector σ_{S_n} is considered as a function of wavelength and calculated by

$$\sigma_{S_n}(\lambda) = \sigma_{Bgd}(\lambda) / S_n(\lambda). \quad (4.21)$$

It depends on the signal level and the noise from the environment such as temperature, integration time but also electromagnetic pulse (EMP) events during the acquisition.

2. The relative error regarding the spectral bandwidth $BW(\lambda)$ of each detector element is obtained from the standard error estimated from the corresponding wavelength fit function with a confidence interval of 95 % and is calculated by

$$\sigma_{\Delta\lambda} = \Delta\lambda / \bar{\lambda} \quad (4.22)$$

3. The error from the relative response calibration σ_{Rel} is estimated regarding the absolute calibration of the LS. This is negligible ($\approx 1\%$) for the BB source and between 8.2% to 9.4% for the QTH lamp in the spectral range of echelle spectrometer.

4. The majority of error contributions originate from the uncertainties in the absolute calibration. The error directly related to the power head calibration is 3%, valid for all utilized calibration lasers. In addition, the individual errors in the power measurements are: for echelle spectrometer 7%, for InGaAs 3% and for MCT on average 12%.

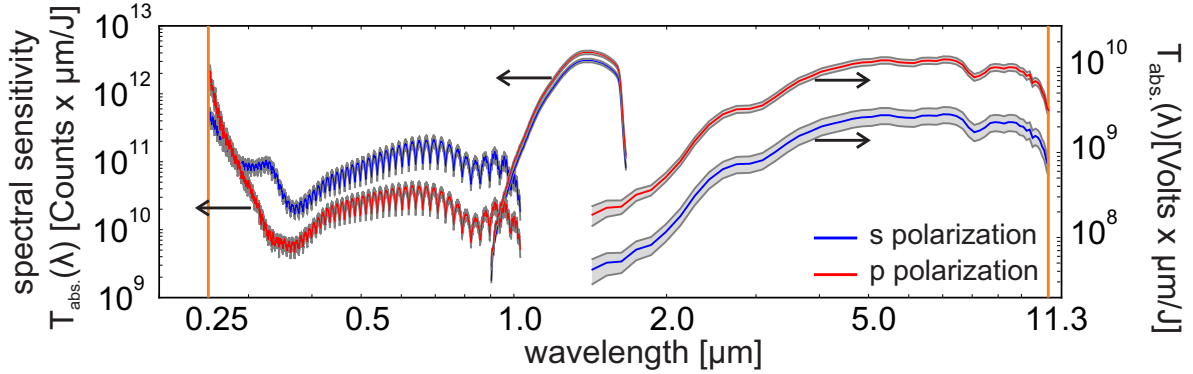


Figure 4.16.: Overview of the bandwidth corrected absolute calibration.

4.2.5. DETECTION THRESHOLD

The amount of radiant energy that can be detected by a detector system is limited on the one hand by the dynamic range of the detector system, on the other hand by the smallest detectable signal given by the presence of noise in the detection process as well as quantum efficiency (QE) of the detector active material. Beside the QE, random fluctuations in the output of a detector set further limits on the minimum detectable spectral flux. Noise-equivalent power (NEP) is defined as the minimum radiant power ϕ on the detector, which yields a signal to noise ratio (SNR) of unity^[143]. In order to give an indication of the minimum radiant energy that can be detected, analogue to NEP, noise-equivalent energy (NEE) is introduced as the ratio of RMS noise level to the responsivity of the detector. The NEE is given in the following in units of [joule per μm] as

$$\text{NEE} = \frac{\sigma_{\phi}}{T_{\text{Abs,BW}}^{s,p}(\lambda)}, \quad (4.23)$$

where σ_{ϕ} denotes the standard deviation of the background fluctuations and $T_{\text{Abs,BW}}^{s,p}$ is the absolute *BW*-normalized response of the spectrometer according to Eq. (4.20). In the Fig. 4.17 the NEE is depicted for the entire spectral range of the TR spectrometer regarding to the polarization of the incident beam.

The lowest detection threshold is achieved by the MCT and InGaAs detectors at 2 pJ/ μm . The Echelle spectrometer shows a detection threshold of about 100 pJ/ μm . The latter can be significantly improved by increasing its EM gain, here is set at 30x amplification. However, an increase in the EM gain reduces the dynamic bandwidth of the detector.

In practice, the sensitivity of each spectrometer arm can be individually adapted to the required dynamic range. This can be realized by utilizing attenuators or polarizers to either spectrometer arms where needed.

The NIR spectrum reveals much less polarization dependency than the echelle and MIR spectra. This is due to the near polarization independent transmission and reflection properties of the spectrometer optics. In particular at $\lambda = 1.31 \mu\text{m}$ this deviation is about 25 % from the mean.

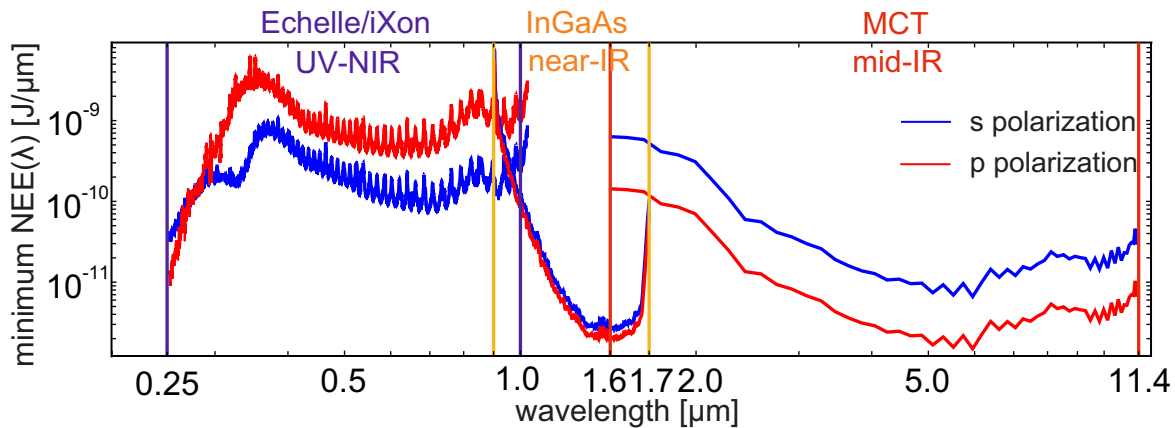


Figure 4.17.: The noise-equivalent energy (NEE) of the TR spectrometer. The NEE is estimated for the three spectral ranges and appropriate detection systems with respect to s- and p-polarization at maximum achievable resolution.

4.3. CONCLUSION

We presented the design, setup and full characterization of a TR spectrometer, which is suitable for measuring the broadband TR spectrum in single-shot. A detailed wavelength calibration, a relative response calibration as well as an absolute photometric calibration procedure are performed for each spectrometer arm. Figure 4.18 shows the top-view of the TR spectrometer setup.

Here, we performed the polarization dependent relative calibration by using continuous spectral sources for individual spectrometer arm. Thereafter each of the spectrometer arms is absolutely calibrated by measuring the transmitted power through the spectrometer with respect to s- and p-polarization. In this way, the detectors and their associated optical elements including the beam splitters are calibrated at once. Notably, additional optics such as polarizers and attenuators, which are occasionally inserted into a certain spectrometer arm, have to be separately taken into account. In fact, the calibration results presented in this chapter demonstrate the highest responsivity of the spectrometer, and this can be extended or modified according to the intensity of the sample light source. For the case of the transition radiation measurements presented in chapters 6 and 7, several polarizers and attenuators are utilized in order to adapt the spectrometer dynamic bandwidth to the experimental conditions. This modifications and their resulting modified calibration curves will be presented in section 6.3.

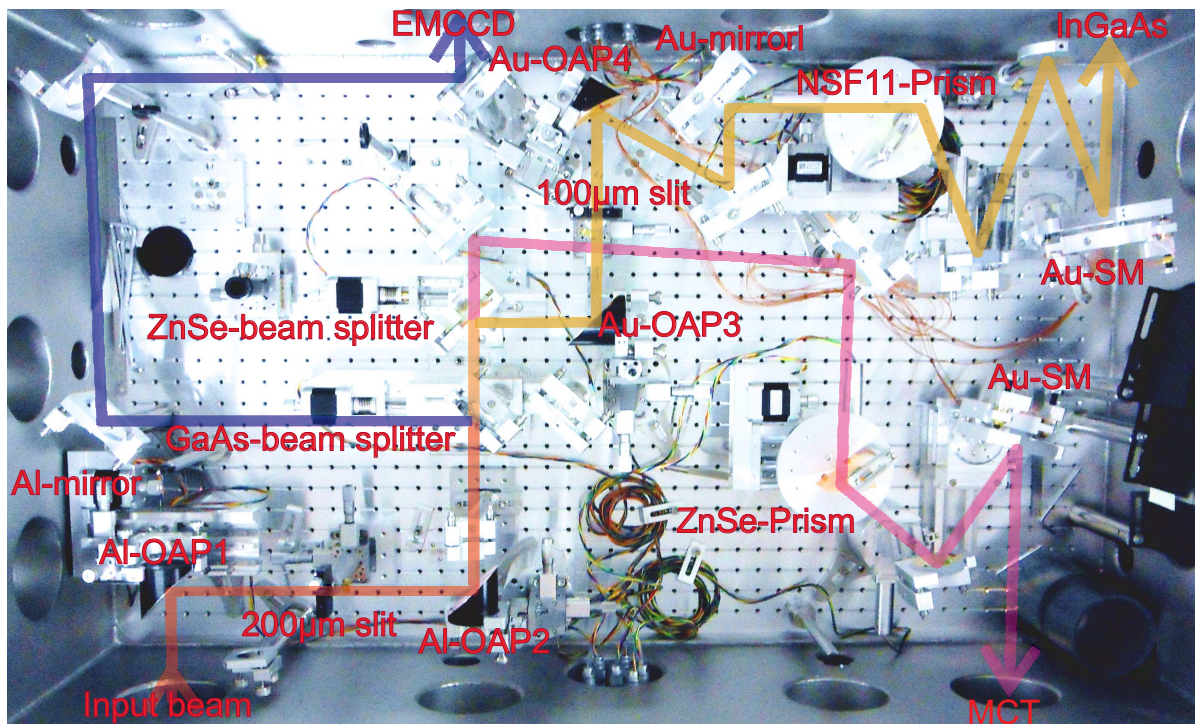


Figure 4.18.: Top-view of the TR spectrometer setup.

5. EXPERIMENTAL SETUP

In this chapter, the technical details of the experimental setup for measuring TR is presented. A short description of the LWFA experiment at the ELBE center for High-Power Radiation Sources is given in the following section 5.1. The experimental setup for TR measurement implemented in the LWFA experimental chamber including the design of TR beam-line from the TR screen to the TR-spectrometer is outlined in section 5.2. Measuring of transverse profile of CTR is presented in section 5.3.

5.1. LWFA EXPERIMENT AT HZDR

Commissioning of the experimental target area for LWFA experiments was started in 2013 following the upgrade of the ELBE center. The ELBE center operates the conventional electron accelerator ELBE (Electron Linac for beams with high Brilliance and low Emittance^[142]) and two high power laser systems: the two beam 150 terawatt / petawatt Ti:Sapphire laser DRACO (Dresden laser acceleration source) and the diode-pumped petawatt laser PEnELOPE (Petawatt, Energy-Efficient Laser for Optical Plasma Experiments)^[144].

A modular vacuum chamber was designed for both LWFA experiments and Thomson back-scattering experiments^[7,10]. The Target area has the unique aspect of being located such that all radiation sources as mentioned above can be combined in one target chamber as seen in figure 5.1. The Target chamber and the LWFA experimental area was mostly developed in the Ph.D. projects of J.P. Couperus^[145], A. Köhler^[9], J. Krämer^[7,10] and the present work.

A schematic view of the LWFA experiment and the associated diagnostics is depicted in figure 5.2. The DRACO laser pulse is coupled into the experimental chamber using a vacuum transport line from the DRACO vacuum compressor. Using a F/20 off-axis parabola (OAP) the laser beam is focused roughly 1.5 mm above the gas-jet target which provides the LWFA acceleration medium (see also subsection 5.1.2).

Several diagnostics are utilized in order to monitor the laser pulse before and after the interaction with the gas-jet as will be outlined in the following:

For focus diagnostic, a movable mirror is placed into the beam's path to redirect it to several offline diagnostics. Following attenuation of the laser pulse by a pair of glass wedges, the OAP focus is imaged onto a CCD using a high-quality objective alternatively on a wave-front sensor (PHASICS SID4) for wave-front optimization in a closed loop with a deformable mirror

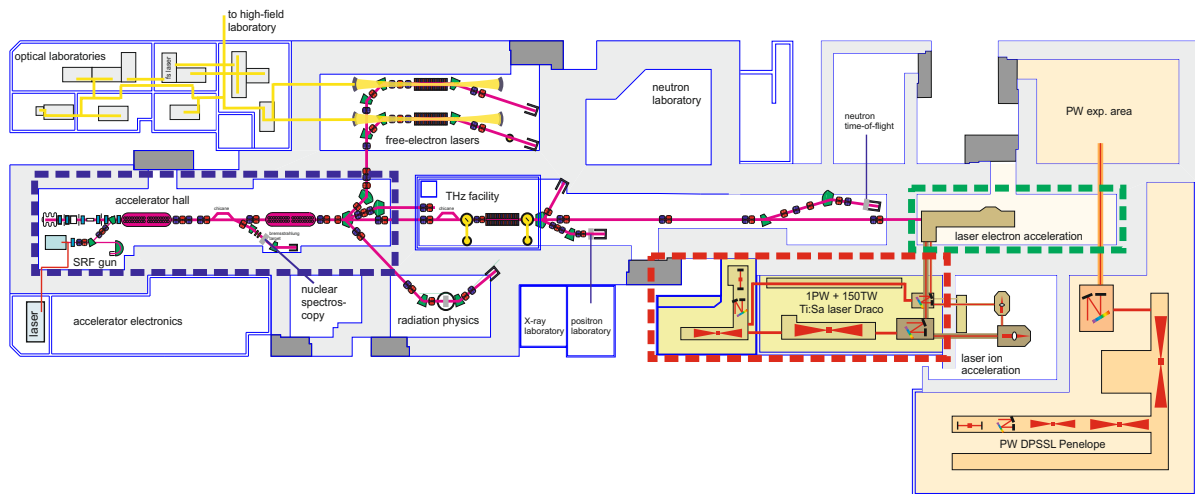


Figure 5.1.: **Layout of the ELBE center for High-Power Radiation Sources.** The dashed green box indicates the target area. The DRACO laser system is indicated by the dashed red box and the conventional electron accelerator by the dashed blue box.

placed in the DRACO vacuum compressor.

Another movable mirror directly behind the laser compressor picks the beam up and couples it out for further offline diagnostics. A self-referenced spectral interferometer (WIZZLER-Fastlite) for single shot spectral phase and intensity measurements is used in closed-loop with an acousto-optic programmable dispersive filter (DAZZLER-fastlite) for spectral phase correction. Other diagnostics which can be positioned here for cross-reference are a spectral-phase interferometer (SPIDER-A.P.E.) for the laser pulse measurement or a scanning third-order cross-correlator (SEQUOIA, Amplitude technologies) for measuring the contrast of the laser pulse.

Laser pulse length stability during the LWFA experiments is monitored using a single-shot second order vacuum autocorrelator. A movable pickup mirror can be inserted into the main beam to redirect a fraction of the beam into the mentioned autocorrelator. Additionally, partial transmission of the beam through a mirror, positioned between the OAP and the LWFA target, is used for online monitoring of the beam in the far-field for pointing and near-field.

Transverse diagnostic of the LWFA process is performed using a probe beam, extracted from the main beam by a pick-off mirror. It incorporates a delay line and an objective system to image the plasma channel onto a camera. The laser pulse length limits the temporal resolution of this diagnostic. The delay line tunes the probe timing with respect to the main laser pulse, enabling to acquire a snapshot of the evolution of the plasma channel.

Diagnostic and alignment of the laser focus onto the target can be done by the exit mode diagnostic (Online diagnostic). It is also used during the LWFA operation to diagnose the laser pulse after interaction with the plasma.

Alternatively, the exit mode diagnostic mirror can be moved from the acceleration axis. This allows for diagnosis of x-rays, either generated by betatron radiation or by Thomson backscattering. X-ray diagnostics is positioned up to twelve meters downstream from the accelerator exit depending on requirements.

A dielectric foil can be positioned directly behind the nozzle, either for the generation of transition radiation (see section 5.2) or to act as a plasma mirror in order to reflect the driver laser pulse. The reflected laser pulse can interact with the electron bunch and generate x-ray radiation by Thomson backscattering process.

The accelerated electron bunch is diagnosed for charge and energy distribution in a permanent dipole magnet spectrometer. This spectrometer is discussed in more details in subsection 5.1.3.

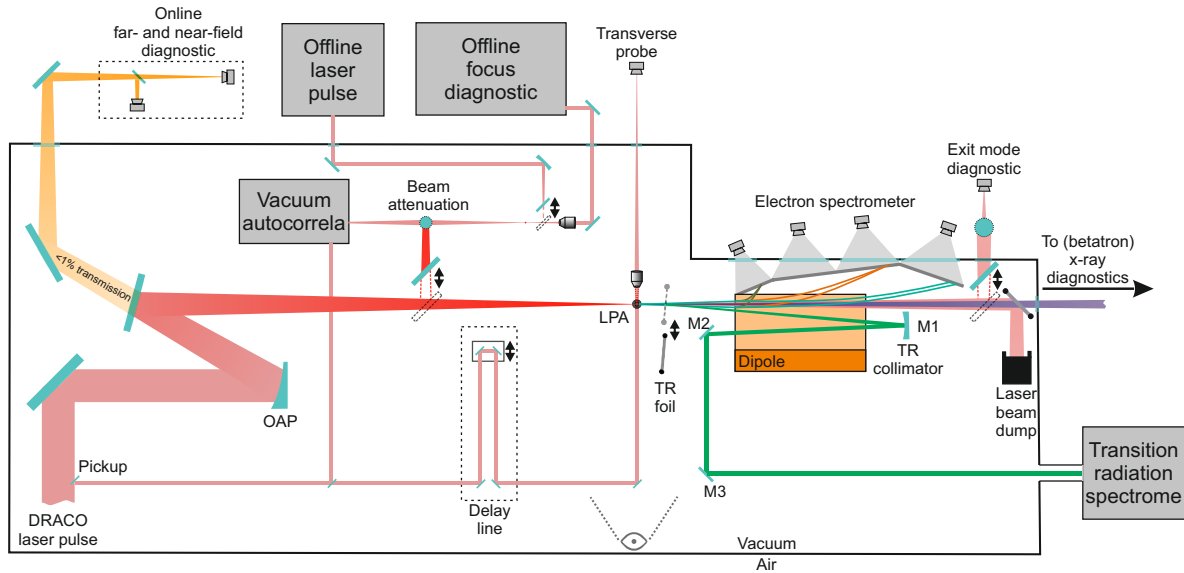


Figure 5.2.: **Schematic view of the LWFA experiment at HZDR.** The laser beam is coupled into the target-chamber using a vacuum beam-line from the laser compressor-chamber as indicated in the figure 5.1. The electron bunch is crossing the TR diagnostics screens and traveling through the permanent dipole electron spectrometer, which bends the electron bunch off from the axis (to the top in the experimental setup). The spherical mirror (SM) collimates the TR emission and redirects the beam toward the TR spectrometer (for details see figure 5.6). The TR screens and SM are mounted on motorized stages and can be translated out of the electron beam axis to diagnose betatron and x-ray radiations exiting from the plasma.

5.1.1. DRACO LASER SYSTEM

In order to drive a LWFA in the bubble regime, a high intensity ultrashort laser driver is required. An a_0 of at least two is needed to enter this regime (see section 2.4), while at the same time the laser pulse should be short enough to fit within the bubble-shaped cavity, i.e., $c_T < R_b$. In order to reach these conditions, the double-chirped pulse amplification (CPA)^[146,147] DRACO high-intensity laser system is used for experiments presented in this thesis. The Recent upgrade of the DRACO system is a dual beam system providing full Petawatt (30 J in 30 fs) and 150 TW (4.5 J in 30 fs) after compression with optimized temporal pulse contrast and high beam quality^[6]. The system is based on titanium-doped sapphire (Ti:Sa) crystals as a gain medium at a central wavelength of 800 nm and a spectral bandwidth of up to 80 nm. A schematic representation of the DRACO laser system is shown in figure 5.3.

After the final amplification, the pulses are expanded to the final beam size of 100 mm and transported to the compressor where the pulses are compressed to a duration of 30 fs. This

final compression and subsequent beam transport occur in a vacuum, as the laser field at this point becomes high enough to cause ionization in the air and subsequent filamentation^[148]. A deformable mirror allows for wavefront optimization in a closed loop with a wavefront sensor (*PHASICS SID4*) situated at the experimental cave. A beam transport switching system allows for transport of the beam either to the ion acceleration area or to the electron acceleration area as shown in figure 5.1.

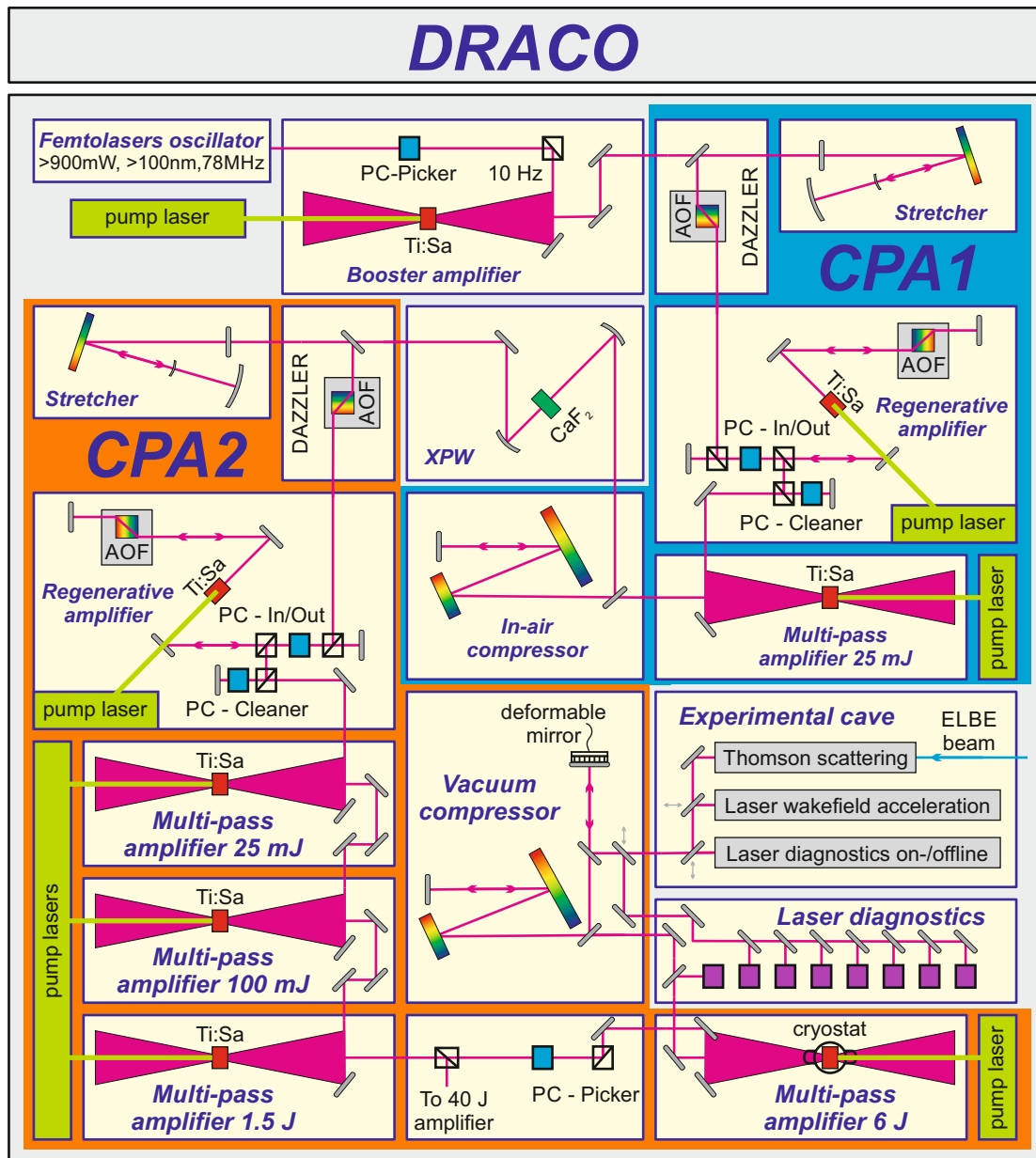


Figure 5.3.: Schematic of the DRACO laser system front-end and 150TW arm.

5.1.2. LWFA TARGET

The plasma medium is one of the essential components in a laser-plasma accelerator. Exact design, tailoring, control, and diagnostic of an LWFA target which provides such a plasma medium is not straightforward and requires many efforts. The intensity of an ultra-short high power laser pulse is sufficiently high to drive highly nonlinear wakefield in the plasma. This interaction is in turn highly sensitive to the plasma density and profile. Furthermore, the laser beam propagation occurs in the vacuum chamber with a pressure of generally below 10^{-5} mbar, since any interaction of such high power laser, i.e., intensities above 10^{18} Wcm $^{-2}$, with air causes strong modulation in the laser pulse and alters its parameters.

In contrast, the plasma densities required for LWFA experiment are generally in the range of 10^{17} to 10^{19} electrons cm $^{-3}$. For a Helium gas medium, this corresponds to nearly atmospheric pressure without mitigating the vacuum condition of the direct surrounding.

Leading providers in LWFA experiments that are capable of fulfilling these requirements are discharge-capillaries, gas cells, and gas-jets. Each of which has advantages and drawbacks.

Discharge capillaries provide a pre-ionized plasma medium by ionizing a gas with a high-voltage discharge, and thus a transverse density gradient (as in an optical fiber) can be created inside the capillary shortly before the laser arrives^[149]. The laser can be therefore guided by the capillary over several Rayleigh length which is advantageous for long acceleration lengths. However, the technical complexity of the discharge makes discharge capillaries challenging to operate.

In contrast to discharge capillaries, gas cells and super-sonic gas jet targets deliver only the gas medium. The ionizing of the gas medium consequently relies on the main laser pulse which requires a high enough laser intensity to reach the self-focusing regime^[150]. Gas-jets create a sharp vacuum-gas border by allowing a super-sonic expansion of the gas into the vacuum. The open design of gas jets allows for easy diagnostics of the acceleration process. A schematic representation of a laser wakefield accelerator using a gas-jet as target provider is shown in figure 5.4. These advantages lead to gas-jets becoming the main acceleration media provider. Generally, only when a low plasma density is required, as needed for longer interaction lengths, gas cells are used instead. The LWFA presented in this thesis uses a gas jet target.

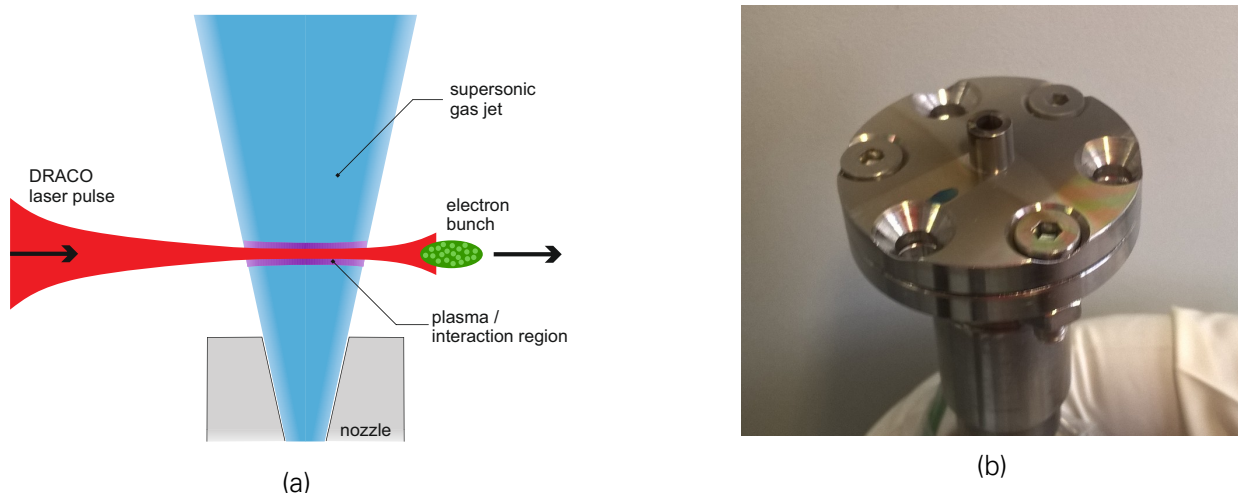


Figure 5.4.: **Gas-jet target for LWFA experiment.** (a) schematic of the gas-jet; The laser is positioned to interact with the gas-jet above the nozzle, typically ~ 1 mm. A supersonic gas-jet is required to ensure a sharp density transition even further above the nozzle. The open design of gas jet targets allows for easy diagnostic of the acceleration process. (b) picture of the nozzle embedded in its nozzle holder

5.1.3. ELECTRON SPECTROMETER

In order to determine the electron beam quality after the LWFA, key beam parameters such as energy, energy spread, charge, divergence, pointing, emittance, and bunch duration need to be determined. Except for emittance and duration, these parameters can be directly inferred from the electron spectrometer. The electron bunch is traveling through the permanent dipole electron spectrometer, which energy-dependently deflects the electrons off-axis (to the top in the experimental setup), hence spatially separating them according to energy on a charge-sensitive scintillating screen. The spectrometer is utilized to diagnose the electron bunch for charge and energy distribution as well as the transverse momentum distribution. It covers energies from a few MeV up to 550 MeV and has an acceptance angle of about ± 20 mrad for high energy electrons. Since the LANEX screens, utilized in this spectrometer, are absolutely calibrated for charge^[11], the energy-dependent charge and transverse momentum distribution of the electron bunch can be precisely measured in a single-shot. The design of the spectrometer allows providing point-to-point imaging up to 200 MeV while at higher energies the measurement uncertainty is kept below 6 %. For typical LWFA operation presented in this work, the high energy electrons reach an energy up to 400 MeV taking into account ± 6 mrad pointing leading to a readout uncertainty of below ± 3 % as shown in figure 5.5.

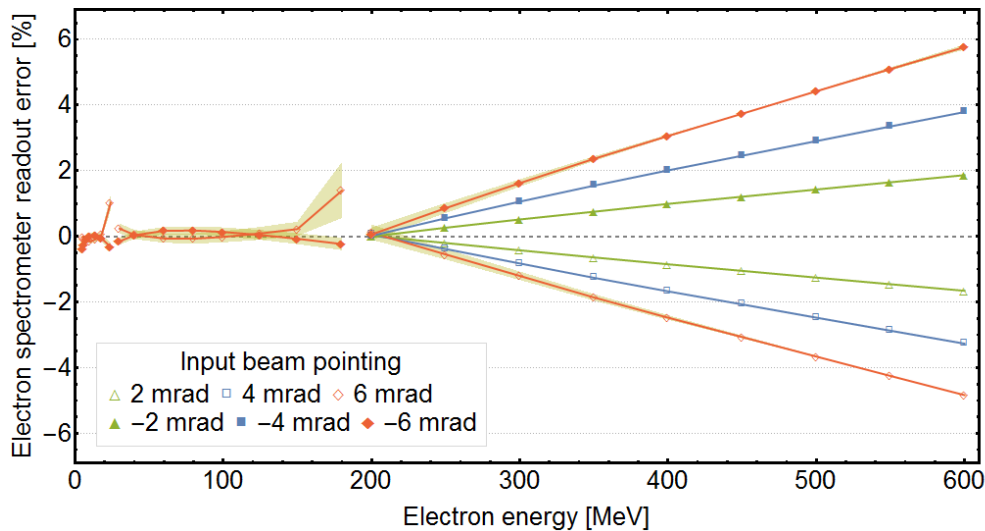


Figure 5.5.: Divergence and electron source position dependent readout error of the electron spectrometer. Results obtained by particle tracing in GPT using the measured field map. Values shown indicate a divergence/pointing of the incoming beam in the bending plane. Shaded areas indicate the influence of vertical position errors of the incoming beam (± 0.2 mm) on top of a ± 6 mrad pointing error. Figure also published in^[6].

5.2. TRANSITION RADIATION BEAM-LINE & SCREEN

Figure 5.6 shows the schematic of the TR experimental setup. The DRACO laser pulse enters from left in the figure and accelerates an electron bunch (blue) downstream, in the propagation direction of the laser. The laser is after that blocked by utilizing a double aluminum tape drive (see figure 5.7). The electron bunch passes the laser blocker and crosses the TR screen, which is placed perpendicular to the beam axis behind the double-tape at a distance of 26 ± 1 mm from the exit of the nozzle. TR from the back surface of the aluminum tape is blocked by the TR screen itself. Forward TR emitted from the surface of the TR foil, co-propagates first with the

electron bunch. The dipole magnet deflects the electron bunch toward the LANEX screens, where its energy spectrum is acquired. A spherical mirror (M1 in the figure) collimates the TR beam and reflects it back through the 4 cm gap in the dipole magnet under a small angle $\sim 4^\circ$. The folding mirrors M2 and M3 indicate the simplified schematic of the TR beam transport optics. In the experimental setup, five aluminum coated folding mirrors are utilized to guide the collimated TR beam into the TR spectrometer. The TR spectrometer chamber is attached to the target chamber using a 10 cm diameter vacuum pipe between them.

The motorized mirror M4 can be remotely translated into the TR beam in order to pick off the beam outside the target chamber into the diagnostics setup for transverse TR profile. The latter is investigated in order to characterize the transverse profile of the emitted TR which is discussed in detail in section 5.3.

Furthermore, a vacuum valve with an embedded vacuum window for visible light transmission is implemented between the target and TR spectrometer chambers, which enables to independently evacuate both chambers and perform alignment at the spectrometer side while the target chamber is in the vacuum and vice versa.

The final alignment of the TR beamline from the TR screen through the TR spectrometer is performed in vacuum by opened vacuum valve following the evacuation of both chambers. The latter is an important issue for a precise alignment since the pumping down either chamber leads to slight deformation of the chambers and hence disturbs the pre-alignment of the TR beamline that is performed in air. For this purpose, two folding mirrors involved in TR beam line inside the target chamber are motorized to steer the alignment laser, here a HeNe laser diode.

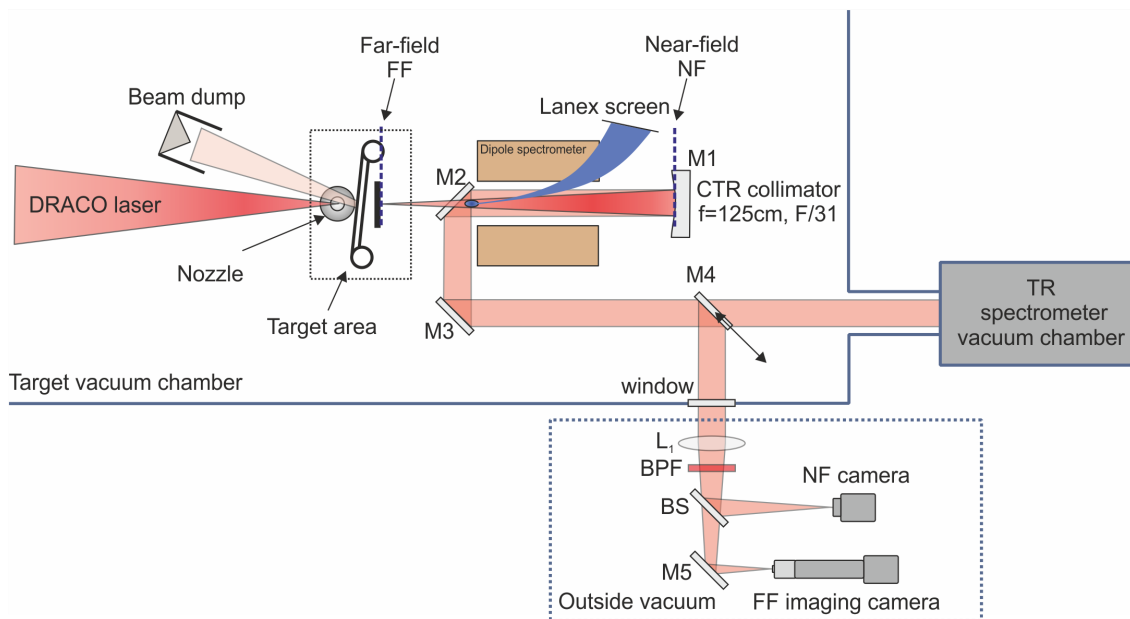


Figure 5.6.: Schematic of TR experimental setup.

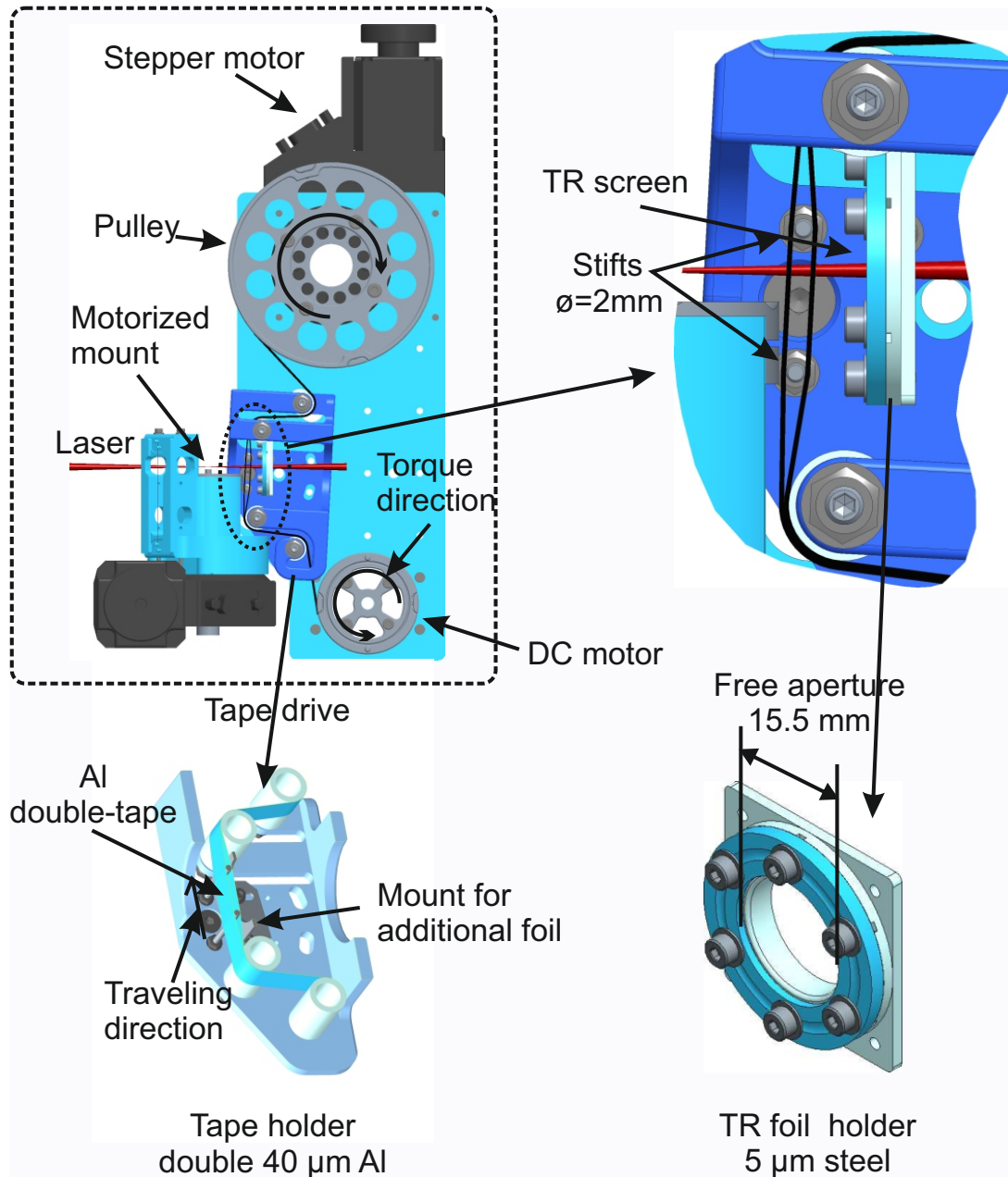


Figure 5.7.: Drawing of the nozzle and tape-drive indicated in the figure 5.6 (dashed square). The tape drive as a stand-alone module is placed behind the nozzle by motorized translation stages, the pulley, attached to the stepper motor, advances the double Al foil after every shot by pulling the fresh foil from the second pulley (bottom in the corresponding drawing), the latter permanently stretches the AL tapes over the tape holder module using a DC motor. The tape holder module is clockwise rotated by 6° in the experimental setup in order to reflect the laser beam into the beam dump, which is places a few centimeters up-streams above the laser axis, as can be seen in figure 5.6). The TR screen consisting of $5\mu\text{m}$ steel foil is mounted in the custom-made CNC machined mount and is placed at $d = 26\text{ mm}$ from the nozzle exit. The screen mount is consisting of a base plate and a cap, which are screwed together. An O-ring shape on the base plate material is intended, and it matches into its counterpart groove in the cap material. The TR screen can be thus gripped between them and stretched out to make the mentioned screen as flat as possible.

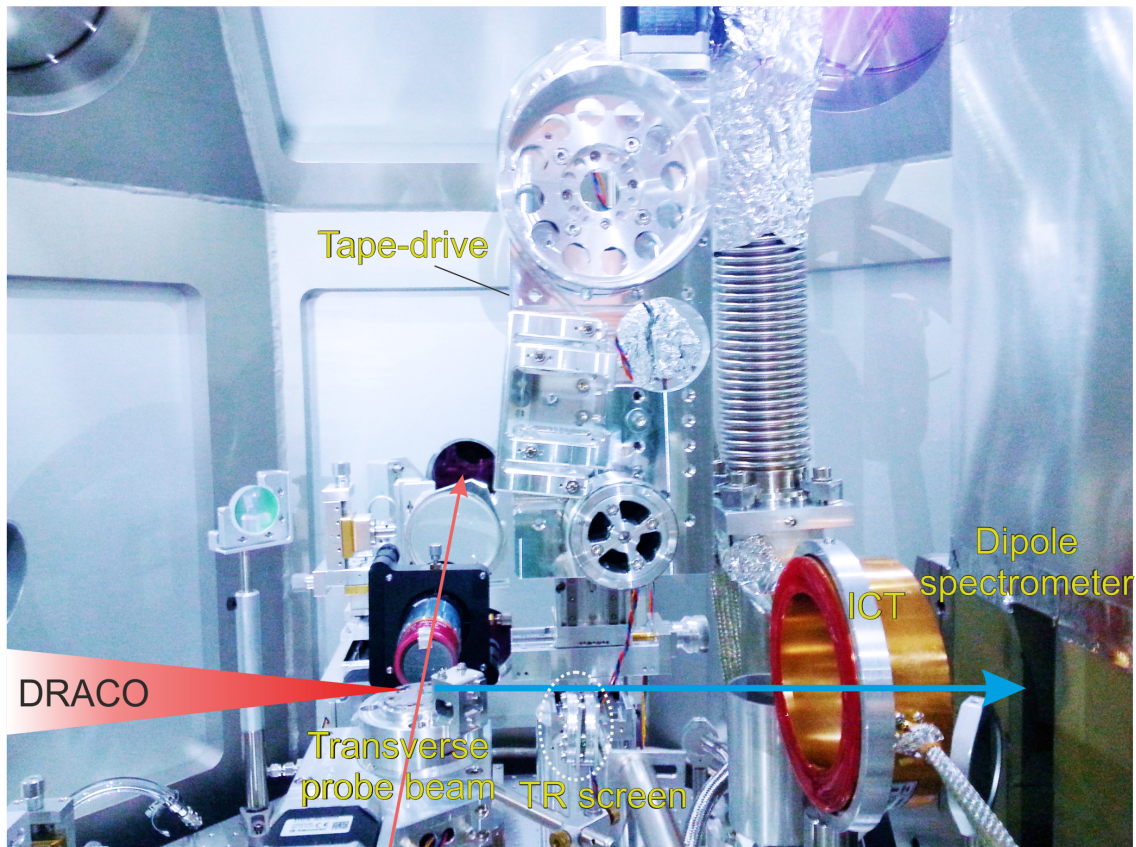


Figure 5.8.: Picture of target area inside the experimental vacuum chamber. The DRACO laser beam propagates from the left side. The double-tape drive and the TR screen are motorized and can be remotely translated to the shooting position (not in shooting position in figure). The generated electrons are diagnosed in the dipole spectrometer visible on the right side. The plasma jet is diagnosed by the transverse probe beam crossing DRACO beam at the nozzle position.

5.3. TRANSVERSE PROFILE OF TR

In order to study the properties of the transverse profile of the emitted TR as well as its free-space propagation, the optical imaging of far-field and near-field of the transverse TR radiation are investigated. As shown in the figure 5.6, the motorized mirror M4 can be placed into the TR beam in order to pick off the beam outside the target chamber into the diagnostics setup for transverse TR profile. The latter consists of two imaging arrangements for far-field as well as near-field, which are corresponding to the surfaces of the TR radiator and the M1 respectively as indicated in the figure 5.6. Following the focusing lens (L1) and the bandpass filter (BPF), the beam splitter (BS) is utilized to split the beam into two arms in order to simultaneously image the far and near-field of the TR profile (see figure 5.6). Various BPFs in the optical and near-IR region are mounted in a motorized filter wheel (not shown in figure) and can be remotely exchanged to perform the measurements with a different wavelength. In order to estimate the transverse dimension of the emitted TR, the field-of-view of the mentioned imaging CCD cameras are calibrated. The existing setup allows resolving the TR profile in far-field down to $2.5 \mu\text{m}$ per detector pixel while the resolution in near-field is obtained to be $\approx 70 \mu\text{m}$ per pixel. The acquired images for BPF=600 nm from an exemplary shot are presented in figure 5.9. Here, the transverse dimension of TR at 600 nm at the surface of the TR screen is on the order of $\approx 250 \text{ nm}$. The structures on the TR profile already hint at the existence of ultra-short longitudinal structures inside the electron bunch (see also chapter 6). Figure 5.9b shows the near-field pattern of the TR profile, i.e., the transverse profile of the collimated TR radiation. This image plane corresponds to the surface of the spherical mirror M1 in figure 5.6. According to the electron beam divergence and the TR angular distribution as well as the focal length of M1, the transverse dimensions of the collimated TR approach up to 20 mm which can be easily transported to the TR spectrometer by using 2" optics and no significant signal loss due to clipping by the optics is expected.

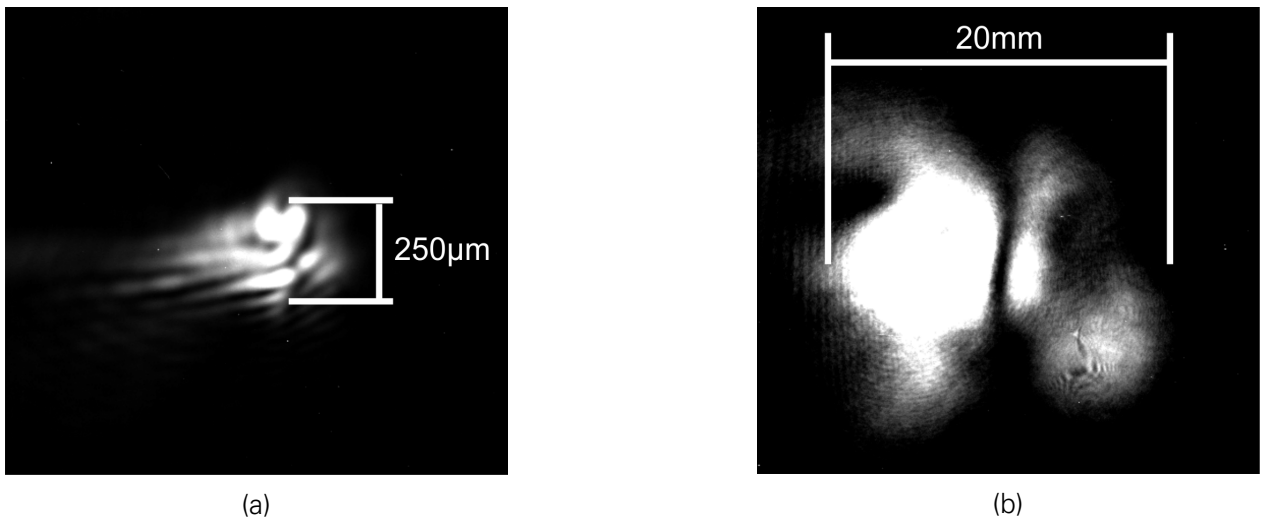


Figure 5.9.: Far- & near-field imaging of transverse CTR profile. (a) shows the far-field image corresponding to the surface of the TR screen. (b) displays the near-field image corresponding to the surface of collimating optic located at 1.25m behind the TR screen. Both images are acquired using a band pass filter at 600nm.

As will be discussed in chapter 6, these electron bunches reveal a highly modulated longitudinal profile. The presence of the substructures in the transverse TR profile demonstrates also the existence of the bunch substructures, however it indicates a transverse displacement of

these structures from the axis since they are distributed over a much larger area than a single beamlet. According to the divergence of the electron peak energy (≈ 5 mrad) obtained from the electron spectrometer and according to the expression (3.17) the transverse coherence cutoff would be at wavelengths much longer than the measured cutoff in the UV range. For instance, for a transverse bunch size of $\sigma = 100 \mu\text{m}$ and a collecting angle of $\theta = 16$ mrad the cutoff would be at $\lambda \approx 4 \mu\text{m}$, however this cutoff is in experiment at about ≈ 300 nm (see figure 6.17b). This is due to the fact that for a superimposed electron bunch the transverse coherence is expressed by an additive expression for F_{\perp} which incorporates all bunch substructures. Hence the final transverse coherence is determined by the size of substructures which are much smaller than the global bunch size at the position of the TR screen. This is also confirmed by measuring the TR spectrum at different distances to the nozzle exit. Figure 5.10 shows the TR spectra from $\lambda = 250$ nm to $1 \mu\text{m}$ measured by the echelle spectrometer at two different distances to the nozzle exit. Comparing the spectrum at $d = 26$ mm (*red*) to the one at $d \approx 1$ mm (*blue*) indicates that the cutoff of TR spectrum in the UV range remains almost unchanged by reducing the distance d to the nozzle. For this reason, throughout the bunch reconstruction presented in this thesis the bunch transverse coherence is assumed to be unity, i.e., $F_{\perp} \sim 1$.

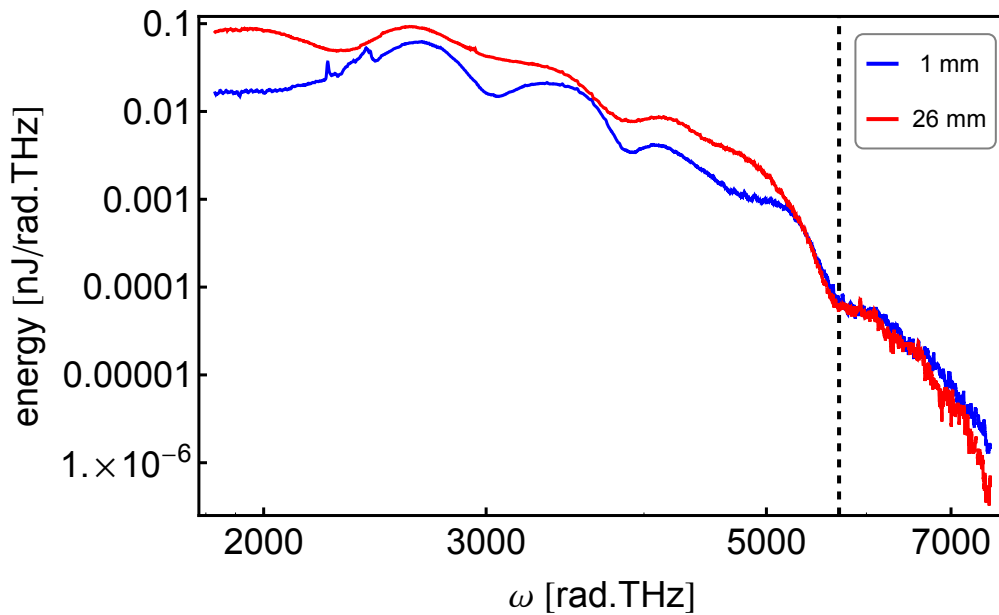


Figure 5.10.: Comparison of OTR spectra measured at different distances. The OTR spectra are absolutely calibrated and depicted in frequency domain. The spectra are measured at $d \approx 1$ mm (*blue line*) and at 26 mm (*red*). The cutoff region is indicated by *vertical dashed line* corresponding to $\lambda = 330$ nm

6. ELECTRON BUNCH PROFILE RECONSTRUCTION

Precise knowledge of the longitudinal profile of laser wake-field accelerated electron bunches is essential for the development of compact secondary radiation sources, most prominent example is LWFA driven free electron lasers. The primary aim of measuring the spectrum of CTR from electron bunches is thus to deduce the bunch duration, and potentially the full longitudinal bunch profile.

In this chapter we describe a phase-retrieval algorithm in section 6.1 and, using synthetic data, demonstrate its capabilities and limitations to reconstruct the phase of the bandwidth limited measured TR spectra presented in section 6.2. Although the unambiguity of the reconstructed bunch profiles is not always guaranteed, however, a second independent method is useful in order to seek the most probable reconstruction. This post-selection algorithm is presented in section 6.2.3. Here, we apply Kramers-Kronig (KK) analysis as a reference profile to the iterative method. We name this reconstruction procedure “Foldwrap” algorithm^[2] recognizing the combination of two independent methods to advance previous work on this topic. The results of the bunch reconstruction on single-shot measured TR spectra are presented and discussed in detail in section 6.3. Here we start first to deduce the corresponding form factor from measured TR spectra in section 6.3.1 and then apply the reconstruction algorithm to extract the bunch longitudinal profile in section 6.3.2.

6.1. INTRODUCTION TO FOLDWRAP RECONSTRUCTION PROCEDURE

In chapter 3 it is shown that the electron bunch profile and form factor are connected by a Fourier transformation. From a measurement of TR spectrum emitted when an electron bunch is passing through a metallic foil, in principle, one can obtain the amplitude of the corresponding form factor. However, a direct Inverse Fourier Transform (IFFT) of the measured form factor and thus obtaining the electron bunch profile is not possible since the phase information is lost during the intensity measurement.

There are several situations in which the phase information can be retrieved by applying proper phase retrieval methods to the measured intensity, examples are, X-ray crystallography^[151], particle scattering^[152], decomposition of the fields of a waveguiding structure^[153], as well as many other problems in optics (see Ref.^[154] for a review).

The first iterative phase-retrieval algorithm was introduced in 1972 by Gerchberg and Saxton^[155] (GS), for the purpose of reconstructing the 2D profile of an object from its diffraction pattern. J.R. Fienup introduced the hybrid-input-output (HIO) algorithm and investigated a comparison of several iterative methods to gradient search methods. He considered the problem of the phase retrieval of both two intensity measurement (in electron microscope or wavefront sensing) and single intensity measurements plus a non-negativity constraint (in astronomy)^[156]. Following the classical treatment of the phase retrieval problems some other iterative phase reconstruction algorithms have been investigated in the past few years and have been successfully tested on both 2D and 1D intensity measurement in order to reconstruct their phase information.

The “Shrinkwrap” algorithm was introduced by Marchesini et al.^[151]. The authors have shown that changing the support constraint (boundary of the object) by applying a threshold level to the current estimate of the object leads to a better estimate without prior knowledge of the object boundaries. The “Bubblewrap” algorithm has been developed in a later study by Bajlekov et al.^[153,157] in order to advance the 2D Shrinkwrap algorithm to the more challenging 1D problem of reconstructing the LWFA electron bunches from their bandwidth limited CTR spectral measurement.^[158]

The “Foldwrap” procedure is presented in figure 6.1. Step 1 presents an overview of the iterative algorithm in which the HIO and GS algorithms are sequentially applied. Besides the well-established constraints (for details see Ref.^[53]), the so-called zero-frequency and odd-phase constraints are implemented in the Fourier space. In contrast to the previously described reconstruction algorithms in which the algorithm parameters are optimized for specific types of distributions such as single Gaussians or well-separated Gaussians, we treat the reconstruction of modulated bunches that pose a more complicated form factor at high frequencies. For a typical scenario of the LWFA electron bunches, the bunch envelope could reach several tens of fs (plasma wavelength) while its potential sub-structures could extend into the sub-fs range (driver laser wavelength). This implies the existence of two different timescales to be simultaneously retrieved. Experimentally determining the form factor near $\omega = 0$ enables to include this additional independent measurement, i.e., $|F(\omega = 0)|$ into the phase retrieval algorithm. This enforces the algorithm to converge to more reproducible reconstructions in the low-frequency region where an experimental measurement normally is not available. This consequently improves the reconstruction of the long timescales, i.e., the bunch envelope. On the other hand, the encoded information from the high-frequency region of the form factor reflects the short timescales bunch structures that can also be retrieved by the algorithm. However, in the case of multi sub-structures, their amplitudes and their order of occurrence might suffer from the ambiguities inherently in the algorithm itself. Thus, a second independent method is useful in order to seek the most probable reconstructions (Step 2 in figure 6.1). The KK method can reasonably deal with the problem of multi Gaussians of short timescales, as will be demonstrated in section 6.1.6. For this reason, the KK method is deployed as the reference profile in the post-selection algorithm (Step 3 in figure 6.1) to seek solutions with a high overlap of their modulation with the KK result.

6.1.1. GERCHBERG-SAXTON ALGORITHM

The Gerchberg-Saxton algorithm (GS) was originally applied to reconstruct the phase information from 2D intensity measurement^[155,159]. It can also be applied to any phase reconstruction problem, in which the original signal $g(x)$ and the measured amplitude signal $|G(u)|$ are connected by a Fourier transform, i.e., $G(u) = \mathcal{F}[g(x)]$. GS algorithm, see figure 6.2, consists of

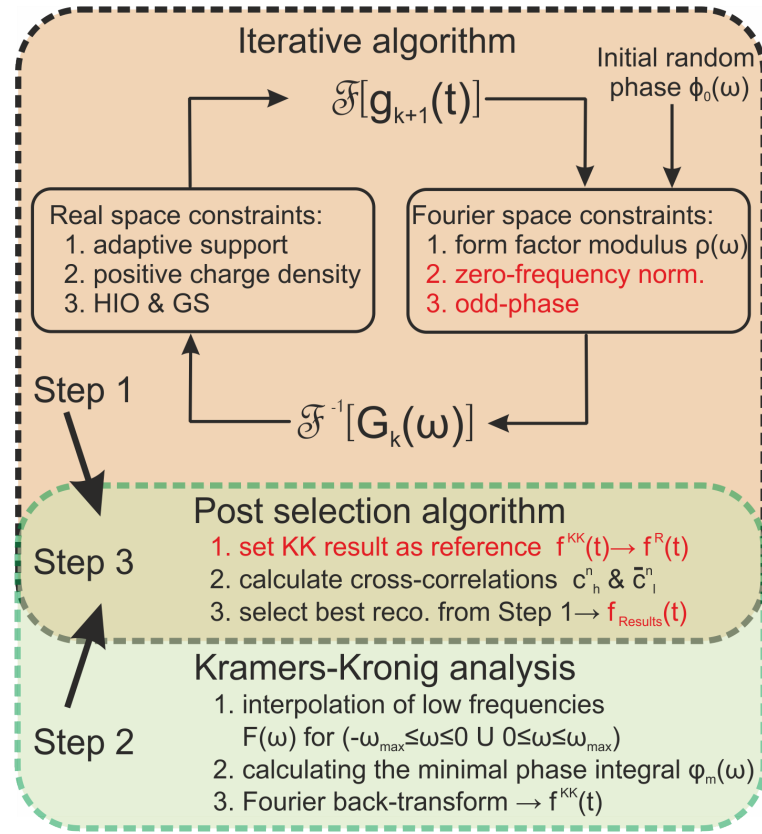


Figure 6.1.: Diagram of the Foldwrap reconstruction procedure

four basic steps:

1. Applying Fourier transform \mathcal{F} to an estimate of the object $g_k(t)$ of the k^{th} iteration and obtain $G_k(\omega)$
2. Replacing the modulus of the estimated Fourier transform $|G_k(\omega)|$ with the measured Fourier modulus, here the amplitude of the form factor, in order to obtain an estimate of the Fourier transform $G'_k(\omega)$
3. Applying inverse Fourier transform $\mathcal{F}^{-1}[G']$ results in a new time domain distribution g'_k (here the electron bunch distribution)
4. Applying the time domain constraints on g'_k in order to form a new estimate $g_{k+1}(t)$

In particular, for the problem of the longitudinal bunch reconstruction, the 4th step of the GS algorithm is given by

$$g_{k+1}(t) = \begin{cases} g'_k(t), & t \notin \gamma, \\ 0, & t \in \gamma, \end{cases} \quad (6.1)$$

where γ is the set of points of which $g'_k(t)$ violates the real space domain constraints (see Step 1 in figure 6.1) and the function value is set to zero. The error of the estimate function at the k^{th} iteration is given by

$$E_k = \sqrt{\sum_t |g_{k+1}(t) - g'_k(t)|^2}, \quad (6.2)$$

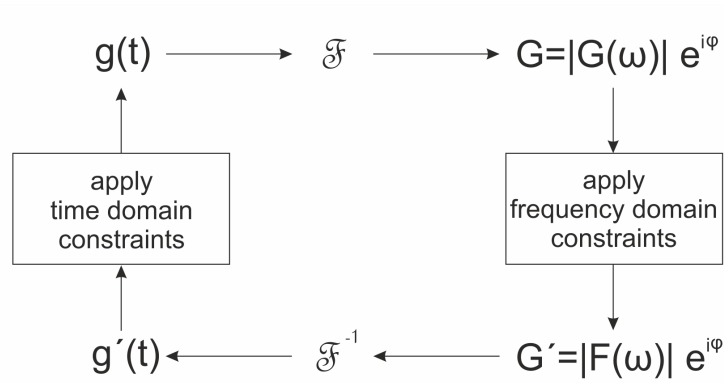


Figure 6.2.: Block diagram of the Gerchberg-Saxton algorithm.(Inspired from^[155])

which tends to be reduced after each iteration in the case of convergence of the algorithm. The GS algorithm is thus known as the error-reduction (ER) algorithm. However stagnation of the algorithm or even converging toward a local minimum counts to the drawbacks of the GS-algorithm.^[156]

6.1.2. HYBRID INPUT OUTPUT ALGORITHM

Instead of forcing the current estimate of function $g_k(t)$ to fully satisfy the real space constraints, applying an arbitrary manipulation to $g_k(t)$ could be beneficial.

The hybrid input-output algorithm (HIO) differs from the Gerchberg-Saxton algorithm only in the last step. In contrast to the GS-algorithm mentioned above, in the 4th step of the HIO algorithm defined by

$$g_{k+1}(t) = \begin{cases} g'_k(t), & t \notin \gamma, \\ g_k(t) - \beta g'_k(t), & t \in \gamma, \end{cases} \quad (6.3)$$

the new estimate $g_{k+1}(t)$ is obtained from the output function $g'_k(t)$ regarding the function support. For the set of points γ at which $g'_k(t)$ violates the support constraints the output function $g'_k(t)$ is altered by the coefficient β . The latter is an arbitrary real number which is normally chosen between 0 and 1.

In this manner, the next estimate, $g_{k+1}(t)$, subsequently converges closer to the target function in order to prevent possible stagnation of the algorithm.

6.1.3. PARAMETER OPTIMIZATION OF FOLDWRAP PROCEDURE

The parameter set in the Bubblewrap algorithm for using in the reconstruction of LWFA electron bunches are described in details in^[53]. The latter is used as a starting point to optimize the iterative part of the Foldwrap procedure (Step 1 in figure 6.1). A summary of the optimum parameters used for the reconstruction of both synthetic and measured CTR spectra is outlined below:

The iteration cycle defined as a sequence of 45 iterations of HIO algorithm followed by 5 iterations of GS algorithm, which can be rearranged when needed in order to achieve an optimum reconstruction with respect to its convergent speed and reproducibility.

The feedback parameter β of the HIO algorithm is initially set to 1.0 and decreased after each iteration cycle by 5.0 %.

The support size is set to an initial value, which is then during the reconstruction after each iteration cycle updated regarding the current threshold level described below. The initial support size has to be large enough to accommodate the entire electron bunch profile. However, experiments with synthetic data have shown, that due to the adaptive varying of the support size, the final result of the reconstruction is most likely insensitive to the initial support size.

The Gaussian filtering is utilized to smooth the current estimate $g_k(t)$ before the new support is calculated. This filtering leads to a smooth shrinking or expanding the support regardless of the noise in the mentioned estimate function. The Gaussian filter function with an initial RMS length σ of 5 data points is applied to the output function of the current iteration cycle $g'_k(t)$ and subsequently a new support for coming iteration cycle is calculated. The value of the initial σ is reduced in each iteration cycle by 1.0 %.

The threshold for support calculation is determined for each iteration cycle concerning the peak of the reconstructed profile. The latter is initially set to 20 % of the mentioned peak and decreased by 5.0 % in each iteration cycle. Note that in the original Shrinkwrap algorithm the threshold level was fixed at 20 %^[151]. A dynamic decreasing the threshold level has the advantage that the calculated support is successively expanded allowing the long tail of an electron bunch or a secondary sub-bunch to be reconstructed as well.

6.1.4. ODD-PHASE CONSTRAINT

The odd-phase constraint^[2] is implemented in the algorithm, in order to improve the stability and reproducibility of the reconstruction algorithm, which is shown in examples of synthetic data presented in the following section. Since the bunch distribution $f(t)$ is a real function, the form factor must be Hermitian, i.e.,

$$\rho(\omega)e^{i\phi(\omega)} = \rho(-\omega)e^{-i\phi(\omega)}. \quad (6.4)$$

The modulus of the form factor $\rho(\omega)$ is therefore an even function of frequency, while the phase $\phi(\omega)$ is an odd function of frequency. However our studies on reconstructed phases of model distributions have shown, that the estimated phase aside from a trivial offset in its magnitude, deviates slightly from its aforementioned anti-symmetry behavior. Therefor the odd-phase constraint is introduced which replaces the estimated phase for negative frequencies with its counterpart for positive frequencies in every iteration as

$$\phi(-\omega_i) = -\phi(\omega_i) + 2\phi(\omega = 0), \quad (6.5)$$

before the new estimate for bunch profile is calculated. $2\phi(\omega = 0)$ denotes an additional offset in order to provide a continuous phase $\phi(\omega)$ at $\omega = 0$.

6.1.5. ZERO-FREQUENCY CONSTRAINT

The Zero-frequency constraint^[2] is schematically depicted in figure 6.3. The electron spectrometer, utilized in the present LWFA experiment (see chapter 7), is absolutely calibrated^[11] for energy, charge and divergence of the electron beam. In this regard, the CTR emission energy $dW_{\text{CTR}}/d\Omega$ for fully coherent emission at frequency $\omega = 0$, can thus be calculated from the electron spectrum. Here, we considered charge, energy and divergence of the electron beam as well as the acceptance angle θ_{max} of the TR collection optic. The latter confines in

particular the collection of TR at high energetic electrons according to the $1/\gamma$ TR cone angle. Normalization of the absolutely calibrated TR spectrum by the calculated CTR emission at $\omega = 0$ allows to obtain the form factor in its absolute values. This can be expressed by

$$\frac{dW^2}{d\omega d\Omega} = |F_{\parallel}(\omega)|^2 \cdot \frac{dW_{\text{CTR}}}{d\Omega} \Big|_{\omega=0}. \quad (6.6)$$

Integrating over the solid angle of interest Ω leads to

$$\frac{dW}{d\omega} = |F_{\parallel}(\omega)|^2 \cdot W_{\text{CTR}} \Big|_{\omega=0}. \quad (6.7)$$

As a consequence the normalized longitudinal bunch form factor at $\omega = 0$ can be set during the phase reconstruction explicitly to unity, i.e. $|F_{\parallel}(\omega = 0)| = 1$. The effect of this constraint is in particular demonstrated in section 6.2.

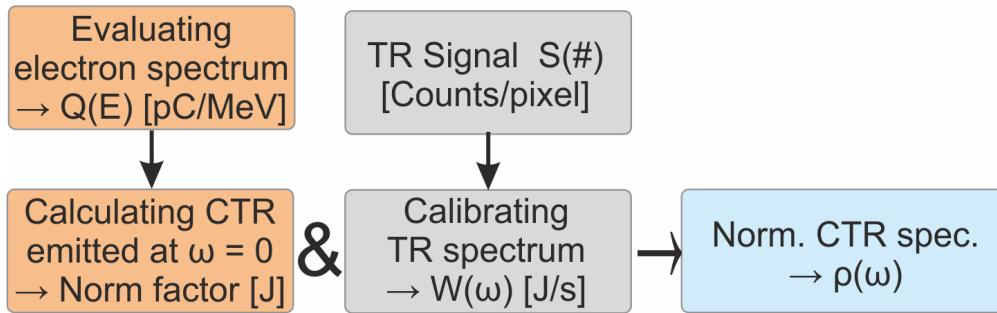


Figure 6.3.: Procedure flowchart for obtaining the form factor.

6.1.6. KRAMERS-KRONIG ANALYSIS

The connection between the modulus and the phase of the electron bunch form factor defined in chapter 3 can be expressed by

$$\ln F(\omega) = \ln \rho(\omega) + i\phi(\omega), \quad (6.8)$$

where ρ and ϕ denote the real and the imaginary part respectively. The modulus of the form factor can be obtained from measuring TR spectrum $W(\omega)$ and is proportional to square root of its intensity i.e., $\rho(\omega) \propto \sqrt{W(\omega)}$. From the causality of the longitudinal electron bunch distribution $f(t)$, the real and imaginary parts of its Fourier transform $\mathcal{F}[f(t)]$ are connected by the Hilbert transform^[160]. Applying the Hilbert transform to the Eq. (6.8), the phase can be written as

$$\begin{aligned} \mathcal{H} [\ln F(\omega)] &= \phi_m(\omega) + \phi_{\text{Blaschke}}(\omega) \\ &= -\frac{2\omega}{\pi} P \int_0^{\infty} dx \frac{\ln \rho(x)}{x^2 - \omega^2} + \sum_j \arg \left(\frac{\omega - \hat{\omega}_j}{\omega - \hat{\omega}_j^*} \right), \end{aligned} \quad (6.9)$$

where ϕ_m is known as the *minimal phase*, $\hat{\omega}_j$ denote the zeros of $F(\omega)$ in the upper half of the complex frequency plane and P signifies that the integral is to be integrated as Cauchy principal value. Thereby the Kramers-Kronig minimal phase relation delivers a correct estimate of the phase as long as $\phi_{\text{Blaschke}}(\omega) = 0$. The Blaschke phase contributions appear as the zeros of the form factor in the upper half of the complex frequency plane and, in principle, are not

accessible without prior knowledge of bunch distribution. Note that zeros on the real axis have no contribution to the phase. Additionally, only zeros close to the spectral range over which the modulus of the form factor is measured contribute to the calculated phase from Eq. (6.9). The first term in the Eq. (6.9) can be written as^[161]

$$\phi_m(\omega) = -\frac{2\omega}{\pi} \int_0^\infty dx \frac{\ln[\rho(x)/\rho(\omega)]}{x^2 - \omega^2}, \quad (6.10)$$

without the obvious singularity at $x = \omega$, since the following equation is entailed

$$-\frac{2\omega}{\pi} P \int_0^\infty dx \frac{\ln \rho(\omega)}{x^2 - \omega^2} = 0.$$

The modulus of the form factor $\rho(\omega)$ has to be experimentally determined over a sufficient spectral range, i.e., $\omega > 2\pi c/\sigma$, where σ denotes the rms bunch length. The minimal phase thus can be calculated by Eq. (6.10) and finally the beam distribution is obtained from the inverse Fourier transform of the form factor,

$$f(t) = \mathcal{F}^{-1}[\rho(\omega)e^{-i\phi_m(\omega)}]. \quad (6.11)$$

6.2. TESTS WITH SYNTHETIC DATA

In this section, we present the results from the Foldwrap algorithm and using synthetic data demonstrate its capability to reconstruct the bunch profiles for many common cases closely. Its limitations are outlined in the context of the actual spectral range in our experiments limited from 250 nm to 11.3 μm , and also accounting for highly structured electron bunches.

6.2.1. MODELING STRUCTURED BUNCHES

The characteristics of both the iterative phase retrieval algorithm and the Kramers-Kronig minimal phase analysis have been excessively studied in many publications. There have been shown that the mentioned methods are applicable in a broad range of reconstruction problems in which the bunch profile indicates either a single quasi Gaussian or multiple Gaussians, which are well separated. In the present work, the TR spectra measured from the LWFA accelerated electron bunches differ from the previous works due to the contribution of coherent optical transition radiation (COTR), which is significant and will have a substantial influence on the bunch distribution. As will be discussed later, the frequency modulations of COTR presented here reflect the indication of highly structured beam distribution. In order to find optimum parameters and test the implementation in the reconstruction algorithm (see section 6.1), a series of synthetic distributions are constituted. It is realized by superposition of several Gaussian distributions along the time axis resembling a bunch with longitudinal sub-structures to prove the advantages and drawbacks of the presented Foldwrap algorithm. The superposition of n Gaussians is modeled by

$$f(t) = \frac{1}{N} \sum_{i=1}^n \alpha_i g_i(t, \mu_i, \sigma_i), \quad -\infty < t < \infty, \quad (6.12)$$

where $N = \sum_{i=1}^n \alpha_i$ denotes the normalization factor, α_i is the weight of the i^{th} Gaussian and g_i the single Gaussian distribution defined as

$$g_i(t, \mu_i, \sigma_i) = \frac{\alpha_i}{\sqrt{2\pi}\sigma_i} e^{-\frac{(t-\mu_i)^2}{2\sigma_i^2}}, \quad 0 < \sigma_i. \quad (6.13)$$

Each Gaussian has an RMS length of σ_i , is placed along the time axis t at μ_i and is weighted with α_i .

The electron bunch form factor can be thus evaluated by applying a Fourier transform to the Eq. (6.12) given by

$$F(\omega) = \int_{-\infty}^{\infty} f(t)e^{i\omega t} dt \quad (6.14)$$

6.2.2. RECONSTRUCTING SINGLE AND TRIPLE GAUSSIANS

The spectral bandwidth of the presented TR spectrometer (see chapter 4) is limited from $\lambda_{\min} = 250$ nm to $\lambda_{\max} = 11.3$ μ m corresponding to frequencies from $\omega_{\max} = 7500$ rad THz to $\omega_{\min} = 166$ rad THz, where the frequencies are given by $\omega = 2\pi c/\lambda$ in units of rad Hz. The form factor calculated from Eq. (6.14) is then truncated to the frequencies between ω_{\min} and ω_{\max} , corresponding to the available spectral bandwidth. The frequencies below 166 rad THz are thus left in order to simulate the bandwidth limited experimental measurement of TR spectrum.

Following the zero-frequency constraint (see section 6.1.5) the value of the form factor at $\omega = 0$ is set to unity. This is justified by the absolute calibration of the TR spectrometer as well as the electron spectrometer (see also section 6.3.1).

Computing the Fourier and time domains are performed as follows:

For relativistic electrons, i.e., $v_e \approx c$ and applying the Nyquist's theorem $\omega_{\max} = 2\pi c/(2\delta z)$, the data point spacing in real space is set to $\delta z = 126$ nm, and $\delta t = 420$ as respectively. Using a reconstruction grid consisting of $M = 2^{12}$ data points, the time domain span is $[-\delta t \cdot M/2, \delta t \cdot M/2]$. Thus, the Fourier domain can be accordingly spanned over $[-\omega_{\max}, \omega_{\max}] = [-\delta\omega \cdot M/2, \delta\omega \cdot M/2]$, where $\delta\omega = 2\pi/(\delta t \cdot M) = 3.66$ rad THz denotes the frequency spacing in the Fourier domain.

The modeled distribution $f(t)$ is thereafter discretized over the time domain $[-t_{\max}, t_{\max}]$, which in this case is $\Delta t = M \cdot \delta t = 1.7$ ps. Performing a Fast Fourier transform (FFT) from $f(t_i)$ yields the form factor $F(\omega_i)$.

We start our discussion with single Gaussian distributions. A summary of single Gaussian reconstructions is listed in the table 6.1 below. The reconstructions are performed with the optimized parameters for the phase retrieval algorithm. Despite the general parameters described in section 6.1.3, the number of the iteration cycles are 120. The support is set to 40 fs and is recalculated regarding the current threshold level. The latter is set initially at 20 % and decreased by 5.0 % after each cycle.

Comparing the reconstruction results indicated by σ' , to the original bunch, i.e., σ shows that applying the zero-frequency constraint leads to almost perfect reconstructions up to a bunch RMS width of $\sigma = 10$ fs. Above 10 fs the reconstruction starts to deviate from the original shape increasingly. The latter is due to the lack of spectral information in the far-infrared region of the TR spectrum since the coherent cut-off of the TR spectrum is shifting toward low frequencies by increasing the bunch width. The relative error at $\sigma = 16$ fs is obtained to be 4.5 %. Above 16 fs the algorithm fails to retrieve the bunch profile correctly. For comparison, reconstruction results without the zero-frequency constraint are indicated as σ^* in the table. Reliable results are achieved only up to 10 fs.

Additionally, the effect of a noisy TR spectrum is exemplary demonstrated at $\sigma = 16$ fs. A relative random noise of 20 % is added to its original form factor. This leads to a relative error of 3.6 % as can be extracted from the table. However this is not further discussed

for different bunch profiles, since the measured TR spectra are rather subject of systematic deviation from the original shape due to possible uncertainties in the relative calibration of the TR spectrometer or due to transmission efficiency of the TR beam line. Accounting for this uncertainties are discussed in section 6.3.2.

Original σ [fs]	Reconstructed σ' [fs] with $F(\omega = 0) = 1.0$	Reconstructed σ' [fs] with $\pm 20\%$ noise	Reconstructed σ^* [fs]
5	4.999		4.996
6	6.000		5.988
7	7.000		6.968
8	8.000		7.913
9	9.000		8.782
10	9.997		9.460
11	10.987		9.943
12	11.963		x
13	12.911		x
14	13.800		x
15	14.597		x
16	15.283	15.427 ± 0.721	x
17	15.854		x

Table 6.1.: **Comparison of phase reconstruction for simple Gaussian distributions.** The initial bunch duration in terms of rms σ is varied between 5 fs and 17 fs. The reconstruction results listed in the table above are averaged over 10 runs each started with a different randomized initial phase. σ' indicates reconstruction runs, in which the value of the corresponding form factor is set to 1.0. In contrast, σ^* is obtained without zero-frequency constraint. Independent determination of $F(\omega = 0)$ leads to significant improvement of the stability and precision of the reconstructions and can overcome the upper limit of long bunches compared to σ^* . The lower limit of σ for both methods is determined by the time resolution $\sigma_{\min} \simeq 0.4$ fs.

Now we go on with the reconstruction of a more complicated electron bunch distribution consisting of three Gaussians presented in figures 6.4 and 6.5. The latter demonstrates the influence of the zero-frequency and odd-phase constraints introduced in the section 6.1.3. The rms width (σ_i) of each Gaussian is 3 fs, placed from left to right at $\mu_i = -13$ fs, 0 fs and 12 fs respectively and weighted with $\alpha_i = 0.6, 1.0, 0.4$ accordingly. Figure 6.4 shows the reconstruction results of the mentioned triple Gaussian bunch without the zero-frequency and the odd-phase constraint. Only 2 of 10 reconstruction runs converged to a good agreement (depicted in *blue and red lines*). In general, for large bunches, i.e., $2\pi\sigma \geq \lambda_{\max}/c$, the algorithm tends to converge at low frequencies to less values than the original, which thus leads to underestimate the bunch length (see table 6.1), since the value of the zero-frequency is equivalent to the integral of the bunch distribution.

For comparison in figure 6.5a the zero-frequency constraint is applied, but the odd-phase constraint skipped. Although the reconstructions are more reproducible compared to figure 6.4, however, there are two different classes of reconstructions visible. In total, only 2 of 10 runs are in a good agreement with the original distribution (*black line*).

Figure 6.5b shows 10 reconstructions with zero-frequency and odd-phase constraints (*blue lines*). The latter showed similar reproducible runs.

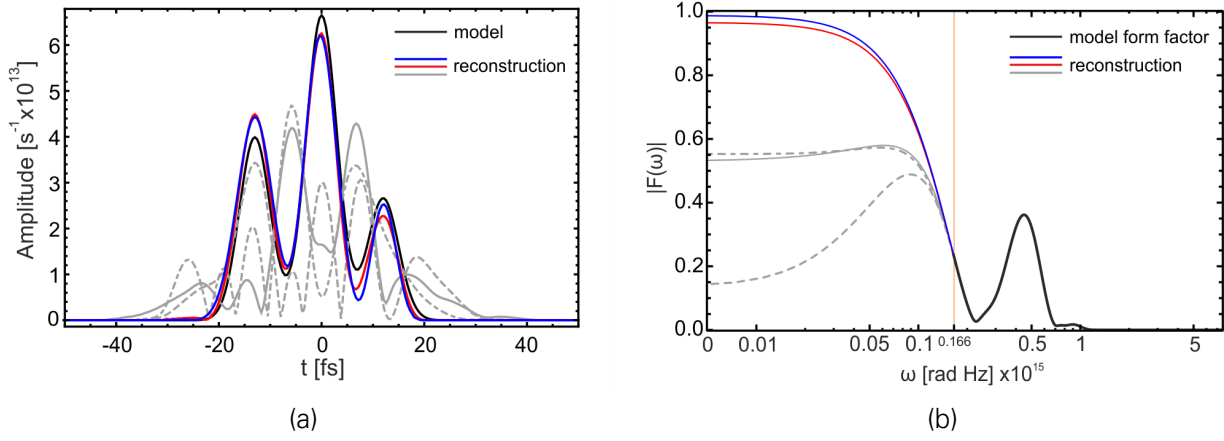


Figure 6.4.: **Reconstruction of a triple Gaussian bunch.** (a) shows the reconstruction results without the zero-frequency and odd-phase constraints. (b) presents the corresponding form factors from (a). Only the frequencies above 166 rad THz are used in the algorithm (*black line*). Only 2 of 10 reconstruction runs (*blue and red lines*) are in good agreement with the original bunch (*black line*). For comparison three incorrect reconstructions are depicted as well (*gray curves*)

6.2.3. POST-SELECTION ALGORITHM FOR HIGHLY MODULATED DISTRIBUTIONS

As the next step for optimizing the reconstruction algorithm, we consider a highly structured sample profile, which is more realistic to the bunch properties from the experiment presented in the next chapter. Beforehand, an algorithm for post-selection of the reconstruction results is outlined below. D. Pellicia presented a method for a *posteriori* reduction of the ambiguities based on the correlation analysis of the solution from N runs of an iterative phase retrieval algorithm with different random starting phases^[162,163]. By monitoring the relative error during the processing of the reconstruction, which is calculated at every iteration in both real space and Fourier space, one can select a reconstruction result from N runs with the smallest error and deploy this as the reference into the post-selection procedure. However, this method is not always applicable to seek the best reference profile, hence by increasing the number of iterations (or iteration cycles) almost all of the reconstruction runs converge to a solution with comparable final relative error as we are observed this effect in the reconstruction of the sample profiles presented here. As mentioned before, the KK method (see section 6.1.6) results in a good approximation of the sample profiles especially in case of modulated bunch distributions. In most of the cases, the modulation distribution is correctly reproduced while its long tail and therefore the global size of the bunch remained underestimated. In order to address this behavior, we first constitute a modulated distribution presented in figure 6.8a. It is modeled from 6 Gaussians by using equation (6.12). A pedestal Gaussian with RMS with σ_1 is modulated by 5 Gaussians, each of which σ_i 's is separated by μ_i and weighted by factors α_i . A summary of the mentioned parameters is documented in the table of figure 6.6.

As mentioned in section 6.1.6, the KK reconstruction might suffer from the Blaschke phase contributions and, in principle, are not accessible without prior knowledge of bunch distribution. This behavior is demonstrated in figure 6.7 by comparing the phase gradient $d\phi/d\omega$ of the model bunches to the corresponding KK analysis. The phase gradient eliminates the offset and the linear phase contributions from the corresponding spectral phase enabling a direct comparison of the relevant phase information for the bunch shape from the aforementioned methods.

The result of the Kramers-Kronig analysis depicted in figure 6.8 is obtained as following:

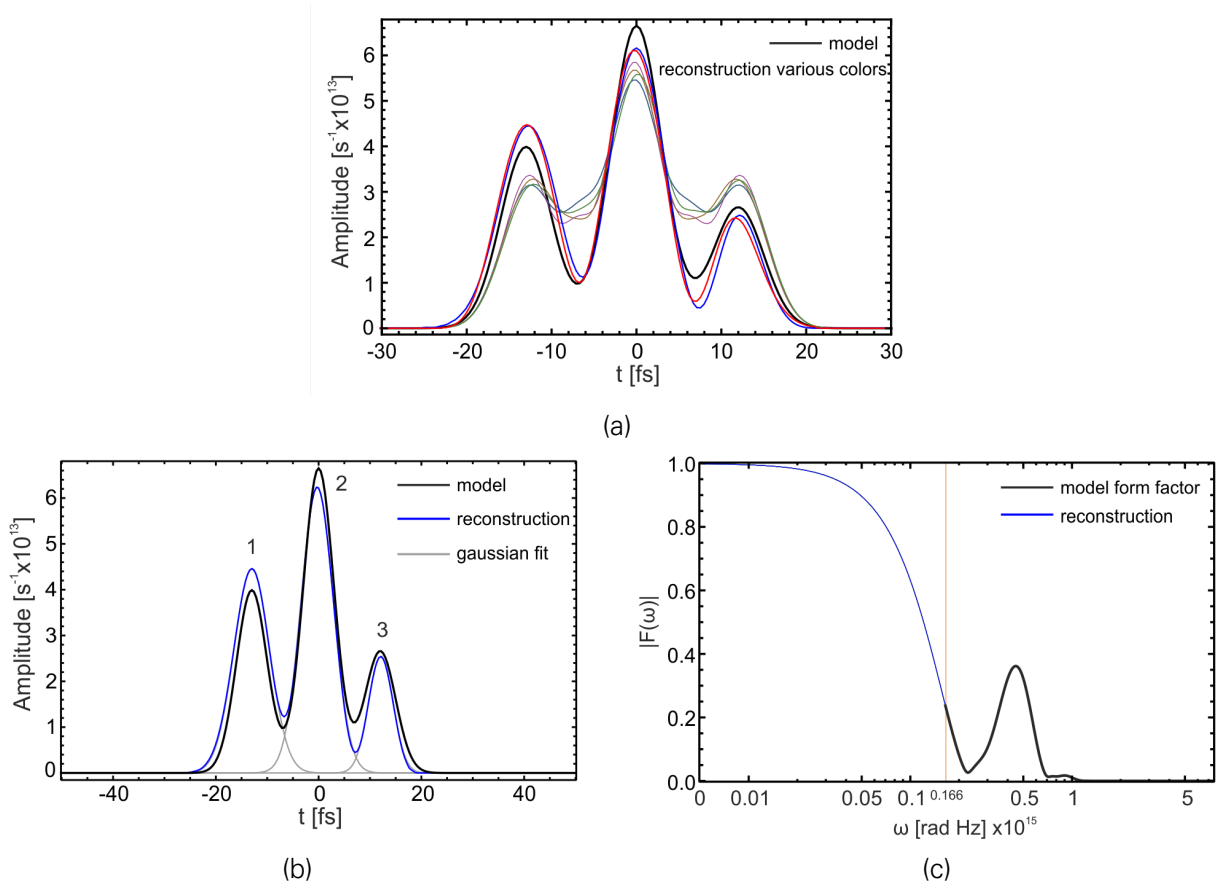


Figure 6.5.: **Reconstruction of a triple Gaussian bunch.** In (a) the zero-frequency is set to unity but the odd-phase constraint skipped. Two distinct sets of reconstruction candidates are evident. Only 2 of 10 are in a good agreement (*blue and red line*) with the original distribution (*black line*). (b) shows 10 reconstructions with both zero-frequency and odd-phase constraints (*blue line*). The reconstructions are all the same. (c) presents the corresponding form factors from (b), only the frequencies above 166 rad THz are used in the algorithm (*black line*).

For calculating the minimal phase integral (Eq. (6.10)) a 1st-order Hermite interpolation is deployed to the truncated and frequency-mirrored form factor in the range of $-\omega_{\max} < \omega_i < \omega_{\max}$ including $|F(\omega = 0)| = 1$ for interpolating the frequencies below ω_{\min} . Since the interpolation of the low frequencies deviated from the real spectral data the integration boundaries of the minimal phase integral (Eq. (6.10)) are set from ω_{\min} to ω_{\max} .

In order to eliminate the ambiguity related to translation shift, time reversal and presence of possible artifacts in the reconstructed profiles, it is crucial to select the best results of N reconstructions. Thereby the result from the Kramers-Kronig method is set as the reference profile f_j^R . Every other sample profile, f_j^n , are then quantitatively compared to the reference by calculating the cross-correlation^[163]:

$$c_h^n = \frac{\sum_j f_j^R f_{j+h}^n}{(\sum_j |f_j^R|^2)^{1/2} (\sum_j |f_{j+h}^n|^2)^{1/2}}. \quad (6.15)$$

The cross-correlation c_h^n is a function of the relative shift h , which in practice denotes a translation of the sample profile in time with respect to the reference. For the time reversal ambiguity the sample profile is first reversed, \tilde{f}_j^n , before the cross-correlation is calculated, the latter can

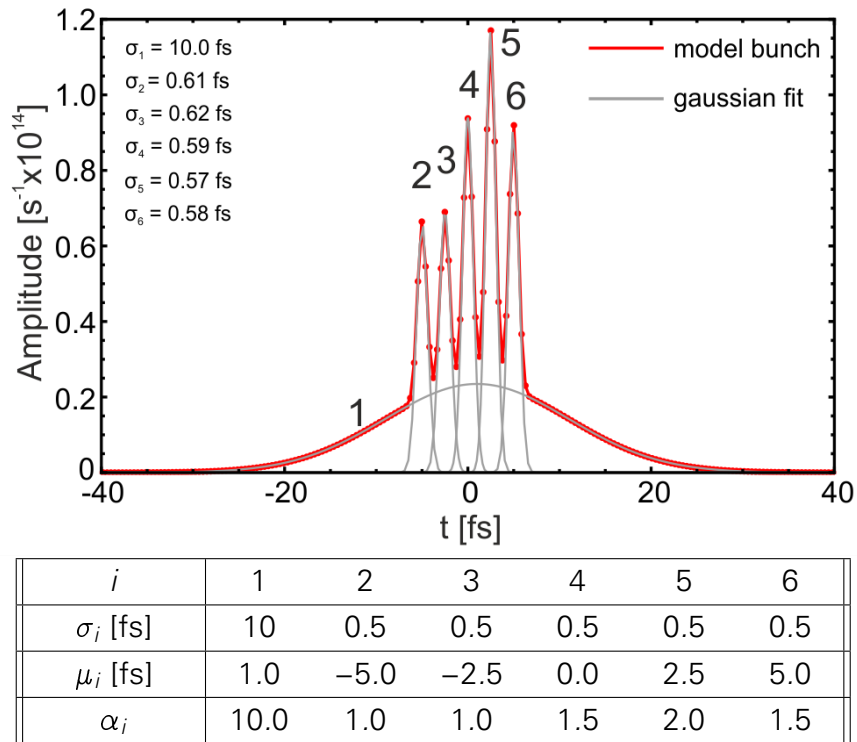


Figure 6.6.: **Highly structured model bunch.** Superposition of the modulations with the pedestal Gaussian, σ_1 , leads to broadening of the modulations, the modified σ_i 's (see inset) are estimated from Gaussian fits, plotted in gray

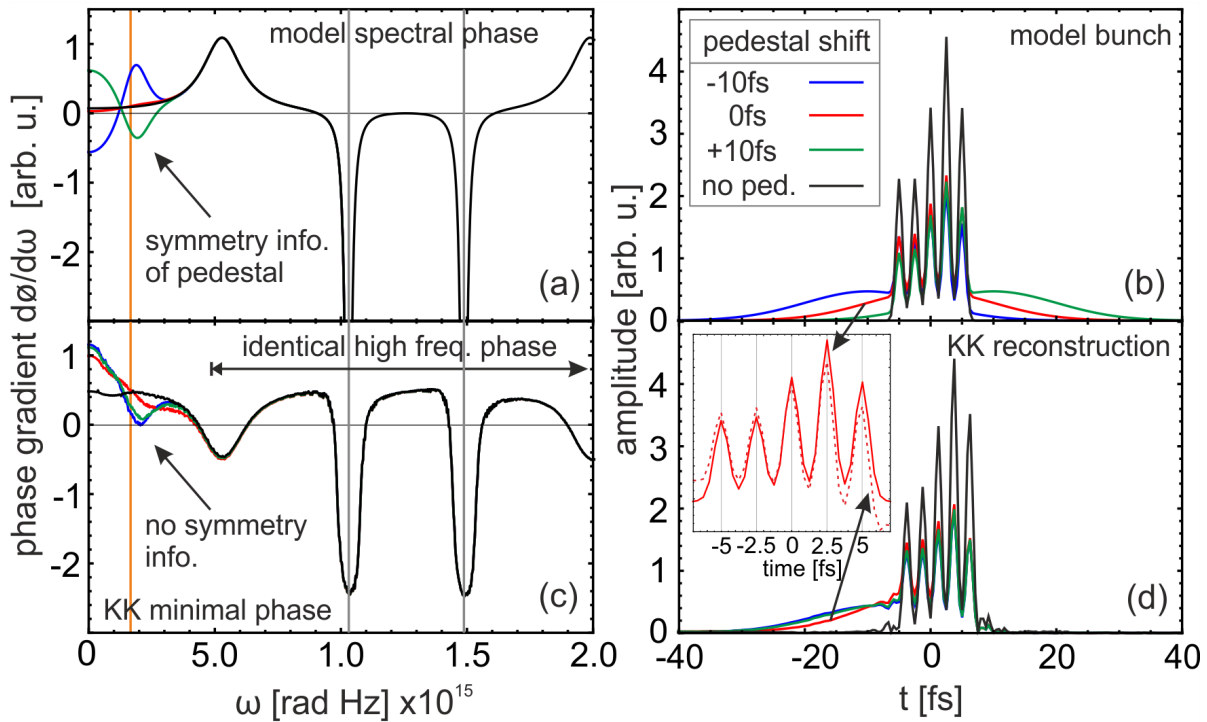


Figure 6.7.: **KK phase analysis.** (a) and (c) show the calculated spectral phases from (b) and (d) according to their analytic model form factors and the KK relation respectively. The low-frequency part of the phase in (a) contains phase information about the relative position and the orientation of the pedestal which is partially destroyed in (b) leading to a truncated bunch reconstruction. The high-frequency phase modulations are responsible for correct recovering of the modulations. The vertical orange line in (a) and (b) indicates the frequency limit of the model form factors.

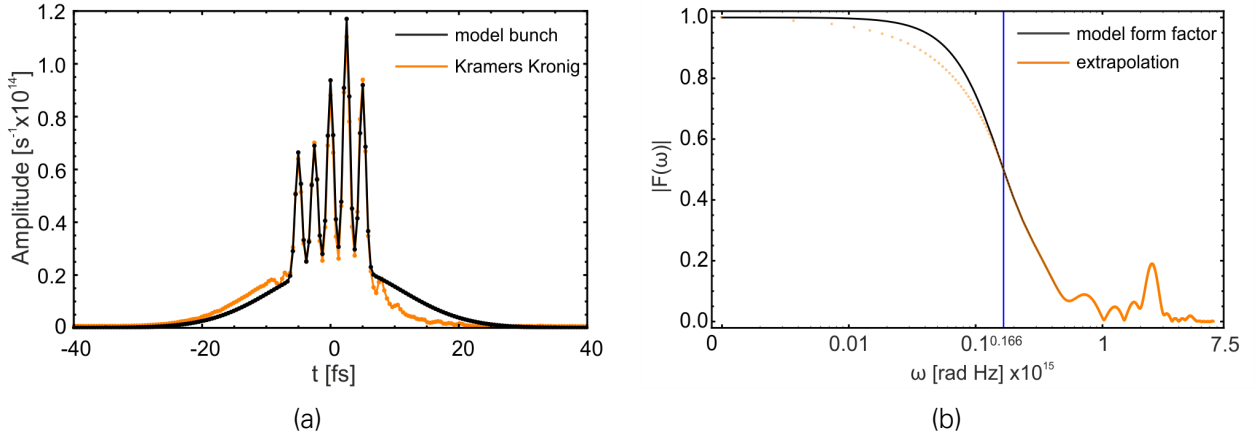


Figure 6.8.: **Reconstruction result for the structured bunch using Kramers-Kronig approach.**(a) shown are the model bunch (*black Line*) and the reconstructed profile from KK minimal phase analysis (*orange line*), (b) the original form factor (*black line*), the extrapolation to the low frequencies below 166 THz(*orange line*). While the modulation in the sample profile are well reconstructed, the evident discrepancy at the long tail is typical for KK method. The latter has to be mostly addressed to existing Blaschke phase terms, which are not taken into account in the calculation of the total phase. Also extrapolating the form factor for low frequencies and hence the associated incorrectness in the low frequency range affected the estimated phase.

be expressed as:

$$\bar{c}_j^n = \frac{\sum_j f_j^R \bar{f}_{j+1}^n}{(\sum_j |f_j^R|^2)^{1/2} (\sum_j |\bar{f}_{j+1}^n|^2)^{1/2}}. \quad (6.16)$$

The highly correlated reconstruction candidates can thus be selected by applying a correlation threshold t_n , here 95 % as

$$\forall f^n(t) : (c_h^n \cup \bar{c}_j^n) \geq t_n, \quad (6.17)$$

where \bar{h} and \bar{l} denote the value of the shift that maximizes equations (6.15) and (6.16), respectively. Hence p_n indicates the degree of correlation between the reference and sample profile. The unambiguous reconstruction candidates can be thus selected by applying a correlation threshold to p_n . The reconstruction algorithm is applied 20 times to the truncated form factor each is initialized with a different randomized phase in the range of $[-\pi/2, +\pi/2]$. Applying the post-selection algorithm with a correlation threshold at 95 % yields a set of highly correlated profiles (27 reconstructions). According to the estimated values of \bar{h} and \bar{l} , the selected profiles are thereafter shifted or reversed accordingly in order to realize the best overlap of the profiles. In figure 6.9 the retrieved profiles from simulated form factor related to the figure 6.8 is presented. Up to now, we have demonstrated the capability of the iterative reconstruction algorithm to retrieve even complex electron bunches as it is the case in the previous example. From figure 6.9c and comparing the retrieved profile (*blue line*) to the original bunch distribution (*black line*), it is obvious that the majority of the modulations in the bunch are correctly retrieved. Additional artifacts at the tail of the bunch occur with almost the same modulation period as in the rest of the bunch. This effect is frequently observed while doing experiments with synthetic data. The latter can be significantly improved by extending the spectral range of the TR spectrometer toward terahertz range of the TR spectrum. However, the global size of the bunch is reasonably reconstructed which mainly defined by the width of the pedestal Gaussian. The reconstruction of the long tail of an electron bunch is previously reported to be very challenging. Here, by applying additional zero-frequency and odd-phase constraint, the reconstruction algorithm could be significantly improved enabling relatively precise and

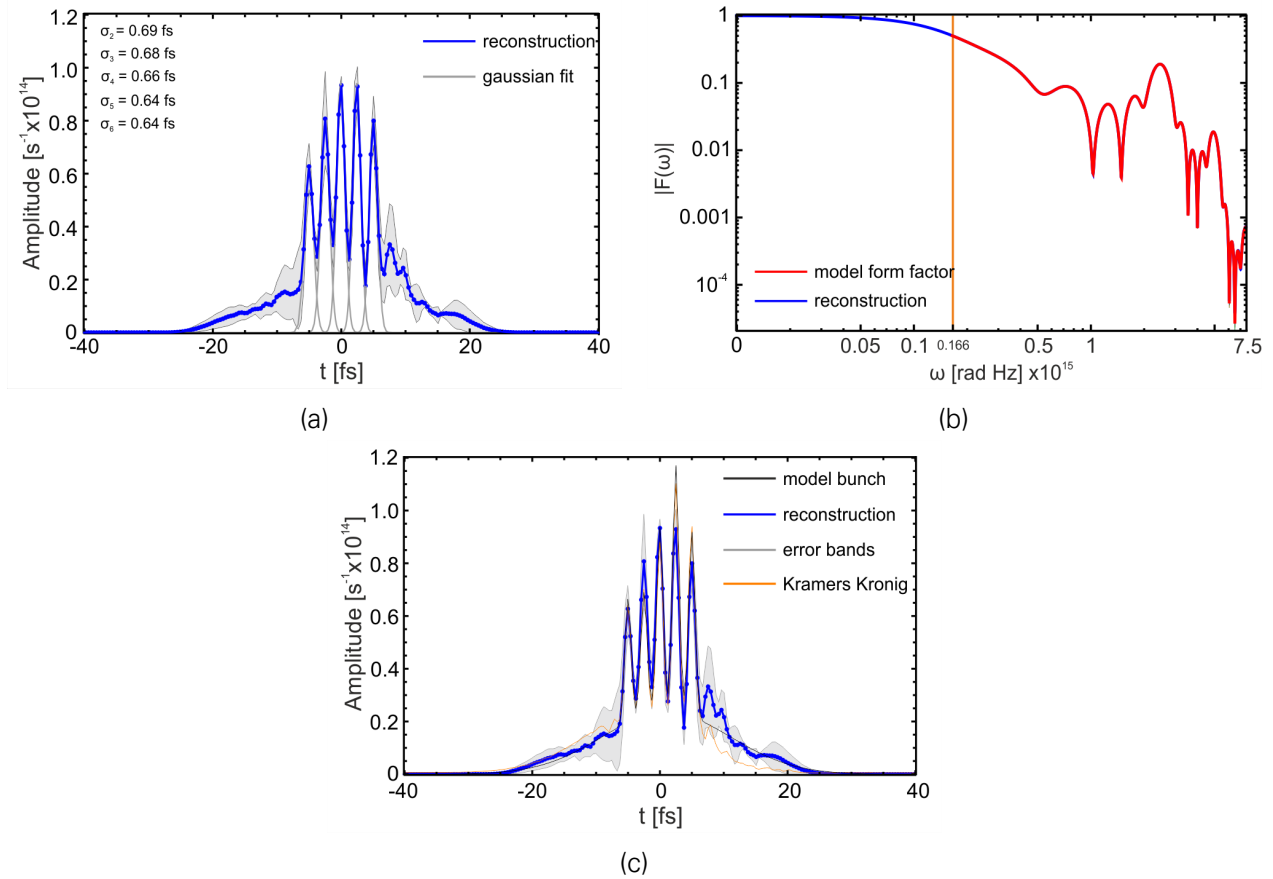


Figure 6.9.: **Reconstruction result for the structured bunch using the iterative method.** (a) shows the representative result from reconstruction averaged over the selected results (*blue line*) (for explanation see text), the *gray* error band denotes one standard deviation of the selected results from the mean. (b) shows the corresponding form factor as in figure 6.8b, here depicted in a logarithmic scale to emphasize the high-frequency range of the form factor. *Red line* indicates the original form factor and *blue line* shows the reconstructed part. Notably, every selected profile exhibits the same shape of the form factor, (c) demonstrates a summary of the results

reproducible reconstruction results of structured as well as long distributions.

6.3. BUNCH PROFILE RECONSTRUCTION FROM EXPERIMENTAL CTR SPECTRA

In this section, the Foldwrap algorithm, described in the previous section, is applied to the experimental CTR spectra. The procedure from raw data to the electron bunch form factor is discussed step-by-step in following section 6.3.1. The result of bunch profile reconstruction including a detailed error analysis for a typical shot is presented in section 6.3.2.

6.3.1. PREPARATION OF CTR DATA

Figure 6.10 shows the flowchart of a pre-analyzing procedure, in which the raw data acquired by the TR spectrometer (for details see chapter 4) and the electron spectrometer are treated in order to obtain the electron bunch form factor. Calibration of the CTR spectra (step 4 in 6.10) are performed by utilizing the absolute calibration curves given in the equation 4.20. Notably,

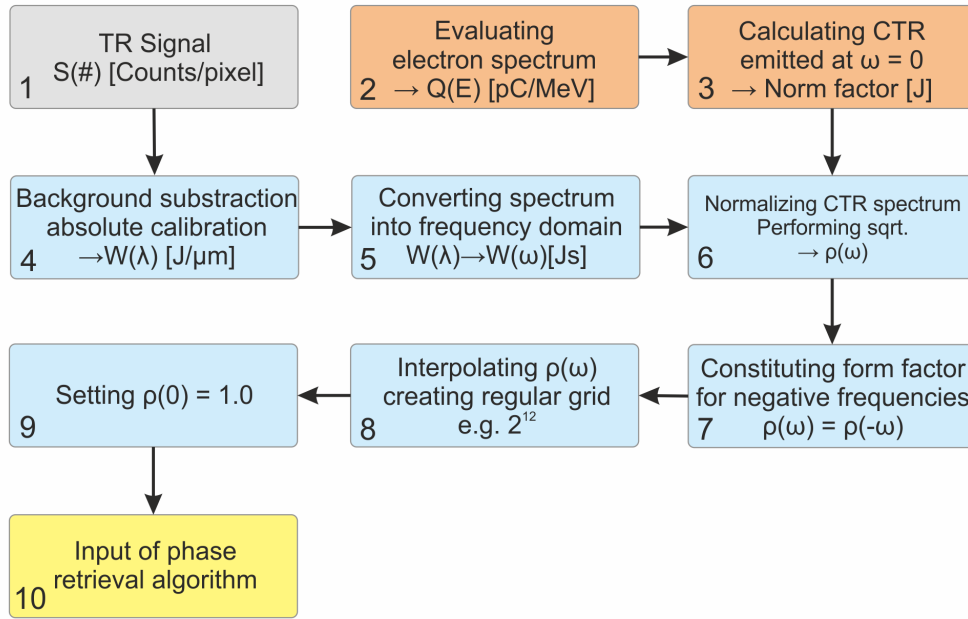


Figure 6.10.: Block diagram illustrates the procedure from the raw TR signal to the form factor.

appropriate ND filters are added to the NIR and MIR arms of the TR spectrometer in order to use full dynamic range of the detectors. Additionally, in the MIR arm, KRS-5 holographic WGP's (Thorlabs WP50H-K) are utilized pairwise, as a cross-polarizer, in order to precisely adjust the throughput to fit the dynamic range of the MCT detector. A dedicated calibration run for TR spectrometer is performed, in which the mentioned ND filters are employed.

The NIR arm could be recalibrated including an ND filter (OD = 2, Thorlabs NENIR20B), but due to the low flux of the BB source in the MIR region, only one cross-polarizer could be added to the beam path during the calibration run. An additional cross-polarizer pair and two ND filters (OD = 1&2, Thorlabs NDIR10B & NDIR20B) are characterized separately by using the FTIR spectrometer. In the case of OD = 3 filter (Thorlabs NDIR30B), the combination of ND1 and ND2 attenuators are used in the calibration curve. In the case of ND filter (OD = 3, Thorlabs NDIR30B), its transmission curve is provided by the manufacturer. Hence the absolute calibration given in Eq. (4.20) can be extended to:

$$T_{\text{Abs.}, \text{BW}}(\lambda) = T_{\text{Rel.}}(\lambda) \cdot T_{\text{polarizer}}(\lambda) \cdot T_{\text{ND filter}}(\lambda) \cdot T_{\text{beam line}}(\lambda) \cdot F_{\text{Abs.}} \cdot \text{BW}(\lambda), \quad (6.18)$$

where $T_{\text{polarizer}}$, $T_{\text{ND filter}}$, $T_{\text{beam line}}$ denote the transmission through the cross-polarizers, transmission through the ND filters and CTR beam line efficiency respectively. Note, that due to the radial polarization of TR emission the entering beam into the spectrometer can be assumed to be "unpolarized". In practice, the polarization dependent calibration curves (Eq. (4.20)) are averaged over the s- and p-polarization, in order to obtain the unpolarized calibration (Eq. (6.18)). An overview of the modified absolute calibration of the TR spectrometer is shown in fig.6.11 below.

Calculation of the CTR emission from electron spectrum is performed as follows (step 3 in 6.10):

The electron bunches from the LWFA experiment contain several hundred pC of charge, accelerated up to 350 MeV. Their highly energetic peaks contain typically 200 pC of charge within a relative energy bandwidth of around 10 %. Under the above-mentioned circumstances, the incoherent TR can be neglected, because of the large number of electrons ($\sim 10^8 - 10^9$). From

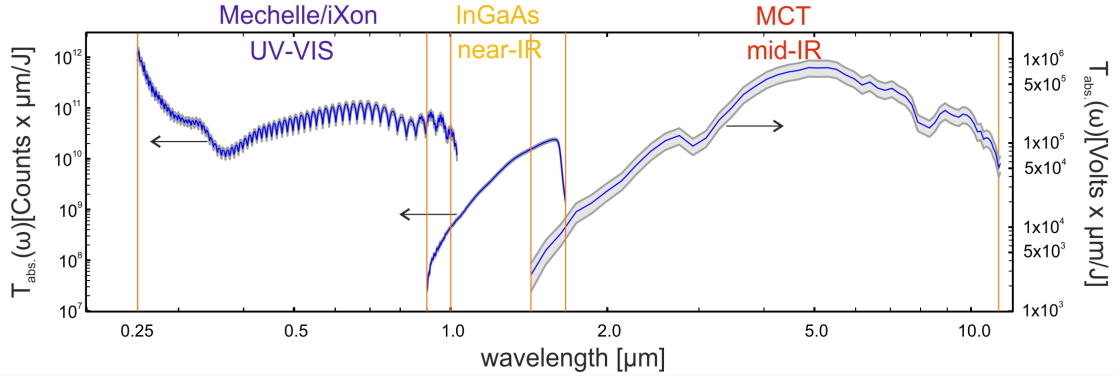


Figure 6.11.: Overview of the modified absolute calibration of the TR spectrometer. It is applied to the majority of experimental TR spectra. The attenuators included in this calibration are as follows: UV-VIS: EM-gain is set to 30x, NIR: one ND2 attenuator, MIR: one ND3 and two cross-polarizer pairs. The grid orientation of the latter is arranged at 0° , 90° , 0° and 40° with respect to the optical plane of the spectrometer.

the chapter 3 theory of TR, we recall the coherent term of the general expression for angular distribution (3.9) as

$$\frac{d^2 W_{\text{CTR}}}{d\omega d\Omega} = \frac{e^2}{4\pi^3 \epsilon_0 c} N(N-1) \left[\left| \int d^3 \mathbf{p} g(\mathbf{p}) \mathcal{E}_{\parallel} F \right|^2 + \left| \int d^3 \mathbf{p} g(\mathbf{p}) \mathcal{E}_{\perp} F \right|^2 \right]. \quad (6.19)$$

The divergence of the beam is, in general, continuously decreasing with increasing energy. However, the geometrical divergence exhibits an increase in the high energy peak (see also section 6.3.2). The typical averaged rms divergence of the high energy peak of the electron beam is measured to be on the order of 5 mrad.

It can be shown, that the contribution of the perpendicular electric field of the TR, \mathcal{E}_{\perp} , for small divergence $\psi \ll 1$ will be several orders of magnitude smaller than the integral over its counterpart (\mathcal{E}_{\parallel}). Therefore the second term on the right hand side of the Eq.(6.19) is negligible.

The transverse momentum distribution of the electron beam is assumed to be Gaussian and is defined as

$$g(\mathbf{p}_{\perp}) = g(\psi, \phi) = \frac{1}{\pi \sqrt{2\pi} \sigma_{\psi}} e^{-\frac{\psi^2}{2\sigma_{\psi}^2}}, \quad (6.20)$$

where ψ and ϕ denote the azimuthal and polar angle coordinates with respect to the direction of traveling electron beam (see Fig. 3.2) and σ_{ψ} is the rms divergence of the beam. Equation (6.20) is a fairly good approximation for the averaged transverse momentum distribution of the peak energy. The longitudinal momentum distribution $g(u)$, i.e., the energy spectrum is measured using a charge calibrated dipole spectrometer covering energies from 1.5 MeV to 600 MeV.

The Eq.(6.19) at the zero frequency (ω_0) is therefore reduced to

$$\frac{dW_{\text{CTR},i}}{d\Omega} \Big|_{\omega=0} = \frac{e^2}{4\pi^3 \epsilon_0 c} N_i(u_i)^2 \left[\left| \int_0^{\psi_{\max}} \int_0^{2\pi} d\psi d\phi g(\psi, \phi) \mathcal{E}_{\parallel}(\theta, \psi, \phi, u_i) \right|^2 \right], \quad (6.21)$$

where $N_i(u_i)$ denotes the number of electrons within the energy bin u_i . This is obtained from the electron energy spectrum evaluated on a discrete grid and is typically binned by 3 MeVs over the entire energy spectrum. Integrating the expression (6.21) over the appropriate solid angle $d\Omega = 2\pi \sin \theta$ and summing up over the energy spectrum of the electron bunch, yields

to the final expression for the total CTR emission:

$$W_{\text{CTR}}|_{\omega=0} = \sum_{i=u_{\min}}^{u_{\max}} \frac{e^2}{2\pi^2\epsilon_0 c} N_i(u_i)^2 \int_0^{\theta_{\max}} d\theta \sin\theta \left. \frac{dW_{\text{CTR},i}}{d\Omega} \right|_{\omega=0}. \quad (6.22)$$

θ_{\max} indicates the acceptance half angle of the collection optic, which is 16 mrad in the experimental setup presented in this work.

Now, following the step 5 in the diagram 6.10, the absolute calibrated CTR spectrum measured by TR-spectrometer is normalized by the value calculated from the Eq. (6.22) in order to obtain the absolute value of the longitudinal form factor (step 6 in 6.10). The angular distribution of TR is expressed as

$$\frac{dW^2}{d\omega d\Omega} = |F_{\parallel}(\omega)|^2 \cdot \left. \frac{dW_{\text{CTR}}}{d\Omega} \right|_{\omega=0} \quad (6.23)$$

and hence integrating over all angles leads to

$$\frac{dW}{d\omega} = |F_{\parallel}(\omega)|^2 \cdot W_{\text{CTR}}|_{\omega=0}. \quad (6.24)$$

Since in the Foldwrap algorithm a complex discrete Fourier transform routine is applied, according to the Eq.(6.4) the form factor is extended for negative frequencies (step 7 in 6.10). As the next step, the form factor is assigned to an equidistant reconstruction grid (2^{12} data points) by performing linear interpolation on the form factor (step 8 in 6.10). This linear interpolation is justified, since the data from visible and near-IR regions of the TR spectrum have a higher resolution than the reconstruction grid spacing. In addition, although the resolution of the MCT detector is less compared to the reconstruction grid, however in the presented TR spectra, the mid-IR region is not a subject of spectral modulations. Hence the linear interpolation and population of the MCT data will not affect the spectral shape of the TR spectrum. Finally, the value of the form factor at $\omega = 0$ is set to unity, since the measured TR spectrum is normalized, as described above (step 6).

In the following section, the reconstruction algorithm is applied to experimental TR data, and the results are demonstrated in representative examples.

6.3.2. RESULTS OF RECONSTRUCTION

In this section, the reconstruction of the bunch profile from a typical measurement is presented. The calibration of the measured TR spectrum is performed according to the procedure described in the previous section (see figure 6.10). Before we start with the reconstruction of the TR spectrum, the properties of the electron spectrum are discussed in the following:

EVALUATION OF ELECTRON SPECTRUM

The evaluation of the electron spectrum is shown in figure 6.12 (step 2 and 3 in figure 6.10). A quasi-mono energetic peak is centered at 268 MeV with an FWHM energy spread of about 36 MeV. It contains 180 pC of charge. The vertical axis corresponds to the transverse momentum of the bunch in the polarization plane of the driver laser (horizontal in the experimental setup, see figure 5.2). It contains information about the beam divergence, which is shown in figure 6.12b. The spectrum is binned by 10 MeV, and a Gaussian fit function is applied to each energy bin in order to estimate its RMS divergence (ψ). The average divergence of the mentioned peak is obtained to be $\bar{\psi} = 5.4$ mrad, which will be used in the calculation of the CTR emission.

Figure 6.12c shows the electron spectrum with integrated charge from the figure 6.12a for all transverse angles (*blue line*) and the calculated CTR emission according to the Eq. (6.22). The latter is strongly scaling with energy and charge (*pink line*). It demonstrates the fact that the majority of the CTR emission into the detection solid angle, here ($\theta_{\max} \approx 16$ mrad), is radiated from the high energy electrons. Therefore, we conclude that the influence of the low energy electrons on the spectral shape of the form factor remains insignificant. Integrating the calculated CTR emission (*pink line* in figure 6.12c) over all energies yields the total CTR emitted from the electron bunch and hence provides the normalization factor.

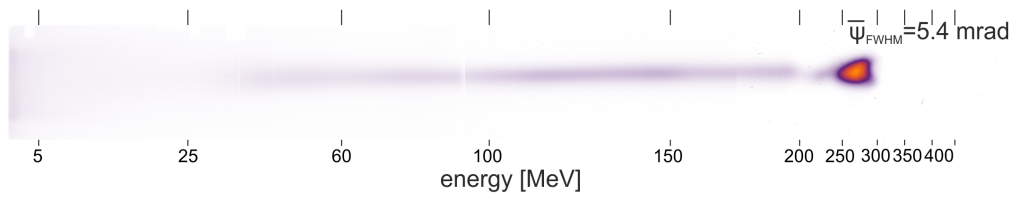
FROM FORM FACTOR TO BUNCH PROFILE

The absolute calibration of the individual detection systems, presented in the figure 6.11, is used first to calibrate the measured TR spectra. As the next step, the partial spectra from the echelle spectrometer and the MCT detector are re-scaled according to their corresponding overlap regions to the spectrum obtained from the InGaAs-detector. The absolutely calibrated TR spectrum thus can be normalized to obtain the form factor. The corresponding form factor of the shot 396 is presented in figure 6.13.

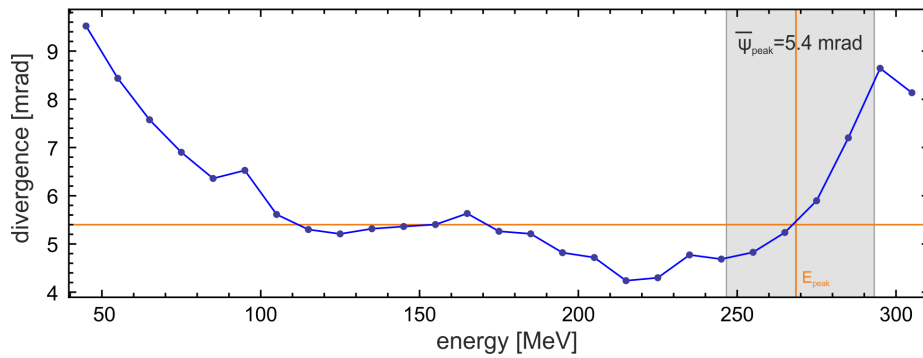
The reconstruction result for the shot 396 is presented in figure 6.14. The results presented here, are the 5 mostly probable reconstructions, which are selected from 50 runs according to the post selection algorithm. The selected profiles exhibit a correlation better than 93 % with respect to the reference profile (*solid orange*). The average profile over the selected reconstructions (*solid blue*) is depicted in figure 6.14c as the representative reconstruction result of this particular shot.

ON THE ERROR ANALYSIS

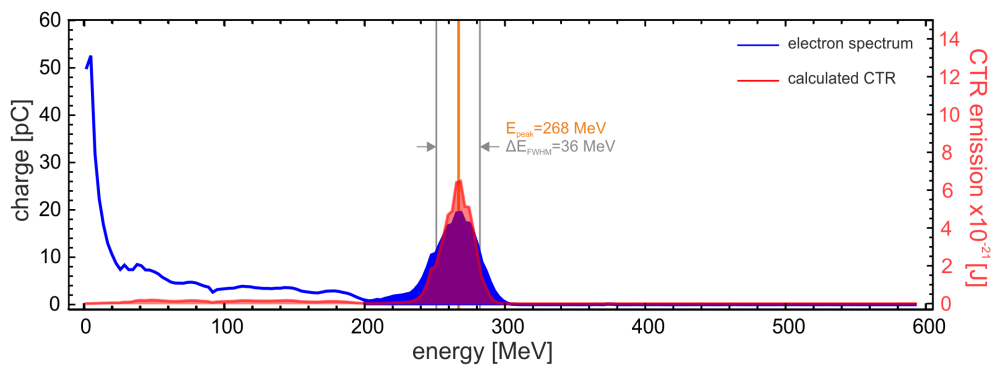
In order to ensure that the TR radiation is correctly transported through the beam-line from the TR source toward the entrance slit of the spectrometer, a fraction of the visible TR in front of the echelle spectrometer is reflected off the beam by using a beam sampler. It aims to image the entrance slit onto a CCD camera (see figure 4.1). Thereby the shot to shot pointing of the TR can be monitored, and the alignment of the TR beam can be optimized. Figure 6.15a



(a) Displays image of lanex screen.



(b) Shows divergence of the beam evaluated for discrete energy bins of 10 MeV.



(c) Evaluation of electron energy spectrum. depicted are the integrated energy spectrum over all transverse angle (*blue line*), calculated CTR emission in dependence of energy (*pink line*), the latter are performed according to the estimated averaged beam divergence.

Figure 6.12.: Illustrates the electron spectrum of an exemplary shot 396 measured in single shot by the electron spectrometer. The experimental parameters for the gas mixture are as follows: 1.5 % Nitrogen doping, 8 bar backing pressure ($n_e = 3.4 \times 10^{18} \text{ cm}^{-3}$), corresponding to a plasma wavelength of $\lambda_p = 17.1 \mu\text{m}$.

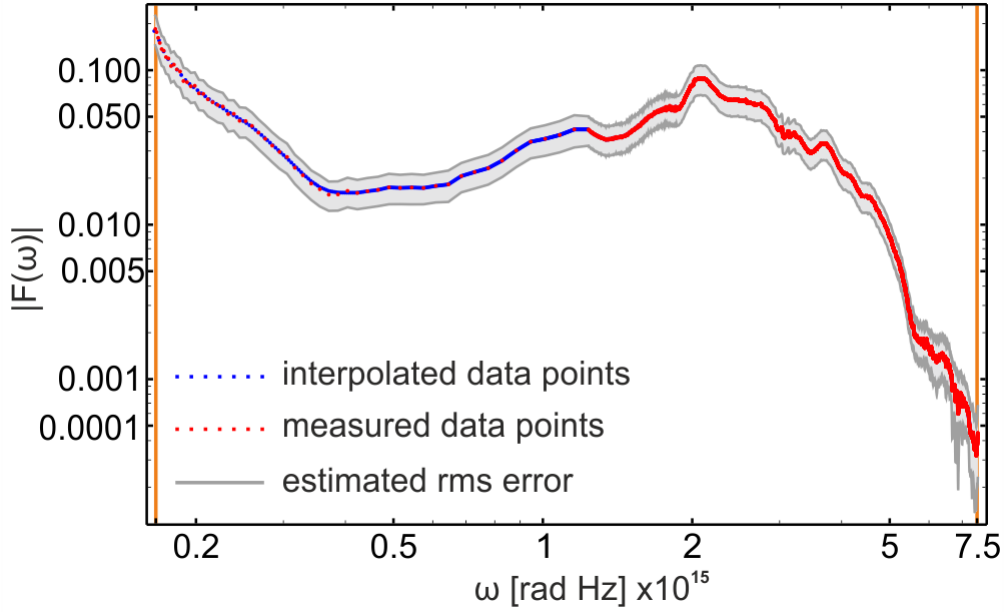


Figure 6.13.: The normalized form factor of the shot 396.

presents the transmitted TR profile behind the slit for the sample shot 396. It shows that the TR spot fits well on the slit and thus no correction for beam clipping by the slit is required.

The absolute measurement of the TR spectrum is subject of the following uncertainties:

Readout noise: The relative error from readout noise of the detector (σ_{S_n}) depends on the signal level, as well as the noise introduced from the environment such as the temperature of the detector head, integration time but also electromagnetic pulse (EMP) events during the acquisition. The latter is evident in this experiment due to, for instance, electron-ion recombination in the plasma medium. However, the mentioned EMP noise is only present at the MCT detector electronics. The fluctuations in the readout noise are estimated for each detector by measuring 181 background signals during the LWFA experiment without the TR foil in the electron beam path. Hence background noise and EMP can be evaluated by performing the standard deviation of the acquired background signals ($\sigma_{Bgd.}$). The relative error is therefore given as

$$\sigma_{S_n} = \frac{\sigma_{Bgd.}}{S_n}$$

Spectral bandwidth: The relative error regarding the spectral bandwidth of each detector element is obtained from the standard error given by the corresponding wavelength fit. The latter is estimated with a confidence interval of 95 % corresponding to 2 rms standard deviations for individual detector elements and thus according to the mean value of each wavelength interval the relative error is obtained as

$$\sigma_{\Delta\omega} = \frac{\Delta\lambda}{\bar{\lambda}} = \frac{\Delta\omega}{\bar{\omega}}$$

Relative response: The error from the relative response calibration $\sigma_{Rel.}$ is estimated from the absolute calibration of the corresponding calibration light source. The spectral emissivity

of the BB source, utilized for the relative calibration of NIR and MIR arms of the spectrum, is better than 99 %. The absolute calibration of the QTH lamp is between 8.2 % to 9.4 % in the spectral region of interest for echelle spectrometer.

Absolute calibration: The absolute calibration of the extended TR spectrum is performed according to the absolute calibration of the InGaAs detector (NIR arm). The power measurement of the calibration laser line ($\lambda = 1.31 \mu\text{m}$) is carried out by utilizing a thermal power head (gentec XLP12) with 3 % relative uncertainty. The fluctuations of the laser during the power measurement leads to an additional error of 3 %.

Divergence: According to the electron bunch transverse momentum distribution, Eq. (6.20), the divergence of the electron bunch leads to a reduction in the collected TR. In the calculation of the collected CTR into the TR spectrometer the averaged RMS divergence with an accuracy of $\pm 1 \text{ mrad}$ is also taken into account. The latter causes a relative error in the calculation of CTR energy of about $\sigma_{\psi} = 15 \%$ for typical electron bunches presented here.

Charge calibration: The main source of the error in the CTR calculation originates from the uncertainty in the charge calibration of the electron spectrometer, which is obtained to be below $\sigma_Q = 20 \%$.

The relative error of $|F_{\parallel}|$ is estimated by taking into account the contributions of the statistical as well as the systematic sources of errors as described above and given as:

$$\sigma_{F_{\parallel}}(\omega) = \frac{1}{2} \sqrt{\sigma_{S_n}^2 + \sigma_{\Delta\omega}^2 + \sigma_{T_{\text{Rel.}}}^2 + \sigma_{T_{\text{Abs.}}}^2 + \sigma_{\psi}^2 + 4\sigma_Q^2}, \quad (6.25)$$

where σ denotes the relative error of each quantity. Notably, the factor 1/2 in the above expression (6.25) is due to the fact that the form factor scales with square root of the measured TR spectrum and hence the corresponding error in the form factor is multiplied by 1/2. In contrast, since the TR intensity scales quadratically with the number of electrons, the corresponding form factor and hence its relative error scales linearly with σ_Q .

Exemplary, the *gray* error band in figure 6.13 indicates the upper and the lower error margins of the corresponding form factor according to the Eq. (6.25).

Note, that the value of the form factor at $\omega = 0$ is unity in any case. Since the contribution of both σ_{ψ} and σ_Q are also applied to the measured form factor, hence the mentioned limits of the error margins contain the total error. From this point, the Foldwrap reconstruction procedure can be applied to the mentioned upper and lower error margins in order to estimate the corresponding limits in the time domain. Figure 6.16 presents the results of this treatment for both the deviations originating from the ambiguities in the reconstruction algorithm presented in figure 6.16a and the uncertainties in the measurement of the form factor presented in figure 6.16b.

According to the estimated limits in the reconstruction of the sample bunch profile (shot 396) the maximum error estimated from all sources of uncertainties is obtained by summing the individual deviations from the mean profile. Figure 6.17 demonstrates a summary of this treatment. Applying the integrated charge contained in the high energy peak of the electron spectrum (*blue filling* in figure 6.12b) to the bunch longitudinal distribution yields the corresponding peak current, plotted in figure 6.17a. The rms width of the global dimension of the bunch is maintained from a Gaussian fit function and is obtained to be $\sigma = 11.0_{-1.3}^{+1.2} \text{ fs}$ within $\pm 11 \%$ of error. The width of the representative sub-structure in the bunch (*pink filling* in figure 6.17a) is obtained to be $\sigma_{\text{sub}} = 0.6_{-0.1}^{+0.7} \text{ fs}$. The latter is corresponding to a peak current as high as $14.5 \pm 3.5 \text{ kA}$.

In order to verify the dimensional boundaries of the reconstructed bunch profile the entire electron bunch form factor including two single Gaussian form factors are presented in figure 6.17b.

Summary of the reconstruction of another three sample shots are presented in Appendix A.2. In contrary to the above verified shot 396, which is acquired with 1.5 % Nitrogen doping in the gas mixture, shot 677 A.3, 657 A.4 and shot 602 A.5 are measured by setting the Nitrogen doping to 0.5 %, 1.0 % and 3.0 % respectively.

SOURCE OF ERRORS REGARDING BEAM FREE PROPAGATION

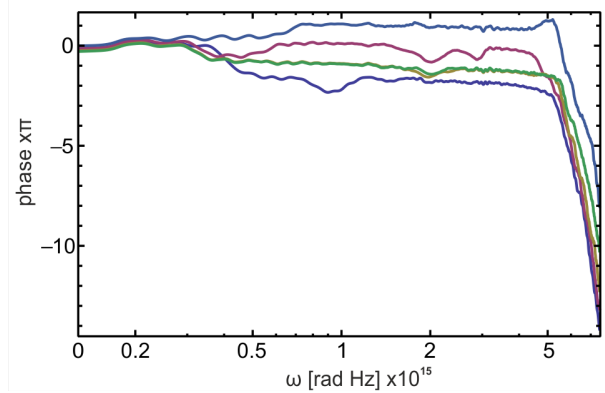
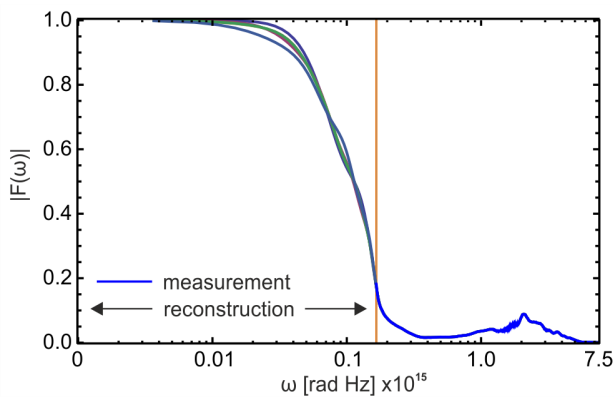
Despite the error analysis presented in the previous section 6.3.2 the free propagation of the electron bunch from the exit of the nozzle to the TR screen and subsequently propagation of the TR from the TR screen to the TR collection optics are potentially subject of additional error sources. In the following, we discuss some relevant issues:

During the beam free space propagation from the exit of the nozzle to the TR screen the transverse phase space will develop a position-angle correlation. The intrinsic divergence in the beam leads to an increase in the beam size at the TR foil, which thus reduces the transverse coherence i.e., $F_{\perp}(\theta, \omega)$. This effect is reduced by narrowing the collection angle of the TR collimation optic.

During the beam propagation, the electrons on-axis travel a shorter distance to TR screen compared to the electrons off axis due to the divergence of the electron bunch. This causes a bunch lengthening with regard to longitudinal charge distribution and can be expressed as $\Delta L \approx (1 - \cos \sigma_{\psi}) L_{\text{drift}}$. According to experimental setup presented here, for an electron bunch with RMS divergence of $\sigma_{\psi} \approx 5$ mrad and a propagation distance of $L_{\text{drift}} \approx 26$ mm the introduced bunch lengthening results in $\Delta L \approx 0.3 \mu\text{m}$. For typical bunch duration of FWHM $\approx 4 \mu\text{m}$ the relative bunch lengthening is $\delta L < 7.5 \%$. The collected TR emission and hence the acquired TR spectrum cannot account for this effect. However, the bunch lengthening of $< 7.5 \%$ is estimated according to the geometry of the setup and the averaged divergence over the entire electron bunch. The modulations inside the bunch could be however displaced from the axis, and each could exhibit a much smaller divergence. These structures cannot be resolved by the existing electron spectrometer and thus appears to be a projection of overlapping multiple structures at the location of the spectrometer's LANEX screen.

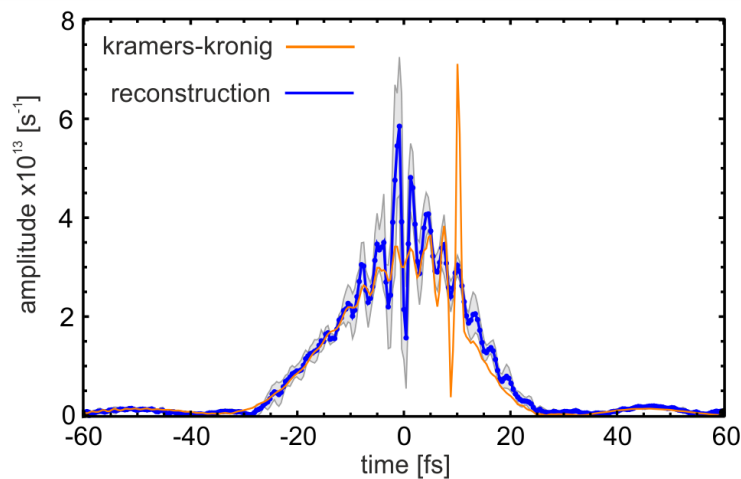
The maximal bunch lengthening due to the spatial energy chirp in the beam during the propagation can be expressed by $\Delta l \approx (1 - \beta_{\text{min}}/\beta_{\text{max}}) L_{\text{drift}}$. For typical quasi-monoenergetic electron bunches presented in this thesis i.e., $E_{\text{mean}} \approx 300$ Mev and $\Delta E \approx 10 \%$, and FWHM ≈ 15 fs, the maximum bunch elongation (or compression in case of negative chirp, i.e. higher energy electrons reside in the rear of the bunch) is in the order of 0.1 % and thus is negligible.

In this section, we presented the result of longitudinal bunch reconstruction from the single-shot measurement of the TR spectrum. The reconstruction result is presented for a few shots in order to demonstrate the capabilities of the presented Foldwrap reconstruction procedure. In the following chapter 7 a systematic analysis of the bunch profile for different experimental parameters is presented.



(a) **Several reconstructed form factors.** The frequencies above 166 rad THz are used in the reconstruction algorithm (*blue line*), only positive frequencies are shown here.

(b) **Corresponding retrieved phases from (a).**



(c) **Reconstructed bunch profiles.** The *solid blue line* shows the average bunch profile over the 5 selected reconstructions, the *gray* error band indicates a standard deviation of the mean (σ). The reference profile obtained from the KK relation (6.10) is depicted in *orange*

Figure 6.14.: **Shown are the reconstruction results for the shot 396.** According to the post-selection algorithm, 5 reconstructions are selected from 50 runs with different initial phase. The selected profiles exhibit a correlation better than 93 % with respect to the reference profile (*solid orange*). The average profile over the selected reconstructions (*solid blue*) is depicted in (c) as the representative result of this particular shot.

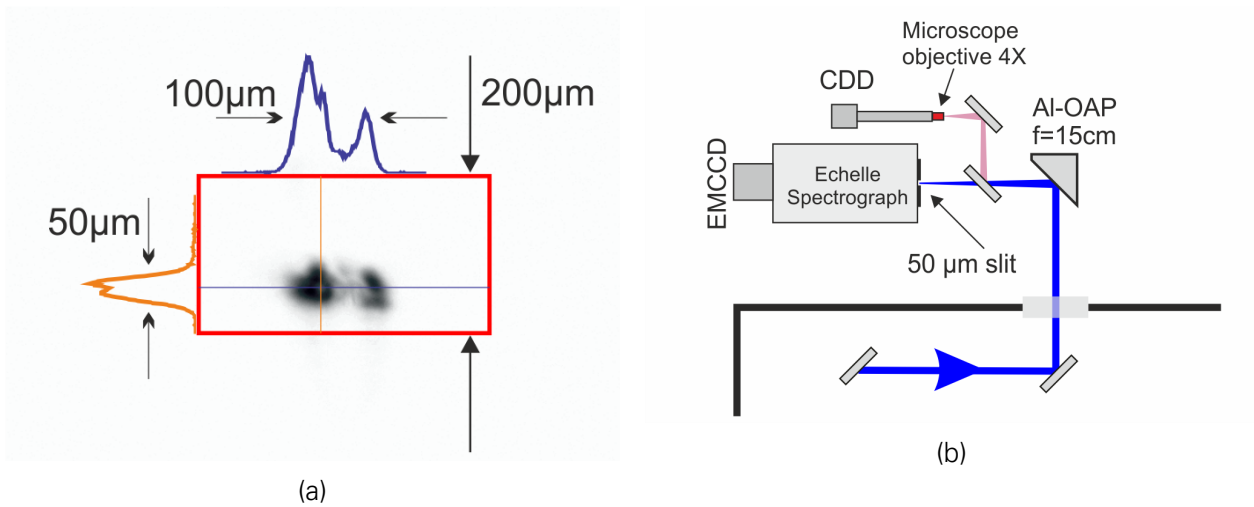


Figure 6.15.: Imaging setup for monitoring the TR transmission through the entrance slit of the TR spectrometer. (a) shows the image of the 200 μm entrance slit. The image is acquired by inserting a beam sampler into the TR beam in front of the echelle spectrometer (b). It reflects 1.0 % of the visible TR into the imaging optics.

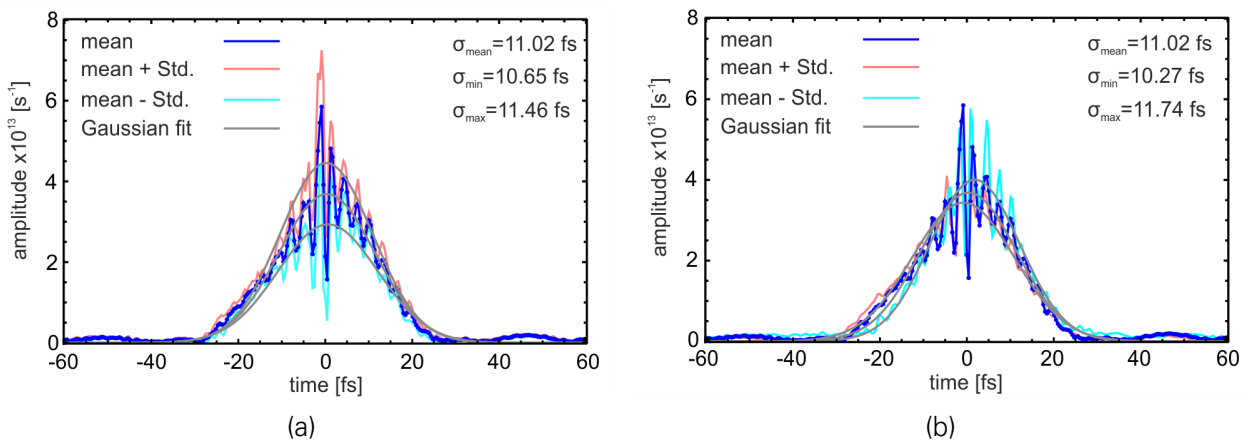
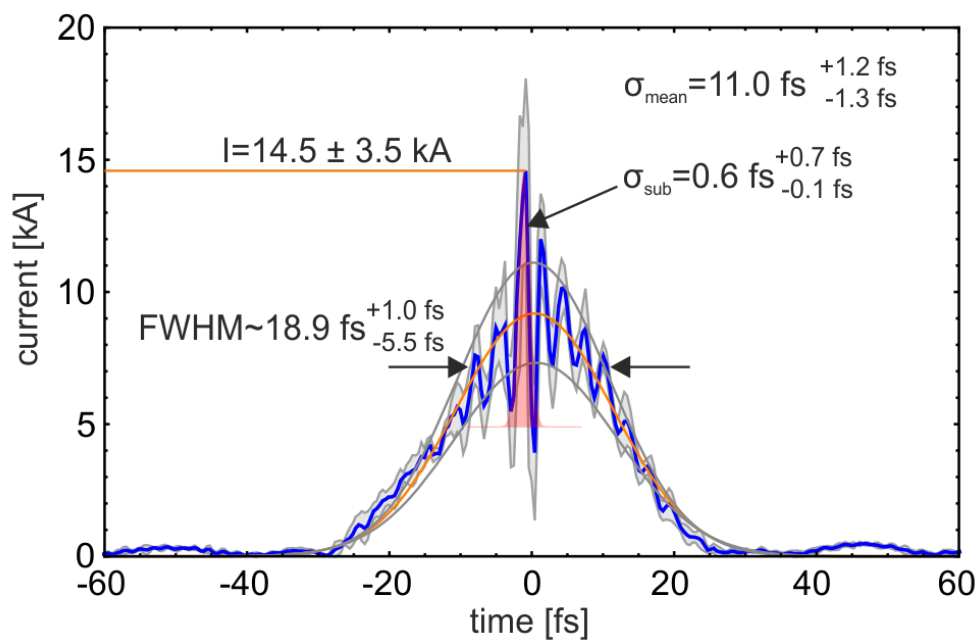
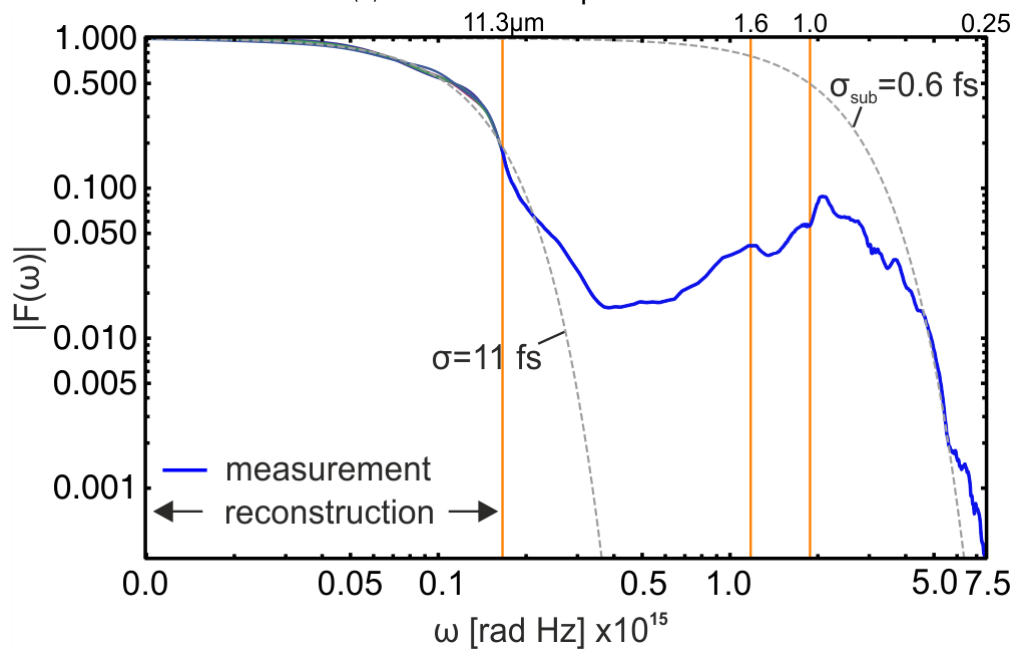


Figure 6.16.: Reconstruction results for shot 396 according to the upper and lower error limits. This originates from the ambiguities in the reconstruction algorithm (a) and the uncertainties in the measurement of the form factor (b). For each of the mentioned limits, plotted in *cyan* and *magenta*, 10 reconstruction runs are performed and the 5 mostly correlated reconstructions to the corresponding kramers-kronig profile are selected. Gaussian fittings on each of the distributions including their rms width are depicted in *gray*.



(a) Bunch current profile.



(b) Bunch form factor.

Figure 6.17.: Summary of the reconstruction results for shot 396.

7. HIGH PEAK CURRENT FROM A NANOCOULOMB-CLASS LASER WAKEFIELD ACCELERATION

High peak current and narrow energy spread beams are of vital importance in order to employ the LWFA accelerated bunches as drivers for future light-sources such as X-ray FELs. However, by increasing the charge in the bunch, the associated beam loading becomes significant modifying the accelerating fields, thus alters the final beam parameters.

Indications of beam loading in LWFA have been reported earlier^[164,165]. An extensive investigation for the case of quasi-monoenergetic bunches in a heavily loaded wakefield is demonstrated experimentally by Couperus et al.^[4,5,145]. For this purpose, the amount of charge injected into the bubble cavity was varied in such a way that a narrow energy spread was retained at various plasma densities.

The beam loading effect, superposition of electron bunch self-fields with the plasma wakefield, is theoretically discussed in section 2.6. In this case, an electron bunch with sufficiently high charge can reshape the wakefield structure. The effective accelerating field along the bunch will be modified affecting the beam dynamics and final beam parameters, i.e., transverse dynamics, emittance, final energy, and energy spread.

We first describe relevant experimental parameters for the presented LWFA experiment in section 7.1. Results on accelerated electrons in the bubble regime are presented in section 7.2. Here, we discuss the effect of the beam loading on the final beam charge and bunch duration as well as peak current. In section 7.3 the associated Particle-In-Cell (PIC) simulations to the presented experiment are discussed. Preliminary results regarding the beam divergence and energy spread in dependence of the injected charge are presented in section 7.4.

7.1. EXPERIMENTAL PARAMETERS

In the following the beam loading effect in the bubble regime and its consequence to the final beam quality over a large and well-controlled parameter range is presented. For this purpose, the self-truncated ionization induced injection (STII) is applied.

The injected charge into the bubble is varied by tuning the nitrogen concentration, C_{N_2} , in the background helium gas. By tuning the injected charge at an equal plasma density n_e , the injection volume can be kept equal for various loaded charges. This enables, in contrast to the work in ref.^[165], to decouple the interplay between the beam loading effect and the initial injection volume to the evolution of energy spread and bunch duration. The results presented here are taken from runs, where the electron density in the gas was set to a fixed value of $n_e = 3.8 \times 10^{18} \text{ cm}^{-3}$ resulting to a linear plasma wavelength of $\lambda_p = 17.1 \text{ }\mu\text{m}$, while C_{N_2} was varied between 0.5%, 0.7%, 1.0%, 1.5% and 3.0%.

Varying the nitrogen doping from 0.5 % to 3.0 % allows tuning of the accelerated high energetic peak charge between roughly 100 pC to 300 pC, as will be discussed in more detail in the following section. After the accelerator performance is optimized, experimental parameters, i.e., laser energy, GVD¹, focus position and focus geometry, are kept constant apart from the C_{N_2} .

The target provider for this experiment is a Mach 10.4 supersonic de-Laval nozzle with a 0.35 mm throat and a 3 mm exit diameter^[8], see section 5.1.2.

In addition to the variation of C_{N_2} , the effect of the down-ramp as well as the up-ramp of the spatial gas profile on the accelerated electron bunches is considered. It is done by changing the distance, d_{LN} , between the laser axis and the exit of the nozzle (see figure 7.1a). In general, by increasing d_{LN} , the gradient of down-ramp and up-ramp become more shallow and the maximum plasma density at the plateau decreases. However by adjusting the corresponding backing pressure, p_N , the created electron density can be kept equal to the nominal value $n_e = 3.8 \times 10^{18} \text{ cm}^{-3}$. Thus for setting distances of $d_{LN} = 1.5 \text{ mm}$, 2.5 mm , 3.5 mm the corresponding backing pressures are $p_N = 8 \text{ bar}$, 10 bar and 12.5 bar respectively in order to reproduce the nominal pressure (see figure 7.1b). The achieved down-ramp gradients, $\Delta n_e / L_{\text{downramp}}$, are obtained to be $\Delta n_e / L_{\text{downramp}} = 6.6 \times 10^{18} \text{ cm}^{-3} / \text{mm}$, $4.4 \times 10^{18} \text{ cm}^{-3} / \text{mm}$ and $3.2 \times 10^{18} \text{ cm}^{-3} / \text{mm}$ accordingly. The down-ramp gradients are calculated with respect to electron density at the plateau and at the FWHM as indicated by *dashed lines* and *dotted lines* in figure 7.1b.

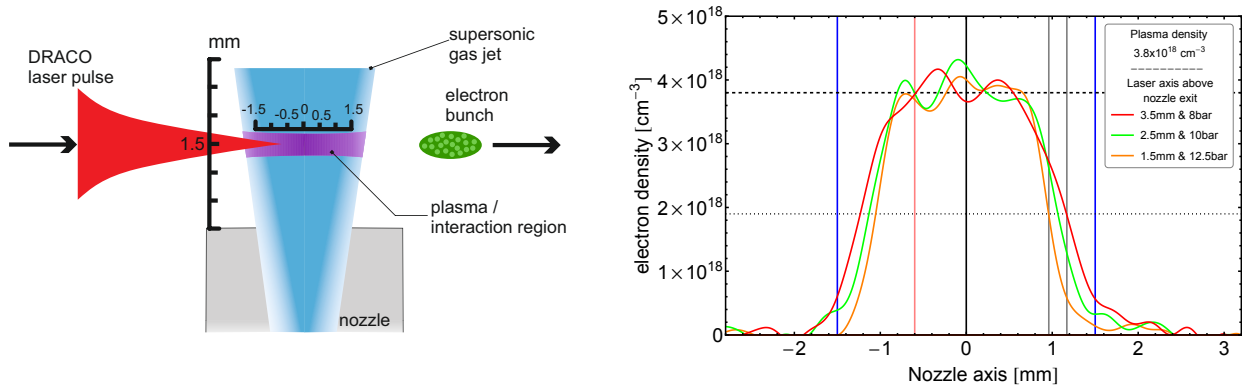
The accelerator parameters for the experiment are shown in figure 7.1. The variation of C_{N_2} requires exchanging the gas mixture reservoir and refilling the associated nozzle pipeline. Due to this time-consuming process but also due to the long term variation of the laser performance, the complete experimental run is split into four consecutive days. The measurement with $C_{N_2} = 0.5 \%$ and 1.5% is performed in a single day while the other dopings are measured each on other day. The laser energy is measured before the final pulse compression stage (see the laser flow chart 5.3) at the beginning of each experimental day. Taking into account the beam line transmission efficiency upon to the nozzle position, the laser energy on target can be precisely determined. We observed a slight variation from 3.7 J to 3.9 J on target between different days. The laser focus profile is also optimized before data is acquired and remained almost unchanged at $\sim 20 \text{ }\mu\text{m}$ within FWHM. It can be reproduced at every experimental day.

The beam quantities are discussed by extracting beam parameters from several data sets, measured under the above mentioned conditions. Note that all of the data presented in the following section 7.2 are extracted from the same measurement data sets. The measurements with $d_{LN} = 1.5 \text{ mm}$ and 2.5 mm are performed at $C_{N_2} = 0.5\%$, 0.7% , 1.0% , 1.5% and 3.0% while with $d_{LN} = 3.5 \text{ mm}$ the data are acquired at $C_{N_2} = 0.5\%$ and 1.0% . Therefore, due to the lack of data points at higher C_{N_2} , a systematic analysis of the beam parameters for this

¹Group Velocity Dispersion [fs²]

d_{LN} can not be carried out accurately. However for completeness the above mentioned two data points also will be incorporated in following figures.

The TR spectrum is measured for each shot in parallel which requires to insert the tape-drive and the TR screen into the electron beam axis. Consequently, the electron energy spectra are acquired with the metallic foils in place. However, Coulomb scattering of the electrons inside the foils can alter the beam parameters. This effect is verified by cross-measurement of certain data sets while the foils are removed from the beam. The latter is discussed for various beam parameters in section 7.4.1.



(a) Schematic of gas jet

(b) Plasma density profiles at different heights

Laser parameters	Plasma parameters
$\lambda_0 = 800 \text{ nm}$	$n_e = 3.8 \times 10^{18} \text{ cm}^{-3}$
$\tau = 30 \text{ fs}$	$\lambda_p = 17.1 \text{ }\mu\text{m}$
$E_0 = 3.6 \text{ J}$	
$P_0 = 120 \text{ TW}$	
$w_0 = 17 \text{ }\mu\text{m}^a$	
$a_0 = 3.4$	

Figure 7.1.: **Experimental parameters.** (a) shows the schematic side-view of the laser focused into the gas-jet. The vacuum focus position is optimized concerning the best performance of the accelerator. Its optimum is found to be at $-0.6 \pm 0.2 \text{ mm}$ with respect to the nozzle center, as indicated in the figure. (b) shows the interferometric measurements of the plasma density profiles at different heights and corresponding backing pressure for the averaged plasma density of $3.8 \times 10^{18} \text{ cm}^{-3}$ over the plateau region. The *vertical blue* lines indicate the geometric dimension of the nozzle exit, *vertical pink* indicates the vacuum focus position and *vertical gray* lines indicate the elongation of the downramp at two different heights. This difference in the downramp length at FWHM of the corresponding densities is obtained to be $\sim 200 \text{ }\mu\text{m}$. The laser and plasma parameters are listed in the table.

^a w_0 is estimated with respect to $1/e^2$ of the peak intensity, given as $w_0 = \text{FWHM}/\sqrt{2 \ln 2}$

7.2. VARIATION OF BUNCH DURATION WITH BEAM CHARGE

The representative results from the longitudinal bunch profile reconstruction presented in the previous chapter 6.3 are selected for the suggested requirements for the reconstruction method from a large number of measurements. The “Foldwrap” reconstruction procedure is sensitive to both the spectral shape of the TR spectrum and the absolute value of its intensity. Pointing jitter and divergence in the electron bunch significantly reduce the intensity of the collected TR radiation and therefore violates the implemented zero-frequency constraint. To recall the functionality of the zero-frequency constraint, it was established in the phase retrieval algorithm in order to normalize the measured electron bunch form factor such that the value of the form factor at $\omega = 0$ can be set to unity.

On the other hand, due to scattering of the electrons inside the tape material and the TR screen as well as the pointing jitter of the electrons, not every electron that emits transition radiation, reaches the LANEX screen of the electron spectrometer. Hence the charge collected by the electron spectrometer possibly remains underestimated. The latter becomes significant if the beam pointing exceeds the acceptance angle of either the electron spectrometer or the TR spectrometer.

Therefore, only a limited number of measurements satisfy all requirements for applying the zero-frequency constraint. However, the spectrum of the electron bunch form factor can be still extracted from the TR spectrum regardless of its absolute values. The latter is investigated on several hundreds of shots, acquired with different C_{N2} at a fixed plasma density of $n_e = 3.8 \times 10^{18} \text{ cm}^{-3}$ to study the behavior of the corresponding bunch profiles as will be presented in section 7.2.3. A comparison of the reconstruction results is presented in section 7.2.1 in order to confirm the reconstruction results obtained by omitting the zero-frequency constraint. Here, the reconstruction results for certain data sets are compared where the measurements fulfilled the requirements for the zero-frequency constraint.

7.2.1. INFLUENCE OF ZERO-FREQUENCY CONSTRAINT ON PRESENT RECONSTRUCTIONS

Tests on synthetic data have shown that for structured electron bunches the unity value at $\omega = 0$ (zero-frequency constraint 6.1.5) in the form factor leads to robust and consistent reconstruction results. Due to this fact and to verify the validity of the reconstruction without the mentioned zero-frequency constraint a comparison between those methods is carried out on a series of TR measurements with the same experimental parameters. The corresponding form factors of the selected shots are normalized according to the mean value of the form factors at the lowest measured frequency, i.e., $\omega_{\min} = 166 \text{ rad THz}$ from the most representative shots. The reconstruction procedure is thus applied to each of the form factors of the mentioned dataset as described in chapter 6. From 10 reconstruction runs 5 reconstructions are thereafter selected and averaged according to the post-selection procedure (see section 6.2.3).

Figure 7.2 shows the comparative reconstruction results obtained from the measurement with various C_{N2} in gas mixture between 0.5 % and 3.0 %. Each dataset consists of between 15 to 25 shots. Comparing the average FWHM from each dataset for certain doping concentrations suggests that the deviation of both methods is at about 1 fs ($\sim 7 \%$) and in most of the cases the FWHM of the bunch obtained by omitting the zero-frequency constraint, is less than the one obtained with the zero-frequency constraint. This addresses the general behavior of the reconstruction algorithm that the reconstructed profile tends to be rather shorter than

the original profile. The latter is demonstrated on single Gaussian sample profiles in table 6.1. However, for the presented experiment, the mentioned deviations are lying within the error margins originating from the shot-to-shot fluctuations.

Hence in order to proceed with the systematic analysis of the bunch profile regarding different experimental parameters such as C_{N_2} and various gas density profiles, the zero-frequency constraint is omitted from the reconstruction algorithm.

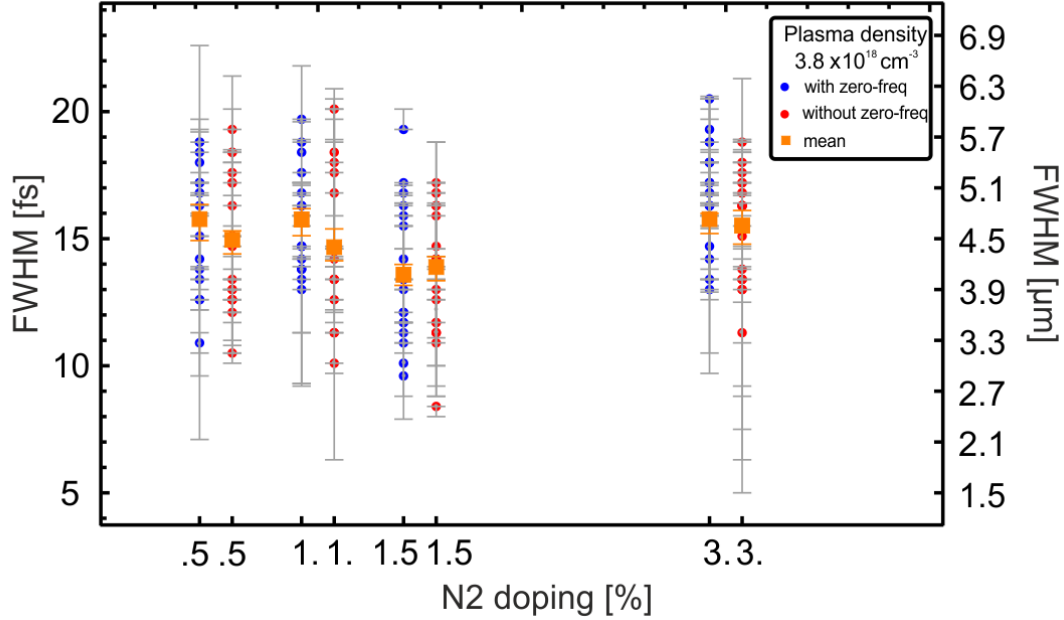


Figure 7.2.: **Influence of the zero-frequency constraint on the bunch profile.** Comparing the reconstruction results and varying the level of doping at the plasma density of $3.8 \times 10^{18} \text{ cm}^{-3}$. The error bars in gray indicate the standard deviation from the mean bunch, obtained from 5 selected reconstructions of the respective shot. The mean FWHM from each data set and its standard error² are marked in orange.

7.2.2. VARIATION OF BUNCH CHARGE WITH NITROGEN DOPING

In this section we carry out more thorough analysis of the accelerated electron bunches while the injected charge into the bubble is varied by tuning the C_{N_2} in the background He jet. Taking advantage of this effort enables to study the effect of the beam loading on the temporal profile of the accelerated bunch while keeping all other parameters constant. The latter is vital in order to avoid any changes in the plasma dynamics before injection, and thus possible changes in the electron bunch profiles regarding the amount of injected charge can address the injection process and acceleration dynamics as will be discussed in the following.

Figure 7.3 shows the accelerated peak charge, Q_{peak} of the high energetic peak in dependence of C_{N_2} . It is visible that the number of injected electrons into the bubble is increasing

²The standard error of the mean sample from repeated measurements $x_i \pm dx_i$ is given as

$$\Delta \bar{x} = \frac{\bar{x} \cdot \Delta(\sum x_i)}{\sum x_i}$$

, where \bar{x} is the mean sample and $\Delta(\sum x_i) = \sqrt{\sum dx_i^2}$.

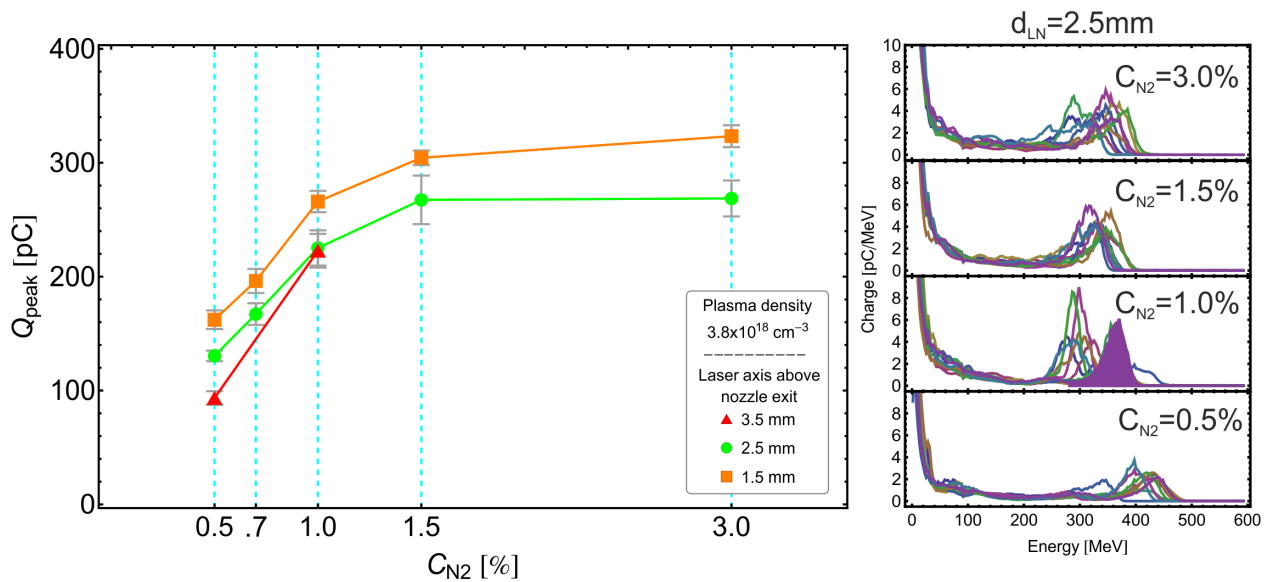


Figure 7.3.: Measured peak charge at the plasma density $3.8 \times 10^{18} \text{ cm}^{-3}$ and with different gas profiles. the graph on the left side shows the charge within the quasi-monoenergetic peak Q_{peak} as a function of the nitrogen concentration C_{N_2} . Data points represent the mean value from a set of shots (sample size between 10 to 25) at equal experimental parameters as in table 7.1. Connected data points show a set of measurements acquired with the same gas profile. The error bars represent the standard error of the sample mean. On the right, the corresponding energy spectra for the data set $d_{\text{LN}} = 2.5 \text{ mm}$ and for 5 typical shots at each data point are shown. The *violet shading* on the panel for $C_{\text{N}_2} = 1.0\%$ indicates the integrated region of a typical spectrum to obtain the corresponding peak charge.

with C_{N_2} , as theoretically predicted. Since once the ionization threshold for STII scheme (see section 2.5) is reached, the available K-shell electrons can be trapped and subsequently become injected into the bubble. Thus the amount of available charge is determined by C_{N_2} . This trend is evident from $C_{\text{N}_2} = 0.5\%$ up to 1.5% , where the charge almost linearly increases with C_{N_2} . Further significant injection by increasing the doping from 1.5% to 3.0% is not observed especially in the peak energy. This trend suggests that the injected charge approaches saturation, which is about 300 pC under these experimental conditions.

Figure 7.4a shows the same charge dependency on the C_{N_2} as in figure 7.3 however it is obtained with regard to the charge within the FWHM Q_{FWHM} . The total measured charge Q_{total} , depicted in figure 7.4b, is obtained by integrating the charge on the measured electron spectra from 1.5 MeV to 600 MeV .

Comparing the measured charge from figure 7.4a at the different gas profiles shows that in general for a sharp down-ramp profile more charge is observed in the quasi-monoenergetic peak (*orange line*). On the contrary, figure 7.4b shows less total charge for the sharp down-ramp which means less background (low energetic) electrons are accelerated, which is of interest for most applications. Thus such low energy background electrons could be attributed from the density down-ramp injection.^[88–92]

7.2.3. ANALYSIS OF PEAK CURRENT

A relevant beam parameter for most of the applications is the peak current I_{peak} . It correlates the amount of accelerated charge to the bunch duration. Although all accelerated electrons

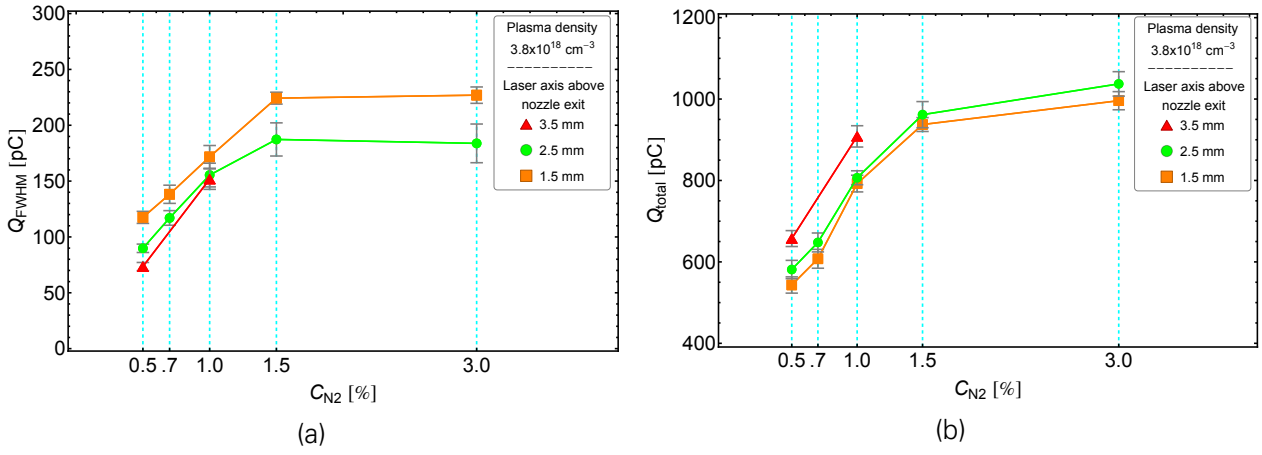


Figure 7.4.: Measured charge at the plasma density $3.8 \times 10^{18} \text{ cm}^{-3}$ and with different gas profiles. (a) shows the charge within the FWHM of the peak energy, Q_{FWHM} , as a function of C_{N_2} , (b) shows the total charge, Q_{total} , integrated from 1.5 to 600 MeV as a function of C_{N_2} . Data points represent the mean value from a set of shot (sample size between 10 to 25) at equal experimental parameters as in table 7.1. Connected data points show a set of measurements acquired with the same gas profile. The error bars represent the standard error of the sample mean.

contribute to the resulting peak current, however, we consider only the electrons within the high energy peak Q_{peak} . The latter provides a direct measurement of the peak current of the quasi-monoenergetic electron bunch. Figure 7.5 presents the results of this analysis.

Considering the data sets for a specific gas profile, the achieved maximum peak current is predominantly determined by the charge. For $d_{LN} = 1.5$ mm, it approaches a peak current as high as 20 kA for a bunch duration of about 14 fs (FWHM).

Figure 7.6 presents results from the reconstructed bunch duration. The bunch duration in terms of FWHM, i.e., τ_{FWHM} , is shown as a function of C_{N_2} in figure 7.6a. The corresponding rms bunch duration is presented in figure 7.6b. From figure 7.6a, it is evident that the FWHM bunch duration depends on both the amounts of injected charge which is tuned by C_{N_2} , and density profile indicated by different colors.

No significant change in τ_{FWHM} is visible for the density profile $d_{LN} = 1.5$ mm. In contrast, the bunch duration for $d_{LN} = 2.5$ is successively reducing with higher doping by 30 % from $\tau_{FWHM} = 16.6$ fs to 12.6 fs. An Interpretation for such differences is still work in progress.

Figure 7.6b shows a reduction in τ_{rms} in both density profiles by 4 % from $C_{N_2} = 0.5$ % to 1.5 %. The quantity τ_{FWHM} is calculated with respect to the maximum charge density of the bunch profile and therefore is rather determined by the substructures within the bunch. The parameter τ_{rms} is obtained from a Gaussian fit on the bunch profile which is insensitive to the mentioned substructures. Thus τ_{rms} corresponds to the global dimension of the bunch. The small change of 4 % in the size of the bunch envelope is not significant indicating an approximately unchanged global boundary of the bunch for a different charge.

To address the FWHM bunch shortening, consider the reconstructed τ_{FWHM} as a function of accelerated charge in the high energy peak, Q_{peak} , presented in figure 7.7. Consider the data set for $d_{LN} = 2.5$ mm, depicted in *green*. Since the point of injection remains unchanged for this data set and the injected charge into the bubble is solely determined by the C_{N_2} , increasing C_{N_2} concentration suggests an injection of a higher amount of charge within a shorter time. Furthermore, from figure 7.3 a saturation in the injected electrons is visible. Hence, it indicates that a higher C_{N_2} not only leads to faster injection but also faster saturation of the bubble volume. The latter leads to an earlier truncation for a higher charge. The amount of charge is not the only relevant parameter for the final bunch duration. The influence of beam loading

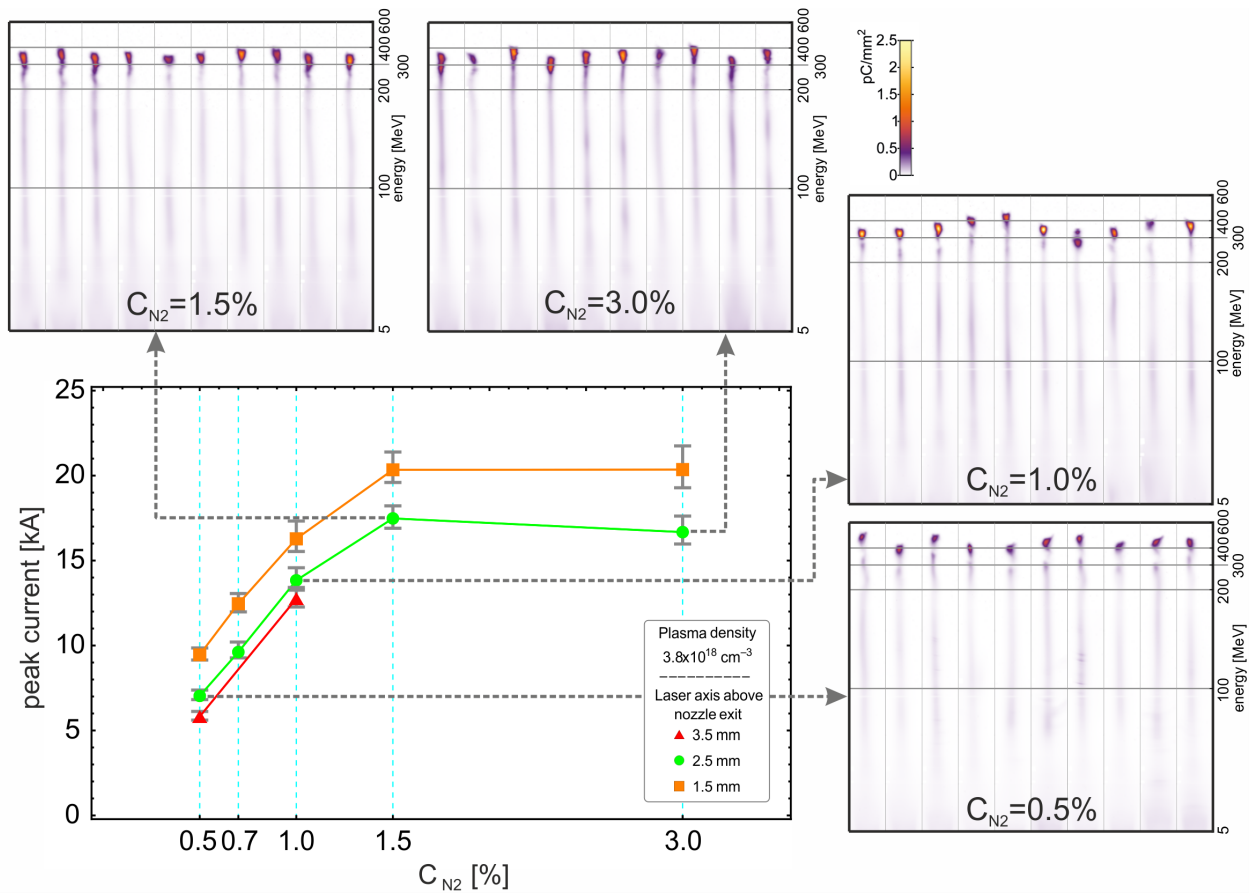


Figure 7.5.: **Analysis of peak current of reconstructed bunch profiles.** The maximum peak current obtained from the reconstructed bunch duration, depicted in figure 7.7, and by taking into account the amount of charge within the peak energy Q_{peak} depicted in figure 7.3. Error bars indicate the standard error of the mean. The panels on the top and right side present the images of the scintillating screen corresponding to the *green* data set as indicated.

on the accelerating field and its consequent effect on the final energy spread can also amend the final bunch duration. However, in the presented results, a direct correlation between the bunch duration and the energy spread is not observed (see also section 7.4.3).

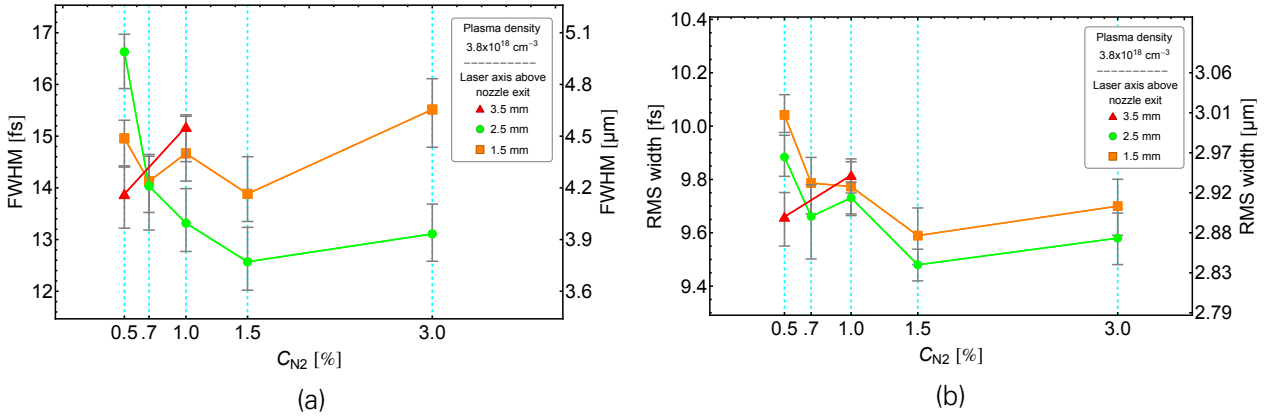


Figure 7.6.: **Analysis of bunch duration in dependency of N₂ doping.** (a) shows the FWHM of bunch profile vs. N₂ concentration for different gas profiles. (b) demonstrate the dependency plot for RMS width of the reconstructed profile obtained from Gaussian fit on sample profiles (see Fig. 6.17a). Error bars indicate the standard error of the mean.

7.3. PARTICLE-IN-CELL SIMULATIONS

In order to gain more insight into the plasma dynamics of the LWFA experiment presented here, an extensive simulation work is conducted using particle-in cell (PIC) code PIconGPU^[166,167] using a 0.2.0 pre-release^[168]. The presented PIC simulations here are set up and performed by Richard Pausch and Alexander Debus using the PIconGPU code on the ZIH cluster. Evaluation and analysis of the simulation results and generating the presented simulation figures are partially performed by the author and Richard Pausch using programming language Python 3 on ZIH cluster.

The simulation box consists of 768x768x2016 cells. The transverse resolution of the box is $\Delta x = \Delta y = \lambda/3 = 265.8$ nm and its longitudinal resolution is $\Delta z = \lambda/18 = 44.3$ nm corresponding to $\Delta t = 148$ as. This spans a total volume of 204.1 μm x 204.1 μm x 89.3 μm according to x, y and z coordinate, where x being the laser polarization axis \vec{E} , y being the laser magnetic field axis \vec{B} and z being the direction of \vec{k} .

The electric and magnetic field calculations are computed by the field solver Yee^[169]. Macroparticles are propagated using the particle pusher by Vay^[170]. The current is computed using the Esirkepov current deposition scheme^[171] with a triangular-shaped density cloud (TSC) interpolation^[172]. The ionization is implemented in the particle-in-cell cycle using the Barrier-suppression ionization (BSI) method^[173].

The simulation is set up as close as possible to the experimental parameters. The laser pulse is modeled with the central wavelength $\lambda = 800$ nm, pulse duration $\tau = 30$ fs and spot size $w_0 = 19$ μm (both FWHM of intensity). This setup leads to a vacuum peak intensity of $a_0 = 2.8$ at the focus. The transverse profile of the laser pulse is also modeled according to the measurements by laser focus diagnostic setup implemented in the LWFA setup. The latter is investigated for both the Gauss-only transverse profile and Gauss-Laguerre profile based on laser focus diagnostic in the experiment. The so-called Laguerre modes of the laser pulse, appearing as outer rings around the Gauss mode, is also included in the simulation.

The plateau region of the gas profile implemented in the simulation is slightly different from the measured profile of the gas jet used in the presented experimental results. It is set to $n_e = 4.4 \times 10^{19}$ cm⁻³ and the nitrogen concentration is set to $C_{N_2} = 1.0$ %.

Figure 7.8 presents the evolution of the laser pulse inside the plasma jet. The laser focus position in vacuum is set at $z = 2.6$ mm, indicated as *dashed lines*. As can be clearly seen, in the

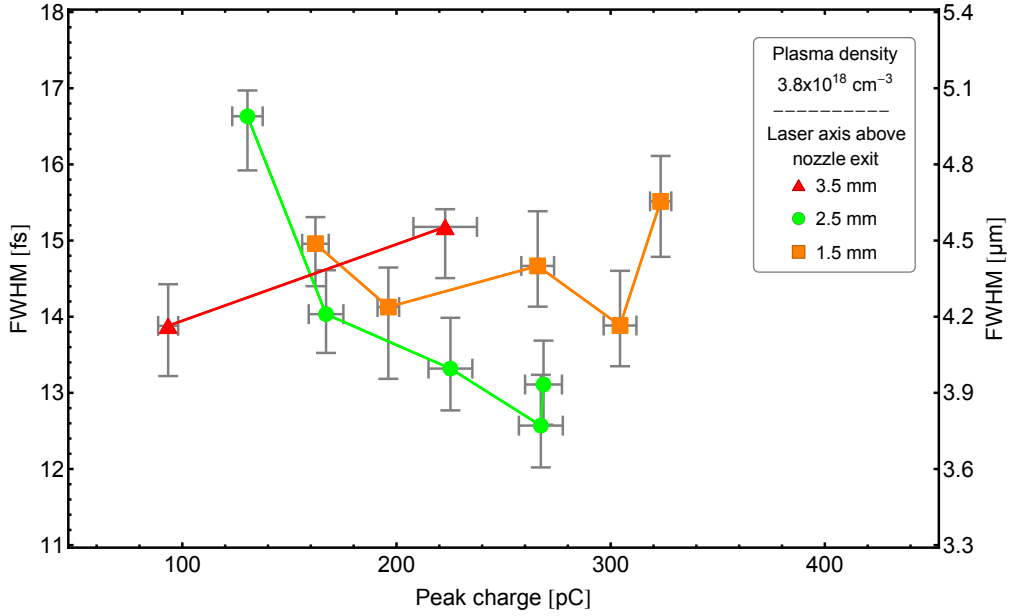


Figure 7.7.: **Analysis of FWHM width of reconstructed bunch profiles.** τ_{FWHM} is depicted as a function of Q_{peak} . Error bars indicate the standard error of mean.

up-ramp region, relativistic self-focusing leads to an early focus of the laser pulse. The beam spot size (FWHM), w_0 , approaches its smallest size at around $z = 1.3$ mm and hence according to the relation $a_0(t) = \frac{q_e}{m_e \omega_0 c} \max[|\vec{E}(\vec{r}, t)|]$, the normalized laser field strength approaches its highest value to $a_0 \approx 6$.

The regime of relativistic self-guiding, indicated as *light blue area*, holds the laser beam waist almost constant over a distance > 1.3 mm which is several times longer than its Rayleigh length. For comparison, the Rayleigh length for a beam waist of ≈ 10 μm is obtained to be $z_R \approx 0.4$ μm . While the plasma density in the down-ramp region decreases, the relativistic focusing effect is therefore mitigated leading to laser diffraction.

Figure 7.9 presents simulation results for energy histogram evolution during the acceleration process and the corresponding longitudinal phase-space diagrams for selected time steps. The upper part of the figure 7.9a presents the energy histogram evolution for k-shell (N^{6+} & N^{7+}) electrons. The energy histogram is acquired during the acceleration process at every 50 time-step. Due to the large size of simulation output data, complete sets of simulation outputs are saved only at every 5000 time-steps corresponding to 220 μm . The output data contain all information about the fields and particle properties, which are used to extract various aspects of the accelerator setup.

The evolution of the laser field strength, a_0 , is recalled from figure 7.8. According to the threshold for ionization of k-shell electrons from nitrogen atoms and connecting these points to the energy histogram, the injection happens already at the end of the up-ramp region of the density profile at $z \approx 0.7$ mm. Following the N^{6+} injection, the N^{7+} electrons are subsequently injected at a distance of $z \approx 0.9$ mm. From this point, while the laser field strength is growing, the injection is stopped, and the trapped electrons into the bubble are accelerated to high energies. An almost constant acceleration gradient is visible over the distance from $z \approx 1$ mm to 2.5 mm. Over this distance, the electrons gain energies up to 400 MeV with an accelerated charge of 108 pC (FWHM) within the peak energy. A significant part of further injection as well as acceleration happens in the down-ramp region indicated by the dashed vertical line at $z \approx 2.3$ mm. In the down-ramp region, due to the decreasing plasma density and consequently increasing the plasma wavelength, electrons are continuously injected into

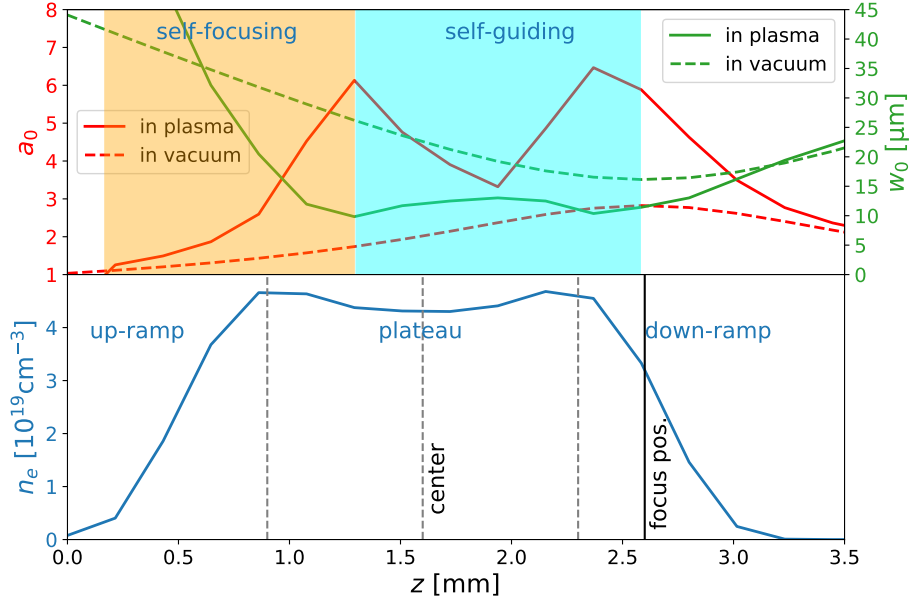


Figure 7.8.: **Laser evolution inside plasma and density profile.** The laser is propagating from left to right. The top half of the figure shows the evolution of the Gauss-Laguerre laser pulse parameters, i.e., peak field strength (*red solid line*) and FWHM spot size (*green solid line*). The corresponding a_0 and w_0 for a Gaussian beam in vacuum are depicted in *dashed lines*. The regions of the relativistic self-focusing and the relativistic self-guiding are highlighted in *brown* and *cyan* respectively. The bottom half of the figure shows the density profile extracted from the PIC simulation. The up-ramp, plateau and down-ramp regions are separated by the *vertical dashed gray lines*. The vacuum focus position is indicated by *vertical black line*.

the bubble leading to a broadband low energy electron spectrum of up to ≈ 100 MeV.

Now, we focus on the high energetic peak of the electron spectrum and discuss the evolution of its longitudinal phase-space inside the plasma.

For this purpose, the longitudinal phase-space histograms of the high energy peak are extracted from the simulation outputs at certain time-steps, indicated by labeled arrows in figure 7.9a. The corresponding phase-space diagrams are depicted in figures 7.9b-7.9f.

Figure 7.9b shows the phase-space diagram during the injection process, here, the electrons are injected within a short time and are energetically spread over a few MeVs. Notable, at this time, the bubble is not completely evacuated from electrons and blow-out regime is not fully attained, as will be demonstrated by electron density plot depicted in figure 7.10b.

At the early stage of the acceleration (figure 7.9c), the electrons which are injected earlier have already gained some energy. The injection continues until the injection truncation occurs due to the violation of the trapping condition (see Eq. (2.15)). The saturation of the injection volume could also stop the further injection. In this manner, the later trapped electrons are subsequently injected behind the early injected electrons and therefore gained less energy. This fact explains the apparent positive longitudinal energy chirp, as indicated by the *green dashed line* in figure 7.9c.

Further acceleration of the electron bunch occurs in the blow-out regime with an almost

linear accelerating electric field (see figure 7.9d and corresponding density plot 7.10d). Here, the electrons that are injected later into the bubble experience a stronger accelerating field than the electrons injected earlier. As a consequence, during the acceleration from time-step (c) to (d), the longitudinal phase space diagram of the electron bunch is rotated such that the resulting energy spread is minimized while the electron bunch length remains constant.

According to figure 7.10d, at this specific time step, the electric wakefield is superimposed by the electrons Coulomb field due to a large amount of load. Hence the electrons along the bunch experience a constant accelerating field independently on their position. This effect is known as the optimal beam loading condition.

Because of the laser beam evolution, the plasma cavity is evolving, changing the accelerating field gradients at each time step. Thus, the optimal beam loading condition is not always fulfilled along the acceleration. The electron bunch longitudinal phase-space, depicted in figure 7.9e, is further rotated such that the electrons located at the tail of the bunch are gained more energy than the electrons at the front. The wakefield is on the one hand affected by the k-shell electrons, which are already accelerated to higher energies, on the other hand, subsequent injections, visible as background electrons in the energy histogram, also alter the wakefield. The corresponding density plot of this time-step is presented in figure 7.10e.

At a further acceleration distance, as in figure 7.9f corresponding to figure 7.10h, due to the down-ramp injection, more electrons are injected into the bubble. This high amount of load, as well as decreasing background electron density in the down-ramp, significantly deform the bubble structure. Consequently, the wakefield is partially overcompensated as can be tracked from figures 7.10f through 7.10h. This field deformation explains the increase of the energy spread by the end of the acceleration mechanism (figure 7.9f).

As the next step in our discussion, we compare the electron bunch duration in simulation to the experimental measurements.

The results from the bunch duration measurements are presented in section 7.2, where bunch profiles for various parameters are considered, i.e., different density profiles and different values of C_{N2} . The global size of the bunch is obtained to be between $\tau_{FWHM} = 12.6$ fs to 16.6 fs corresponding to $3.8 \mu\text{m}$ to $5.0 \mu\text{m}$ respectively. In the presented PIC simulation the bunch length is obtained to be $\approx 4 \mu\text{m}$ FWHM which is in the range of the measurements. This value is estimated from the density plot of nitrogen k-shell electrons at a time-step shortly after the injection is stopped, depicted in figure 7.10d.

At further acceleration length, the electron bunch expands more and more both in the longitudinal and transversal direction. This beam expansion is also observed in the simulations with different initial parameters, e.g., different gas profiles, doping, and vacuum focus position. At the time of writing this thesis, the correctness of this bunch expansion as well as the evidence of sub-structures inside the bunch cannot be quantitatively verified. Due to the limited resolution of the PIC simulation and thus accumulated numerical errors during the field calculation, especially close to its Nyquist frequency, the so-called "numerical Cherenkov radiation" leads to nonphysical radiation in the upstream. This radiation can thus interact with electron bunch and induce artificial modulations in the bunch.

Since this is an accumulating source of error in the resulting bunch structure, only the early stages of the simulation are reliable regarding the bunch dynamic and bunch duration (figure 7.10a - 7.10c).

A prominent periodic sub-structure in the early stage of the acceleration is observed in the simulation (see figures 7.10b and 7.10c). Compared to the measurement, however, the smallest period of the sub-structures is at around half of the central wavelength of the driver laser,

i.e., at 400 nm, which is much shorter than the structure period observed in the experiment. The latter is for a large number of shots between 600 nm to 1 μm (see figure 6.17 and supplementary A.2 for different charge).

A couple of publications predicted via PIC simulations that an interaction between electron bunch and the driver laser within the bubble is possible^[174,175] if the electron bunch and the driver laser overlap over a sufficient distance. According to the presented experimental parameters, i.e., the plasma wavelength ($\lambda_p = 17.1 \mu\text{m}$) and the laser pulse length ($\tau = 30 \text{ fs}$), an interaction between the electron bunch and the driver laser pulse over the acceleration distance ($\sim 2 \text{ mm}$) is unlikely to occur, since their separation is in good condition. This is also supported by the PIConGPU simulations.

In this regard, measurement of the bunch duration at different plasma densities as well as changing the laser pulse duration could verify if an electron-laser interaction is evident. This will be the subject of future investigations.

Regarding the simulation results, the bunch substructures could also originate from the injection process as suggested by Xu et al.^[176]. Since the nitrogen k-shell electrons are successively injected into the bubble as soon as their initial ionization threshold is reached and due to the laser phase-dependent ionization rate and the trapping dynamics within the non-linear wake, the electrons could be discretely injected and therefore mapped to a modulated phase space structure. The injection is continued until the trapping condition is violated or the injection volume is saturated, and no more electron can be injected.

Keeping this in mind, depending on the local laser field strength the ionized electrons can gain different initial momentum leading to a slightly different injection location. Thus, during the injection, the trapped electrons inside the injection volume can be transversally or longitudinally displaced relative to each other. This fact is clearly visible by comparing the figure 7.10b, where the injection is just started to figure 7.10c, where the injection is completed. Here, the length of the electron bunch is increased due to the further injection.

7.4. DISCUSSIONS & OUTLOOK

In this chapter, a detailed analysis of beam parameters from LWFA electron bunches has been carried out. The results have shown that the beam with several hundred pC of charge highly loads such that the final beam parameters are significantly affected by the beam loading effect.

Tuning the nitrogen concentration C_{N_2} enables tuning the injected charge. It is a robust and reproducible method for increasing the charge and hence for studying the influence of the beam loading on the wakefield. Under our experimental conditions, we clearly observed that the amounts of load could be increased almost linearly by a factor of two by increasing the C_{N_2} from 0.5 % to 1.5 %. We showed that further injection into the bubble is not possible for greater C_{N_2} . This hints at saturation of the injection volume that prevents further injections into the bubble.

The focus of this work is on the measuring the longitudinal bunch duration and the corresponding peak current. For this purpose, the bunch duration measurement method, the Foldwrap procedure, is introduced in chapter 6 and is applied to all datasets presented in section 7.1 in order to achieve a detailed analysis of bunch duration for charge and density profile. The results show a systematic decrease of the FWHM bunch length with increasing charge (see figure 7.6). At $C_{N_2} = 1.5 \%$ corresponding to 150 pC a minimum in bunch duration is observed hinting at the influence of the beam loading on the bunch duration evidence.

To address the mechanism behind our findings on the bunch duration measurements as well as gaining more insight into the evolution of the electron bunch inside the plasma, several 3D-PIC simulations are performed via PIConGPU code. An exemplary simulation run is presented in section 7.3. Although the PIC simulations are subject of the numerical uncertainties regarding the detailed fine-structures inside the electron bunch or the attained final energy and charge, they give a good insight into the firstly, evolution of the laser pulse propagating through the plasma and clarification of the relativistic effects occurring in conduction with high power laser pulse and plasma cavity. Secondly, the injection mechanism and injection truncation can be clearly identified and additionally, the evolution of the beam parameters during the acceleration can be tracked. Here, we focused on the evolution of the energy and longitudinal phase-space of the high energy peak presented in figure 7.9.

On the one hand, the evidence of the longitudinal energy chirp and its evolution inside the plasma and on the other hand the measurement results showing femtosecond substructures inside the electron bunch conduct the possibility of a consistent arrangement of the longitudinal substructures in its phase-space. In this manner, each of these substructures could have an ultra-narrow energy bandwidth ($\sim 1\%$) and at the same time exploits sub-fs duration with a peak current of multi 10 kA. Spatial separation of such substructures by employing e.g., energy selective dipole magnets could provide a sub-fs, mono-energetic and high peak current electron bunch as the driver for an X-ray LWFA-FEL.

Since the bunch profile reconstruction via TR spectral measurement cannot account for the energy chirp and the currently used electron spectrometer does not have a sufficient resolution for energies around the peak charge, a dedicated high-resolution electron spectrometer, as well as more precise simulation runs, are needed to quantify the correlation between the sub-structures and their individual energy bandwidth.

7.4.1. INFLUENCE OF METALLIC FOILS ON ELECTRON BUNCH QUALITY

The diagnostic of the LWFA accelerated electron bunches presented in the previous sections are acquired with the tape-drive and the TR screen in the beam. Due to the scattering the electrons inside the metallic material, the properties of the electrons i.e., charge, energy, and energy spread as well as divergence can be altered. In the following, these effects are pointed out by comparing the data sets without the foils on the beam path.

Figure 7.11 demonstrates this comparison. The accelerated electrons cover a large energy range from a few MeVs up to several hundreds of MeVs. Absorption and scattering of the electron inside the materials is energy dependent. In order to verify this fact, two comparisons are performed. Figure 7.11a shows the total charge dependency while in figure 7.11b only the charge within FWHM of the high energy peak is considered. Comparing 7.11a and 7.11b indicates that the low energy electrons are more affected by the laser blocker/TR screen. While the total charge reduced by down to 200 pC ($\sim 20\%$) with the foil configuration, the charge within the FWHM is altered statistically only around $\pm 10\%$. This behavior is expected since the higher the energy of particles the lower is the interaction with metallic materials.

Next, energy spread and divergence of the high energy peak is presented in 7.11c and 7.11d respectively. Increasing the energy spread due to the effect of TR screens in most of the C_{N2} remains a few percents. In contrast, the divergence is increased by about 1 mrad ($\sim 20\%$). In summary, the final beam parameters within the peak energy such as peak charge and energy spread are not much degraded while the divergence is significantly worse.

7.4.2. QUASI-MONOENERGETIC AND HIGH ENERGY ELECTRON BEAM

The Peak energy E_{peak} is presented as a function of the charge within FWHM of the peak Q_{FWHM} in figure 7.12. Considering data sets for a specific gas profile, E_{peak} decreases by increasing the Q_{FWHM} . This energy reduction is attributed to the accelerating field suppression of the wakefield due to the loading since the injection dynamics, i.e., the position and volume of injection does not change. This behavior was also observed by Couperus et al.^[4] by investigation of the beam loading effect under comparable experimental conditions to the presented experiment.

Comparing two data sets measured at different gas profile i.e., *orange and green* markers in figure 7.12) shows that the flattening of gas profile ramps leads to an increase in attained energy. To address this fact, considering the expansion of the gas profile with respect to the center of the nozzle leads to an earlier relativistic self-focusing and therefore an earlier injection. Additionally, the created plasma channel is extended due to the lengthening of down-ramp which supports a longer acceleration length and hence higher electron energies.

7.4.3. ANALYSIS OF ABSOLUTE AND RELATIVE ENERGY SPREAD

As discussed in section 2.6, beam loading deforms the wakefield such that the accelerating field strength experienced by the trailing electrons is reduced. Under the optimum loading condition, a beam with a narrow energy spread is expected since the majority of the injected electrons experience the same accelerating field. This fact is demonstrated in figure 7.13. In Figure 7.13a the absolute energy spread ΔE is presented as a function of Q_{FWHM} . An optimum load is clearly seen only in the case of $d_{\text{LN}} = 2.5 \text{ mm}$ & $p_{\text{N}} = 10 \text{ bar}$, which is attained with $C_{\text{N}_2} = 1.0 \%$ at $Q_{\text{FWHM}} = 150 \text{ pC}$. A deviation from this charge leads to an increase in the energy spread. This behavior is in line with the physics of beam loading. When an overloaded electron bunch overshoots the condition for the constant accelerating field, this induces a negative energy chirp in the bunch. In the case of $d_{\text{LN}} = 1.5 \text{ mm}$ & $p_{\text{N}} = 8 \text{ bar}$, the absolute energy spread continuously decreases with higher charge and no minimum is evident. The latter is because of the interplay between the maximum achieved energy and the induced energy spread in the bunch. To decouple the energy spread from E_{peak} , the relative energy spread is calculated as a function of Q_{FWHM} as presented in figure 7.13b. Here, a minimum in the relative energy spread is visible in both cases at around 150 pC.

This indicates the correlation between the amount of the necessary charge to reach the optimum beam loading and plasma dynamic which is comprised by the driver laser.

In fact, the laser evolution in plasma, which is affected by the up-ramp can alter the cavity and the associated wakefield. Thus, the point of injection is changed for different gas profiles leading different initial beam parameters. On the other hand, the beam parameters can also be influenced during further injection and acceleration in the down-ramp.

7.4.4. ANALYSIS OF GEOMETRICAL AND NORMALIZED DIVERGENCE

In order to study the transverse momentum distribution of the electron beams, normalized divergence $\gamma \cdot \psi$ and geometrical divergence ψ are extracted from the acquired data sets and presented in figures 7.14a and 7.14b respectively. For ψ the detected electrons within the FWHM of the peak energy Q_{FWHM} is accounted. Divergence ψ is obtained from Gaussian fitting on the transversal extension of Q_{FWHM} of the corresponding energy spectrum and is given in terms of root-mean-square (rms). The normalized divergence is obtained by multiplying the geometrical divergence by the corresponding γ , where $\gamma = E_{\text{peak}} \text{ MeV} / 0.511$ is the Lorentz factor of the corresponding E_{peak} . Notably, since the electron spectrometer deflects

the electron beam onto a charge sensitive LANEX screen (see section 5.1.3), all transversal dimensions of the bunch are projected onto the LANEX screen. Hence, ψ is a measure of the average of divergence over all transversal directions.

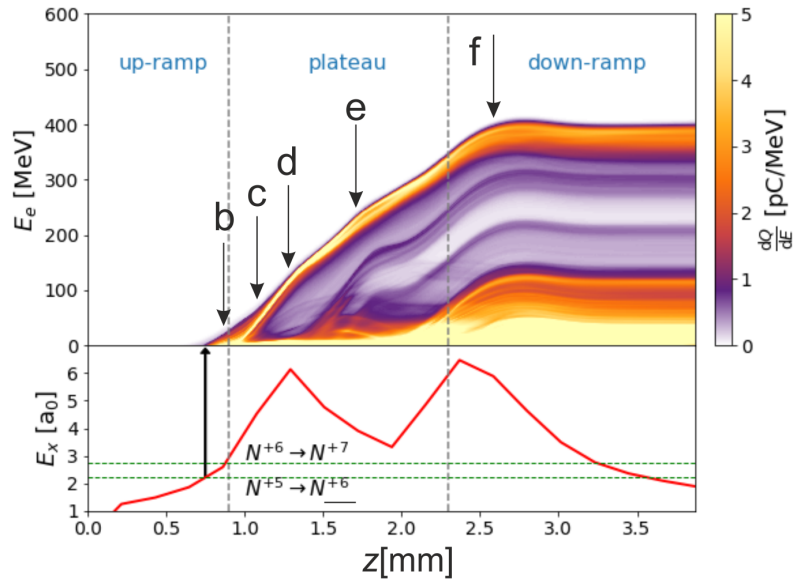
The normalized divergence shows a similar behavior as the energy spread, presented in figure 7.13a. Only the *green* data set shows a minimum attained with $C_{N2} = 1.0\%$. A minimum in geometrical divergence is present in both data sets at a charge of about 150 pC, which coincides with the minimum of the energy spread.

Varying the gas profile also influences the transverse dynamic of the electron bunch. In particular, it is expected that a low gradient of the gas density in the down-ramp leads to an elongation of the betatron oscillation and a decrease in its amplitude at the exit of the nozzle. Consequently, the transverse momentum of the electrons will be suppressed by this change in the density. This will reduce the geometrical divergence as the electron bunch exits the plasma. The data sets for $d_{LN} = 3.5$ mm and 1.5 mm in figure 7.14b correspond to two extremes in the down-ramp gradients for low and high plasma gradient respectively. A reduction in ψ of 10 % is visible in this case. However the measurements at $d_{LN} = 1.5$ mm and 2.5 mm exhibit no general decrease in divergence.

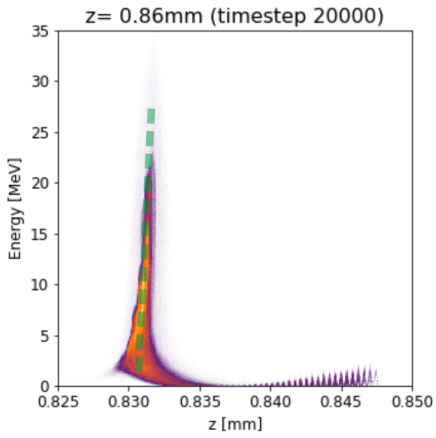
Figure 7.14a presents the correlation of the geometrical divergence with the kinetic energy of the main peak, obtained by calculating $\gamma \cdot \psi$ as a function of Q_{FWHM} . Here the measurement with a greater d_{LN} shows in general a larger $\gamma \cdot \psi$. This indicates, in contrast, to figure 7.14b, that the gain in energy for larger d_{LN} is the dominant parameter in the final beam divergence compared to the shape of the down-ramp.

Considering the data sets for $d_{LN} = 2.5$ mm, the $\gamma \cdot \psi$ decreases by 23 % by increasing the injected charge from $Q_{FWHM} = 90$ pC to 150 pC corresponding to $C_{N2} = 0.5\%$ to 1.0 % accordingly. A higher amount of charge leads to an increase in $\gamma \cdot \psi$. In contrast, the data set for $d_{LN} = 1.5$ mm exhibits a continuously decreasing normalized divergence by 23 % as well while the charge increases from $Q_{FWHM} = 117$ pC to 225 pC.

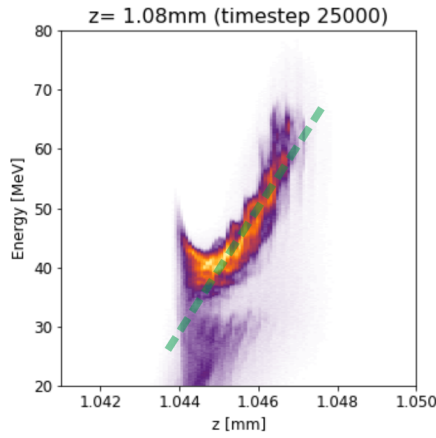
For analysis of the beam divergence without the TR foils in the beam we refer to section 7.4.1.



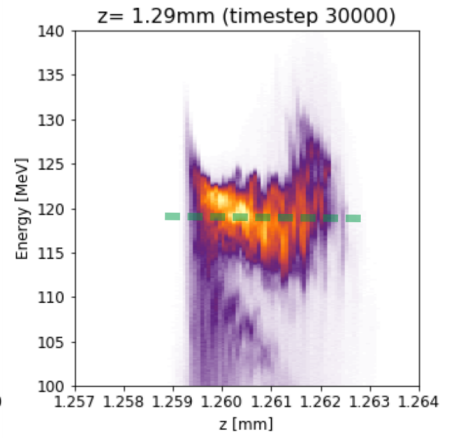
(a)



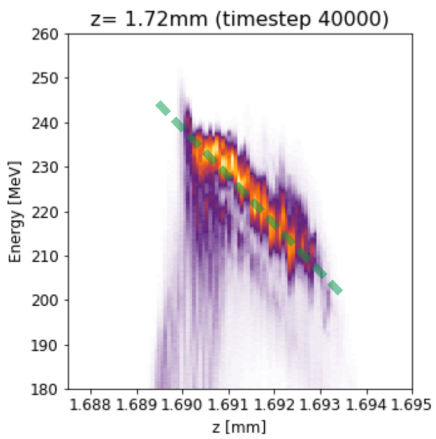
(b)



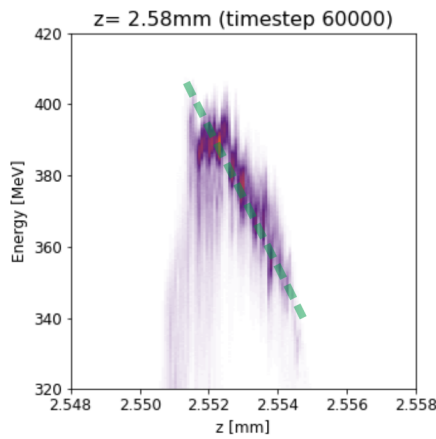
(c)



(d)



(e)



(f)

Figure 7.9.: **Electron energy evolution and longitudinal phase-space evolution.** The upper half of (a) shows the energy evolution of k-shell electrons as a function of the simulation position along the laser propagation axis. The lower half of (a) shows the corresponding laser field strength a_0 , recalled from figure 7.8. (b) through (f) show longitudinal phase-space of the high energy electrons, extracted from simulation outputs at certain time-steps (marked on (a) by arrows). The sub-figures (b)-(f) share the same color bar depicted on bottom right of the figure. z steps are calculated according to the laser peak position in the bubble.

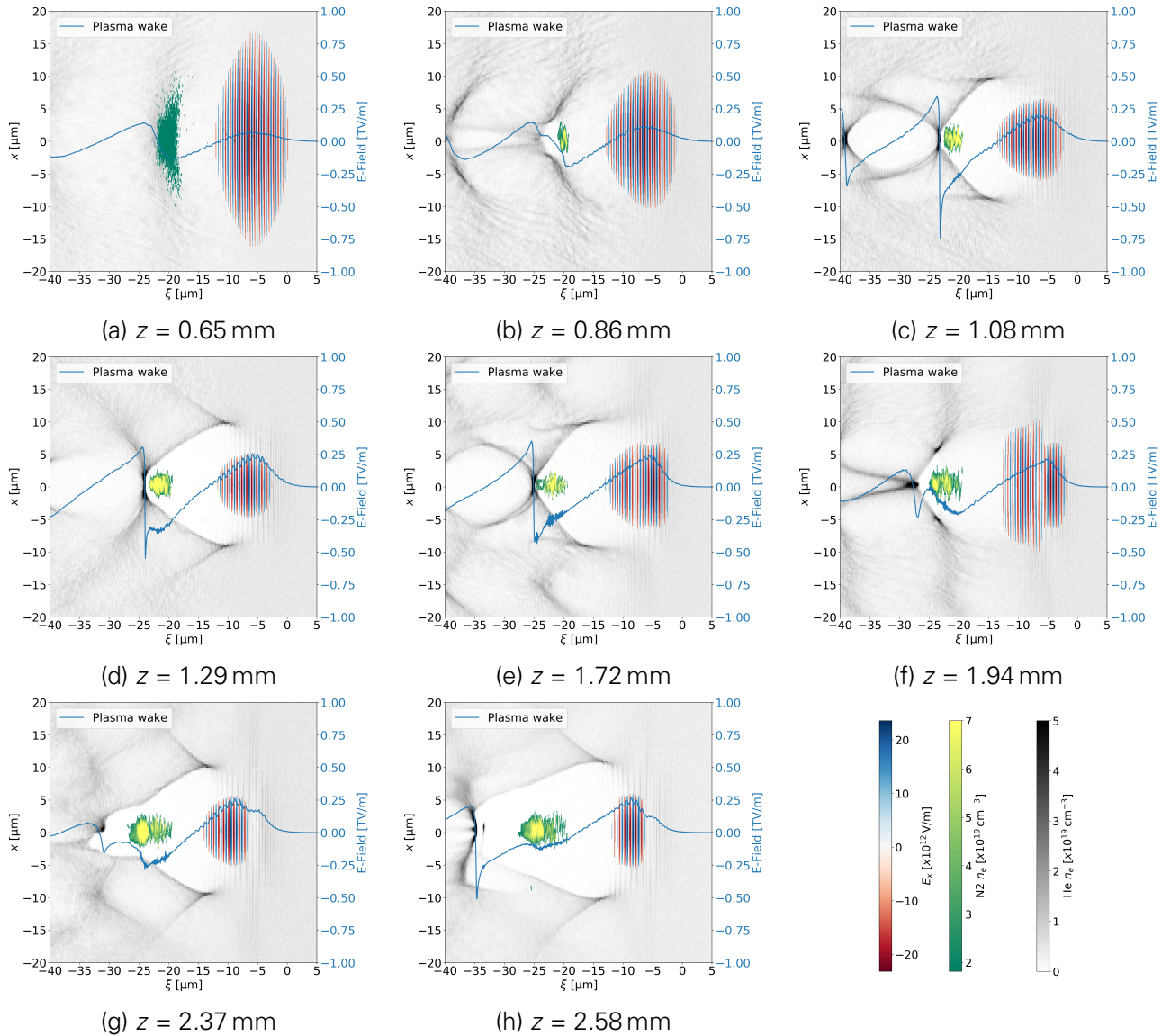


Figure 7.10.: Snap-shot of bubble structure for different acceleration length z , extracted from 3D PIC simulation. The figures show sliced plane of the simulation box through the middle of the bubble in polarization direction x as a function of the longitudinal coordinate in the moving-frame of laser $\xi = z - c \cdot t$. Shown are the electric field of the laser pulse (E_x color bar), the k-shell electrons from nitrogen atoms ($N_2 n_e$ color bar) and background electrons from He and L-shell N_2 atoms ($He n_e$ color bar). The longitudinal wakefield E_{Field} is calculated on axis and depicted in *solid blue line*. The laser field is truncated to FWHM of its field maximum. The electron densities are truncated with respect to $1/e^2$ of the corresponding maximum density. All the sub-figures share the same color bars depicted on the bottom right of the figure.

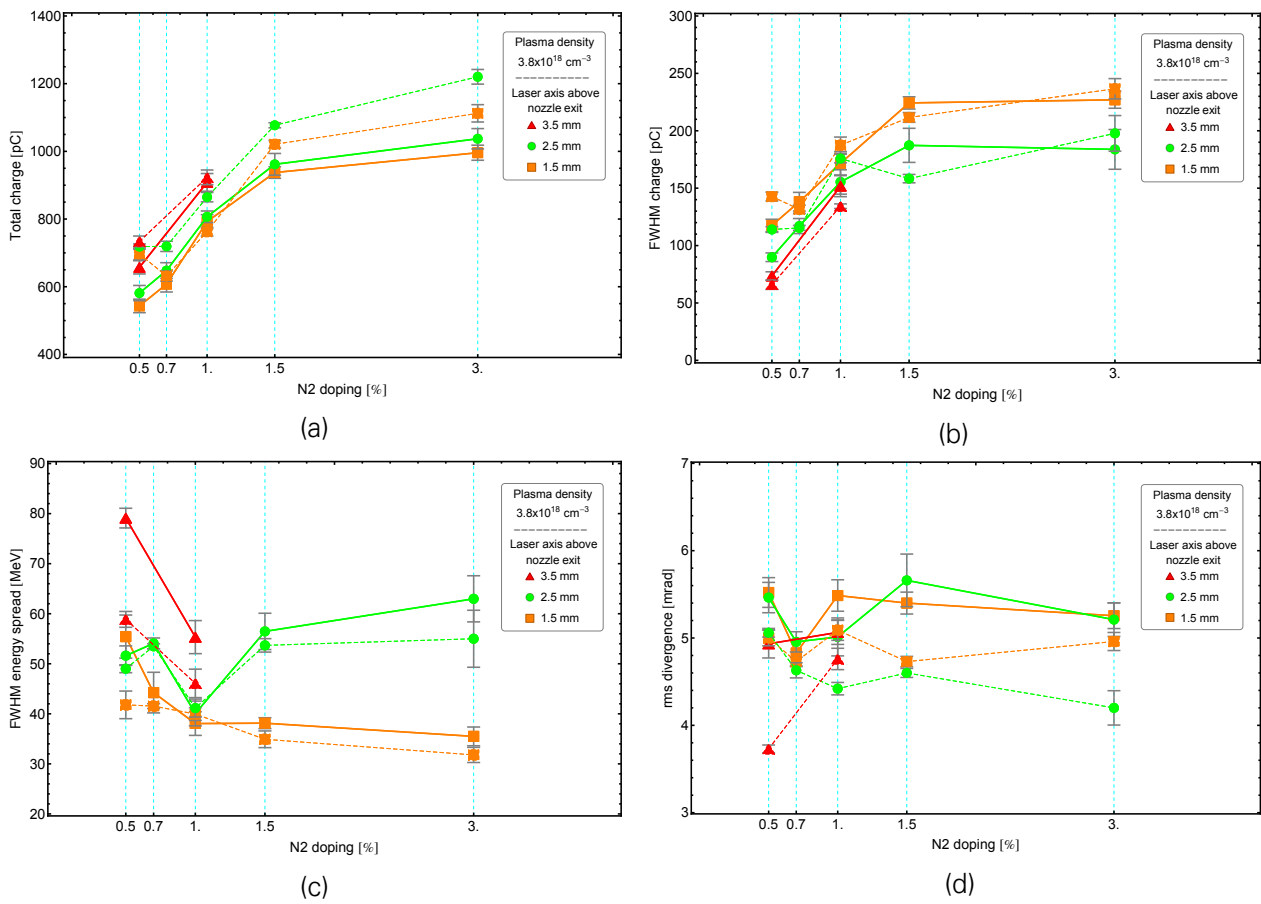


Figure 7.11.: Influence of the TR screen on the beam parameters. Data sets are acquired with and without laser blocker/TR screen, depicted with *solid* and *dashed* lines respectively.

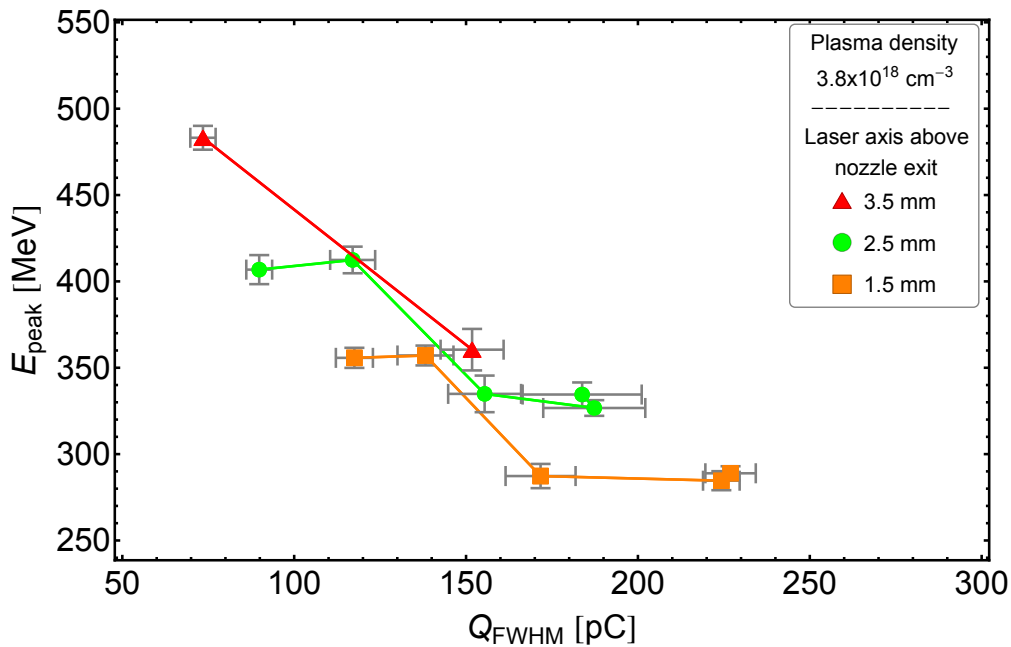


Figure 7.12.: Statistics for peak energy E_{peak} as a function of Q_{FWHM} . E_{peak} denotes the mean peak energy and is obtained from the charge within the FWHM of the peak. The error bars indicate the standard error of the mean. The same data sets are used as in figure 7.4

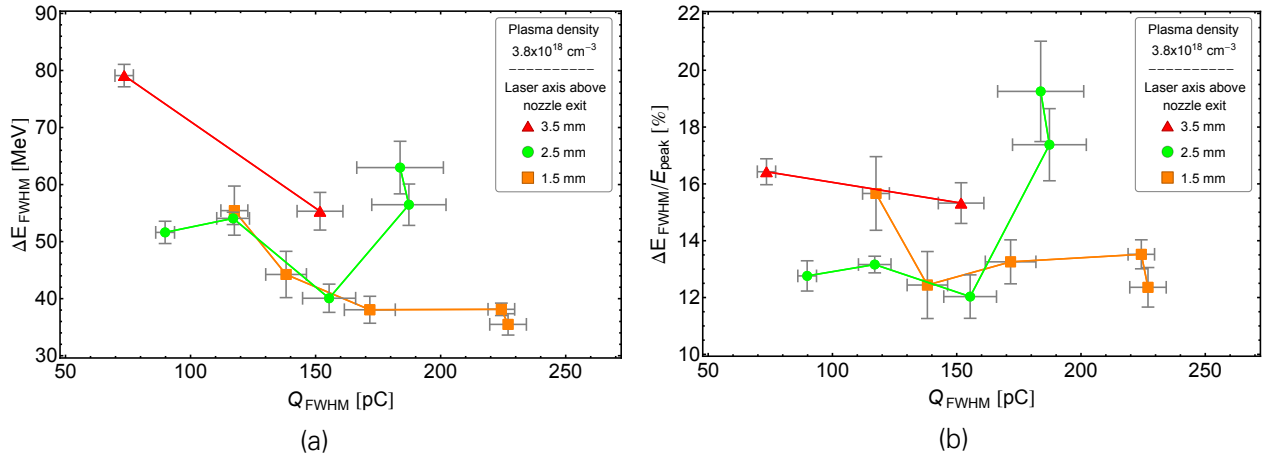


Figure 7.13.: **Statistics for the absolute and relative energy spread.** (a) shows the absolute energy spread of the bunch FWHM, ΔE_{FWHM} , as a function of Q_{FWHM} . (b) shows the corresponding relative energy spread. The same data sets are used as in figure 7.4

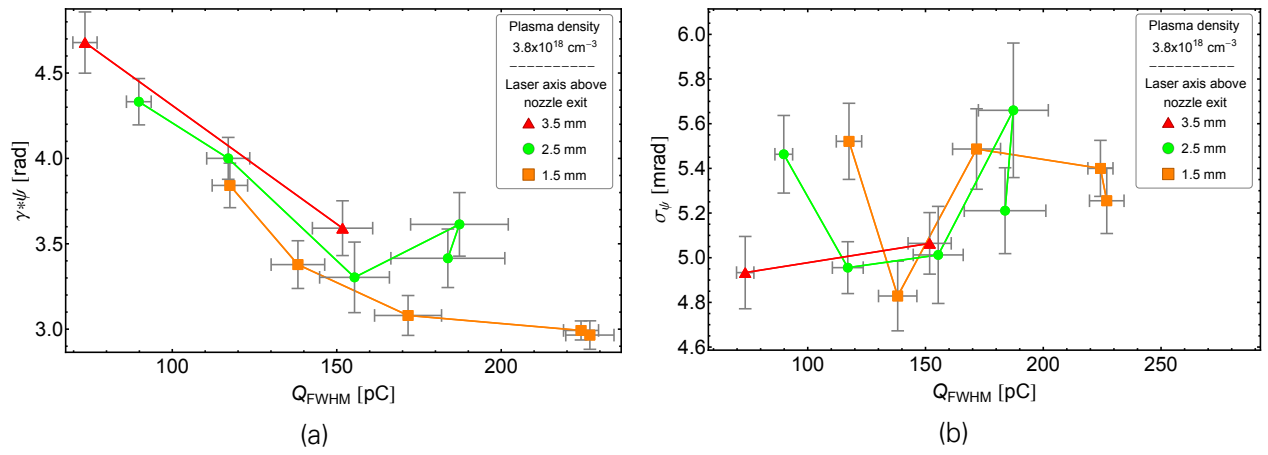


Figure 7.14.: **Statistics for the normalized divergence and rms divergence.** (a) shows $\gamma \cdot \psi$ as a function of Q_{FWHM} . ψ is calculated in terms of rms of the peak energy. (b) shows rms ψ of the peak energy as a function of Q_{FWHM} . The same data sets are used as in figure 7.4

8. SUMMARY & OUTLOOK

In the presented thesis, for the first time, the ultra-short substructures within the longitudinal electron bunch from LWFA accelerator are measured in single-shot. For this measurement forward transition radiation is used. It is emitted from the surface of a $5\ \mu\text{m}$ steel foil when the electron bunch traverses its metal-vacuum boundary.

In order to measure a significant range of the emitted TR, an ultra-broadband, modular spectrometer is designed and commissioned^[3]. Combining three dedicated detection systems enables to measure the spectrum of TR in the range from 250 nm to $11.35\ \mu\text{m}$ (5.5 optical octaves) in single-shot. A detailed wavelength calibration, a relative response calibration as well as an absolute photometric calibration procedure are performed for each spectrometer arm and with respect to s- and p-polarization. The calibration is done by using an ensemble of calibration light sources.

Each of the spectrometer arms can be independently operated allowing more flexibility in the measuring broadband spectra. The modular feature of the spectrometer facilitates a straightforward extension of its spectral bandwidth towards THz (far-IR), e.g., by employing a further similar prism-based spectrometer to the existing MIR arm. This is advantageous especially for characterizing the electron bunches beyond a few 10 fs duration, which is of great interest for many linear accelerator facilities. The scalability of this spectrometer enables measuring of high intensity modulated spectra up to 8 orders of magnitude over a broadband of spectrum at a single shot.

Besides bunch length determination, the TR spectrometer can also be used for measurement of plasma radiation emission in LWFA. The spectrally resolved plasma radiation can provide essential insights into the plasma dynamics which can nowadays only be gained via large-scale Particle-In-Cell (PIC) radiation simulations^[177,178].

The “Foldwrap” procedure for the reconstruction of structured electron bunches generated from LWFA accelerators via broadband TR measurements is investigated^[2]. It is employed to retrieve the phase of the electron bunch form factor in the frequency domain. From there, the longitudinal electron bunch profile is calculated.

The algorithm is tested on synthetically generated model distributions. The presented phase retrieval algorithm delivers promising results which reflect the most relevant features of the electron bunch within a reasonable error margin.

The reconstruction of the long tail of an electron bunch is previously reported to be very challenging. By applying additional zero-frequency and odd-phase constraint, the reconstruction

algorithm could be significantly improved enabling to deal with the reconstruction of fs-scale modulations saddled on tens of fs long pedestal distributions. Here, Gaussian model bunches up to $\sigma = 16$ fs (RMS width) could be accurately reconstructed. It is shown, that even if the maximum measured wavelength is smaller than the quantity $2\pi\sigma_z$, it is possible to perform appropriate reconstruction results if the TR spectrometer is absolutely calibrated and the electron spectrometer is charge calibrated.

The post-selection algorithm combined with the Kramers-Kronig (KK) method is useful in particular due to the presence of two timescales. While the global bunch dimension can be reproducibly retrieved using the iterative method, the bunch modulations can be reasonably recovered by the KK method.

Systematic analysis of bunch duration as well as analyzing various beam parameters such as charge, energy, energy spread, and divergence are performed. For this analysis, several hundred shots are evaluated for a wide range of experimental parameters. The focus of this treatment is the variation of the beam parameters with respect to the amount of injected charge, i.e., tuning the nitrogen concentration and applying different gas density profiles.

It is shown that the amount of injected charge into the bubble can be tuned by varying the nitrogen concentration^[4,5]. However, the injected charge can alter the accelerating field leading to the beam loading effects. The beam loading will not only affect the beam parameters such as the energy, energy spread, and divergence but also leads to the saturation of the injected charge. Therefore, depending on the applied plasma density, the injected charge is limited.

Results on the bunch reconstruction suggest bunch durations between 13 to 16.6 fs (FWHM) from the presented LWFA experiment. In conduction to the measured bunch duration, the saturation of injection is also the predominant parameter in the highest reachable peak current, here electron bunches with $Q_{\text{FWHM}} \approx 250$ pC are accelerated to energies up to $E_{\text{peak}} \approx 300$ MeV with a relative energy spread of $\Delta E/E_{\text{peak}} \approx 12$ % and a divergence of $\sigma_\psi \approx 5$ mrad as well as a bunch duration of $\tau_{\text{FWHM}} \approx 14$ fs resulting to a peak current of as high as $I_{\text{peak}} \approx 20$ kA.

While the STII injection scheme provides a highly reproducible and robust acceleration mechanism, measuring the bunch profile has shown that these bunches are highly modulated. Taking advantage of the 3D PIC simulation enables a more profound understanding of the correlation between the bunch profile and the existing longitudinal energy chirp inside the electron bunch. This work demonstrates experimentally, for the first time, the existence of the ultra-short sub-femtosecond substructures. First indications on possible correlations between the sub-structures and the injection mechanism is pursued by several complementary 3D PIC simulations.

The simulations assist the understanding of relevant effects within the LWFA process which are crucial to the final beam parameters. The formation of the periodic sub-structures during the injection mechanism could be qualitatively conducted. The electrons are successively injected into the bubble leading to the formation of longitudinal bunch lengths of about $4 \mu\text{m}$ (FWHM). This bunch duration is in line with the presented experimental bunch duration measurement.

Besides, the emergence of the longitudinal energy chirp during the acceleration process suggests that these substructures could have an ultra-narrow energy bandwidth (~ 1 %) and at the same time exploit sub-fs duration with a peak current of multi 10 kA. Spatial separation of such substructures by employing e.g., energy selective dipole magnets could provide an unprecedented sub-fs, mono-energetic and high peak current electron bunch enabling the driver for an X-ray LWFA-FEL.

In order to gain more insight into the transversal bunch distribution, a dedicated coherent

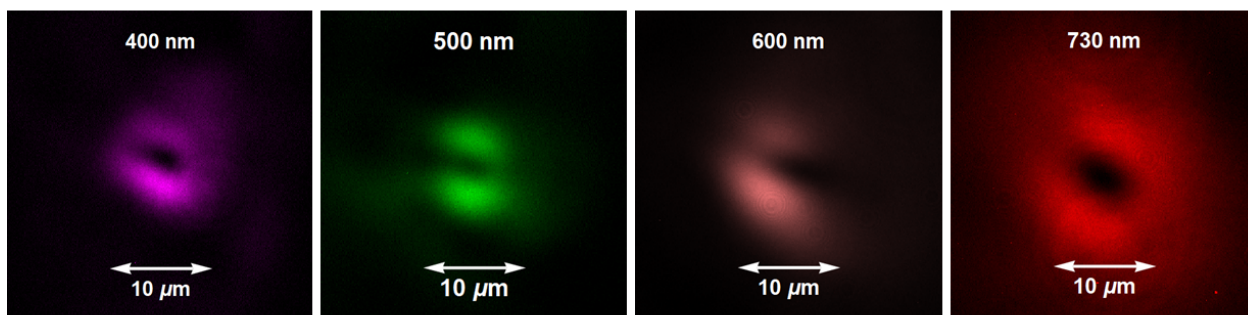


Figure 8.1.: CTR point spread function measurement. Courtesy of M. LaBerge

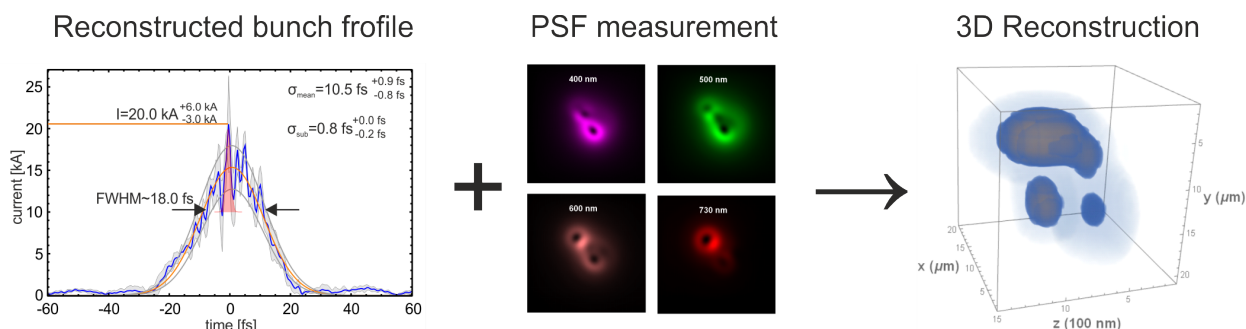


Figure 8.2.: Schematic of 3D bunch reconstruction.

optical transition radiation (COTR) beam profile measurement is investigated in the framework of the Ph.D. thesis of Maxwell LaBerge, who is, at the time of writing this thesis, extensively investigating this approach. For this experiment, a motorized wheel is placed right at the exit of the nozzle. The front surface of the wheel provides an aluminum foil which reflects the laser beam into a beam dump. Its back surface provides a thin aluminized capton foil and is placed ~ 1 mm from the exit of the gas jet. It acts as the CTR radiator. A thin aluminized silicon wafer redirects the CTR beam from the electron beam axis into a high-quality objective. A dedicated imaging system consisting of the high-resolution objective and several CCD cameras is set up to image the surface of the CTR source enabling to obtain the point spread function (PSF) of the electron bunch. The CTR beam is split many times in order to realize the simultaneous imaging for different wavelength and polarization.

Figure 8.1 presents preliminary results from the PSF measurement. The PSF of an electron bunch could be simultaneously measured in four different wavelengths. By analyzing this measurement, the transverse distribution of the bunch can be calculated. This approach is a precise beam size measurement method with sub-micrometer resolution.

Combination of the mentioned method with the bunch duration measurement presented in this thesis could enable full a 3D reconstruction of the electron bunch distribution. Figure 8.2 demonstrate the schematic of this treatment. The ongoing effort will be of great importance for all future applications of the electron beam that require a well understanding of the beam structure such as SASE-FEL light source.

Another improvement on the presented bunch duration diagnostic is to partially provide the spectral phase of the TR spectrum from an independent channel. A few-cycle probe laser beam is recently investigated by S. Schöbel^[179] in her M.Sc. thesis at HZDR. The setup is able to generate ultra-short laser pulses down to 6 fs. The spectral phase of this probe beam poses a stable and reproducible shape in the range of its spectral bandwidth, i.e., roughly from

700 nm to 900 nm. This beam can be coupled into the TR beam line and provides a reference phase spectrum. Convolution of this reference spectrum with the one from the TR allows to determine the spectral phase of the TR spectrum fractionally. This additional information provides a vital phase constraint in the phase retrieval algorithm resulting in a more robust and unique bunch reconstruction.

The bunch reconstruction methods based on TR measurement allows to measure the bunch profile outside the plasma. However, information about the bunch size inside the plasma and its evolution during the acceleration process has also a high impact to characterize, e.g., the corresponding betatron source and to gain insight into the plasma dynamic.

Measuring the betatron radiation spectrum allows to precisely determine the beam size inside the plasma. This radiation is emitted during the acceleration process. Due to the strong focusing fields inside the plasma cavity, the electrons oscillate around the propagation axis and thus emit radiation, typically in the soft X-ray range with energies of a few keV. Since the betatron oscillations and thus the emitted X-ray spectrum are related to the source of the radiation, measuring this spectrum enables to determine the source size and its trajectory inside the plasma cavity^[108–110,180]. This approach is extensively investigated in the Ph.D. thesis of Alexander Köhler for source size characterization of the LWFA experiment presented here^[9].

Besides the ongoing 3D bunch reconstruction, the combination of the betatron radiation diagnostic and the bunch diagnostic via TR spectrum and PSF function measurement results in an ultimate bunch diagnostic, which enables to diagnose the electron bunch evolution from the point of injection upon to the TR screen on a single shot basis. Simultaneous measurement of TR spectrum, PSF function, and betatron spectrum requires, however, an enormous technical effort and will be the topic of future diagnostics development.

A. SUPPLEMENTARY FIGURES

A.1. TRANSITION RADIATION SPECTRA

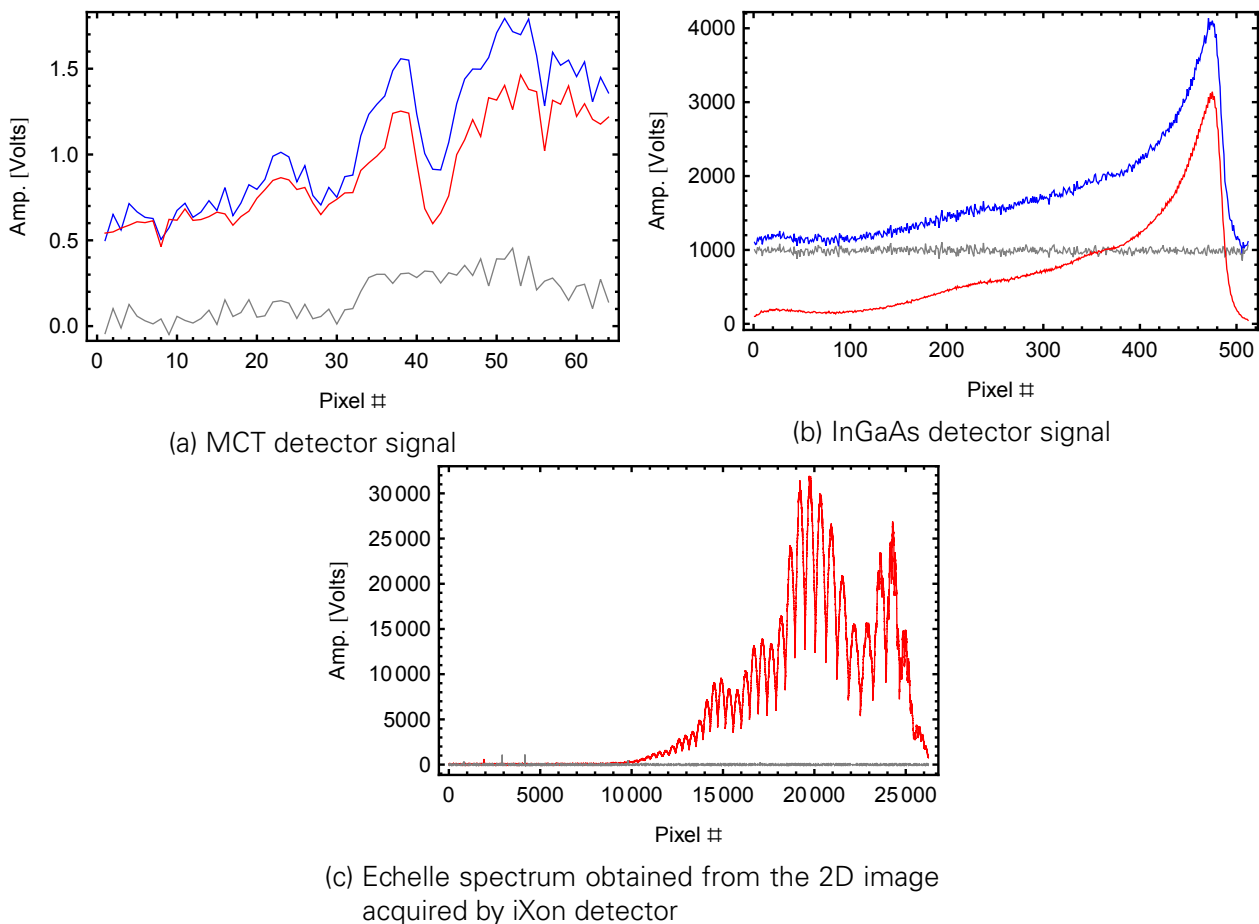
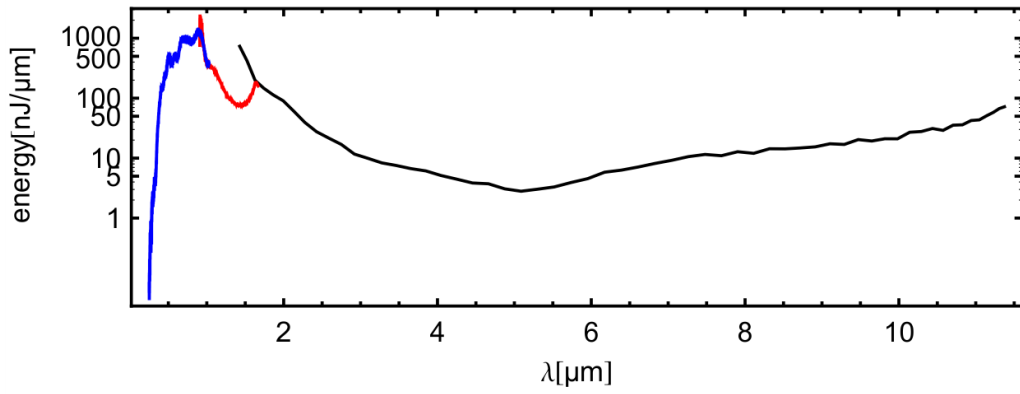
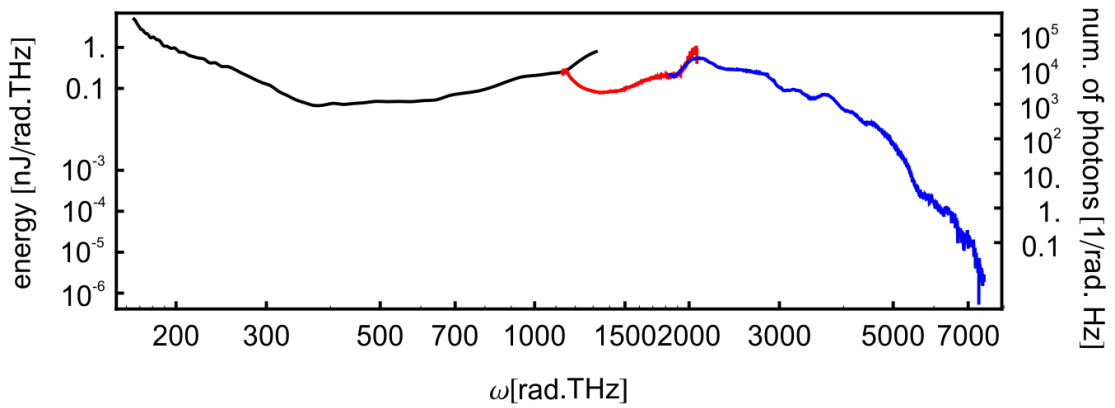


Figure A.1.: Supplementary to figure 6.13. The single-shot signals acquired by detectors MCT, InGaAs and Echelle spectrometer are shown in (a), (b) and (c) respectively for the exemplary shot 396, which were analyzed in detail in subsection 6.3.2. The raw signal, background signals and background-corrected signals are presented in blue, gray and red accordingly.



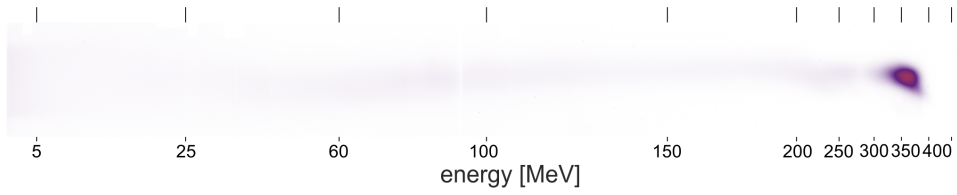
(a) Extended TR spectrum by splicing the partial spectra from UV-VIS, near-IR and mid-IR regions of spectrum in units of nJ per μm .



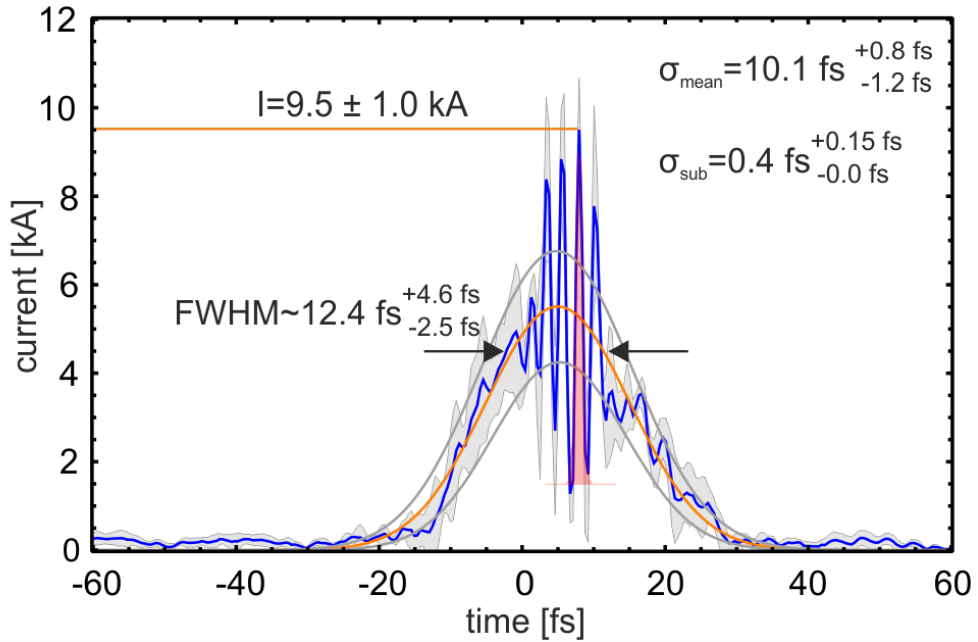
(b) Expanded TR spectra in units of nJ per rad THz on left scales and number of photons per rad Hz on the right scales

Figure A.2.: Absolute calibrated spectra from exemplary shot 396, the raw signals were presented in the previous figure A.1, the spectra acquired by MCT, InGaAs and Echelle spectrometer are plotted in black, red and blue respectively. The absolute calibration of the Echelle and MCT spectra were performed according to the absolute calibration of InGaAs detector.

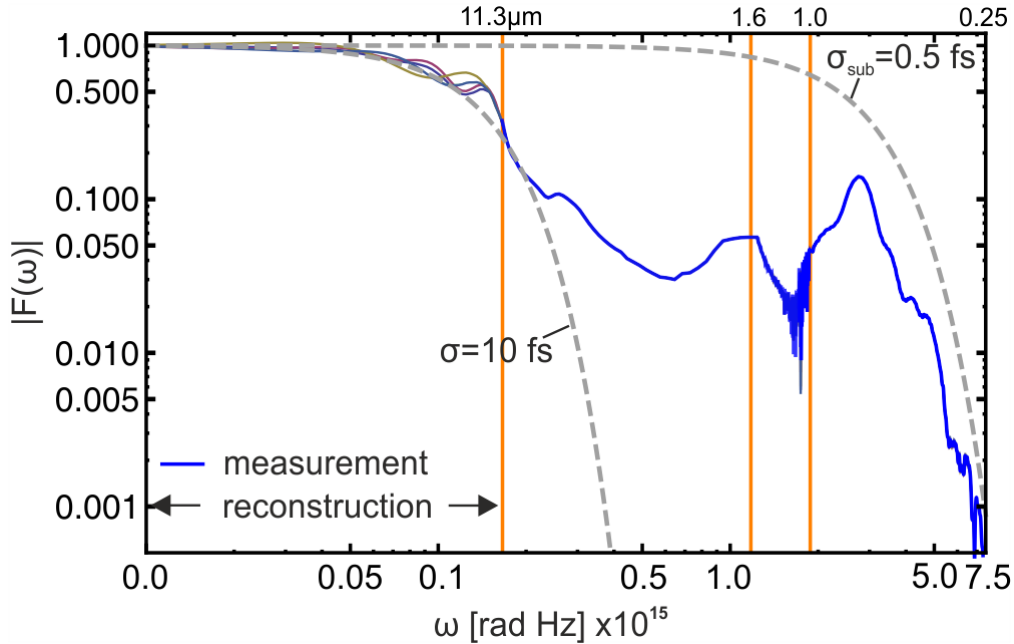
A.2. EXAMPLES FOR BUNCH RECONSTRUCTION



(a) image of lanex screen

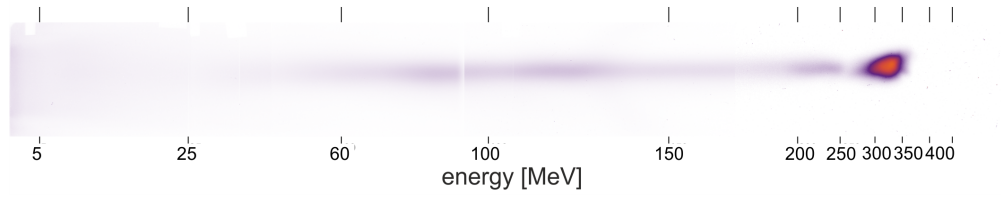


(b) bunch current profile

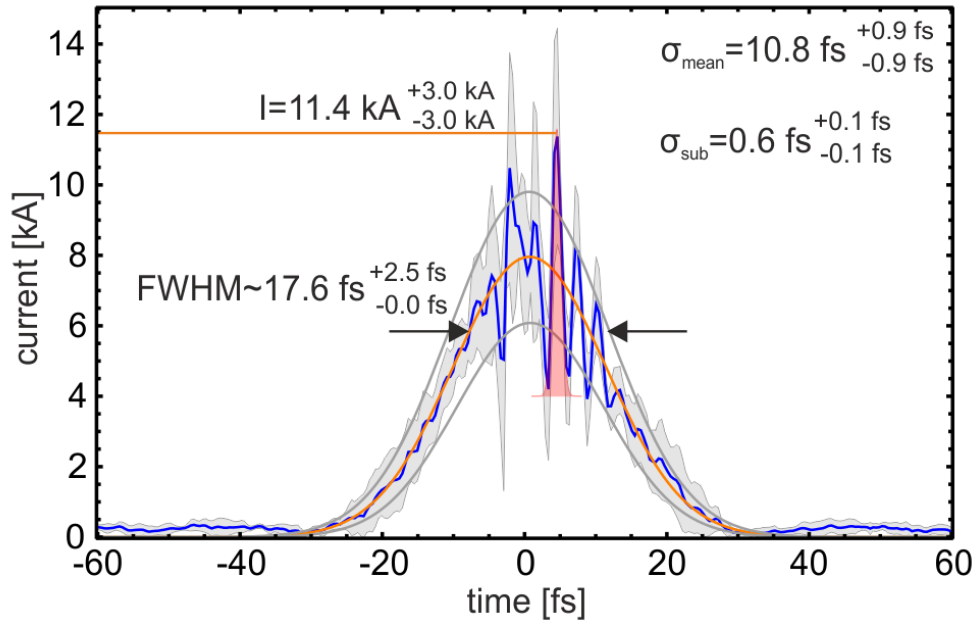


(c) bunch form factor

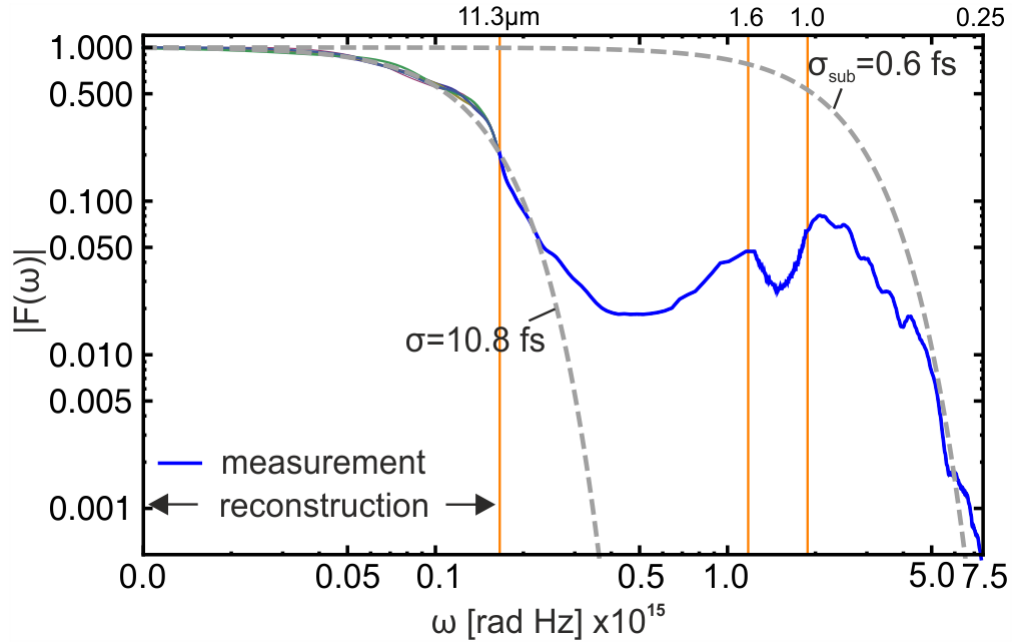
Figure A.3.: summarizes the reconstruction results for the exemplary shot 677, the experimental parameters for the gas mixture utilized here were as follows: 0.5% Nitrogen doping, 8 bar backing pressure ($n_e = 3.81 \times 10^{18} \text{cm}^{-3}$), corresponding the plasma wavelength $\lambda_p = 17.1 \mu\text{m}$.



(a) image of lanex screen

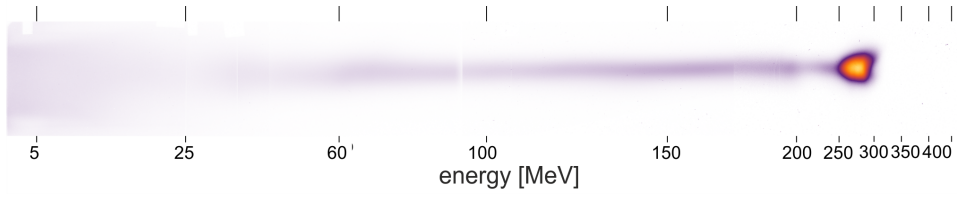


(b) bunch current profile

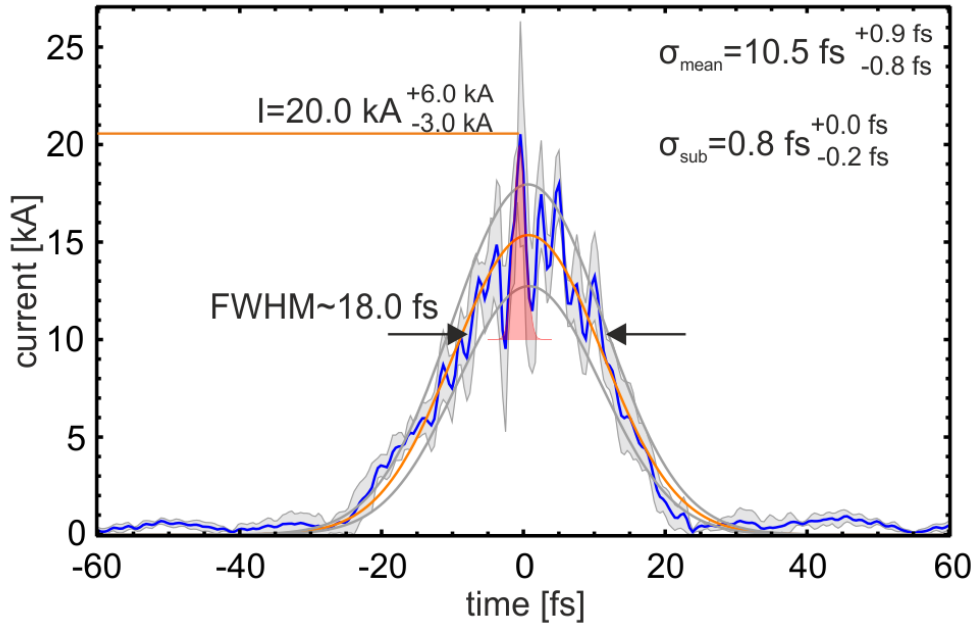


(c) bunch form factor

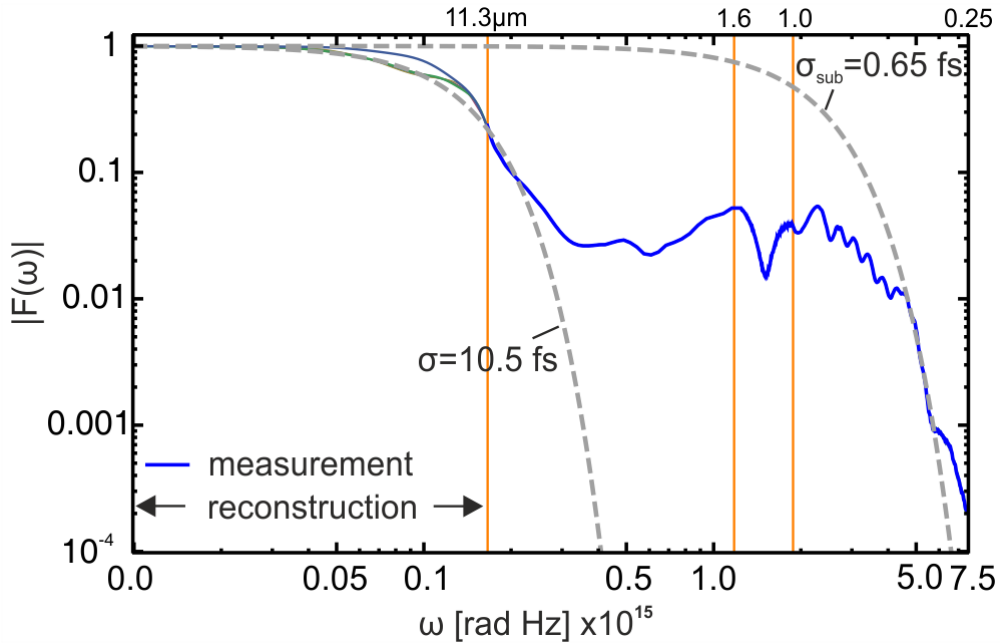
Figure A.4.: summarizes the reconstruction results for the exemplary shot 657, the experimental parameters for the gas mixture utilized here were as follows: 1.0 % Nitrogen doping, 8 bar backing pressure ($n_e = 3.81 \times 10^{18} \text{cm}^{-3}$), corresponding the plasma wavelength $\lambda_p = 17.1 \mu\text{m}$.



(a) image of lanex screen



(b) bunch current profile



(c) bunch form factor

Figure A.5.: summarizes the reconstruction results for the exemplary shot 602, the experimental parameters for the gas mixture utilized here were as follows: 3.0 % Nitrogen doping, 8 bar backing pressure ($n_e = 3.81 \times 10^{18} \text{cm}^{-3}$), corresponding the plasma wavelength $\lambda_p = 17.1 \mu\text{m}$.

BIBLIOGRAPHY

- [1] O. Zarini, "Entwicklung eines breitbandigen optischen Spektrometers zur Pulsdauermessung ultrakurzer Elektronenpulse" (Technische Universität Dresden, 2013).
- [2] O. Zarini et al., "Advanced methods for temporal reconstruction of modulated electron bunches", 1–5 (2018) 10.1109/AAC.2018.8659388.
- [3] O. Zarini et al., "A single-shot, ultra-broadband and highly sensitive spectrometer for short pulse, high resolution and low light diagnostic applications", Phys. Rev. AB (in preparation), 2018.
- [4] J. Couperus et al., "Demonstration of a beam loaded nanocoulomb-class laser wakefield accelerator", Nature communications **8**, 487 (2017) 10.1038/s41467-017-00592-7.
- [5] A Irman et al., "Improved performance of laser wakefield acceleration by tailored self-truncated ionization injection", Plasma Physics and Controlled Fusion **60**, 044015 (2018).
- [6] U Schramm et al., "First results with the novel petawatt laser acceleration facility in dresden", Journal of Physics: Conference Series **874**, 012028 (2017).
- [7] J. Krämer et al., "Making spectral shape measurements in inverse compton scattering a tool for advanced diagnostic applications", Scientific reports **8**, 1398 (2018) 10.1038/s41598-018-19546.
- [8] J. Couperus et al., "Tomographic characterisation of gas-jet targets for laser wakefield acceleration", NIM-A: Accelerators, Spectrometers, Detectors and Associated Equipment **830**, 504–509 (2016) 10.1016/j.nima.2016.02.099.
- [9] A. Köhler et al., "Single-shot betatron source size measurement from a laser-wakefield accelerator", Nuclear Instruments and Methods in Physics Research Section A: Accelerators, Spectrometers, Detectors and Associated Equipment **829**, 2nd European Advanced Accelerator Concepts Workshop - EAAC 2015, 265–269 (2016) 10.1016/j.nima.2016.02.031.
- [10] J. Krämer et al., "Bunch arrival-time monitoring for laser particle accelerators and thomson scattering x-ray sources", Proc. IBIC, 8–10 (2016) 10.18429/JACoW-IBIC2016-TUPG53.
- [11] T. Kurz et al., "Calibration and cross-laboratory implementation of scintillating screens for electron bunch charge determination", Review of Scientific Instruments **89**, 093303 (2018) 10.1063/1.5041755.

- [12] T. Heinemann et al., "Investigating the key parameters of a staged laser-and particle driven plasma wakefield accelerator experiment", 1703–1706 (2017) 10.18429/JACoW-IPAC2017-TUPIK010.
- [13] J. Cockcroft and E. Walton, "Experiments with high velocity positive ions", Proceedings of the Royal Society of London A: Mathematical, Physical and Engineering Sciences **129**, 477–489 (1930) 10.1098/rspa.1930.0169.
- [14] S Doebert, "Gradient limitations for high-frequency accelerators", (2004) 10.2172/833031.
- [15] T. Katsouleas, "Accelerator physics: electrons hang ten on laser wake", Nature **431**, 515 (2004) 10.1038/431515a.
- [16] T. Tajima and J. M. Dawson, "Laser electron accelerator", Phys. Rev. Lett. **43**, 267–270 (1979) 10.1103/PhysRevLett.43.267.
- [17] P. Chen, J. M. Dawson, R. W. Huff, and T. Katsouleas, "Acceleration of electrons by the interaction of a bunched electron beam with a plasma", Phys. Rev. Lett. **54**, 693–696 (1985) 10.1103/PhysRevLett.54.693.
- [18] A Modena et al., "Electron acceleration from the breaking of relativistic plasma waves", nature **377**, 606 (1995) 10.1038/377606a0.
- [19] V. Malka et al., "Electron acceleration by a wake field forced by an intense ultrashort laser pulse", Science **298**, 1596–1600 (2002) 10.1126/science.1076782.
- [20] W. P. Leemans et al., "Electron-yield enhancement in a laser-wakefield accelerator driven by asymmetric laser pulses", Phys. Rev. Lett. **89**, 174802 (2002) 10.1103/PhysRevLett.89.174802.
- [21] C. G. R. Geddes et al., "High-quality electron beams from a laser wakefield accelerator using plasma-channel guiding", Nature **431**, 538–541 (2004) 10.1038/nature02900.
- [22] S. P. D. Mangles et al., "Monoenergetic beams of relativistic electrons from intense laser-plasma interactions", Nature **431**, 535–538 (2004) 10.1038/nature02939.
- [23] J. Faure et al., "A laser-plasma accelerator producing monoenergetic electron beams", Nature **431**, 541 (2004) 10.1038/nature02963.
- [24] A. Buck et al., "Real-time observation of laser-driven electron acceleration", Nature Physics **7**, 543 (2011) 10.1038/nphys1942.
- [25] O Lundh et al., "Few femtosecond, few kiloampere electron bunch produced by a laser-plasma accelerator", Nature Physics **7**, 219–222 (2011) 10.1038/nphys1872.
- [26] A. D. Debus et al., "Electron bunch length measurements from laser-accelerated electrons using single-shot thz time-domain interferometry", Phys. Rev. Lett. **104**, 084802 (2010) 10.1103/PhysRevLett.104.084802.
- [27] S. Gordienko and A. Pukhov, "Scalings for ultrarelativistic laser plasmas and quasimonoenergetic electrons", Physics of Plasmas **12**, 043109 (2005) 10.1063/1.1884126.
- [28] W. Lu et al., "Generating multi-gev electron bunches using single stage laser wakefield acceleration in a 3d nonlinear regime", Phys. Rev. ST Accel. Beams **10**, 061301 (2007) 10.1103/PhysRevSTAB.10.061301.
- [29] Y. F. Li et al., "Generation of 20ka electron beam from a laser wakefield accelerator", Physics of Plasmas **24**, 023108 (2017) 10.1063/1.4975613.
- [30] W. P. Leemans et al., "Observation of terahertz emission from a laser-plasma accelerated electron bunch crossing a plasma-vacuum boundary", Phys. Rev. Lett. **91**, 074802 (2003) 10.1103/PhysRevLett.91.074802.

- [31] B Green et al., “High-field high-repetition-rate sources for the coherent thz control of matter”, *Scientific reports* **6**, 22256 (2016) 10.1038/srep22256.
- [32] A. Jochmann et al., “High resolution energy-angle correlation measurement of hard x rays from laser-thomson backscattering”, *Phys. Rev. Lett.* **111**, 114803 (2013) 10.1103/PhysRevLett.111.114803.
- [33] N. D. Powers et al., “Quasi-monoenergetic and tunable x-rays from a laser-driven Compton light source”, *Nature Photonics* **8**, 28 (2014) 10.1038/nphoton.2013.314.
- [34] G. Sarri et al., “Ultrahigh brilliance multi-mev γ -ray beams from nonlinear relativistic thomson scattering”, *Phys. Rev. Lett.* **113**, 224801 (2014) 10.1103/PhysRevLett.113.224801.
- [35] H.-P. Schlenvoigt et al., “A compact synchrotron radiation source driven by a laser-plasma wakefield accelerator”, *Nature Physics* **4**, 130 (2008) 10.1038/nphys811.
- [36] K. Steiniger et al., “Optical free-electron lasers with traveling-wave thomson-scattering”, *Journal of Physics B: Atomic, Molecular and Optical Physics* **47**, 234011 (2014).
- [37] A. Martinez de la Ossa, J. Grebenyuk, T. Mehrling, L. Schaper, and J. Osterhoff, “High-quality electron beams from beam-driven plasma accelerators by wakefield-induced ionization injection”, *Phys. Rev. Lett.* **111**, 245003 (2013) 10.1103/PhysRevLett.111.245003.
- [38] A. Martinez de la Ossa, T. J. Mehrling, L. Schaper, M. J. V. Streeter, and J. Osterhoff, “Wakefield-induced ionization injection in beam-driven plasma accelerators”, *Physics of Plasmas* **22**, 093107 (2015) 10.1063/1.4929921.
- [39] F. Grüner et al., “Design considerations for table-top, laser-based VUV and x-ray free electron lasers”, *Applied Physics B: Lasers and Optics* **86**, 431–435 (2007) 10.1007/s00340-006-2565-7.
- [40] M. Fuchs et al., “Laser-driven soft-X-ray undulator source”, *Nature Physics* **5**, 826–829 (2009) 10.1038/nphys1404.
- [41] S Dusterer et al., “Femtosecond x-ray pulse length characterization at the linac coherent light source free-electron laser”, *New Journal of Physics* **13**, 093024 (2011).
- [42] N. Rohringer et al., “Atomic inner-shell x-ray laser at 1.46 nanometres pumped by an x-ray free-electron laser”, *Nature* **481**, 488 (2012) 10.1038/nature10721.
- [43] C Behrens et al., “Few-femtosecond time-resolved measurements of x-ray free-electron lasers”, *Nature communications* **5**, 3762 (2014) 10.1038/ncomms4762.
- [44] O. H. Altenmueller, R. R. Larsen, and G. A. Loew, “Investigations of traveling-wave separators for the stanford two-mile linear accelerator”, *Review of Scientific Instruments* **35**, 438–442 (1964) 10.1063/1.1718840.
- [45] K. Floettmann and V. V. Paramonov, “Beam dynamics in transverse deflecting rf structures”, *Phys. Rev. ST Accel. Beams* **17**, 024001 (2014) 10.1103/PhysRevSTAB.17.024001.
- [46] S. Molloy et al., “Energy-z correlation measurements of electron bunches”, *Phys. Rev. ST Accel. Beams* **13**, 082802 (2010) 10.1103/PhysRevSTAB.13.082802.
- [47] G. Berden et al., “Electro-optic technique with improved time resolution for real-time, nondestructive, single-shot measurements of femtosecond electron bunch profiles”, *Phys. Rev. Lett.* **93**, 114802 (2004) 10.1103/PhysRevLett.93.114802.
- [48] G. Berden et al., “Benchmarking of electro-optic monitors for femtosecond electron bunches”, *Phys. Rev. Lett.* **99**, 164801 (2007) 10.1103/PhysRevLett.99.164801.

- [49] J. van Tilborg et al., "Temporal characterization of femtosecond laser-plasma-accelerated electron bunches using terahertz radiation", *Phys. Rev. Lett.* **96**, 014801 (2006) 10.1103/PhysRevLett.96.014801.
- [50] S. Casalbuoni, B. Schmidt, and P. Schmäser, "TESLA REPORT: Far-Infrared Transition and Diffraction Radiation", (2005).
- [51] V. Ginzburg and I. Frank, "To the Theory of Transition Radiation", *Sov. Phys. JETP* **16** (1946).
- [52] C. B. Schroeder, E. Esarey, J. van Tilborg, and W. P. Leemans, "Theory of coherent transition radiation generated at a plasma-vacuum interface", *Phys. Rev. E* **69**, 016501 (2004) 10.1103/PhysRevE.69.016501.
- [53] S. I. Bajlekov et al., "Longitudinal electron bunch profile reconstruction by performing phase retrieval on coherent transition radiation spectra", *Phys. Rev. ST Accel. Beams* **16**, 040701 (2013) 10.1103/PhysRevSTAB.16.040701.
- [54] K. Nakajima et al., "Observation of ultrahigh gradient electron acceleration by a self-modulated intense short laser pulse", *Phys. Rev. Lett.* **74**, 4428–4431 (1995) 10.1103/PhysRevLett.74.4428.
- [55] C. Joshi, T. Tajima, J. M. Dawson, H. A. Baldis, and N. A. Ebrahim, "Forward raman instability and electron acceleration", *Phys. Rev. Lett.* **47**, 1285–1288 (1981) 10.1103/PhysRevLett.47.1285.
- [56] C. Joshi et al., "Ultrahigh gradient particle acceleration by intense laser-driven plasma density waves", *Nature* **311**, 525 (1984) 10.1038/311525a0.
- [57] C. E. Clayton et al., "Ultrahigh-gradient acceleration of injected electrons by laser-excited relativistic electron plasma waves", *Phys. Rev. Lett.* **70**, 37–40 (1993) 10.1103/PhysRevLett.70.37.
- [58] P. Gippson, *Short pulse laser interactions with matter: an introduction* (Imperial College Press, 2005).
- [59] E. Esarey, P. Sprangle, J. Krall, and A. Ting, "Overview of plasma-based accelerator concepts", *IEEE T-PS* **24**, 252–288 (1996) 10.1109/27.509991.
- [60] B. Quesnel and P. Mora, "Theory and simulation of the interaction of ultraintense laser pulses with electrons in vacuum", *Phys. Rev. E* **58**, 3719–3732 (1998) 10.1103/PhysRevE.58.3719.
- [61] E. A. Startsev and C. J. McKinstrie, "Multiple scale derivation of the relativistic ponderomotive force", *Phys. Rev. E* **55**, 7527–7535 (1997) 10.1103/PhysRevE.55.7527.
- [62] W. B. Mori, "The physics of the nonlinear optics of plasmas at relativistic intensities for short-pulse lasers", *IEEE Journal of Quantum Electronics* **33**, 1942–1953 (1997) 10.1109/3.641309.
- [63] E. Esarey, R. F. Hubbard, W. P. Leemans, A. Ting, and P. Sprangle, "Electron injection into plasma wakefields by colliding laser pulses", *Phys. Rev. Lett.* **79**, 2682–2685 (1997) 10.1103/PhysRevLett.79.2682.
- [64] C. D. Decker, W. B. Mori, K. Tzeng, and T. Katsouleas, "The evolution of ultra-intense, short-pulse lasers in underdense plasmas", *Physics of Plasmas* **3**, 2047–2056 (1996) 10.1063/1.872001.
- [65] P. Sprangle, C. M. Tang, and E. Esarey, "Relativistic self-focusing of short-pulse radiation beams in plasmas", *IEEE Transactions on Plasma Science* **15**, 145–153 (1987) 10.1109/TPS.1987.4316677.

- [66] M. Feit, A. Komashko, and A. Rubenchik, "Relativistic self-focusing in underdense plasma", *Physica D: Nonlinear Phenomena* **152-153**, Advances in Nonlinear Mathematics and Science: A Special Issue to Honor Vladimir Zakharov, 705–713 (2001) 10.1016/S0167-2789(01)00203-2.
- [67] M. D. Feit, A. M. Komashko, S. L. Musher, A. M. Rubenchik, and S. K. Turitsyn, "Electron cavitation and relativistic self-focusing in underdense plasma", *Phys. Rev. E* **57**, 7122–7125 (1998) 10.1103/PhysRevE.57.7122.
- [68] E. Esarey, C. B. Schroeder, and W. P. Leemans, "Physics of laser-driven plasma-based electron accelerators", *Rev. Mod. Phys.* **81**, 1229–1285 (2009) 10.1103/RevModPhys.81.1229.
- [69] S. Bulanov, V. Kirsanov, and A. Sakharov, "Excitation of ultrarelativistic plasma waves by pulse of electromagnetic radiation", *JETP Lett* **50**, 4–25 (1989).
- [70] P. Sprangle, E. Esarey, and A. Ting, "Nonlinear interaction of intense laser pulses in plasmas", *Phys. Rev. A* **41**, 4463–4469 (1990) 10.1103/PhysRevA.41.4463.
- [71] P. Sprangle, E. Esarey, and A. Ting, "Nonlinear theory of intense laser-plasma interactions", *Phys. Rev. Lett.* **64**, 2011–2014 (1990) 10.1103/PhysRevLett.64.2011.
- [72] P. Sprangle, E. Esarey, J. Krall, and G. Joyce, "Propagation and guiding of intense laser pulses in plasmas", *Phys. Rev. Lett.* **69**, 2200–2203 (1992) 10.1103/PhysRevLett.69.2200.
- [73] E. Esarey, P. Sprangle, J. Krall, A. Ting, and G. Joyce, "Optically guided laser wakefield acceleration", *Physics of Fluids B* **5**, 2690–2697 (1993) 10.1063/1.860707.
- [74] P. Mora and T. M. Antonsen, "Electron cavitation and acceleration in the wake of an ultraintense, self-focused laser pulse", *Phys. Rev. E* **53**, R2068–R2071 (1996) 10.1103/PhysRevE.53.R2068.
- [75] A. Pukhov and J. Meyer-ter Vehn, "Laser wake field acceleration: the highly non-linear broken-wave regime", *Applied Physics B* **74**, 355–361 (2002) 10.1007/s003400200795.
- [76] W. Lu et al., "A nonlinear theory for multidimensional relativistic plasma wave wakefields", *Physics of Plasmas* **13**, 056709 (2006) 10.1063/1.2203364.
- [77] J. B. Rosenzweig, B. Breizman, T. Katsouleas, and J. J. Su, "Acceleration and focusing of electrons in two-dimensional nonlinear plasma wake fields", *Phys. Rev. A* **44**, R6189–R6192 (1991) 10.1103/PhysRevA.44.R6189.
- [78] M. Everett et al., "Trapped electron acceleration by a laser-driven relativistic plasma wave", *Nature* **368**, 527 (1994).
- [79] F. Amiranoff et al., "Observation of laser wakefield acceleration of electrons", *Phys. Rev. Lett.* **81**, 995–998 (1998) 10.1103/PhysRevLett.81.995.
- [80] M. Kando et al., "Experimental results of laser wakefield acceleration using a femtosecond terawatt laser pulse", *Japanese Journal of Applied Physics* **38**, L967 (1999).
- [81] A. Irman et al., "Design and simulation of laser wakefield acceleration with external electron bunch injection in front of the laser pulse", *Journal of Applied Physics* **102**, 024513 (2007) 10.1063/1.2759878.
- [82] A. Khachatryan et al., "Conceptual design of a laser wakefield acceleration experiment with external bunch injection", *NIM-A: Accelerators, Spectrometers, Detectors and Associated Equipment* **566**, 244–249 (2006) 10.1016/j.nima.2006.07.007.

- [83] A. G. Khachatryan, F. A. van Goor, K.-J. Boller, A. J. W. Reitsma, and D. A. Jaroszynski, "Extremely short relativistic-electron-bunch generation in the laser wakefield via novel bunch injection scheme", *Phys. Rev. ST Accel. Beams* **7**, 121301 (2004) 10.1103/PhysRevSTAB.7.121301.
- [84] I. Kostyukov, A. Pukhov, and S. Kiselev, "Phenomenological theory of laser-plasma interaction in bubble regime", *Physics of Plasmas* **11**, 5256–5264 (2004) 10.1063/1.1799371.
- [85] S. Bulanov, N. Naumova, F. Pegoraro, and J. Sakai, "Particle injection into the wave acceleration phase due to nonlinear wake wave breaking", *Phys. Rev. E* **58**, R5257–R5260 (1998) 10.1103/PhysRevE.58.R5257.
- [86] J. Faure et al., "Controlled injection and acceleration of electrons in plasma wakefields by colliding laser pulses", *Nature* **444**, 737 (2006) 10.1038/nature05393.
- [87] H. Kotaki, S. Masuda, M. Kando, J. K. Koga, and K. Nakajima, "Head-on injection of a high quality electron beam by the interaction of two laser pulses", *Physics of Plasmas* **11**, 3296–3302 (2004) 10.1063/1.1751171.
- [88] H. Suk, N. Barov, J. B. Rosenzweig, and E. Esarey, "Plasma electron trapping and acceleration in a plasma wake field using a density transition", *Phys. Rev. Lett.* **86**, 1011–1014 (2001) 10.1103/PhysRevLett.86.1011.
- [89] C. G. R. Geddes et al., "Plasma-density-gradient injection of low absolute-momentum-spread electron bunches", *Phys. Rev. Lett.* **100**, 215004 (2008) 10.1103/PhysRevLett.100.215004.
- [90] J. Faure, C. Rechatin, O. Lundh, L. Ammoura, and V. Malka, "Injection and acceleration of quasimonoenergetic relativistic electron beams using density gradients at the edges of a plasma channel", *Physics of Plasmas* **17**, 083107 (2010) 10.1063/1.3469581.
- [91] K. Schmid et al., "Density-transition based electron injector for laser driven wakefield accelerators", *Phys. Rev. ST Accel. Beams* **13**, 091301 (2010) 10.1103/PhysRevSTAB.13.091301.
- [92] A. Buck et al., "Shock-front injector for high-quality laser-plasma acceleration", *Phys. Rev. Lett.* **110**, 185006 (2013) 10.1103/PhysRevLett.110.185006.
- [93] A. Pak et al., "Injection and trapping of tunnel-ionized electrons into laser-produced wakes", *Phys. Rev. Lett.* **104**, 025003 (2010) 10.1103/PhysRevLett.104.025003.
- [94] C. McGuffey et al., "Ionization induced trapping in a laser wakefield accelerator", *Phys. Rev. Lett.* **104**, 025004 (2010) 10.1103/PhysRevLett.104.025004.
- [95] M. Chen, E. Esarey, C. B. Schroeder, C. G. R. Geddes, and W. P. Leemans, "Theory of ionization-induced trapping in laser-plasma accelerators", *Physics of Plasmas* **19**, 033101 (2012) 10.1063/1.3689922.
- [96] M. Tzoufras et al., "Beam loading in the nonlinear regime of plasma-based acceleration", *Phys. Rev. Lett.* **101**, 145002 (2008) 10.1103/PhysRevLett.101.145002.
- [97] M. Zeng, M. Chen, Z.-M. Sheng, W. B. Mori, and J. Zhang, "Self-truncated ionization injection and consequent monoenergetic electron bunches in laser wakefield acceleration", *Physics of Plasmas* **21**, 030701 (2014) 10.1063/1.4868404.
- [98] M Mirzaie et al., "Demonstration of self-truncated ionization injection for gev electron beams", *Scientific reports* **5**, 14659 (2015).
- [99] E. Oz et al., "Ionization-induced electron trapping in ultrarelativistic plasma wakes", *Phys. Rev. Lett.* **98**, 084801 (2007) 10.1103/PhysRevLett.98.084801.

- [100] T Katsouleas, S Wilks, P Chen, J. M. Dawson, and J. J. Su, "Beam loading in plasma accelerators", *Particle Accelerators* **22**, 81–99 (1987).
- [101] S van der Meer, Improving the power efficiency of the plasma wakefield accelerator, tech. rep. (CM-P00058040, 1985).
- [102] M. Tzoufras et al., "Beam loading in the nonlinear regime of plasma-based acceleration", *Phys. Rev. Lett.* **101**, 145002 (2008) 10.1103/PhysRevLett.101.145002.
- [103] M. Tzoufras et al., "Beam loading by electrons in nonlinear plasma wakes", *Physics of Plasmas* **16**, 056705 (2009) 10.1063/1.3118628.
- [104] V. Ginzburg, "Transition radiation and transition scattering", 16th International Cosmic Ray Conference **14**, 42–50 (1979).
- [105] M. Ter-Mikaelian, High-energy Electromagnetic Processes in Condensed Media (John Wiley & Sons Inc, 1972), p. 468.
- [106] B. Bolotovskii and A. Serov, "Electro-optic technique with improved time resolution for real-time, nondestructive, single-shot measurements of femtosecond electron bunch profiles", *Physics-Uspekhi* **52**, 487 (2009).
- [107] R. Weingartner et al., "Ultralow emittance electron beams from a laser-wakefield accelerator", *Phys. Rev. ST Accel. Beams* **15**, 111302 (2012) 10.1103/PhysRevSTAB.15.111302.
- [108] S. Kneip et al., "Characterization of transverse beam emittance of electrons from a laser-plasma wakefield accelerator in the bubble regime using betatron x-ray radiation", *Phys. Rev. ST Accel. Beams* **15**, 021302 (2012) 10.1103/PhysRevSTAB.15.021302.
- [109] G. R. Plateau et al., "Low-emittance electron bunches from a laser-plasma accelerator measured using single-shot x-ray spectroscopy", *Phys. Rev. Lett.* **109**, 064802 (2012) 10.1103/PhysRevLett.109.064802.
- [110] K. T. Phuoc et al., "Imaging electron trajectories in a laser-wakefield cavity using betatron x-ray radiation", *Phys. Rev. Lett.* **97**, 225002 (2006) 10.1103/PhysRevLett.97.225002.
- [111] A. H. Lumpkin et al., "Evidence for anomalous optical transition radiation linear polarization effects in beam-profile monitors", *Phys. Rev. ST Accel. Beams* **16**, 102801 (2013) 10.1103/PhysRevSTAB.16.102801.
- [112] V. Lebedev, "Diffraction-limited resolution of the optical transition radiation monitor", *NIM-A: Accelerators, Spectrometers, Detectors and Associated Equipment* **372**, 344–348 (1996) 10.1016/0168-9002(95)01400-4.
- [113] X. Artru, R. Chehab, K. Honkavaara, and A. Variola, "Resolution power of optical transition radiation: theoretical considerations", *NIM-B: Beam Interactions with Materials and Atoms* **145**, 160–168 (1998) 10.1016/S0168-583X(98)00402-9.
- [114] M. Castellano and V. A. Verzilov, "Spatial resolution in optical transition radiation beam diagnostics", *Phys. Rev. ST Accel. Beams* **1**, 062801 (1998) 10.1103/PhysRevSTAB.1.062801.
- [115] A. P. Potylitsyn, M. I. Ryazanov, M. N. Strikhanov, and A. A. Tishchenko, "Radiation from Relativistic Particles", (2010).
- [116] T. J. Maxwell et al., "Coherent-radiation spectroscopy of few-femtosecond electron bunches using a middle-infrared prism spectrometer", *Phys. Rev. Lett.* **111**, 184801 (2013) 10.1103/PhysRevLett.111.184801.

- [117] S Wunderlich, M Yan, B Schmidt, and E Hass, "A double-prism spectrometer for the longitudinal diagnosis of femtosecond electron bunches with mid-infrared transition radiation", in 3rd international beam instrumentation conference, PUBDB-2014-04764 (Forschung Linear Accelerator, 2014).
- [118] S. Wunderlich, "Development and Commissioning of a Double-Prism Spectrometer for the Diagnosis of Femtosecond Electron Bunches", PhD thesis (Universität Hamburg, 2016).
- [119] P. Martinsen, B. Jordan, A. McGlone, P. Gaastra, and T. Laurie, "Accurate and precise wavelength calibration for wide bandwidth array spectrometers", *Applied Spectroscopy* **62**, PMID: 18801240, 1008–1012 (2008) 10.1366/000370208785793399.
- [120] J. M. Lerner and R. M. Zucker, "Calibration and validation of confocal spectral imaging systems", *Cytometry Part A: The Journal of the International Society for Analytical Cytology* **62**, 8–34 (2004) 10.1002/cyto.a.20087.
- [121] X. Du, C. Li, Z. Xu, and Q. Wang, "Accurate wavelength calibration method for flat-field grating spectrometers", *Applied Spectroscopy* **65**, PMID: 21929865, 1083–1086 (2011) 10.1366/11-06280.
- [122] W. S. Hurst, S. J. Choquette, and E. S. Etz, "Requirements for relative intensity correction of raman spectra obtained by column-summing charge-coupled device data", *Applied Spectroscopy* **61**, 694–700 (2007) 10.1366/000370207781393235.
- [123] M. D'orazio and B. Schrader, "Calibration of the absolute spectral response of raman spectrometers", *Journal of Raman Spectroscopy* **2**, 585–592 (1974) 10.1002/jrs.1250020606.
- [124] W. Demtroeder, *Laser spectroscopy*, 4th ed., Vol. 1 (Springer-Verlag, 2008).
- [125] T. Wilson, "The role of the pinhole in confocal imaging system", *Handbook of Biological Confocal Microscopy*, edited by J. B. Pawley, 167–182 (1995) 10.1007/978-1-4757-5348-6_11.
- [126] D. T. F. Marple, "Refractive index of znse, znte, and cdte", *Journal of Applied Physics* **35**, 539–542 (1964) 10.1063/1.1713411.
- [127] D. Meschede, "Optics, light and lasers: the practical approach to modern aspects of photonics and laser physics", (2017).
- [128] G. Ghosh, "Sellmeier coefficients and dispersion of thermo-optic coefficients for some optical glasses", *Applied optics* **36**, 1540–1546 (1997).
- [129] W. Mathematica, "Wolfram research", Inc., Champaign, Illinois (2009).
- [130] N. Hagen and T. S. Tkaczyk, "Compound prism design principles, i", *Appl. Opt.* **50**, 4998–5011 (2011) 10.1364/AO.50.004998.
- [131] N. Hagen and T. S. Tkaczyk, "Compound prism design principles, ii: triplet and janssen prisms", *Appl. Opt.* **50**, 5012–5022 (2011) 10.1364/AO.50.005012.
- [132] N. Hagen and T. S. Tkaczyk, "Compound prism design principles, iii: linear-in-wavenumber and optical coherence tomography prisms", *Appl. Opt.* **50**, 5023–5030 (2011) 10.1364/AO.50.005023.
- [133] "Shott glass data sheets",
- [134] D. T. F. Marple, "Refractive index of znse, znte, and cdte", *Journal of Applied Physics* **35**, 539–542 (1964) 10.1063/1.1713411.
- [135] U. Andor Technology Belfast, *Mechelle manual* (<http://www.andor.com>, 2011).

- [136] A. K. Gaigalas, L. Wang, H.-J. He, and P. DeRose, "Procedures for wavelength calibration and spectral response correction of ccd array spectrometers", *Journal of research of the National Institute of Standards and Technology* **114**, 215 (2009) 10.6028/jres.114.015.
- [137] N Bibinov, H Halfmann, P Awakowicz, and K Wiesemann, "Relative and absolute intensity calibrations of a modern broadband echelle spectrometer", *Measurement Science and Technology* **18**, 1327 (2007).
- [138] H. Budzier and G. Gerlach, *Thermal infrared sensors: theory, optimisation and practice* (John Wiley & Sons, 2011).
- [139] A. Rogalski, *Infrared detectors* (CRC press, 2010).
- [140] "National instruments, labview", National Instruments, LabVIEW: www.ni.com (2016).
- [141] "Postgresql", Web resource: <http://www.PostgreSQL.org/about> (2010).
- [142] F. Gabriel et al., "The rossendorf radiation source elbe and its fel projects", *Nuclear Instruments and Methods in Physics Research Section B: Beam Interactions with Materials and Atoms* **161-163**, 1143–1147 (2000) 10.1016/S0168-583X(99)00909-X.
- [143] A. Daniels, "Field guide to infrared systems, detectors, and fpas", in (SPIE, 2010).
- [144] M Siebold, F Roeser, M Loeser, D Albach, and U Schramm, "PEnELOPE: a high peak-power diode-pumped laser system for laser-plasma experiments", *Proc.SPIE* **8780**, 8780 – 8780 –14 (2013) 10.1117/12.2017522.
- [145] J. P. Couperus, "Optimal beam loading in a nanocoulomb-class laser wakefield accelerator", PhD thesis (Technische Universität Dresden, Sept. 2018), 10.5281/zenodo.1463710.
- [146] D. Strickland and G. Mourou, "Compression of amplified chirped optical pulses", *Optics Communications* **55**, 447–449 (1985) 10.1016/0030-4018(85)90151-8.
- [147] P. Maine, D. Strickland, P. Bado, M. Pessot, and G. Mourou, "Generation of ultrahigh peak power pulses by chirped pulse amplification", *IEEE Journal of Quantum Electronics* **24**, 398–403 (1988) 10.1109/3.137.
- [148] Y. Petit et al., "1-j white-light continuum from 100-tw laser pulses", *Phys. Rev. A* **83**, 013805 (2011) 10.1103/PhysRevA.83.013805.
- [149] M. Messmer, "Führung von laserstrahlen hoher intensität in plasmakanälen", MA thesis (Technische Universität Dresden, Nov. 2014).
- [150] G.-Z. Sun, E. Ott, Y. C. Lee, and P. Guzdar, "Self-focusing of short intense pulses in plasmas", *The Physics of Fluids* **30**, 526–532 (1987) 10.1063/1.866349.
- [151] S. Marchesini et al., "X-ray image reconstruction from a diffraction pattern alone", *Phys. Rev. B* **68**, 140101 (2003) 10.1103/PhysRevB.68.140101.
- [152] U. Weierstall et al., "Image reconstruction from electron and x-ray diffraction patterns using iterative algorithms: experiment and simulation", *Ultramicroscopy* **90**, 171–195 (2002) 10.1016/S0304-3991(01)00134-6.
- [153] O. Shapira, A. F. Abouraddy, J. D. Joannopoulos, and Y. Fink, "Complete modal decomposition for optical waveguides", *Phys. Rev. Lett.* **94**, 143902 (2005) 10.1103/PhysRevLett.94.143902.
- [154] R. P. Millane, "Phase retrieval in crystallography and optics", *J. Opt. Soc. Am. A* **7**, 394–411 (1990) 10.1364/JOSAA.7.000394.

- [155] R. W. Gerchberg and W. O. Saxton, "A practical algorithm for the determination of the phase from image and diffraction plane pictures", *Optik (Jena)* **35** (1972).
- [156] J. R. Fienup, "Phase retrieval algorithms: a comparison", *Appl. Opt.* **21**, 2758–2769 (1982) 10.1364/AO.21.002758.
- [157] S. Bajlekov, "Towards a Free-Electron Laser Driven by Electrons from a Laser-Wake-field Accelerator: Simulations and Bunch Diagnostics", PhD thesis (University of Oxford, 2011).
- [158] M. Heigoldt et al., "Temporal evolution of longitudinal bunch profile in a laser wakefield accelerator", *Phys. Rev. ST Accel. Beams* **18**, 121302 (2015) 10.1103/PhysRevSTAB.18.121302.
- [159] R. W. Saxton, "Computer techniques for image processing in electron microscopy", (1978).
- [160] R. Lai and A. J. Sievers, "Determination of a charged-particle-bunch shape from the coherent far infrared spectrum", *Phys. Rev. E* **50**, R3342–R3344 (1994) 10.1103/PhysRevE.50.R3342.
- [161] R. Lai and A. Sievers, "On using the coherent far ir radiation produced by a charged-particle bunch to determine its shape: i analysis", *Nuclear Instruments and Methods in Physics Research Section A: Accelerators, Spectrometers, Detectors and Associated Equipment* **397**, 221–231 (1997) 10.1016/S0168-9002(97)00690-6.
- [162] D. Pelliccia et al., "Iterative retrieval of one-dimensional x ray wave field using a single intensity measurement", *Opt. Lett.* **37**, 262–264 (2012) 10.1364/OL.37.000262.
- [163] D. Pelliccia and T. Sen, "A two-step method for retrieving the longitudinal profile of an electron bunch from its coherent radiation", *Nuclear Instruments and Methods in Physics Research Section A: Accelerators, Spectrometers, Detectors and Associated Equipment* **764**, 206–214 (2014) 10.1016/j.nima.2014.07.024.
- [164] E. Guillaume et al., "Physics of fully-loaded laser-plasma accelerators", *PR-STAB* **18**, 061301 (2015) 10.1103/PhysRevSTAB.18.061301.
- [165] C. Rechatin et al., "Observation of beam loading in a laser-plasma accelerator", *Phys. Rev. Lett.* **103**, 194804 (2009) 10.1103/PhysRevLett.103.194804.
- [166] H. Bureau et al., "Picongpu: a fully relativistic particle-in-cell code for a gpu cluster", *IEEE Transactions on Plasma Science* **38**, 2831–2839 (2010) 10.1109/TPS.2010.2064310.
- [167] M. Bussmann et al., "Radiative signatures of the relativistic kelvin-helmholtz instability", in *Proceedings of the international conference on high performance computing, networking, storage and analysis, SC '13* (2013), 5:1–5:12, 10.1145/2503210.2504564.
- [168] A. Huebl et al., *Picongpu 0.2.0: beta release - full multiple species support & openpmd*, Nov. 2016, 10.5281/zenodo.168390.
- [169] K. Yee, "Numerical solution of initial boundary value problems involving maxwell's equations in isotropic media", *IEEE Transactions on Antennas and Propagation* **14**, 302–307 (1966) 10.1109/TAP.1966.1138693.
- [170] J.-L. Vay, D. P. Grote, R. H. Cohen, and A. Friedman, "Novel methods in the particle-in-cell accelerator code-framework warp", *Computational Science & Discovery* **5**, 014019 (2012).
- [171] T. Esirkepov, "Exact charge conservation scheme for particle-in-cell simulation with an arbitrary form-factor", *Computer Physics Communications* **135**, 144–153 (2001) 10.1016/S0010-4655(00)00228-9.

- [172] R. W. Hockney and J. W. Eastwood, Computer simulation using particles (crc Press, 1988).
- [173] P. Mulser and D. Bauer, High power laser-matter interaction, Vol. 238 (Springer, 2010).
- [174] K. Németh et al., "Laser-driven coherent betatron oscillation in a laser-wakefield cavity", *Phys. Rev. Lett.* **100**, 095002 (2008) 10.1103/PhysRevLett.100.095002.
- [175] F. S. Tsung et al., "Near-gev-energy laser-wakefield acceleration of self-injected electrons in a centimeter-scale plasma channel", *Phys. Rev. Lett.* **93**, 185002 (2004) 10.1103/PhysRevLett.93.185002.
- [176] X. L. Xu et al., "Nanoscale electron bunching in laser-triggered ionization injection in plasma accelerators", *Phys. Rev. Lett.* **117**, 034801 (2016) 10.1103/PhysRevLett.117.034801.
- [177] R. Pausch et al., "How to test and verify radiation diagnostics simulations within particle-in-cell frameworks", *Nuclear Instruments and Methods in Physics Research Section A: Accelerators, Spectrometers, Detectors and Associated Equipment* **740**, Proceedings of the first European Advanced Accelerator Concepts Workshop 2013, 250 –256 (2014) <https://doi.org/10.1016/j.nima.2013.10.073>.
- [178] R. Pausch et al., "Identifying the linear phase of the relativistic kelvin-helmholtz instability and measuring its growth rate via radiation", *Phys. Rev. E* **96**, 013316 (2017) 10.1103/PhysRevE.96.013316.
- [179] S. Schöbel, "Development and Characterization of a Few-Cycle Probe-Beam setup" (Technische Universität Dresden, 2018).
- [180] M. Schnell et al., "Deducing the electron-beam diameter in a laser-plasma accelerator using x-ray betatron radiation", *Phys. Rev. Lett.* **108**, 075001 (2012) 10.1103/PhysRevLett.108.075001.

ACKNOWLEDGMENTS

Firstly, i would like to thank Prof. Ulrich Schramm for the opportunity to be part of the world-class laser-electron acceleration team at HZDR. His management abilities and scientific expertise gave me enough room to develop my work from different perspectives.

I would also like to thank Prof. Thomas Cowan for the many diverse discussions. His enthusiasm not only for physics but also for metaphysics and religion is exemplary!

Special thanks go to my experimental supervisor Dr. Arie Irman for facilitating the experimental cave and LWFA experiments. Thank you Arie for your unrelenting help and advice throughout my work!

Great thanks go to my theoretical supervisor Dr. Alexander Debus for his continuous support and interest during my work. Without his broad knowledge finishing this work would not have been possible!

Many thanks to the electron team, in particular, Jurjen Couperus Cabadağ, Alexander Köhler, Jacob Krämer, Susanne Schöbel, Thomas Kurz and Yen-Yu Chang for their great supports in many experimental campaigns.

Special thanks go to Prof. Michael Downer from the university of Texas at Austin and his team: Maxwell LaBerge, Andrea Hannasch, Rafal Zgadzaj and Brant Bowers for the fruitful collaboration at HZDR.

I would also like to thank the members of the theory group for providing the PIConGPU simulations: Dr. Michael Bussmann, Richard Pausch, Dr. Klaus Steiniger, Axel Hüble, René Widera, Marco Garten, Heide Meißner and Hauke Mewes.

I want to express my gratitude to Manfred Sobiella for constructing several optomechanical components, specifically the tape-drive, Armin Winter for constructing the spectrometer chamber, Dr. Wolfgang Seidel for advising and providing me many components, Christoph Eisenmann, Simon Grams and René Gebhardt, Stephan Bock and Uwe Helbig for their technical support and the rest of the members of the institute: Karl Zeil, Stephan Kraft, Lieselotte Obst-Hüble, Martin Rehwald, Tim Ziegler, Josephine Metzkes-Ng, Markus Löser, Lingen Huang, Thomas Kluge, Mathias Siebold, Melanie Rödel, Jan Vorberger and many others.

Finally, i want to thank my family and especially my wife for all the support during the final stage of my PhD. Thank You Shadi!

SELBSTÄNDIGKEITSERKLÄRUNG

Hiermit versichere ich, dass ich die vorliegende Arbeit ohne unzulässige Hilfe Dritter und ohne Benutzung anderer als der angegebenen Hilfsmittel angefertigt habe; die aus fremden Quellen direkt oder indirekt übernommenen Gedanken sind als solche kenntlich gemacht. Die Arbeit wurde bisher weder im Inland noch im Ausland in gleicher oder ähnlicher Form einer anderen Prüfungsbehörde vorgelegt.

Die Dissertation wurde unter der wissenschaftlichen Betreuung von Dr. Arie Irman, Dr. Alexander Debus & Prof. Dr. Ulrich Schramm am Helmholtz-Zentrum Dresden–Rossendorf angefertigt.

Die Promotionsordnung, Technische Universität Dresden, Fakultät Mathematik und Naturwissenschaften vom 23.02.2011 mit letzten Änderungen vom 18.06.2014 erkenne ich an.

STATEMENT OF AUTHORSHIP

I herewith declare that I have produced this thesis without the prohibited assistance of third parties and without making use of aids other than those specified; notions taken over directly or indirectly from other sources have been identified as such. This paper has not previously been presented in identical or similar form to any other German or foreign examination board. This dissertation has been prepared at the Helmholtz-Zentrum Dresden–Rossendorf at the Institute for Radiation Physics under supervision of Dr. Arie Irman, Dr. Alexander Debus & Prof. Dr. Ulrich Schramm.

I hereby recognize the Doctoral regulations, Dresden University of Technology, Faculty of Mathematics and Natural Sciences dated 23rd February 2011, last amended 18th June 2014.

Dresden, 17th December 2018

Omid Zarini

.....



Bautzner Landstr. 400
01328 Dresden, Germany
Tel. +49 351 260-2354
Fax +49 351 260-12354
o.zarini@hzdr.de
<http://www.hzdr.de>